Study of the Magneto-structural Transition and Associated Functional Properties in the Ni-Mn-In and Ni-Mn-Sn Alloys

By

Vishnu Kumar Sharma

(Enrolment No PHYS 03200704003)

Raja Ramanna Centre for Advanced Technology
Indore-452 013
India

A thesis submitted to the
Board of Studies in Physical Sciences
In partial fulfillment of requirements
For the Degree of
DOCTOR OF PHILOSOPHY
of
HOMI BHABHA NATIONAL INSTITUTE

September, 2011

Homi Bhabha National Institute

Recommendations of the Viva Voce Board

As members of the Viva Voce Board, we certify that we have read the dissertation prepared by **Vishnu Kumar Sharma** entitled "**Study of the Magneto-structural Transition and Associated Functional Properties in the Ni-Mn-In and Ni-Mn-Sn Alloys**" and recommend that it may be accepted as fulfilling the dissertation requirement for the Degree of Doctor of Philosophy.

Date: 24.02.2012

Chairman – Dr. P. K. Gupta

SBRoy

Date: 24.02.2012

Guide - Dr. S. B. Roy

Date: 24.02.2012

Member 1 - Dr. G. S. Lodha

Date: 24.02.2012

Member 2 - Dr. R. Mukhopadhyay

Skdhar

Date: 24.02.2012

External examiner-Prof. S. K. Dhar

Final approval and acceptance of this dissertation is contingent upon the candidate's submission of the final copies of the dissertation to HBNI.

I hereby certify that I have read this dissertation prepared under my direction and recommend that it may be accepted as fulfilling the dissertation requirement.

Date: 24.02.2012
Place: Indore

Guide: SBRoy
(Dr. S. B. Roy)

STATEMENT BY AUTHOR

This dissertation has been submitted in partial fulfillment of requirements for an advanced degree at Homi Bhabha National Institute (HBNI) and is deposited in the Library to be made available to borrowers under rules of the HBNI.

Brief quotations from this dissertation are allowable without special permission, provided that accurate acknowledgement of source is made. Requests for permission for extended quotation from or reproduction of this manuscript in whole or in part may be granted by the Competent Authority of HBNI when in his or her judgment the proposed use of the material is in the interests of scholarship. In all other instances, however, permission must be obtained from the author.

(Vishnu Kumar Sharma)

DECLARATION

I, hereby declare that the investigation presented in the thesis has been carried out by me. The work is original and has not been submitted earlier as a whole or in part for a degree / diploma at this or any other Institution / University.

(Vishnu Kumar Sharma)

I dedicate this work

to my parents

who taught me basic lessons of life,

and to my children

whose nurturing is still helping me to learn newer lessons.

ACKNOWLEDGEMENTS

I am extremely thankful to my thesis guide *Dr. S. B. Roy* for his valuable guidance, constant support, encouragement and motivation, and patience throughout the course of this work. I am highly obliged to him for his constructive criticism and valuable suggestions, which helped me to present the scientific results in an efficient and effective manner in this thesis.

I am highly thankful to *Dr. M. K. Chattopadhyay* for his enthusiastic support in planning of experiments, analysis of the experimental data and scientific interpretation of the results.

I am thankful to my colleagues *Dr. L. S. Sharath Chandra*, *Dr. A. Khandelwal*, *Smt. P. Arora*, *Dr. K. J. S. Sokhey*, *Shri M. Manekar*, *Shri. S. Nath*, *Shri A. Chouhan* and *Shri R. K. Meena* for their help at different stages of this work and for providing friendly environment.

I thank *Dr. T. Ganguli* and *Shri R. Kumar* for x-ray diffraction characterization of samples, *Smt. P. Tiwari* for energy dispersive analysis of samples. I also thank *Dr. M. K. Tiwari* and *Dr. Gurvinderjit Singh* for characterizing some of the samples with x-ray fluorescence and x-ray diffraction respectively.

My thanks are due to *Dr. K. Morrison*, *Dr. J. D. Moore* and *Prof. L. F. Cohen* of Imperial College, London for helping in scanning Hall probe imaging experiments.

I am also thankful to staff of Cryogenics Section for providing cryogens for various experimental setups used during this work, members of Glass Blowing Facility for helping in ampoule sealing for sample annealing and members of mechanical workshops for their help in fabrication of different components as and when required. I thank *Shri A. K. Sarkar* for his help in design, fabrication and assembly of parts of strain measurement setup.

Thanks, as well, to members of my PhD advisory committee *Dr. P. K. Gupta*, *Dr. G. S. Lodha* and *Dr. R. Mukhopadhyay* for their helpful discussions.

My thanks are due to all of the friends who encouraged and supported me during this work

I am thankful to my wife *Sunita* for the support and care she had provided me during this work. I thank my son *Ritvij* and daughter *Shreyanshi* for providing cheerful atmosphere at home. Last but not the least I would like to express my sincere gratitude to my parents for their never-ending love, and affection to me.

Vishnu Kumar Sharma

Contents

4. Functional properties of the $Ni_{50}Mn_{34}In_{16}$ alloy 101

5. Disorder-influenced first-order phase transition and thermomagnetic history dependence of functional properties in the $Ni_{50}Mn_{34}In_{16}$ alloy **117**

6. Tuning the useful temperature regime of functional properties in the Ni-Mn-In alloy 151

7. Non-equilibrium dynamics of the austenite to martensite transition in the Ni-Mn-In based alloys 203

Synopsis

Heusler alloys showing the magnetic shape memory effect have drawn much attention during last 15 years. Large strain up to 10% has been reported in some of these alloys under application of magnetic field. Various applications have been proposed which can utilize field controlled strain in these alloys. These include linear motors, brakes and clamps, valves, robots, position manipulator, switches, loudspeakers, drills and sonar transducer etc. The magnetic shape memory effect is closely related with the conventional temperature induced shape memory effect observed in special class of alloys like NiTi (Buehler W.J., Gilfrich *J.*V. and Wiley R.C., *J. Appl. Phys*. **34**, 1475 (1963)). A first-order displacive structural phase transition from the high temperature austenite phase to the low temperature martensite phase, known as martensitic transition, plays the key role in the shape memory effect (Ostuka K. and Wayman C. M., *Shape Memory Materials* (Cambridge: Cambridge University Press, 1998)). The martensite state in a shape memory alloy forms a twin structure. The magnetic shape memory alloys can show large strain due to the magnetic field induced reorientation of the twin domains. For example field induced strain as large as 10% has been observed in ferromagnetic Ni-Mn-Ga alloys through such reorientation of the martensite twins (Ullakko K., Huang J. K., Kanther C. and O'Handley R.C., *Appl. Phys. Lett.* **69,** 1966 (1996); Sozinov A., Likhachev A. A., Lanksa N. and Ullakko K., *Appl. Phys. Lett.* **80,** 1746(2002)).

Though Ni-Mn-Ga based alloys seemed to be very promising for field controlled actuation related applications, but the highly brittle nature of these alloys has restricted the use for practical applications. In the quest of better ferromagnetic shape memory alloys some new alloy systems are being investigated. In this regard off-stoichiometric Heusler alloys Ni-Mn-X (X=In,Sn, Sb) have been proposed to be potential candidates for ferromagnetic shape memory effect (Sutou Y., Imano Y., Koeda N., Omori T., Kainuma R., Ishida K. and Oikawa K., *Appl. Phys. Lett.* **85**, 4358 (2004)). In these alloys the martensitic transition is accompanied by a large decrease in magnetization. This magneto-structural transition can be induced by temperature as well as magnetic field. We anticipate that this field induced martensite-austenite transition with the significant change in magnetization may possibly lead to interesting functionalities over and above shape memory effect in these alloys. We expect newer functional properties like magnetic field induced strain arising from the martensite-austenite transition (which is a different mechanism as compared to the twin reorientation), large magnetoresistance and magnetocaloric effect in these alloys. From our exploratory studies we indeed found the existence of such multi-functional properties in some Ni-Mn-In alloys. We also found that the underlying magneto-structural transition is a disorder-influenced first-order phase transition. These findings motivated us to study these Heusler alloys in detail. We have chosen Ni-Mn-In and Ni-Mn-Sn based Heusler alloy systems and have performed detailed experimental studies of the temperature and magnetic field dependence of the electrical, magnetic, thermal and mechanical properties of these alloys across the martensitic transition with the following objectives: (i) to explore the expected multi-functionalities in these alloys, (ii) to study the role of the martensitic transition in the observed multi-functional properties (iii) tuning the functionalities for better practical applications. Chapter-wise summary of this work is given below.

Chapter 1 presents (i) a brief introduction to essentials of magnetism required for understanding of the ferromagnetic shape memory effect, (ii) a discussion on the disorder-influenced first-order phase transition - a phenomenon essential for the understanding of the experimental results presented in the subsequent chapters, (iii) a brief discussion on the martensitic transition and how it gives rise to the shape memory effect and (iv) a brief introduction to Ni-Mn-Ga Huesler alloys showing magnetic shape memory effect and a literature survey on Ni-Mn-X (In, Sn) Heusler alloys .

The details of sample preparation, characterization and working principle of all the experimental setups used in the present study are discussed in **Chapter 2.** We have prepared the alloys by arc melting the required amount of elements in inert argon gas atmosphere. The samples were characterized with x-ray diffraction and energy dispersive x-ray analysis. A brief discussion on the sample preparation and characterizing techniques is given in this **Chapter 2**. The methodology adopted for investigations in the alloy samples is the study of temperature and magnetic field dependence of electrical transport, magnetic, thermal and mechanical properties of the alloy samples. Some of the studies were done in commercial setups namely superconducting quantum interference device (SQUID) magnetometer, vibrating sample magnetometer (VSM) and thermal properties measurement system. Working principle of these setups is discussed in this **Chapter 2**. Two experimental set ups, one for differential scanning calorimetry (DSC) and other for strain measurement, were developed in house during the course of the present work. The differential scanning calorimeter works in the temperature range 100-330 K in zero magnetic field. The strain measurement set up can be used for strain measurement in the temperature range of 30-300K and in magnetic field up to 50 kOe. The same set up has also been used for magnetoresistance measurements. The details of the home made DSC and strain measurement setups are described in **Chapter 2**.

Results of electrical transport, magnetic and thermal properties measurements in $Ni_{50}Mn_{34}In_{16}$ and $Ni_{50}Mn_{34}Sn_{16}$ alloys are discussed in **Chapter 3**. We found that both the $Ni_{50}Mn_{34}In_{16}$ and $Ni_{50}Mn_{34}Sn_{16}$ alloys undergo a martensitic transition from austenite to martensite phase with decreasing temperature in similar temperature regime. Thermal hysteresis associated with a first-order phase transition has been observed in the temperature dependence of all these physical properties. It has been found that the transition in $Ni_{50}Mn_{34}Sn_{16}$ alloy takes place over a comparatively broader temperature regime. Further we observed that the austenite phase has larger value of magnetization as compared to that in the martensite phase in both the alloys. It is also found that in both the alloys the transition shifts to lower temperature with increasing magnetic field. However, this shift is much larger in $Ni_{50}Mn_{34}In_{16}$ alloy. Isothermal magnetization measurements as a function of applied magnetic field show a prominent magnetic field induced martensite to austenite transition in $Ni_{50}Mn_{34}In_{16}$ alloy, while there is only weak signature of such field induced transition in $Ni_{50}Mn_{34}Sn_{16}$ alloy. The correlation between the field induced transition, and the magnitude of magnetization change across the martensitic transition and the width of the associated thermal hysteresis in the corresponding alloy is discussed in this **Chapter 3**. Results of investigations on $Ni_{50}Mn_{34.5}In_{15.5}$ and $Ni_{50}Mn_{35}In_{15}$ alloys are also presented in **Chapter 3**. We show that while $Ni_{50}Mn_{34.5}In_{15.5}$ alloy also undergoes magnetic field induced martensite-austenite transition, $Ni_{50}Mn_{35}In_{15}$ alloy exhibit no detectable signature of field induced transition up to magnetic field of 80 kOe. We expect that this sensitiveness of field induced transition (in the off-stoichiometric Ni-Mn-In Heusler alloys) to the small change in the composition arises from the random distribution of Mn and In atoms at 4(b) lattice site. 4(b) site is occupied by In atom in the stoichiometric ($Ni_{50}Mn_{25}In_{25}$) alloy; in the studied off-stoichiometric Ni-Mn-In alloys 4(b) site is partially occupied by both In and Mn atoms.

The magnetic field induced martensite–austenite transition in Ni-Mn-In alloys imparts interesting functional properties to these alloys. We have studied the properties of $Ni_{50}Mn_{34}In_{16}$

alloy across the martensite –austenite transition in details. **Chapter 4** describes the multi-functional properties observed across the martensite-austenite transition in the $Ni_{50}Mn_{34}In_{16}$ alloy. It has been found that the alloy shows peak magnetoresistance of nearly 45 % near 240 K in magnetic field of 10 kOe, which increases to 65% in magnetic field of 50 kOe. Isothermal magnetic entropy change has also been calculated from isothermal (iso-field) magnetization vs. field (temperature) curves at various temperatures (fields) using Maxwell's equation. It has been found that the peak value of isothermal magnetic entropy change occurs near 240K with value of 14 J/kg-K for field excursion of 20 kOe. This increases to 18 J/kg-K for field excursion of 50 kOe. Estimated refrigerant capacity of the $Ni_{50}Mn_{34}In_{16}$ alloy for various field excursions is also discussed in this **Chapter 4**. This alloy also shows large strain across the temperature and magnetic field induced martensite-austenite transition. We found strain of 0.06% across the temperature induced transition in zero magnetic fields. Similar order of magnitude of strain has also been observed across the magnetic field induced transition in the alloy.

In **Chapter 5** we show that the temperature and magnetic field induced transition in the $Ni_{50}Mn_{34}In_{16}$ is a first-order transition, which is influenced by quenched disorder. The various aspects of the experimental results are understood in the framework of the Imry-Wortis model of disorder-influenced first-order phase transition (Imry Y. and Wortis M., *Phys. Rev.* **B 19**, 3580 (1979)). It is shown that the inverted Arrott plot (i.e isothermal H/M vs. M^2 curves) does not show negative slope at all the temperatures in the temperature regime of first-order martensite-austenite transition as would be expected from widely used Bannerjee's criterion (Banerjee S. K., *Phys. Lett.* **12,** 16 (1964)). The phase coexistence arising from the disorder-influenced first-order nature of the martensite-austenite transition in $Ni_{50}Mn_{34}In_{16}$ alloy leads to thermomagnetic history dependence in the functional properties of the alloy. It is shown that the magnitude and reversibility of the functional response under application of magnetic field depend on the thermomagnetic history of the sample. To get the insight in the thermomagnetic history dependence of the functional properties of the alloy, scanning Hall probe imaging has been performed across the field induced transition. This study gives visual evidence of phase coexistence across the martensite-austenite transition. Thermomagnetic history dependence of the volume fraction of phases has been obtained from this scanning Hall probe imaging study. The presence of a landscape of transition field in the alloy sample obtained from local Hall voltage is also discussed in this **Chapter 5** along with the nucleation and growth mechanism across the transition as suggested by the field dependence of the volume fractions.

The interesting multi-functional properties observed in the $Ni_{50}Mn_{34}In_{16}$ alloy occur around the temperature regime of the martensitic transition around 240 K. For practical applications it is desirable that the useful temperature regime should be near room temperature. Literature suggests that the temperature of martensitic transition increases with the application of external pressure. Elemental substitution is also reported to be affecting the martensitic transition temperature. Further the magnetic properties in Ni-Mn-X alloys arise mainly from Mn sub-lattice. The elemental substitution is expected to modify the magnetic interactions in these alloys. We have chosen Cr and Fe to substitute Mn. Both Cr and Fe are of smaller atomic size as compared to Mn; such substitutions are equivalent to positive external pressure on the sample and the transition temperature is expected to shift to higher temperature. Also there exists some evidence that hybridization of the Ni 3d states with the Mn 3d states affects the martensitic transition in Ni-Mn-Sn alloy. Expecting similar effects in the Ni-Mn-In alloys, we have substituted Ni by Cu in order to increase the hybridization with the Mn 3d states. The results of these elemental substitutions on the martensitic transition in $Ni_{50}Mn_{34}In_{16}$ alloy and associated functional properties have been described in **Chapter 6**. We show that substitution of Mn by Cr and substitution of Ni by Cu elevates the temperature regime of functional properties to room temperature with improved functional properties. Results on the effect of hydrostatic pressure on the martensite-austenite transition and associated properties in $Ni_{50}Mn_{34}In_{16}$ alloy have also been described in this chapter. We show that the effect of applied pressure as well as elemental substitution on the martensitic transition temperature can be correlated with the change in ferromagnetic interaction in these alloys.

We have observed that under certain conditions of temperature and magnetic field the process of austenite to martensite phase transition in $Ni_{50}Mn_{34}In_{16}$ and $Ni_{50}(Mn,1\%Fe)_{34}In_{16}$ alloys is not completed; the transition gets kinetically arrested. The degree of kinetic arrest is shown to decrease with the application of external pressure. This arrested state is a non-equilibrium state, and its dynamical property is quite similar to those observed in structural glasses. This non-equilibrium state has been investigated with time relaxation measurements and temperature cycling experiments. The results of these studies are discussed in **Chapter 7**.

Finally, in **Chapter 8** we conclude the thesis with a summary of the results. Our results show the potential of the off-stoichiometric Heusler alloy $Ni_{50}Mn_{34}In_{16}$ for magnetic refrigeration, magnetic field controlled actuation and magnetoresistance based applications. Our results shed light on how and why these functionalities in the $Ni_{50}Mn_{34}In_{16}$ alloy depend on the thermomagnetic history of the alloy sample. Our results also suggest on how to tune the temperature regime of these functionalities for making the alloy more useful for practical room temperature applications. This **Chapter** also provides a brief discussion on possible future work.

Publications based on the results presented in thesis:

Publications in refereed Journals:

1. The effect of external pressure on the magnetocaloric effect of Ni–Mn–In alloy.

   J. Phys.: Condens. Matter **23**, 366001 (2011).

   Sharma V. K., Chattopadhyay M. K. and Roy S. B.

2. Elevating the temperature regime of the large magnetocaloric effect in a Ni–Mn–In alloy towards room temperature.

   J. Phys. D: Appl. Phys. **44**, 145002 (2011).

   Sharma V. K., Chattopadhyay M. K., Sharathchandra L. S., and Roy S. B.

3. Martensitic transition near room temperature and the temperature- and magnetic-field-induced multifunctional properties of $Ni_{49}CuMn_{34}In_{16}$ alloy.

   Phys. Rev. B **82**, 172411 (2010).

   Sharma V. K, Chattopadhyay M. K., Khandelwal A., and Roy S. B.

4. The effect of substitution of Mn by Fe and Cr on the martensitic transition in the $Ni_{50}Mn_{34}In_{16}$ alloy.

   J. Phys.: Condens. Matter. **22**, 486007 (2010).

   Sharma V. K., Chattopadhyay M. K., Nath S. K., Sokhey K. J. S., Kumar R., Tiwari P., and Roy S. B.

5. Contrasting magnetic behavior of $Ni_{50}Mn_{35}In_{15}$ and $Ni_{50}Mn_{34.5}In_{15.5}$ alloys. *J. Appl. Phys*. **108,** 073909 (2010).

   Chattopadhyay M. K., Manekar M. A., **Sharma V. K.**, Arora P., Tiwari P., Tiwari M. K., and Roy S. B.

6. Large magnetocaloric effect in $Ni_{50}Mn_{33.66}Cr_{0.34}In_{16}$ alloy.

   J. Phys. D: Appl. Phys. **43,** 225001 (2010).

   Sharma V. K., Chattopadhyay M. K., and Roy S. B.

7. Temperature and magnetic field induced strain in $Ni_{50}Mn_{34}In_{16}$ alloy.

J. Phys. D: Appl. Phys. **42**, 185005 (2009).

Sharma V.K., Chattopadhyay M.K., Chouhan A., Roy S.B.

8. A scanning Hall probe imaging study of the field induced martensite-austenite phase transition in $Ni_{50}Mn_{34}In_{16}$ alloy.

   J. Phys.: Condens. Matter. **22**, 016008 (2009).

   Sharma V.K., Moore J. D., Chattopadhyay M.K., Morrison K., Cohen L. F., and Roy S.B.

9. Thermomagnetic history dependence of magnetocaloric effect in $Ni_{50}Mn_{34}In_{16}$. *Appl. Phys. Lett.* **92**, 022503 (2008).

   Chattopadhyay M. K., **Sharma V.K.**, and Roy S. B.

10. Studies on the field-induced martensite to austenite phase transition in $Ni_{50}Mn_{34}In_{16}$.

    J. Phys.: Condens. Matter. **20**, 425210 (2008).

    Sharma V. K., Chattopadhyay M. K., and Roy S. B.

11. Large inverse magnetocaloric effect in $Ni_{50}Mn_{34}In_{16}$.

    J. Phys. D: Appl. Phys. **40**, 1869 (2007).

    Sharma V. K., Chattopadhyay M. K., and Roy S. B.

12. Kinetic arrest of the first order austenite to martensite phase transition in $Ni_{50}Mn_{34}In_{16}$: dc magnetization studies.

    Phys. Rev. B **76**, 140401 (2007).

    Sharma V. K., Chattopadhyay M. K., and Roy S. B.

13. Magnetocaloric effect in Heusler alloys $Ni_{50}Mn_{34}In_{16}$ and $Ni_{50}Mn_{34}Sn_{16}$. *J. Phys.: Condens. Matter* **19**, 496207 (2007).

    Sharma V. K., Chattopadhyay M. K., Kumar R., Ganguli T., Tiwari P., and Roy S. B.

14. Large magnetoresistance in $Ni_{50}Mn_{34}In_{16}$ alloy.

    Appl. Phys. Lett. **89**, 222509 (2006).

    Sharma V. K., Chattopadhyay M. K., Shaeb K. H. B., Chouhan A., and Roy S. B.

Publications in conferences:

1. Large magnetocaloric effect in $Ni_{50}Mn_{33.66}Cr_{0.34}In_{16}$ alloy.

   Proceedings of the DAE Solid State Physics Symposium, Vol. 54, 1017 (2009).

   Sharma V. K., Chattopadhyay M. K., Kumar R., and Roy S. B.

2. Thermomagnetic history dependence of magnetic field induced strain in $Ni_{50}Mn_{34}In_{16}$.

   Proceedings of the DAE Solid State Physics Symposium, Vol. 54 , 1015 (2009).

   Sharma V.K., Chattopadhyay M.K., and Chouhan A.

3. Study of magnetization and Magnetoresistance across the field induced martensite to austenite transition in $Ni_{50}Mn_{34}In_{16}$.

   Proceedings of the DAE Solid state physics symposium , Vol. 53, 1101 (2008).

   Sharma V.K., Chattopadhyay M.K., and Roy S.B.

4. Field induced martensite to austenite transition in $Ni_{50}Mn_{34}In_{16}$ alloy.

   Proceedings of the DAE Solid State Physics Symposium, Vol. 52 , 1035 (2007).

   Sharma V.K., Chattopadhyay M.K., Chouhan A., Arora P., and Roy S.B.

5. Effect of annealing on the martensitic transition in $Ni_{50}Mn_{34}In_{16}$ alloy.

   Proceedings of the DAE Solid State Physics Symposium, Vol. 52 , 1031(2007).

   Sharma V.K., Chattopadhyay M.K., Chouhan A., Arora P., Kumar R., Ganguli T., and Roy S.B.

Symbols and Abbreviations

- AFM : antiferromagnetic
- β_{G} : temperature coefficient of strain gauge resistance
- AST : austenite
- C : heat capacity
- χ : susceptibility
- χ_{ac} : ac susceptibility
- EDX : energy dispersive x-ray
- DSC : differential scanning calorimetry
- ε : strain
- $\Delta L/L$: relative length change
- ΔS_{M} : isothermal magnetic entropy change
- ΔT_{ad} : adiabatic temperature change
- d_{hkl} : inter-planar spacing of planes with Miller indices (*hkl*)
- f : phase fraction
- F : gauge factor
- fcc : face centred cubic
- FCC : field cooled cooling
- FCW : field cooled warming
- FM : ferromagnetic
- G : free energy
- γ : gyromagnetic ratio
- H : magnetic field
- H^{*} : limit of supercooling while decreasing magnetic field
- H^{**} : limit of superheating while increasing magnetic field
- H_{M} : martensite start field

○ H_{A} : austenite start field

○ I : current

○ J : angular momentum

○ J_{ex} : exchange parameter

○ K : thermal conductance

○ K_{DSC} : sensitivity of DSC setup

○ $\mathcal{K}$: anisotropy constant

○ L : length

○ λ : wavelength

○ λ_{m} : magnetostriction

○ L_{Q} : latent heat

○ M : magnetization

○ μ : magnetic moment

○ MCE : magnetocaloric effect

○ MR : magnetoresistance

○ MST : martensite

○ MT : martensitic transition

○ N : demagnetizing factor

○ P : hydrostatic pressure

○ ϕ : angle

○ PM : paramagnetic

○ P_w : power

○ Q : heat

○ R : resistance

○ ρ : resistivity

○ RC : refrigerant capacity

○ $\mathrm{RC}_{\mathrm{EFF}}$: effective refrigerant capacity

○ S : entropy

○ s : spin

○ ψ : order parameter

○ SQUID : superconducting quantum interference device

○ t : time

○ T : temperature

○ T^{*} : limit of supercooling of the high-T phase

○ T^{**} : limit of superheating of the low-T phase

○ T_{AF} : temperature of austenite finish

○ T_{AS} : temperature of austenite start

○ T_{C} : thermodynamical phase transition temperature,
Curie temperature for PM to FM transition

○ T_{CA} : Curie temperature of the austenite phase

○ T_{CM} : Curie temperature of the martensite phase

○ θ : rescaled temperature

○ θ_{p} : paramagnetic Curie temperature

○ $T_{\mathrm{MCE\text{-}peak}}$: temperature of ΔS_{M} peak

○ T_{MF} : temperature of martensite finish

○ T_{MS} : temperature of martensite start

○ σ : stress

○ V : volume

○ $\mathcal{V}$: voltage

○ VF : volume fraction

○ VSM : vibrating sample magnetometer

○ XRD : x-ray diffraction

○ ZFC : zero field cooled

List of Figures

Chapter 1

Chapter 2

Chapter 3

Chapter 4

Chapter 5

Chapter 6

Chapter 7

List of Tables

Chapter 1

Chapter 4

Chapter 5

Chapter 6

Chapter 7

Chapter 1

Introduction

1.1 General introduction

Heusler alloys form a special class of materials that crystallize in the $L2_1$ crystal structure. The Heusler alloy system is the first alloy system reported to show ferromagnetism where none of the constituents was ferromagnetic (e.g. Cu_2MnSn and Cu_2MnAl alloys). Recently, the ferromagnetic shape memory Heusler alloys have attracted considerable attention for their potential for magnetic field (H) controlled actuation applications. Some of these alloys have been reported to show magnetic field induced strain as large as 10%. This strain is almost two orders of magnitude larger than ~0.1 % strain observed in the piezoelectric materials, and ~0.2% strain exhibited by the leading magnetostrictive material Terfenol-D. The shape memory effect observed in ferromagnetic shape memory alloys is closely related with the conventional temperature induced shape memory effect observed in some special classes of alloys, in which NiTi [1.1] alloys are the most famous. A first-order displacive structural phase transition from the high temperature austenite (AST) phase to the low temperature martensite (MST) phase, also known as martensitic transition (MT), plays the key role in the shape memory effect [1.2] (in the rest of the thesis the term 'martensitic transition' will be represented interchangeably by MT, 'AST-MST phase transition' or 'MST-AST phase transition'). The MST phase in a shape memory alloy has a twin structure. The twins can reorient under the application of an external stress resulting in a large recoverable strain in the material. This leads to the conventional shape memory and superelasticity in materials like NiTi alloys. When the MST phase is ferromagnetic in nature and has large magnetocrystalline anisotropy, an applied magnetic field can also lead to twin reorientation. Such magnetic field controlled reorientation of MST twins [1.3] is responsible for the large magnetic field induced strain of the order of 10% observed in some ferromagnetic Ni-Mn-Ga alloys ($Ni_{48.8}Mn_{29.7}Ga_{21.5}$) [1.4]. Interesting applications have been proposed utilizing this large magnetic field controlled strain. These include linear motors, brakes and clamps, valves, robots, position manipulators, switches, loudspeakers, drills and sonar transducers etc.

With the discovery of large magnetic field induced strain in the Ni-Mn-Ga based ferromagnetic shape memory alloys, these alloys seemed to be very promising for magnetic field controlled actuation related applications. However, their highly brittle nature has restricted the use of these alloys in practical applications. In the search of other suitable ferromagnetic shape memory alloys some new alloy systems are being investigated. In this context, off-stoichiometric Heusler alloys $Ni_{50}Mn_{50-y}X_y$ (X = In,Sn, Sb and y = 10 - 16.5) have been identified as potential candidates for ferromagnetic shape memory effect [1.5] during the last decade. Unlike the Ni-Mn-Ga alloys where the difference between magnetization of the MST and AST phases is not large, the MT in these Ni-Mn-X alloys is accompanied with a large decrease in magnetization. This magneto-structural transition can be induced by temperature (T) as well as magnetic field. We anticipate that this magnetic field induced MST-AST phase transition is likely to give rise to appreciable changes in various thermodynamic and transport properties. This in turn would lead to new and interesting functionalities in these alloys apart from shape memory effect. We expect magnetic field induced strain in these alloys arising from the magnetic field induced MST-AST phase transition. This mechanism is different from the twin reorientation observed in the Ni-Mn-Ga alloys. We also anticipate the magnetic field induced MST-AST phase transition to give rise to a large magnetoresistance (MR) and magnetocaloric effect (MCE) in these alloys. We have chosen Ni-Mn-In and Ni-Mn-Sn based Heusler alloy systems for detailed experimental investigations. We have performed a detailed study of the temperature and magnetic field dependence of various physical properties of these alloys across the MT. Our objectives of this study are: (i) to explore the anticipated multi-functional properties in these alloys, (ii) to study the role of the martensitic transition in the observed multi-functional properties and (iii) to find the ways of tuning the functionalities for better practical applications. From our experimental studies we show the existence of enhanced multi-functional properties in some compositions of Ni-Mn-In alloys. These functional properties depend on thermomagnetic history the alloy. Our study has revealed that the temperature regime of these functionalities can be tuned by the chemical substitution and external pressure for practical room temperature applications.

In the rest of this Chapter 1, we present a brief discussion on the essentials of the subject of magnetism and phase transitions required for the understanding of the experimental work presented in this thesis. This is followed by an introduction to the MT and how it leads to the conventional shape memory effect in alloy systems like NiTi. Finally, a discussion on the ferromagnetic shape memory effect in the Ni-Mn-Ga alloys and a literature survey on the new classes of potential ferromagnetic shape memory alloys Ni-Mn-In and Ni-Mn-Sn, are presented.

The details of sample preparation, characterization and working principles of the experimental setups (commercial setups used for the present study as well as the experimental setups developed during the course of this work) used in the present study are discussed in Chapter 2**.** Results of various experimental measurements in the $Ni_{50}Mn_{34}In_{16}$ and $Ni_{50}Mn_{34}Sn_{16}$ alloys are discussed in Chapter 3. Compositional dependence of the physical properties in the Ni-Mn-In alloys is also investigated in Chapter 3. The multi-functional properties observed across the MST-AST phase transition in the $Ni_{50}Mn_{34}In_{16}$ alloy are described in Chapter 4. We show that the temperature and magnetic field induced MST-AST phase transition in the $Ni_{50}Mn_{34}In_{16}$ alloy is a disorder-influenced first-order phase transition, and this leads to a phase coexistence across the transition. In Chapter 5 we discuss how this phase coexistence gives rise to the thermomagnetic history dependence of the functional properties of the $Ni_{50}Mn_{34}In_{16}$ alloy. Results on the effect of chemical substitutions and external pressure, on the MST-AST phase transition in $Ni_{50}Mn_{34}In_{16}$ alloy and associated functional properties are described in Chapter 6. In Chapter 7 we show that under certain conditions of temperature and magnetic field, the process of the AST to MST phase transition in $Ni_{50}Mn_{34}In_{16}$ and $Ni_{50}(Mn,1\%Fe)_{34}In_{16}$ alloys is not completed; the kinetics of the phase transition gets arrested. This arrested state is a non-equilibrium state, and its dynamical properties are quite similar to those observed in structural glasses. Our investigations in this non-equilibrium state are discussed in Chapter 7. In Chapter 8 we conclude the thesis with a summary of the results and a brief discussion on possible future work.

1.2 Fundamentals of magnetism

The magnetic properties of a material arise from existence of a magnetic moment (μ) in the material even in the absence of an applied magnetic field and from induction of magnetic moment in response to an applied magnetic field. Classically, a magnetic moment is equivalent to a current loop [1.6]. However, Bohr-van Leeuwen theorem defies the existence of any magnetic moment in a classical system of electrons [1.6]. Quantum mechanically, the magnetic properties of a material owe their origin ultimately to the magnetic moment of the electrons and nucleons in the atoms of the material. The magnetic moment of the nucleons is three orders of magnitude smaller than that of the electrons [1.6] and is negligible for the kind of work described in the present thesis. The electronic magnetic moment has two sources. First is the magnetic moment associated with the intrinsic spin angular momentum (sometimes simply referred as spin) of the electron and designated as 'spin magnetic moment', and second is that arising from the orbital angular momentum of the electron around the nucleus of the atom and denoted as 'orbital magnetic momentum'. The spin and orbital components of magnetic moment of an electron are related to the respective angular momentum as $\mu = \gamma J$. Here μ and J represent spin magnetic moment and spin angular momentum in case of spin of the electron. In case of orbital motion of the electron, μ represents orbital magnetic moment and J stands for orbital angular momentum. γ is the gyromagnetic ratio and has different values for spin and orbital motion of the electron. The spin and orbital angular momenta combine to form a net angular momentum which gives rise to net magnetic moment to the atom. The magnetization (M) of the material is the net magnetic moment per unit volume. Sometimes, in the solid state, the orbital angular momentum does not contribute to magnetism because it is quenched under the environment of the neighboring atoms (designated as crystal field effect). Further, the completely filled electronic shells in the atom give rise to a diamagnetic response. Various aspects of magnetism in materials are introduced briefly in the following sections.

1.2.1 Localized magnetic moment and itinerant magnetic moment

In some solids the electrons carrying the magnetic moment are not free to move inside the solid. They are rather bound to the respective atoms. These electrons impart certain magnetic moment to the atom and the magnetic moment is localized at the respective atom [1.7]. Such atoms/ions in the system are called magnetic ions. 3d transition metal oxide insulators, and rare earth metals and their intermetallic compounds are examples of such systems.

In some cases, the electrons carrying the magnetic moment are not localized to atoms in solid and can move from one location to another (electrons are itinerant) inside the solid. In this case magnetic moment is not localized at the atom but is a property of the collection of electrons in the solid and is termed as itinerant magnetic moment [1.7]. Fe, Ni and Co are examples of such systems.

1.2.2 Exchange interaction

Quite often the magnetic moments (or spins) are able to interact with the neighbors and assume a specific orientation with respect to the neighbouring moments. The driving force for aligning the different spins in a particular fashion arises from exchange interaction between the spins. The exchange interaction is of a quantum mechanical origin. It is a direct consequence of the Pauli Exclusion Principle and the Coulomb interaction for a system of electrons [1.6-1.8]. In the case of isotropic interaction, the interaction energy (exchange energy) between two spins s_i and s_j can be written as

$$E_{ij} = -2J_{\mathrm{ex}} \mathrm{s}_i \mathrm{s}_j \cos\phi \qquad (1.1)$$

where J_{ex} is the exchange parameter and ϕ is the angle between the two spins. For a positive J_{ex} the parallel configuration of spins has a lower energy, while for a negative J_{ex} the anti-parallel configuration is lower in energy. Parallel and anti-parallel configurations of spins are referred as ferromagnetic and antiferromagnetic configurations respectively. Various types of exchange interaction are listed below.

(a) Direct exchange: In this case the neighbouring spins interact directly. Systems with itinerant magnetic moment can be considered as examples of such systems.

(b) Indirect exchange: In many of the cases the distance between the spins is such that direct exchange is not possible. In such cases the spins can interact through some inter-mediatory and the interaction is termed as indirect exchange.

(i) Super exchange: It is the interaction between two magnetic ions separated by a non magnetic ion and has been observed in antiferromagnetic insulators like MnO, NiO etc.

(ii) Ruderman-Kittel-Kasuya-Yosida (RKKY) interaction: In some cases the exchange interaction is mediated by conduction electrons. Localized magnetic moment on one atom spin-polarizes the conduction electrons. This spin polarization which has spatial oscillatory character and diminishes with distance, couples magnetic atoms at a distance. This is known as the RKKY interaction. The resultant configuration of the two spins (of the magnetic ions) can be ferromagnetic or anti-ferromagnetic depending on the separation between them.

(iii) Double exchange. This is the interaction between magnetic ions of mixed valence via non magnetic ions. Examples of this are alloys containing Mn which can exist as Mn^{3+} or Mn^{4+}.

1.2.3 Types of magnetic materials

Different relative orientation of the neighbouring spins leads to various magnetic orders. Though there is a whole list of types of magnetic materials [1.9], only five basic types of magnetic materials are discussed below briefly.

(i) Diamagnetic: In some materials application of magnetic field induces a very small magnetic moment in the direction which is opposite to the applied magnetic field. This phenomenon is known as diamagnetism. This phenomenon arises from the completely filled atomic orbital (electronic magnetic moments sum to zero). Diamagnetism is present in all materials but is generally overshadowed by other magnetic order.

(ii) Paramagnetic: In paramagnetic materials there is a magnetic moment at atomic scale with no ordering at finite temperature leading to net zero magnetization in the absence of magnetic field. These magnetic moments have a tendency to align along the direction of the applied magnetic field leading to a finite magnetization in applied magnetic field. A paramagnetic system with localized magnetic moments obeys Curie's law which states that the magnetic susceptibility (χ) varies inversely as temperature. If a small applied magnetic field H gives rise to magnetization M. Then

$$\chi = \underset{H \to 0}{Lim} \frac{M}{H} = \frac{C_{Curie}}{T} \qquad (1.2)$$

The proportionality constant C_{Curie} is material specific. From C_{Curie} the value of magnetic moment per moment carrier can be extracted. Inverse χ vs. temperature plot intercepts the temperature axis at zero (see Fig. 1.1). Conduction electrons in metals exhibit Pauli paramagnetism which shows a temperature independent magnetic susceptibility.

(iii) Ferromagnetic: A ferromagnetic material has a spontaneous magnetization even in the absence of an applied magnetic field and there is a long range order of the magnetic moments at temperatures lower than T_C known as the Curie temperature of the ferromagnetic system. As already mentioned, the ferromagnetic ordering arises from the exchange interaction between the magnetic moments with a positive value of exchange constant. Temperature dependence of the susceptibility at temperatures above T_C follows the Curie-Weiss law

$$\chi = \underset{H \to 0}{Lim} \frac{M}{H} = \frac{C_{Curie}}{T - \theta_p} \qquad (1.3)$$

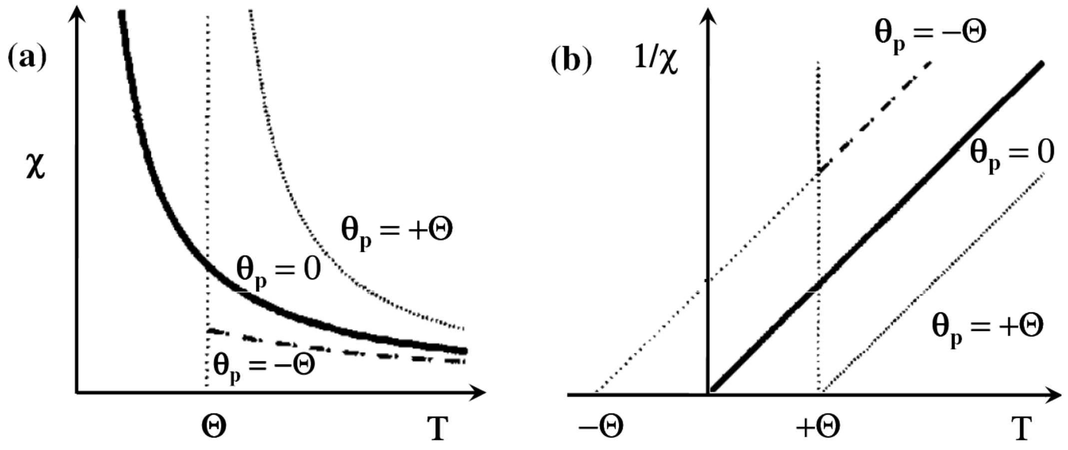

Fig. 1.1: (a) Magnetic susceptibility (χ) vs. temperature (T) plot at $T>\theta_p$ for paramagnet ($\theta_p = 0$), ferromagnet ($\theta_p > 0$) and antiferromagnet ($\theta_p < 0$) (from Ref. 1.6). Here θ_p is the paramagnetic Curie temperature. (b) $1/\chi(T)$ plot for the three cases. In paramagnet, ferromagnet and antiferromagnet, intercept on the temperature axis is at zero, positive and negative value respectively.

Where θ_p is the paramagnetic Curie temperature and its value depends on the strength of the exchange interaction and number of neighbors. Inverse χ vs. temperature plot intercepts the temperature axis at θ_p (see Fig. 1.1).

(iv) Antiferromagnetic: When the exchange parameter is negative, neighboring magnetic moments are aligned anti-parallel and the resultant order is known as the antiferromagnetic order. Very often in an antiferromagnetic material there are two sub-lattices with equal magnetic moments pointing in opposite directions. Each of the sub-lattices has a spontaneous magnetization even in the absence of an applied magnetic field just like a ferromagnet. The two sub-lattices order antiferromagnetically at temperature lower than T_N known as the Neel temperature. At $T>T_N$ the two sub-lattices show paramagnetic behavior and the temperature dependence of susceptibility at $T> T_N$ follows

$$\chi = \lim_{H\to 0} \frac{M}{H} = \frac{C_{Curie}}{T+\Theta} \qquad (1.4)$$

Comparing with the Curie-Weiss law in a ferromagnet (see eqn. (1.3)), this gives a negative paramagnetic Curie temperature $\theta_p = -\Theta$ in the present case. Inverse χ vs. temperature plot intercepts the temperature axis at negative value (see Fig. 1.1). This gives a method to differentiate between paramagnetic, ferromagnetic and antiferromagnetic materials as shown in Fig.1.1 [1.6].

(v) Ferrimagnetic: In some cases two the sub-lattices with antiferromagnetic order, do not have equal magnetic moments. Then contrary to the case of an antiferromagnet, the net magnetization is not zero. Such a magnetic order is known as the ferrimagnetic order. The net magnetic moment can have very different temperature dependences depending on the temperature dependences of the magnetic moments of the two sub-lattices. Such systems do not follow the Curie-Weiss law [1.6].

1.2.4 Energy of a magnetic moment in an applied magnetic field

The energy of a magnetic moment μ lying in a magnetic field H with an angle ϕ with the magnetic field is given by

$$E = -\mu(\mu_0 H)\cos\phi \qquad (1.5)$$

where μ_0 is the permeability of free space. This energy is minimum when the magnetic moment is aligned with the magnetic field direction (at $\phi = 0$). So the magnetic moment tends to align along the applied magnetic field to minimize the energy.

1.2.5 Magnetic anisotropy

In an isotropic material its physical properties are independent of direction. However, most of the magnetic materials show some preferred direction of magnetization and are said to be anisotropic in nature. Magnetic anisotropy simply means that because of one or other reason it is relatively easy to magnetize a ferromagnetic material (crystal) along certain direction/directions. This magnetic anisotropy arises from the dependence of the energy of the system on the orientation of the magnetization with respect to the crystal axes. The energy of the system is minimum for magnetization lying along a particular direction known as the easy axis of magnetization. It is maximum for magnetization lying along some other direction called as the hard axis of magnetization. Rotation of magnetization from an easy axis towards a hard axis increases the energy of the system. The magnetic anisotropy can be intrinsic to the system e.g. magnetocrystalline anisotropy, or it can be extrinsic e.g. magneto-elastic anisotropy and shape anisotropy [1.7]. These are discussed in the following sub-sections.

(a) Magnetocrystalline anisotropy: This anisotropy arises from the spin–orbit coupling. This coupling causes the electronic spin to bind to the respective electronic orbital to some extent. However the electronic orbitals are highly directional as determined by the symmetry of the crystal (due to lattice-orbital coupling). This tends to align the spin along some specific direction, with respect to the lattice axes, which is determined by the orbital orientation. Spin alignment along this direction corresponds to the minimum energy configuration of the system. Alignment of the magnetic moment along a direction different from this easy axis results in an increase in the energy of the system, and this energy is a maximum when the direction is along a hard axis. This magnetocrystalline anisotropy plays a crucial role in ferromagnetic shape memory effect (discussed in section 1.5.2 of this Chapter). Type of the magnetocrystalline anisotropy and expression for it depends on the crystal structure.

(i) Uniaxial anisotropy is exhibited by hexagonal and tetragonal crystals. These have a single axis, along which the alignment of magnetic moment corresponds to either minimum energy (easy axis) or maximum energy (hard axis) of the system. In such a case the energy of the system arising from magnetic anisotropy is expressed as [1.6, 1.8]

$$E_{\mathcal{K}} = \mathcal{K}_1 \sin^2 \phi + \mathcal{K}_2 \sin^4 \phi + ... \qquad (1.6)$$

where ϕ is the angle between the magnetization direction and this (easy/hard) axis. $\mathcal{K}_i$ (i = 1,2,..) are anisotropy constants of the system. For example in hexagonal cobalt [0001] (c axis) is the easy axis of magnetization [1.8].

(ii) Cubic anisotropy is found in cubic crystals. In this case, the energy of the system arising from magnetic anisotropy is given by [1.6, 1.8]

$$E_{\mathcal{K}} = \mathcal{K}_1(\alpha_1{}^2\alpha_2{}^2 + \alpha_1{}^2\alpha_3{}^2 + \alpha_2{}^2\alpha_3{}^2) + \mathcal{K}_2(\alpha_1{}^2\alpha_2{}^2\alpha_3{}^2) + ... \qquad (1.7)$$

Where $\alpha_n (n = 1,2,3)$ are the direction cosines of the magnetic moment with respect to the cubic axes and $\mathcal{K}_i$ (i=1, 2, ...) are the material specific anisotropy constants. In the body centered cubic iron the [100] direction is the easy axis and [111] is the hard axis [1.8]. In the face centered cubic Ni the [111] direction is the easy axis and [100] is the hard axis [1.8] (for designation of the directions in a crystal see section 2.2.2 of Chapter 2).

(b) Magneto-elastic (or stress) anisotropy: Anisotropy arising from the mechanical deformation in a magnetic system is known as magneto-elastic or stress anisotropy. The magneto-elastic effect arises from the spin-orbit coupling. The spin moments are coupled to the lattice through the orbital motion (mediated by the spin-orbit and orbit-lattice coupling). When the lattice is deformed, the distances between the magnetic atoms are altered and hence the interaction energies vary. Alignment of the magnetic moment along certain direction may lower the energy as compared to the alignment along other directions. This produces magneto-elastic anisotropy. Magneto-elastic anisotropy is the inverse of magnetostriction in which the magnetic system gets deformed when it is magnetized. For an elastically isotropic medium with isotropic magnetostriction λ_m, the magneto-elastic energy per unit volume under stress σ is given by the following equation [1.7].

$$E_{me} = -\frac{3}{2}\lambda_m \sigma \cos^2\phi = \mathcal{K}_\sigma \cos^2\phi \tag{1.8}$$

where ϕ is the angle between the magnetization and stress directions, and $\mathcal{K}_\sigma$ represents the stress anisotropy constant.

When λ_m is negative ($\mathcal{K}_\sigma$ is positive), as for nickel under tension; the stress axis becomes a hard axis [1.7]. On the other hand, stress axis is easy axis for the system with positive λ_m (negative $\mathcal{K}_\sigma$) as in case of iron [1.7].

(c) Shape anisotropy: In a ferromagnetic material having an arbitrary shape, the internal energy is different for the magnetization lying along the different axes of the sample. This effect is called the shape anisotropy. It appears as a result of the magnetostatic energy due to the magnetic free poles at the outer surface of the specimen. This is also termed as magnetic dipolar anisotropy. The effect can be best represented by a scalar N (known as the demagnetizing factor) along three perpendicular directions such that $N_x+N_y+N_z = 1$. The magnetostatic energy originating due to the magnetic free poles can be expressed as $E_{ms} \approx NM^2V$, where M is the magnetization, N is the direction and shape dependent demagnetizing factor, and V is the volume of the sample. For example, in a thin film N is zero in the plane of the film and is 1 along the normal to the film. This results in a preferred orientation of the magnetization in the plane of the film. For a sphere $N_x = N_y = N_z = 1/3$, so no direction has preference from shape anisotropy. Further the demagnetizing field due to the free poles in a particular orientation of the sample is given by $H_D = -NM$. Here N is the demagnetizing factor for that orientation of the sample and M is the magnetization of the sample [1.6].

1.3 Phase transitions

A phase of a material is defined as a region of spatially uniform macroscopic properties like density, atomic arrangements, crystal structure, chemical composition, magnetic order etc. A material can exist in different phases at different values of the control variable (temperature/pressure/magnetic field etc.). The transition from one phase to the other is termed as a phase transition.

1.3.1 Ehrenfest's scheme of classification of phase transitions

When a material undergoes a phase transition from a high temperature phase to a low temperature phase, the free energies of both the phases are equal at a temperature T_C (known as the thermodynamical phase transition temperature), but certain order of the derivative of the free energy with respect to a control variable may differ. In Ehrenfest's scheme, the order of the phase transition is defined by the lowest order of the derivative of free energy which is discontinuous across the phase transition [1.10-1.12]. If G_1 and G_2 are the free energies of the phases on the two sides of a thermodynamical phase transition temperature, then a phase transition will be of nth order if

$$\left.\frac{\partial^n G_1}{\partial T^n}\right|_{T_C} \neq \left.\frac{\partial^n G_2}{\partial T^n}\right|_{T_C} \quad \text{and} \quad \left.\frac{\partial^m G_1}{\partial T^m}\right|_{T_C} = \left.\frac{\partial^m G_2}{\partial T^m}\right|_{T_C} \quad \text{for } 0 \leq m < n \qquad (1.9)$$

m and n both being integers.

Some of the derivatives of free energy are given below.

$$\left.\begin{array}{rl}
\textit{Entropy} & S=-\left(\dfrac{dG}{dT}\right)_P \\
\textit{Volume} & V=\left(\dfrac{dG}{dP}\right)_T \\
\textit{Magnetization} & M=-\left(\dfrac{dG}{dH}\right)_{T,P} \\
\textit{Heat capacity} & C=T\left(\dfrac{dS}{dT}\right)=-T\left(\dfrac{d^2G}{dT^2}\right) \\
\textit{Isothermal compressibility} & K_T=-\dfrac{1}{V_0}\left(\dfrac{dV}{dP}\right)_T=-\dfrac{1}{V_0}\left(\dfrac{d^2G}{dP^2}\right)_T \\
\textit{Susceptibility} & \chi=\left(\dfrac{dM}{dH}\right)=-\left(\dfrac{d^2G}{dH^2}\right)
\end{array}\right\} \qquad (1.10)$$

As per the Ehrenfest's criterion discontinuous change in the first derivative of free energy i.e. volume, entropy, magnetization etc., across the phase transition qualifies the phase transition

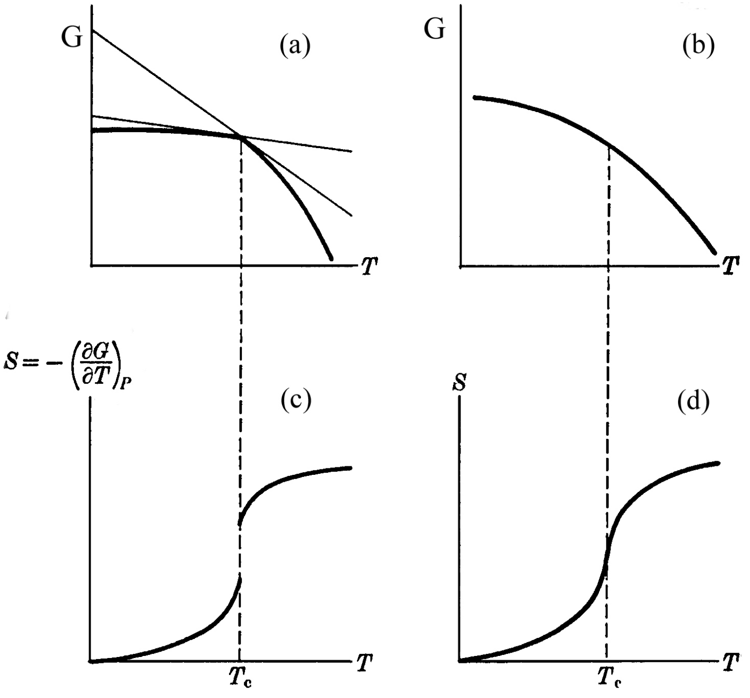

Fig. 1.2: Ehrenfest's scheme for identification of the order of a phase transition. Free energy as a function of temperature (T) across (a) a first-order phase transition and (b) a higher order phase transition. Here T_C is the thermodynamical phase transition temperature. Temperature dependence of entropy (S) is also shown for (c) a first-order phase transition and (d) a higher order phase transition (Ref. 1.12).

as first-order (see Fig. 1.2(c)). On the other hand a continuous first-order derivative and a discontinuous second-order derivative (e.g. heat capacity, susceptibility and compressibility) qualify the phase transition as second-order (see Fig. 1.2(d)). In a first-order phase transition, a discontinuity of entropy leads to latent heat (L_Q) of the phase transition amounting to $L_Q = T_C \Delta S$ where $\Delta S = [S_2 - S_1]_{T_C}$ is the difference in entropy between the two phases at T_C. All the higher order phase transitions do not have a latent heat. However, experimentally it has been found that in most of the phase transitions which do not have a latent heat, the heat capacity either diverges or exhibits a cusp, and hence do not fit in Ehrenfest's scheme [1.10].

Modern classification of phase transitions: A phase transition is termed as discontinuous (or first order) if it has a latent heat. All other phase transitions which do not have a latent heat are termed as continuous phase transitions (it includes the second and higher order phase transition in Ehrenfest's sense).

Table 1.1: Order parameters for phase transitions in various systems.

Phase transition	Order parameter
Ferromagnetic	Spontaneous magnetization
Antiferromagnetic	Sublattice magnetization
Ferroelectric	Polarization

Order parameter: The concept of order parameter in a phase transition was introduced by L. D. Landau. It is an entity or observable, which is zero in the high temperature phase and is non-zero in the low temperature phase [1.13] (see Table 1.1 for some examples). If the order parameter is zero at the thermodynamical phase transition temperature and gradually grows with decreasing temperature, the phase transition is second order. On the other hand if it grows discontinuously

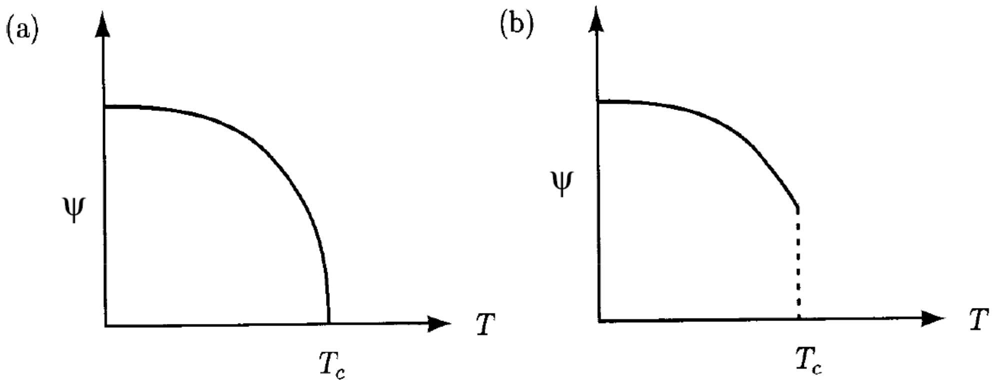

Fig. 1.3: Temperature (T) dependence of the order parameter (ψ) for (a) a second-order phase transition and (b) a first-order phase transition. T_C is the thermodynamical phase transition temperature (Ref. 1.13).

from zero to a finite value at the transition temperature, the transition is called a first-order phase transition [1.13] (see Fig. 1.3(b)).

1.3.2 Landau theory of phase transitions

1.3.2.1 Second-order phase transition

Landau theory of phase transition assumes that the order parameter is small and uniform near the phase transition and the free energy density is assumed to be an analytical function of the order parameter (Ψ). For a second-order phase transition the expansion of free energy (G) as a power series of order parameter Ψ can be written as given below [1.13].

$$G = G_0 + a(T - T_C)\Psi^2 + D\Psi^4 + \ldots \qquad (1.11)$$

Here G_0 is the free energy of the system associated with the degrees of freedom of the system which are not related to the order parameter. The coefficients a and D are system dependent. T_C is the thermodynamical phase transition temperature, the temperature where both the phases have equal free energies.

The plot of free energy in eqn. (1.11) at various temperatures is shown in Fig. 1.4. With decreasing temperature, $\Psi = 0$ is the only minimum down to the transition temperature T_C. So,

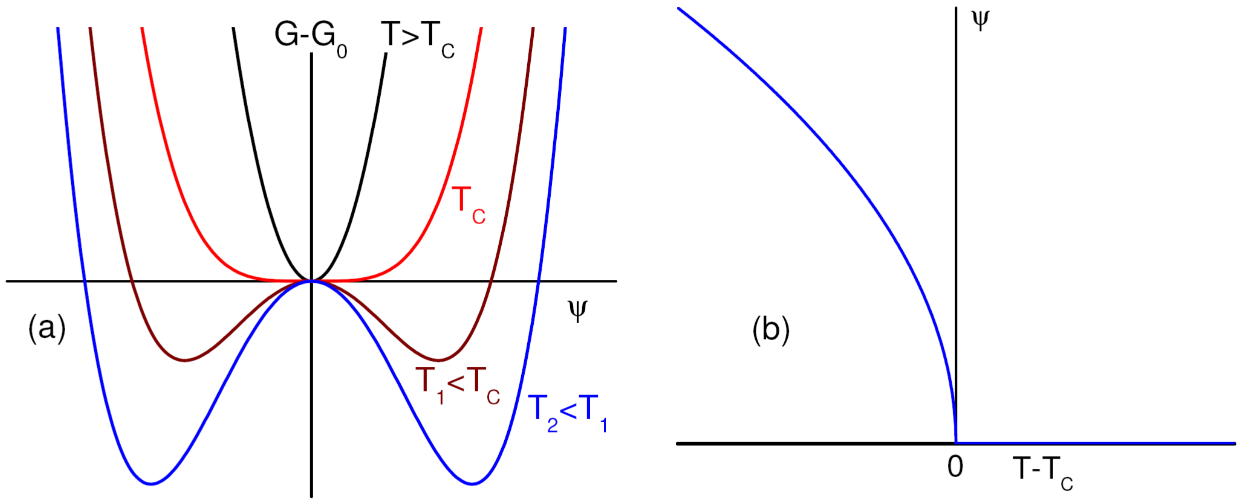

Fig. 1.4: (a) Variation of Landau free energy (G) with order parameter (ψ) at different temperatures (T) as per eqn. (1.11). (b) Temperature dependence of order parameter. T_C is the thermodynamical phase transition temperature.

the high temperature phase with $\Psi = 0$ is stable down to $T = T_C$. At T<T$_C$, $\Psi = 0$ becomes a maximum and there are two minima with positive and negative values of Ψ of equal magnitude. The order parameter Ψ evolves continuously across the transition (see Fig. 1.4(b)) and there is no latent heat involved [1.13].

1.3.2.2 First-order phase transition

Across a first-order phase transition the change in order parameter is discontinuous, so the order parameter jumps to a finite value at the transition temperature. If symmetry considerations do not prohibit a third order term in the expression of the free energy, then the free energy can be written as

$$G = G_0 + a\left(T - T^*\right)\Psi^2 - C\Psi^3 + D\Psi^4 + ... \qquad (1.12)$$

Here T^* is the temperature where the free energy at $\Psi = 0$ ceases to be a minimum. This free energy function is plotted in Fig. 1.5.

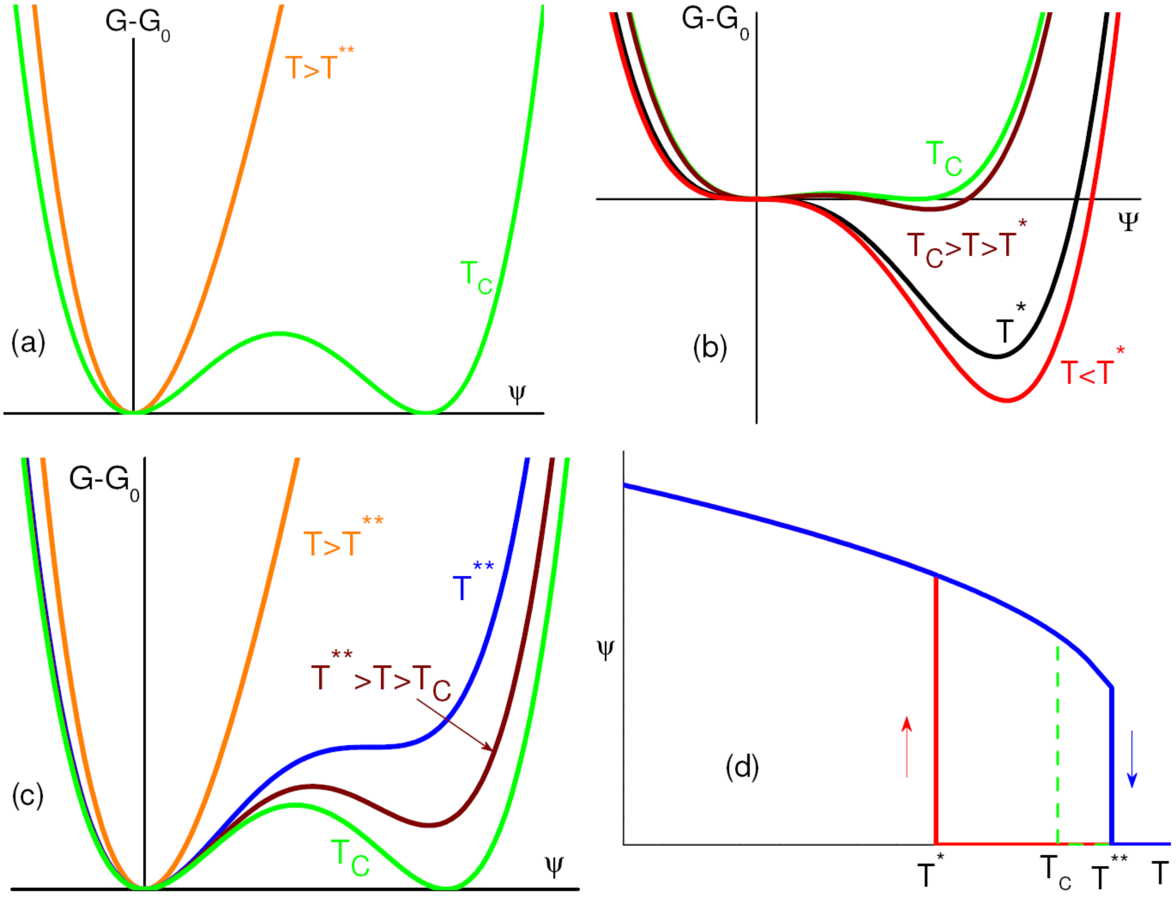

Fig. 1.5: Variation of Landau free energy (G) in eqn. (1.12) with order parameter (ψ) at (a) temperature (T) much higher than thermodynamical transition temperature (T_C) and at $T = T_C$, (b) $T \leq T_C$ while cooling and (c) $T \geq T_C$ while heating. The temperatures T^* and T^{**} are the limits of metastability while cooling and heating respectively. (d) T dependence of order parameter.

Supercooling and superheating: From the equation (1.12) and Fig. 1.5 it is clear that the free energy has multiple maxima/minima in certain temperature range. With decreasing temperature, at T_C there are two minima with $\Psi = 0$ and $\Psi \neq 0$ with equal free energy values. This temperature is known as the thermodynamical transition temperature of the phase transition from $\Psi = 0$ phase to $\Psi \neq 0$ phase. At T_C, the order parameter Ψ increases discontinuously (see Fig. 1.5(d)). However, $\Psi = 0$ remains a local minimum down to T^* while cooling. Similarly, with increasing temperature the free energy minimum at $\Psi > 0$ persists up to T^{**}. This predicts a thermal hysteresis during a thermal cycling across the transition temperature (see Fig. 1.5(d)).

Thermal hysteresis is a generic feature of first-order phase transitions [1.13] and is a qualifying criterion for a first-order phase transition in the cases where latent heat is difficult to ascertain [1.14].

Thermodynamically the phase transition should occur at T_C. However during cooling, the high temperature phase is stable against small energy fluctuations down to T^*. A sufficiently large energy fluctuation can convert this high temperature $\Psi = 0$ phase to low temperature $\Psi > 0$ phase. So, high temperature phase is a metastable phase. The temperature T^* is the limit of metastability of the high temperature phase while cooling. Thus the higher temperature phase can be supercooled down to T^*. Similarly the low temperature phase can remain as a metastable phase up to T^{**} while heating. Thus the system can be superheated up to T^{**}. It can be shown that equation (1.12) predicts a change in entropy across the phase transition and hence the phase transition has a latent heat [1.13].

First-order phase transition with a negative fourth order term in free energy expansion:

A first-order phase transition can also occur in Landau scheme even if a third order term is prohibited by symmetry. The following free energy function symmetric in order parameter

$$G = G_0 + a(T - T^*)\Psi^2 - D\Psi^4 + F\Psi^6 + ... \tag{1.13}$$

also describes a first-order phase transition. The function is plotted in Fig. 1.6. In this case the free energy also has multiple minima in a certain temperature range. This free energy function has minima on both sides of $\Psi = 0$. The high temperature phase ($\Psi = 0$) can exist as a metastable phase down to the temperature T^* (see Fig. 1.6(a)) and the low temperature phase ($\Psi \neq 0$) can exist as a metastable phase up to the temperature T^{**} (see Fig. 1.6(b)). Eqn. (1.13) also predicts a discontinuous change in order parameter similar to that shown in Fig. 1.5(d), an

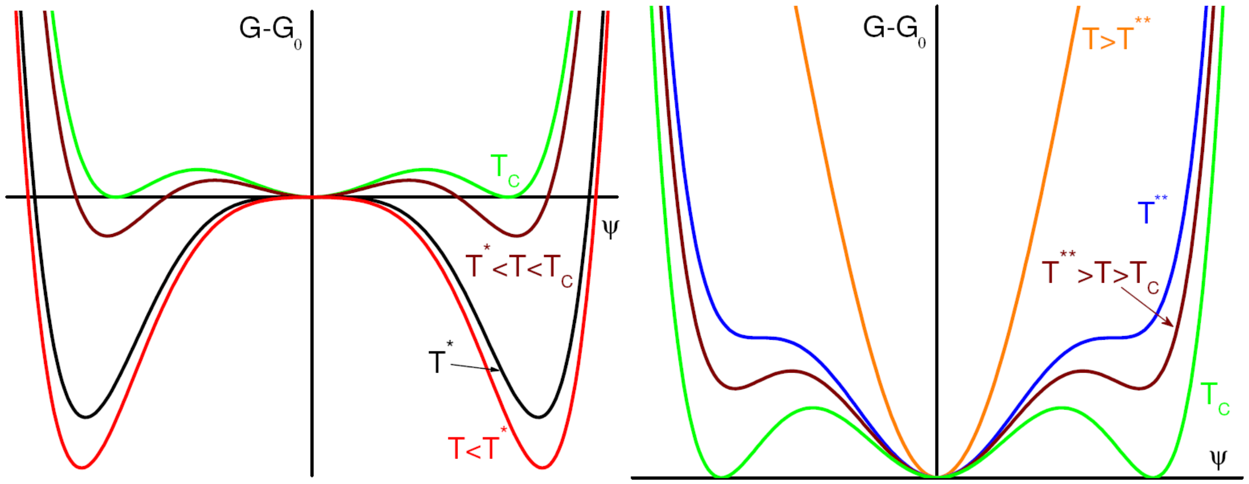

Fig. 1.6: Variation of Landau free energy (G) in eqn. (1.13) with order parameter (ψ) at (a) temperature (T) $\leq T_C$ and (b) $T \geq T_C$. T_C is thermodynamical transition temperature, and the temperatures T^* and T^{**} are limits of metastability while cooling and heating respectively.

entropy jump and a latent heat across the phase transition [1.13]. The eqn. (1.13) is appropriate for discussing first-order magnetic phase transitions.

1.3.3 Disorder broadened first-order phase transition

In an extremely pure system, a first-order phase transition has a single thermodynamical transition temperature T_C as shown by the thick dashed line in schematic Fig. 1.7(a). As discussed in earlier paragraphs, such a system can be supercooled through careful cooling. In that case the phase transition follows the solid line marked by T_3-T^*. Similarly, the system can be superheated and the superheated phase would follow the solid line T_1-T^{**}. Such transitions are single shot, i.e., the entire sample transforms at the same temperature. In such a case, $T_3 = T^*$ and $T_1 = T^{**}$. If the first-order phase transition is diffused, the supercooled and superheated phases will follow the dotted curves T_{3a}-T_4-T^* and T_{1a}-T_2-T^{**} respectively. Note that in such a case the two phases can coexist over certain temperature range. Impurities and disorder in the sample can result in such diffused transition. Microscopic random-quenched disorder in a sample leads to a landscape of transition temperature across the volume of the sample. This can smear out the

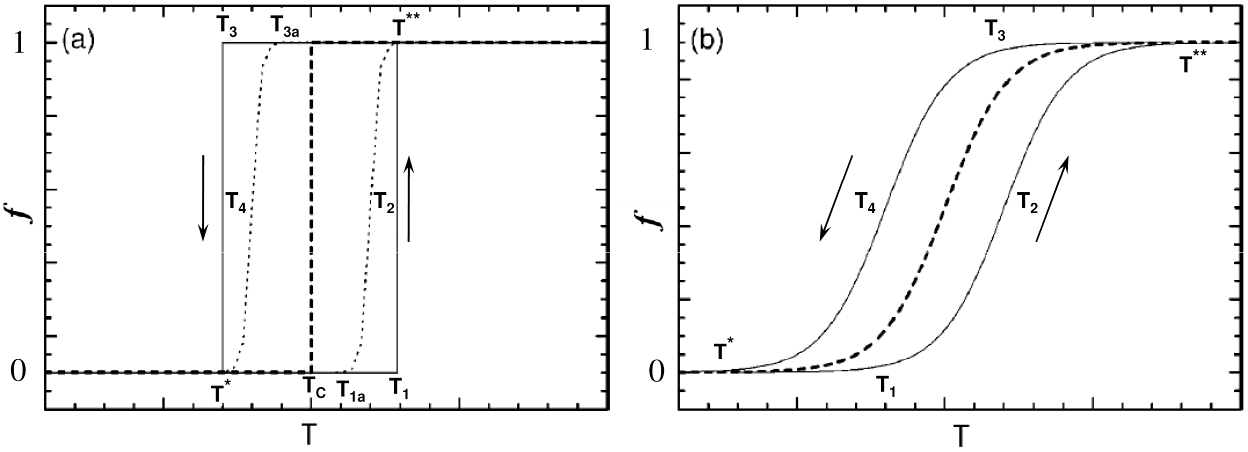

Fig. 1.7: Temperature (T) dependence of phase fraction (f) of high temperature phase across a first-order phase transition. (a) The temperature cycle T_3-T^*-T_1-T^{**} represents a transition in a pure system with sharp transition with supercooling and superheating. The temperature cycle T_{3a}-T_4-T^*-T_{1a}-T_2-T^{**} corresponds to a diffuse transition. (b) Landscape of thermodynamical transition temperature leads to a situation where the temperature of onset of phase transition during cooling cycle (T_3) is higher than the temperature of onset of phase transition during heating cycle (T_1) (from Ref. 1.17).

sharpness of the first-order phase transition discussed above and the transition takes place over a finite range of temperature [1.15, 1.16]. The thick dashed line of Fig. 1.7(b) represents such a transition. In the presence of supercooling and superheating, the complete phase transition will follow the solid curves T_3-T_4-T^* and T_1-T_2-T^{**} respectively. In such a disorder-broadened first-order phase transition, the onset of nucleation of the low-temperature phase during cooling can take place at a temperature higher than the onset of nucleation of the high-temperature phase during warming [1.17] (see Fig. 1.7 (b)). It is worth noting here that in such cases the latent heat across the first-order phase transition might be difficult to be observed experimentally, and then thermal hysteresis is used as a qualifying criterion for a first-order phase transition [1.14].

1.4 Martensitic transition

An MT is a first-order solid-solid displacive phase transition [1.18-1.19]. It is the key behind the shape memory effect and super-elasticity. Ferromagnetic shape memory effect is also closely related to the conventional shape memory effect. A brief introduction to the MT is presented below.

1.4.1 Classification of solid-solid phase transitions

A solid can exist in different phases at different values of control variable (temperature / pressure / magnetic field). For example iron can exist in face centred or body centred cubic crystal structure depending upon the temperature. The solid-solid phase transitions are broadly classified in two categories: diffusive and displacive (or diffusionless). In the diffusive solid-solid phase transitions long range diffusion of atoms takes place during the transition as in disorder-order transitions in solids. The displacive or diffusionless transition as the name suggests, do not require long range diffusion of atoms in the course of phase change; only small atomic movements usually over distance less than the inter-atomic spacing are involved [1.18]. Such a transition occurs by coordinated shifts of atoms in an organized manner relative to their neighbours. During the shift, the atoms maintain their relative relationship during the phase transition.

The displacive transitions have two subcategories. The classification scheme adopted by Cohen et al. [1.18] is presented in Fig. 1.8. A displacive transition can be via atomic shuffle or homogeneous lattice distortive strain. A shuffle is a (small scale) coordinated movement (displacement much less than inter-atomic distance) of atoms that alters the symmetry of the crystal by modifying the atomic positions within the unit cell. An ideal shuffle will result in no change of size or shape of the unit cell, and only involves interfacial energy. No strain energy is involved in this case [1.18, 1.19]. On the other hand, a homogenous lattice distortive strain transforms one lattice to another. The lattice distortive transition produces change in the size and/or shape of the unit cell [1.18, 1.19]. The volume change and/or shape change during the

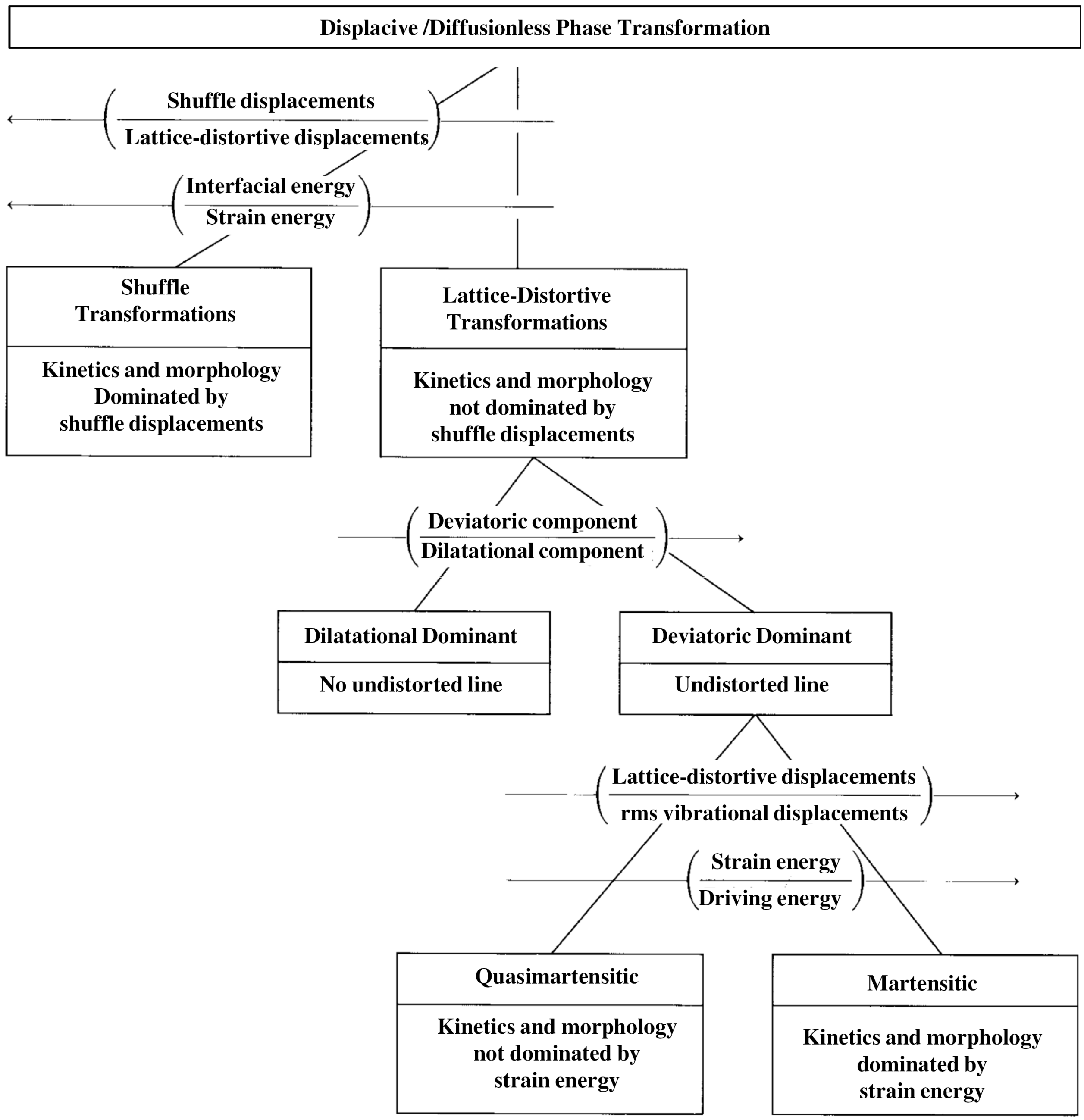

Fig. 1.8: Classification scheme for the displacive/diffusionless phase transformations as proposed by Cohen et al. (Refs. 1.18 and 1.19).

appearance of the daughter phase inside the parent phase produces strain. An interface created between the parent and daughter phases also leads to interfacial energy. Actual displacive transitions involve a combination of both the lattice distortive strain and shuffle to varying amounts. Depending on the relative contribution of the above mentioned two atomic displacements (shuffle and lattice distortive) and hence the ratio of the interfacial/ strain energy, the displacive phase transitions are divided in two subcategories, shuffle transitions and lattice distortive transitions.

The lattice-distortive transitions are further subdivided according to the relative magnitudes of the two components of the homogeneous lattice deformation, namely the dilatational and the deviatoric (shear) components. In a dilatational lattice deformation there is no change in shape of the unit cell, only size of unit cell changes [1.19]. A cube remains a cube. On the other hand, in case of deviatoric lattice deformation the unit cell undergoes a change in the structure (a cube becomes say a tetragonal).

If the magnitude of the lattice-distortive displacement is large as compared to that of lattice vibrational displacement, high elastic strain energies are involved, and dominate the kinetics and morphology of the transition. Such a transition is called a martensitic transition [1.18, 1.19]. On the other hand, if lattice distortive displacement is comparable to the lattice vibrational displacement the strain-energy is small and hence does not dominate the kinetics and morphology the transition. In this case, the transition is called quasi-martensitic. Alternatively quasi-martensitic transition can be differentiated from the martensitic transition using the ratio of strain energy to the driving force (difference in chemical free energies of the two phases). In the case of a quasi- martensitic transition, the ratio is small because of the small lattice distortion. Further, in most of the cases the quasi- martensitic transition is a second-order phase transition (except for some alloys where the transition is weakly first order) and does not proceed through nucleation, while martensitic transition is a first-order phase transition and proceeds through nucleation and growth mechanism [1.19].

Above discussion defines the martensitic transition as a "*shear dominant, lattice-distortive, diffusionless first-order phase transition*".

1.4.2 Various aspects of martensitic transition

In following sections some important aspects of MT will be discussed briefly.

(i) Characteristic temperatures of MT: The MT occurs with decrease in temperature. The high temperature phase is called as AST phase, and the lower temperature phase is called as MST phase. Generally, the transition takes place over a range of temperature. For AST-MST phase transition, the characteristic temperatures are defined as follows (see Fig. 1.9) [1.2].

T_{MS}: MST start temperature while cooling
T_{MF}: MST finish temperature while cooling
T_{AS}: AST start temperature while heating
T_{AF}: AST finish temperature while heating

(ii) MST variants: As the AST phase has higher symmetry compared to the MST phase, the phase transition from AST to MST can result in more than one structural configuration of MST.

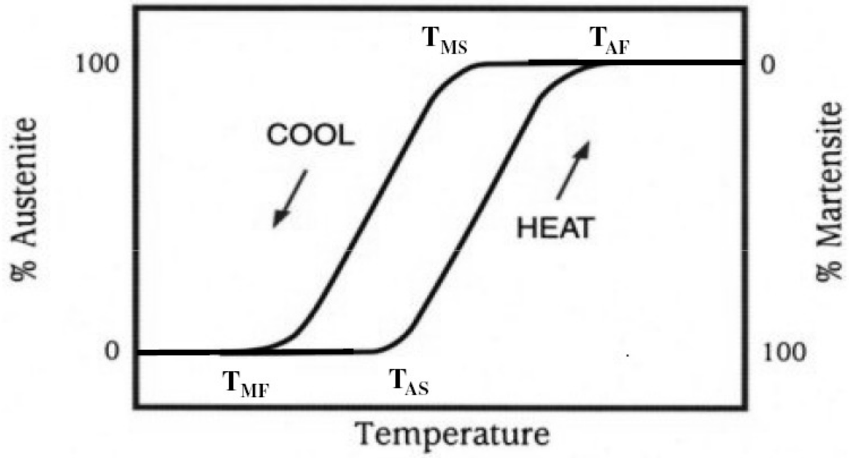

Fig. 1.9: Schematic temperature dependence of the martensite and austenite phase fractions across the martensitic transition. Characteristic temperatures of the martensitic transition are marked.

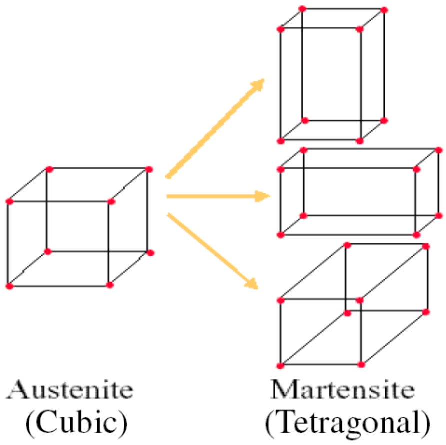

Fig. 1.10: Martensite variants for the martensitic transition from cubic austenite phase to tetragonal martensite phase.

These are known as the MST variants [1.2, 1.20, 1.21]. For example three MST variant are possible in the MT from cubic AST phase to tetragonal MST phase (see Fig. 1.10).

(iii) **Lattice correspondence**: As MT is diffusionless, there exists a well defined lattice correspondence between the planes and directions of the lattices of AST and MST [1.2] phases. This correspondence details the relationship between the directions and planes in the MST phase with the directions or planes in the AST phase.

(iv) **Strain accommodation**: MT being a first-order phase transition proceeds by nucleation and growth mechanism [1.19]. Since the MST and AST phases have different crystal structures, a large strain arises around the MST boundary when it forms in the parent AST matrix (see Fig. 1.11). Further progress of the nucleation and growth process requires reduction in this strain energy. To reduce the strain the nucleated MST phase must fit in the surrounding AST phase. The minimization of strain energy can be achieved with a lattice invariant strain. Slip and twinning are typical lattice invariant strain. The process of minimization of the strain is called strain accommodation [1.2]. The accommodation of strain by these two ways is presented in Fig. 1.12. Slip results in plastic deformation while twinning results in no such plastic

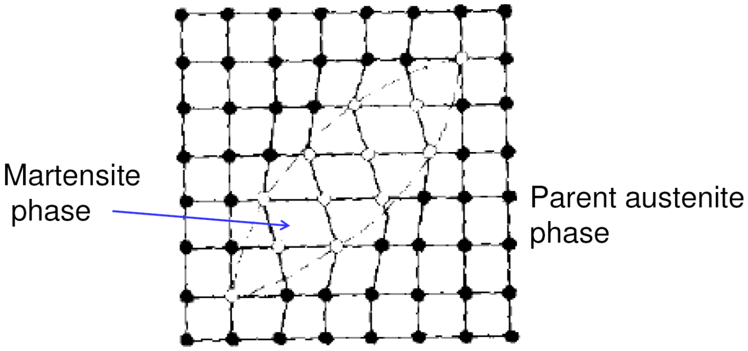

Fig. 1.11: Schematic of strain generated due to nucleation of martensite phase in austenite phase.

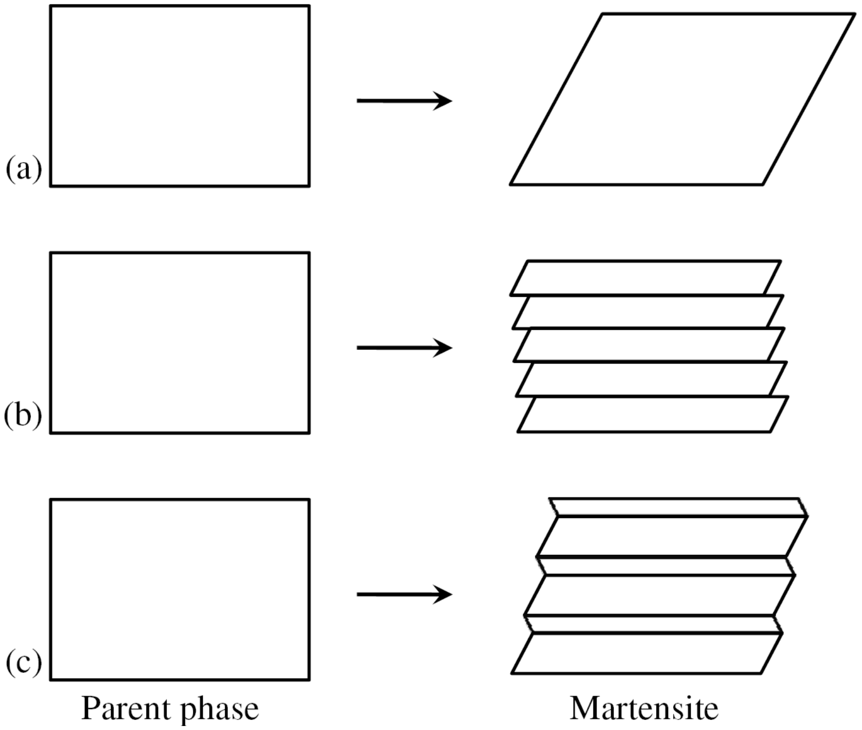

Fig. 1.12: (a) Schematic view of shape change in martensitic transition. Strain accommodation by (b) slip and (c) twinning (from Ref. 1.2).

deformation. However, the requirement of coherency of lattices at the contact plane still generates strain in the lattices of AST and MST phases. The interface between twins is called as twin boundary. In some case this boundary can be highly mobile. A number of materials undergo MT but not all of them reduce the strain energy by twinning. .

(v) Microstructure: As discussed in the previous sections minimization of strain energy is achieved by self accommodation of strain through the lattice invariant strain. This gives rise to rich microstructure in the MST phase. A multi-variant arrangement is the most commonly observed microstructure [1.21]. This microstructure is visible under an optical microscope and the length scale depends on the system.

(vi) Thermo-elastic martensitic transition: In case the strain is accommodated elastically (by twin formation) and the phase transition is crystallographically reversible, the MT is thermo-elastic. The crystallographic reversibility of the thermo-elastic MT combined with the mobile twin boundaries in the MST phase leads to interesting properties of shape memory effect and superelasticity across this transition.

(vii) Effect of stress on the characteristic temperatures of martensitic transition: Under the application of stress the characteristic temperatures of the MT (T_{MS}, T_{MF}, T_{AS} and T_{AF}) increase [1.2]. This is because under applied stress the MST variant having strain along the applied stress can form more easily as compared to the zero stress condition.

1.5 Shape memory effect

Under special conditions, some material has the ability to remember the prior deformation shape. This ability is termed as the shape memory effect and alloys showing such behavior are known as the shape memory alloys.

1.5.1 Conventional shape memory effect

This kind of shape memory effect is observed in the alloys like Ni-Ti when deformed at temperature below T_{MF} and subsequently heated to temperatures above T_{AF} [1.2] as shown in Fig. 1.13(a). Recoverable strain as high as 8% has been observed in the Ni-Ti alloy.

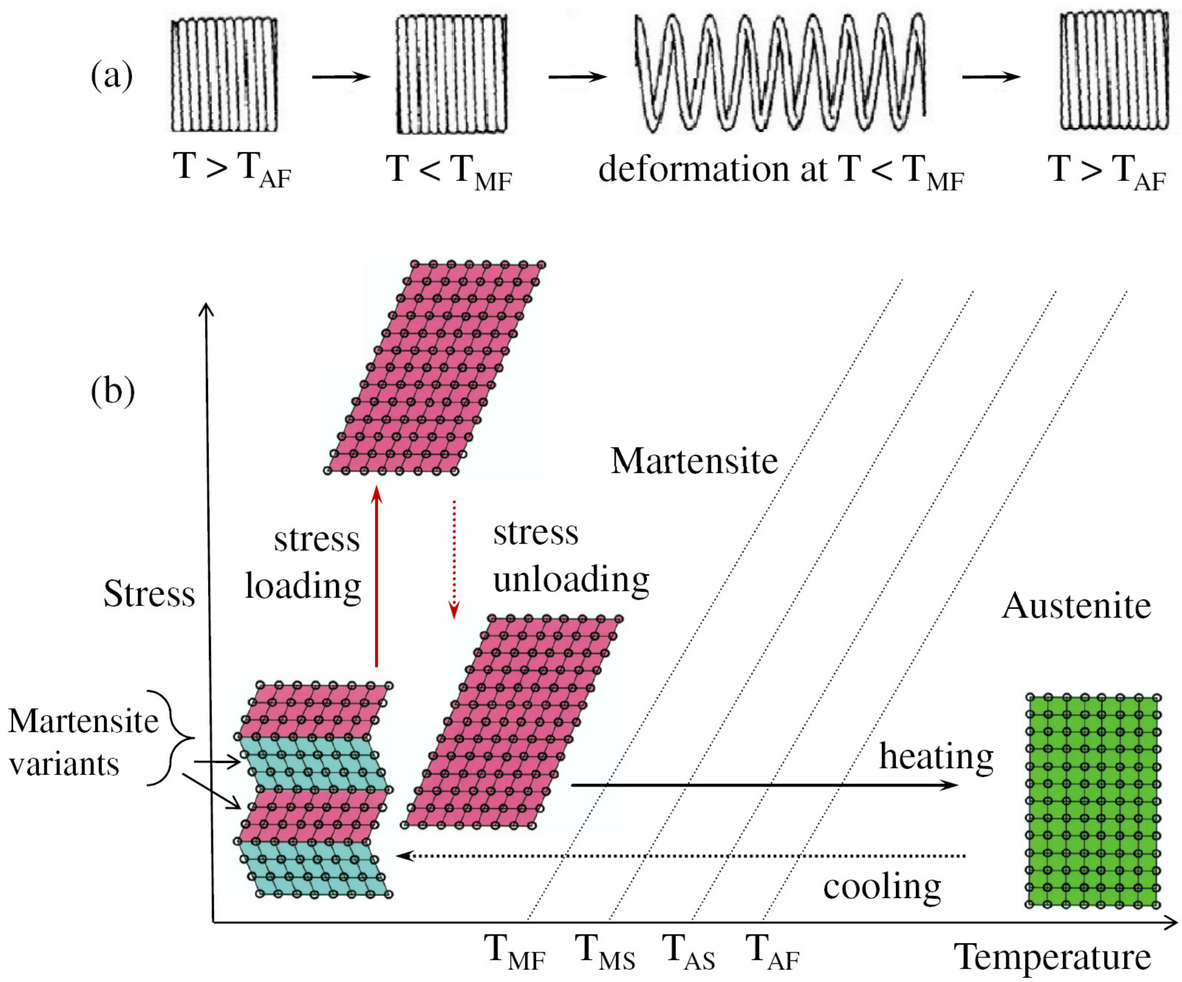

Fig. 1.13: (a) Shape memory effect and (b) schematic explanation for the same (part of the picture is taken from Ref. 1.20).

The shape memory effect is explained schematically in Fig. 1.13(b). When the material is cooled below the T_{MF} across a thermo-elastic MT, MST variants form to accommodate strain. Under application of stress, a suitable MST variant grows which has strain in the direction of stress by virtue of mobile twin boundaries. The macroscopic shape change occurs without any plastic defect creation. When the temperature is increased above T_{AF}, the MST to AST phase transition being crystallographically reversible results in the AST phase in the configuration same as at the starting point. Thus the original shape is regained. The necessary conditions for shape memory effect are (i) the MT must be thermo-elastic so that strain is accommodated with twin formation and the transition is crystallographically reversible, (ii) the deformation under stress in the MST phase should be solely by movement of the twin boundaries between MST variants, so that no plastic defects are created [1.2]. This requires that the critical stress for plastic deformation in the material should be high [1.20].

If stress is applied to the shape memory alloy in AST phase ($T>T_{\mathrm{AF}}$), under sufficient stress (must not cross the critical stress required for plastic deformation) the AST phase will transform to the MST variant favoured by the applied stress leading to a large deformation (see Fig. 1.13(b)). When the stress is withdrawn, the MST phase transforms back to the AST phase recovering the original shape. This phenomenon is termed as superelasticity [1.2, 1.21] because recoverable strain, much larger than observed in normal material within elastic limits, is observed in such process.

1.5.2 Ferromagnetic shape memory effect

The conventional shape memory effect is exhibited when the strain is accommodated elastically. If the MST phase is ferromagnetic, under the application of magnetic field the magnetic moments of the MST variants tend to align along the magnetic field direction. The driving force for aligning the magnetic moment arises from the minimization of energy for the orientation of the magnetic moments along the magnetic field (see section 1.2.4 of this Chapter). An interesting case arises when the MST phase has such a large magnetocrystalline anisotropy that the energy cost of the magnetic moment rotation (from the easy axis towards the direction of the applied magnetic field) is larger than the energy required for twin boundary motion of the MST variants. In such a situation the MST variants will rearrange under sufficient high magnetic field for the alignment of the easy axis along the direction of the magnetic field, and lead to a

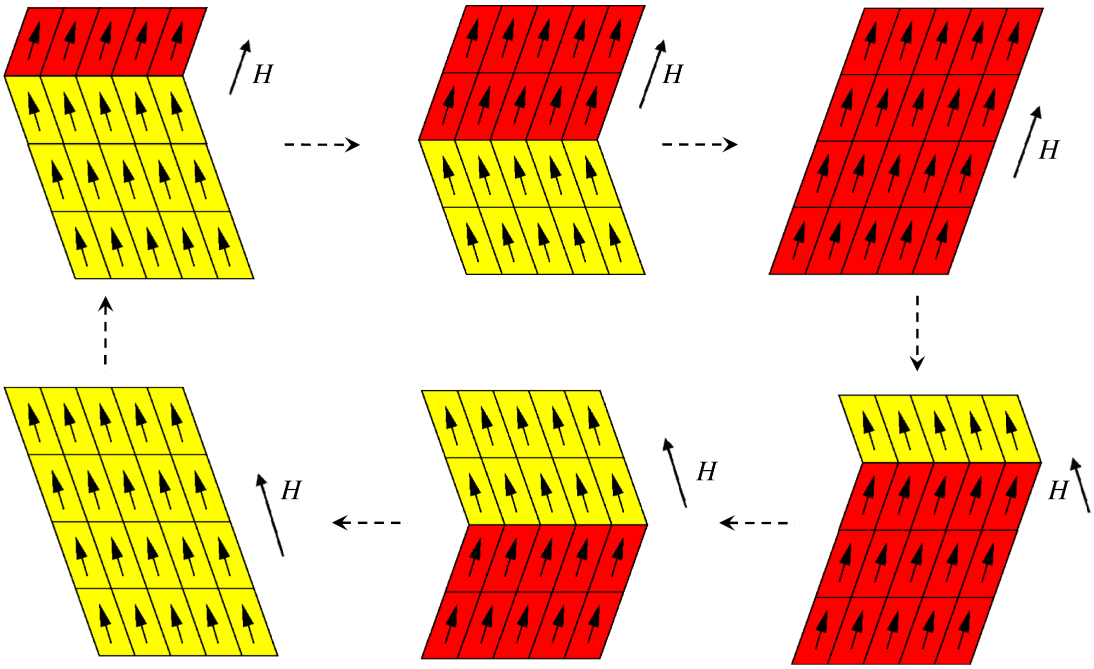

Fig. 1.14: Rearrangement of the martensite variants in the magnetic field (*H*) when magnetocrystalline anisotropy is high. Favourably oriented variants grow at the expense of unfavourably oriented variants to align the magnetization (represented by arrows within martensite variants) along applied *H* (part of the picture is taken from Ref. 1.22).

change in the dimension of the material [1.22]. This dimension change can be controlled with magnetic field. The idea is presented in the schematic in Fig. 1.14. Large strain ~10% has been obtained in this mechanism in some of the Ni-Mn-Ga alloy (see section 1.6 of this Chapter). Such magnetic field controlled deformation is called as the ferromagnetic shape memory effect and materials with this capability are termed as ferromagnetic shape memory alloys. The mechanism of magnetic field induced strain in ferromagnetic shape memory effect is very different from the usual magnetostriction observed in ferromagnets due to spin-orbit coupling. In magnetostriction it is the magnetic moment which rotates to align along the magnetic field direction while in the present case it is the structural domain (MST variants) which rotates to align the magnetic moment along the magnetic field direction. Conventional shape memory effect requires the flow of heat for actuation; hence the actuation response is slow. On the other hand, in the case of magnetic field controlled shape change as discussed above, the actuation can be much faster.

1.6 Ni-Mn-Ga alloys

The Ni-Mn-Ga alloy with a composition of Ni_2MnGa belongs to a special class of materials known as the Heusler alloys. Cu_2MnSn and Cu_2MnAl belong to this class of alloys, which had shown ferromagnetism even though none of the constituents was ferromagnetic and this has contributed to the understanding of magnetism. Heusler alloys crystallize in the $L2_1$ crystal structure. The Heusler alloy structure will be discussed in more detail in the Chapter 2 (see section 2.2.2). The stoichiometric Ni_2MnGa alloy undergoes a paramagnetic to ferromagnetic transition with a lowering of the temperature with a Curie temperature near 350 K, which is followed by an AST to MST phase transition near 270 K. The AST phase has $L2_1$ crystal structure while the MST phase has tetragonal structure [1.3]. Both the AST and MST phases have ferromagnetic character and the MST phase has a higher value of saturation magnetization as compared to the AST phase [1.23]. The easy axis of magnetization lies along the c-axis of the tetragonal MST phase. An unstressed single crystal of this alloy was reported to show magnetic field induced strain of 0.2% in the MST phase [1.3]. Under compressive stress, the magnetic field induced strain in a single crystal sample of Ni_2MnGa alloy increases up to 6% [1.23]. The mechanism of this magnetic field induced strain is twin reorientation through twin boundary motion under applied magnetic field (see section 1.5.2 of this Chapter). The magnetic field induced strain is found further increased in some off-stoichiometric compositions of the Ni-Mn-Ga alloy. A magnetic field induced strain of ~10% has been reported in a single crystal sample of $Ni_{48.8}Mn_{29.7}Ga_{21.5}$ alloy [1.4]. This magnitude of strain is almost two orders of magnitude larger than ~0.1 % observed in piezoelectric materials and ~0.2% exhibited by the leading magnetostrictive material Terfenol-D [1.24]. Ni-Mn-Ga alloys are also reported to show the magnetocaloric effect [1.25]. The magnetocaloric effect is an adiabatic change in temperature or a isothermal change in the entropy of the system under application/removal of a magnetic field [1.26]. The magnetocaloric effect along with the technique of its estimation will be discussed in Chapter 2 (see section 2.6) on experimental techniques. An adiabatic increase (decrease) in temperature during application (removal) of a magnetic field, and an isothermal decrease (increase) in entropy during application (removal) of magnetic field as observed in a ferromagnet is termed as conventional magnetocaloric effect. The sense of change in temperature/entropy is the opposite in the inverse magnetocaloric effect. The first observation of magnetocaloric effect in Ni-Mn-Ga alloy was reported for an alloy with MT near 200 K which was found to show inverse magnetocaloric effect [1.27] below magnetic field of 10 kOe. In an alloy with slightly different composition with MT near 290 K conventional magnetocaloric effect was reported for magnetic field above 10 kOe [1.28]. The inverse magnetocaloric effect in Ni-Mn-Ga in low magnetic field was explained in terms of strong uniaxial magnetocrystalline anisotropy, which caused lower magnetization in the MST phase in low magnetic field [1.25]. This leads to a positive dM/dT across the transition in low magnetic field leading to a positive MCE. The conventional MCE in higher magnetic field was attributed to higher magnetization of MST phase as compared to that of AST phase in that magnetic field [1.29, 1.30]. This leads to a negative dM/dT across the transition resulting in conventional MCE in high magnetic field. With variation of the composition the MT can approach Curie temperature, in such case the anisotropy weakens and conventional magnetocaloric effect is found to dominate in all magnetic fields. MST twin reorientation under applied magnetic field is reported to lead to a large magnetoresistance in single crystals of Ni-Mn-Ga alloys [1.31, 1.32]. This arises from a crystallographic anisotropy of the resistivity of the MST variant of the Ni-Mn-Ga alloy [1.31, 1.32].

1.7 Ni-Mn-X (X = In, Sn) alloys

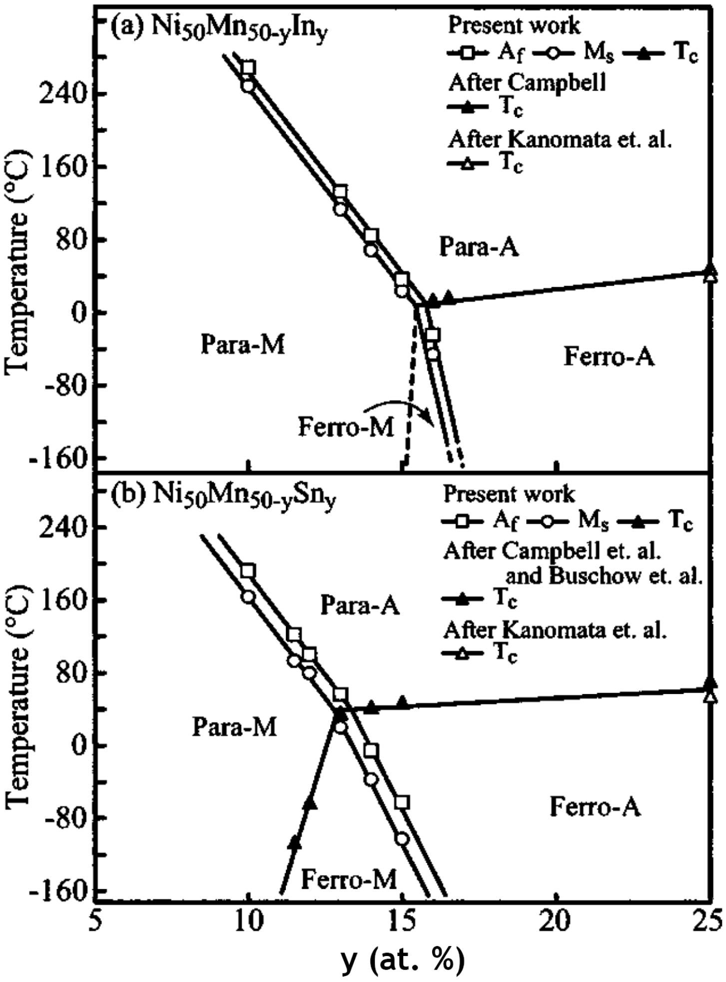

Fig. 1.15: Martensitic and magnetic transition temperatures of the (a) $Ni_{50}Mn_{50-y}In_y$, (b) $Ni_{50}Mn_{50-y}Sn_y$ alloys (from Ref. 1.5), where Para and Ferro mean paramagnetic and ferromagnetic respectively, and A and M indicate the austenite and martensite phases respectively.

The highly brittle nature of Ni-Mn-Ga alloys has limited the use of these alloys in many practical applications. In search of better ferromagnetic shape memory alloys new Heusler alloy systems have been investigated during the last one decade. In this regard off-stoichiometric Heusler alloys $Ni_{50}Mn_{50-y}X_y$ (X = In, Sn, Sb) have been identified as potential candidates for ferromagnetic shape memory effect [1.5]. These alloys were shown to undergo an MT from cubic AST phase to orthorhombic MST phase. The phase diagram of $Ni_{50}Mn_{50-y}X_y$ (X = In, Sn) alloys as reported by Sutou et al. is presented in Fig. 1.15. In our present work we have chosen Ni-Mn-In and Ni-Mn-Sn based alloys for study.

The alloys $Ni_{50}Mn_{50-y}In_y$ (y = 5-25) have been investigated in detail by Krenke et al. [1.33]. It has been observed that the crystal structure of AST phase is cubic while the structure of MST phase depends on the composition of the alloy. The alloys $Ni_{50}Mn_{50-y}Sn_y$ (y = 5-25) have also been investigated by Krenke et al. [1.34]. It was observed that the AST phase had a cubic structure while the structure of the MST phase depended on the composition of the alloy.

Chapter 2

Experimental techniques

The present work has involved the preparation of various samples of Ni-Mn-In and Ni-Mn-Sn based Heusler alloys and characterization of these samples for determining their actual composition and crystal structure. These alloy samples were then investigated for temperature (T) and magnetic field (H) dependence of their electrical, magnetic, thermal and mechanical properties. In the present Chapter we will describe the sample preparation and characterization techniques along with the experimental methods used for the measurement of various physical properties.

2.1 Sample preparation

The alloy samples were prepared under an inert argon gas atmosphere in an arc melting furnace. The working of arc melting furnace is briefly described below.

Arc melting Furnace: In an arc melting furnace, an electrical arc is used to melt the constituent elements for making an alloy. The arc melting furnace consists of mainly two parts: (i) a hearth with cups of one electrical polarity and (ii) electrodes with opposite polarity. Elements to be melted are placed in a cup of the hearth and the electrodes are used to strike the arc for melting the material. Temperatures in excess of 3000°C can be attained in such a furnace.

We have used a Centorr Vacuum Industries make 5TA tri-arc furnace (shown in Fig. 2.1) [2.1] to prepare alloys for the present study. This furnace consists of upper and lower water-

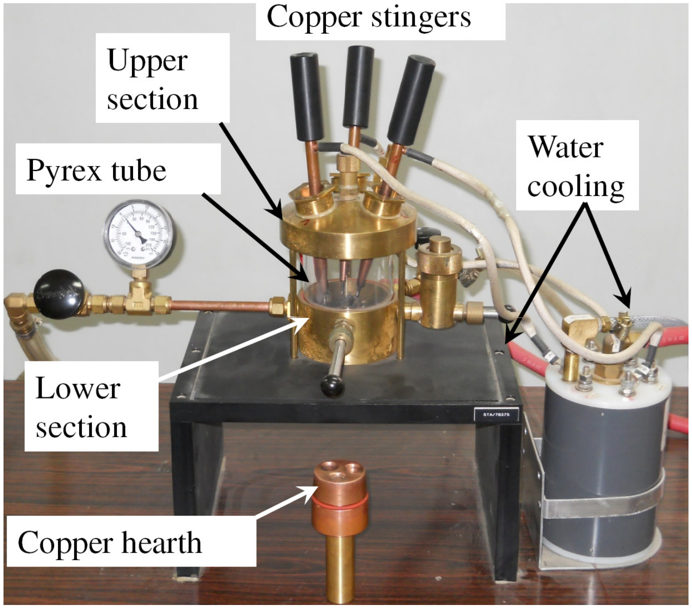

Fig. 2.1: Arc melting furnace model 5TA.

cooled sections separated by a pyrex observation tube. There are three copper stinger rods penetrating the top section which carry tungsten electrodes. Each rod is mounted into a swivel ball to allow angular as well as vertical movement of the electrode. The bottom section has a tapered opening which accepts a variety of copper hearths. A mechanical pump is attached for evacuation prior to inert gas backfilling. There are ports provided for inert gas inlet and outlet also. This furnace is used for melting mainly metallic materials.

To use this furnace the material to be melted is placed in the cup of the hearth. A small piece of titanium is also placed in a small, separate cup of the hearth. The hearth is inserted into the tapered hole in the bottom of the furnace and clamped into position. The furnace is then purged by a mechanical pump, followed by backfilling with inert argon gas. A suitable current is then set in the power supply. First, the piece of titanium is melted by striking arc to remove any possible oxygen impurity from the argon gas. Then the arc is struck on the material to be melted under the continuous flow of argon gas. The stingers are moved around and over the material in order to obtain a uniform and homogeneous melt. The specimen is turned over and remelted several times to ensure the homogeneity of the sample. Then the arc is turned off by gradually decreasing the current from the power supply.

2.2 Sample Characterization

The Ni-Mn-In and Ni-Mn-Sn samples prepared in arc melting technique were cut with a low speed diamond saw (Buehler, USA) into various shapes and sizes according to the need of the experiments. Parts of the samples were encapsulated in a quartz glass tube under argon gas and were annealed at 900^0C for 24 hours, and subsequently quenched in ice water. The actual composition of the alloys thus prepared was determined with energy dispersive x-ray (EDX) analysis, and the crystal structure of the alloys was determined with x-ray diffraction (XRD) study. In the following sections, both these techniques are described in brief.

2.2.1 Energy dispersive x-ray analysis: This is a useful technique to determine the elemental composition of material. It works on the principle that atoms of each element have a unique electronic structure with characteristic binding energies of electrons in different electronic levels [2.2, 2.3]. When the high energy electron beam interacts with atoms within the material, it can excite the electrons from the inner levels of the atom or eject the electrons out from the atom, thus creating a vacancy in a particular electronic level. An electron in some higher energy level fills this vacancy and the difference in energy is released in the form of electromagnetic radiation. The schematic of this process is shown in Fig. 2.2. The energy of the emitted radiation is in x-ray range for the innermost K levels. The energy of this x-ray is characteristic of the atom and can be used as fingerprint of the particular atom [2.2]. The number of x-ray photons and the energy of the same are measured with an energy dispersive analyzer. The information from the analyzer (see for example Fig. 2.3) is used for quantitative analysis of elemental composition of the material. We have performed EDX analysis of our samples using a Philips XL-30pc machine. A typical EDX spectrum taken with this machine is shown in Fig. 2.3.

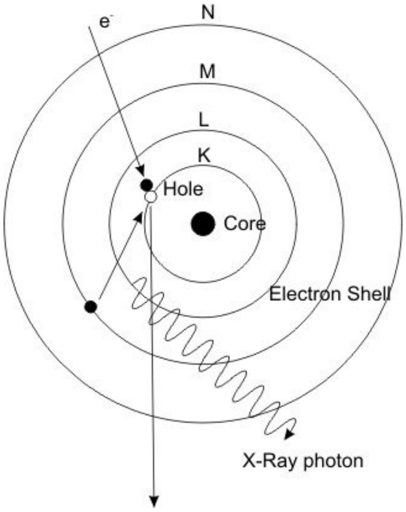

Fig. 2.2: Schematic of x-ray emission from an atom when an electron from higher energy level fills the vacancy created due to excitation of an inner level electron by a high energy electron beam [2.3].

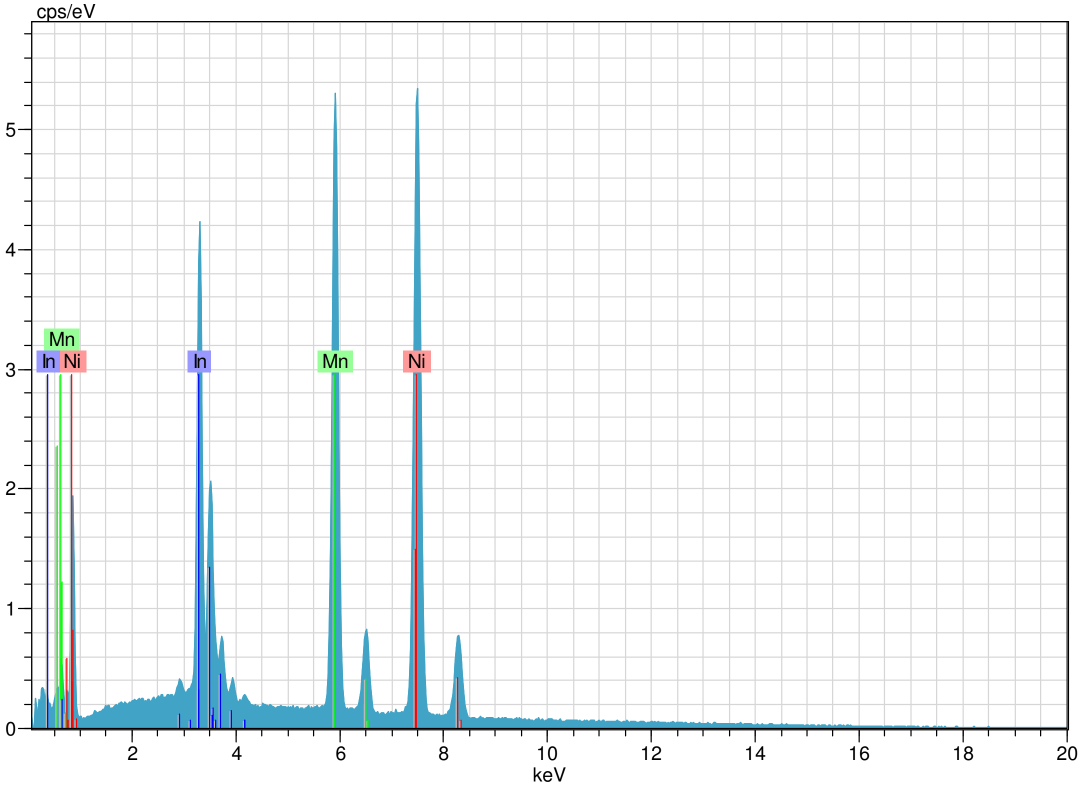

Fig. 2.3: Energy dispersive x-ray (EDX) spectrum of the $Ni_{50}Mn_{34}In_{16}$ alloy.

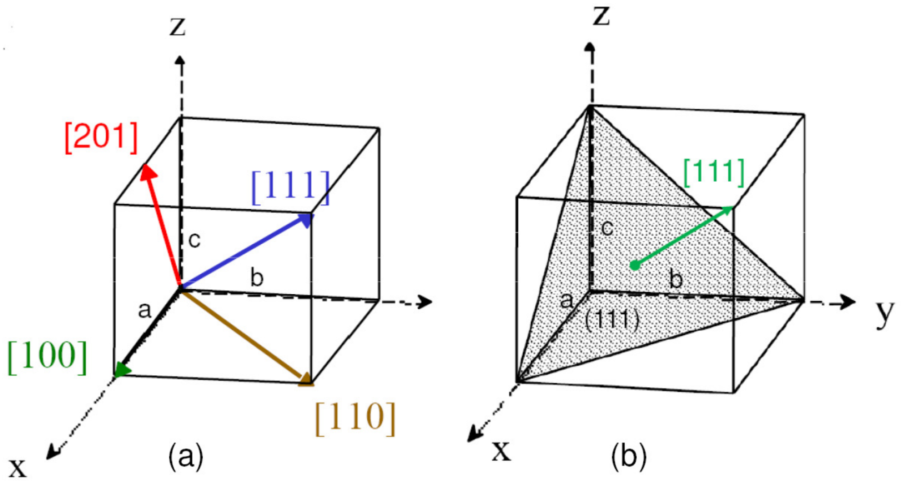

Fig. 2.4: Lattice directions and planes in a cubic unit cell. (a) Lattice directions [100], [110], [111] and [201]. (b) Lattice plane (111); note that the normal to (111) plane has Miller indices [111] (Refs. 2.5 and 2.6).

2.2.2 X-ray diffraction: Very often the solids have the constituents (atoms/molecules) arranged in a periodic structure known as crystal structure. The crystal structure can be thought of as if a unit of constituents designated as 'motif' is attached with each point of a periodic pattern of points known as 'lattice' [2.4, 2.5]. Thus crystal structure = lattice + motif. The lattice can be generated by repeating a block of lattice points named as 'unit cell' of the lattice [2.4, 2.5]. The unit cell of a three dimension lattice is described by three lattice vectors **a**, **b** and **c** (or equivalently by magnitudes a, b, c of these three vectors and the mutual angles α, β and γ) along the edges of the unit cell. The directions along these lattice vectors are known as crystallographic axes. A direction in the lattice, such that a unit vector along this direction passing through origin has projections along the crystallographic axes in the ratio *h*: *k*: *l*, is denoted by Miller indices [*hkl*]. Similarly a set of lattice planes is denoted with Miller indices (*hkl*) where *h*, *k*, *l* are the reciprocals of the fractional intercepts which the plane makes with the crystallographic axes [2.5]. The vector normal to the planes with magnitude $\frac{2\pi}{d_{hkl}}$ has Miller indices [*hkl*]. Here d_{hkl} is

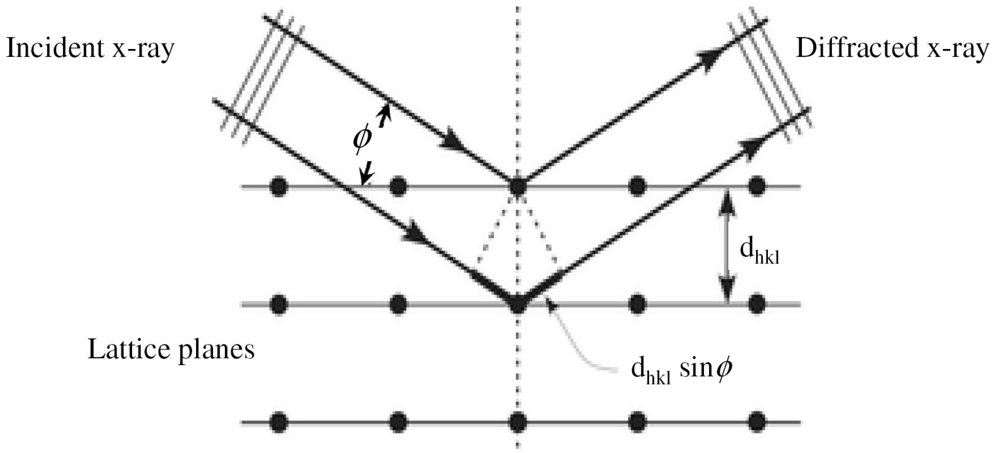

Fig. 2.5: X-ray (wavelength λ) diffraction from lattice planes with spacing d_{hkl}. The diffraction maximum appears at an angle ϕ whenever the path difference $2d_{hkl}\sin\phi$, between x-rays diffracted from consecutive lattice planes, is an integral multiple of the wavelength (Ref. 2.6).

the inter-planer distance of the set of planes. Examples of some lattice directions and (111) plane in a cubic lattice are shown in Fig. 2.4.

X-ray diffraction is one of the techniques to determine the crystal structure of a material. It works on the principle that x-ray, having wavelength comparable to the inter-atomic distance in the solids, gets diffracted from the regular arrangement of atoms when incident on the material. The position of the diffraction maxima is related to the spacing between the lattice planes in the crystalline solid. For an incident plane wave x-ray at an angle ϕ to a set of atomic planes in the specimen, the diffraction maximum appears at an angle ϕ (as shown in Fig. 2.5). The position of the maximum in the diffraction pattern and the spacing between the corresponding set of lattice planes are related as per the Bragg's law given below [2.6].

$$2d_{hkl}\sin\phi = n\lambda \tag{2.1}$$

Here d_{hkl} is the spacing between the (*hkl*) lattice planes, λ is the wavelength of x-ray and n is an integer. Bragg's law ascertains the basic condition of constructive interference that the path difference ($2d_{hkl}\sin\phi$ from Fig. 2.5) between x-rays, diffracted from two consecutive lattice

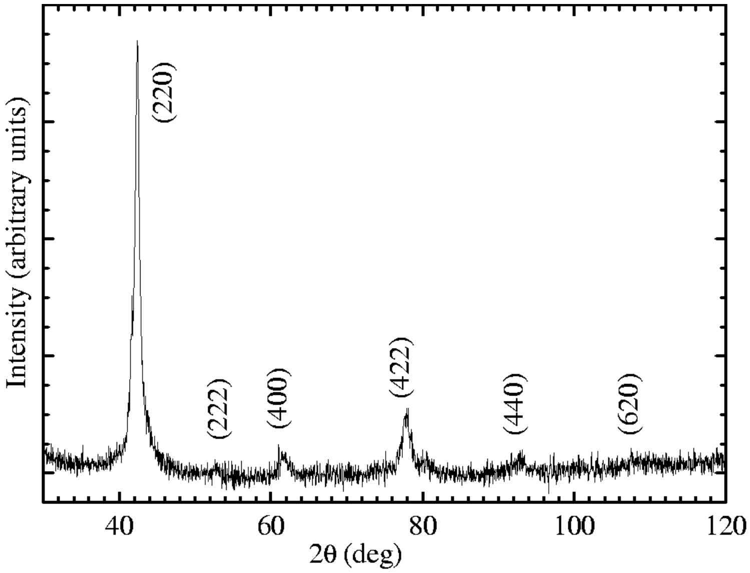

Fig. 2.6: X-ray diffraction (XRD) pattern of $Ni_{50}(Mn,1\%Fe)_{34}In_{16}$ alloy. The peaks are indexed to the $L2_1$ structure.

planes, is an integral multiple of wavelength of x-ray. The positions of these maxima (peaks) in the diffraction pattern give information about the parameters of the unit cell. The intensity of diffraction peaks has the information about the internal structure of unit cell (for example, whether cubic unit cell is simple or body centered or face centered).

We have used a PANalytical X-'Pert PRO MRD machine for determination of X-ray diffraction patterns of the alloys. A typical x-ray diffraction pattern is presented in Fig. 2.6.

Heusler alloy structure: The Ni-Mn-In and Ni-Mn-Sn samples studied in this work belong to the family of Heusler alloys. So a look at the Heusler alloy structure will be helpful for discussing the results presented in the later Chapters. The Heusler alloy system is the first ever alloy system reported to show ferromagnetism where none of the constituents was ferromagnetic [2.7]. This discovery has played an important role in the understanding of magnetism because at that time all the ferromagnetic materials, natural or synthetic, had ferromagnetic constituents.

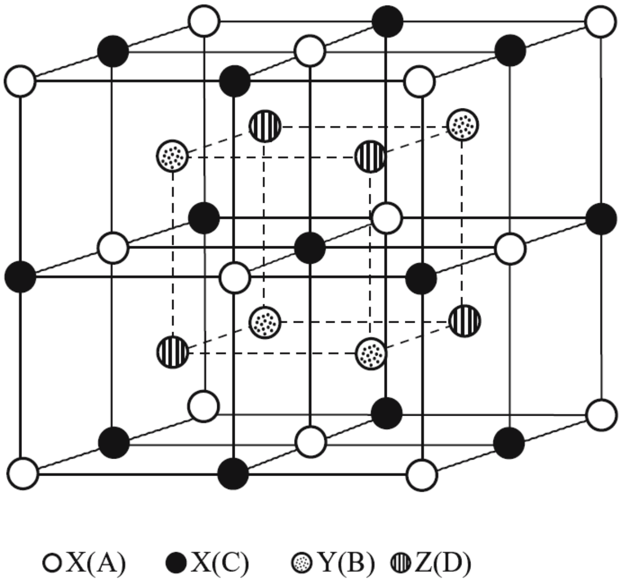

Fig. 2.7: Structure of stoichiometric Heusler alloy X_2YZ (from Ref. 2.7). There are four face centred cubic sub-lattices denoted as A, B, C and D which are occupied by X, Y, X and Z atom respectively.

Heusler alloys have the general formula X_2YZ, where X and Y are transition metal elements and Z is an s-p group element. They crystallize in the $L2_1$ structure. This structure has four interpenetrating face centered cubic (fcc) sub-lattices [2.8] A, B, C and D as shown in Fig. 2.7. The A and C sub-lattices with Wyckoff coordinates (0,0,0) and (1/2,1/2,1/2) are occupied by X atoms, while the B and D sub-lattices with coordinates (1/4,1/4,1/4) and (3/4,3/4,3/4) are occupied by the Y and Z atoms, respectively. The X-ray diffraction pattern of a Heusler alloy shows three types of reflections with structure factor amplitude F(hkl) [2.9] as follows.

$$\left.\begin{array}{r l}
\text{(i)} & \text{h, k, l all odd, e.g., } F(1,1,1) = 4\left|\{(f_A - f_C)^2 + (f_B - f_D)^2\}^{1/2}\right| \\
\text{(ii)} & \text{h, k, l all even and } (h + k + l)/2 = 2n + 1\text{, e.g. } F(200) = 4\left|f_A - f_B + f_C - f_D\right| \\
\text{(iii)} & \text{h, k, l all even and } (h + k + l)/2 = 2n\text{, e.g. } F(220) = 4\left|f_A + f_C + f_B + f_D\right|
\end{array}\right\} \quad (2.2)$$

In the above expressions f_A, f_C, f_B, and f_D are the average scattering factors of atoms at the corresponding lattice sites. For a stoichiometric alloy X_2YZ with the $L2_1$ structure, sites A and C are occupied by X atoms while sites B and D are occupied by Y and Z atoms respectively. So the expressions in eqn. (2.2) reduce to the following [2.8, 2.9] eqns.

$$\left.\begin{array}{l}\text{(i) h, k, l all odd, e.g., } F(1,1,1) = 4 \,|\, (f_B - f_D) \,| \\ \text{(ii) h, k, l all even and } (h + k + l)/2 = 2n + 1, \text{ e.g. } F(200) = 4 \,|\, 2f_A - (f_B + f_D) \,| \\ \text{(iii) h, k, l all even and } (h + k + l)/2 = 2n, \text{ e.g. } F(220) = 4 \,|\, 2f_A + f_B + f_D \,| \end{array}\right\} \quad (2.3)$$

Reflections with $(h + k + l) = 4n$ are the principal reflections. As seen from the above expressions, all the average scattering factors simply add up and so any interchange in positions will not affect the structure factor amplitude F in this case. Thus, the intensity of the principal reflections are unaffected by the state of ordering. However, the structure factor amplitude in the other two groups with h, k, l all odd and $(h + k + l) = 4n + 2$, is sensitive to ordering. These groups are superlattice reflections. The group with h, k, l all odd, is categorized as type-I superlattice reflections. The other group with $(h + k + l) = 4n + 2$ is designated as type-II superlattice reflections. Site disorder in the alloy affects the intensities of these superlattice reflections. For example when there is a total disorder in site B and D, $L2_1$ structure will reduce to B2 structure with lattice constant half that of $L2_1$ structure (see Fig. 2.7) and superlattice reflection of type-I will be absent altogether. This sort of situation will be present inherently in the alloys with Y and Z atoms in non-stoichiometric proportions. Further, the structure factor amplitudes in eqns. (2.2) and (2.3) have been calculated assuming sites A, B, C and D all with fcc structure. In such a case the reflections with mixed indices have zero intensity [2.5]. However, in the fcc unit cell such reflections can have non-zero intensity if individual site (say site D) is not occupied by the same kind of atom. This situation is expected in the off-stoichiometric alloys.

2.3 Electrical resistivity measurement

It is well understood that a perfect crystalline infinite solid with the constituent atoms at rest, causes no scattering of electrons passing through it [2.10], and hence will offer zero electrical resistance. However, in real solids at finite temperature, the electrons suffers scattering from various sources and hence a real solid offers non-zero resistance to the flow of current [2.11]. The scattering arises from the departure from perfect periodicity that can be (i) imperfections in lattice and (ii) phonons arising from thermal vibrations of atoms about their mean position in a crystalline solid. Apart from these two, there can be other sources of departure from some periodicity other than the crystal lattice which also contribute to the resistance to the flow of electrons. For example, magnons in magnetic materials arise from departure from the perfect periodic arrangement of spins. Generally, the scattering mechanisms can be assumed to be independent and as per the Matthiessen's rule $\rho = \rho_0 + \rho_{\mathrm{ph}} + \rho_{\mathrm{mag}}$. Here ρ is the measured resistivity, and ρ_0, ρ_{ph} and ρ_{mag} are the contributions from lattice imperfections, phonons and magnons respectively. The resistivity can be calculated from the resistance R of the sample estimated from the voltage signal V_{m} across the sample when a current I is passed. If the length and cross sectional area of sample be L and A respectively, then $R = V_{\mathrm{m}}/I$ and $\rho = R\,A/L$.

The measured resistivity contains information about the scattering mechanism. One can find trend in the experimentally measured resistivity which is characteristic of the scattering mechanism involved (impurity, phonon etc.). Temperature dependence of resistivity can differentiate between a conductor and semiconductor/insulator, and even give estimate of band gap in semiconductor/insulator. Resistivity measurement can be used to ascertain a phase transition like martensitic transition which generally is accompanied with a large change in electron scattering and hence large change in resistivity.

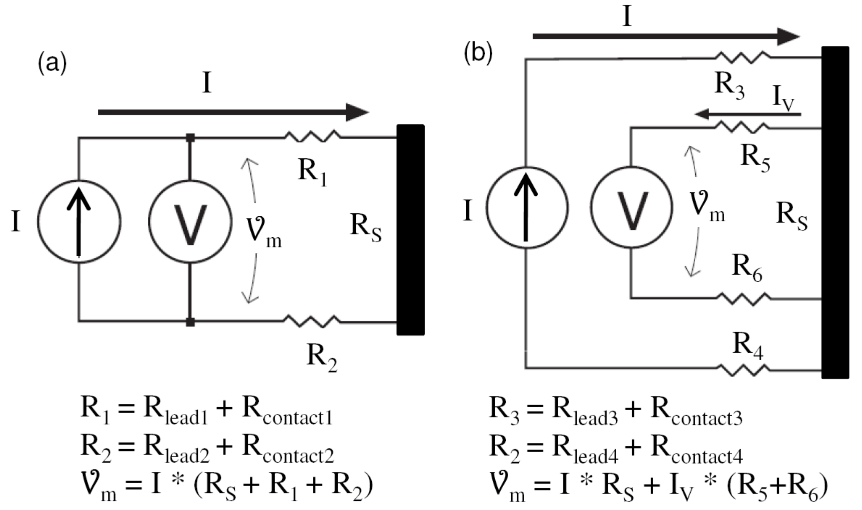

Fig. 2.8: Electrical resistivity measurement techniques. (a) Two-probe technique: Measured voltage signal (V_m) also has contributions from the lead-resistances (R_{lead1} and R_{lead2}) and contact resistances ($R_{contact1}$ and $R_{contact2}$) along with the sample resistance (R_S). (b) Four-probe technique: Current lead-resistances (R_{lead3} and R_{lead4}) and contact resistances ($R_{contact3}$ and $R_{contact4}$) do not contribute to V_m. The voltage signal from voltage lead resistances (R_5 and R_6) are practically zero, as current I_V through the voltage leads is negligible as compared to the measuring current. So $V_m = I*R_S$ effectively.

The method of measurement of resistivity, in which two probes are used to send current as well to measure voltage signal across the sample, is known as two-probe technique. The resistance measured in this method has contributions from the lead resistance and contact resistance along with the sample resistance (see Fig. 2.8(a)). This puts serious limitations on the method in cases where either the sample resistance is comparable to the lead resistance (metallic samples) or contact resistance is appreciable (for example, metal to semiconductor junction). These limitations are overcome by connecting two extra leads on the sample for voltage signal measurement. The voltage signal in this four-probe technique has contribution from the sample only, and there is no contribution from lead resistance or contact resistance as explained in the caption to Fig. 2.8.

We have done zero-field electrical resistivity measurements using two different homemade setups. One of them works in the temperature range 78-350 K and uses liquid nitrogen as coolant. While the second one is a cryo-refrigerator based setup which works in the temperature range 30-350 K. These setups have Pt-100 thermometer and a manganin heater mounted on the sample holder for measuring and controlling the temperature. The heater and thermometer are connected to a commercial temperature controller (Lakeshore Model 350). Commercial dc current source (Keithley model 6220) and nanovoltmeter (Keithley model 2182) are employed for electrical resistivity measurements using the four-probe technique. In these setups data are collected typically in steps of 0.6 K with the ramp rate of 0.6 K/minute.

2.4 Magnetization measurement

Magnetization (*M*) is defined as magnetic moment per unit volume. Experimental measurement of magnetization is required to find out the magnitude of magnetic moment. It can be measured either isothermally with increasing magnetic field or with changing temperature in a constant magnetic field. Magnetization can be measured by the so called direct techniques as these consist of direct involvement of magnetic moment in the measurement. These include, (i) force techniques which involves determining the force/torque on a magnetised specimen and (ii) flux techniques which involve either determining the magnetic flux or determining the rate of change of flux linked with the magnetized sample [2.12]. Force techniques include Faraday balance, torque magnetometer etc., while flux techniques includes vibrating sample magnetometer (VSM), Superconducting Quantum Interference Device (SQUID) magnetometer etc. Magnetization can also be measured by various indirect techniques which make use of known relationships between the phenomenon detected and the magnetic properties of the specimen. These include Hall Effect, magneto-optical Kerr effect, Faraday effects, nuclear magnetic resonance, ferromagnetic resonance, Mossbauer effect, neutron scattering, muon spin resonance etc. Each of the methods has pros and cons but we will not go into the details of all these methods. In the present work we have used a SQUID magnetometer and a VSM for magnetization measurement. Both of them fall under the category of flux measurement technique. The working principle of these instruments is described in the following sections.

2.4.1 SQUID magnetometer

The basic element of this magnetometer is a ring of superconducting metal containing Josephson junctions known as SQUID. It works on the principle that the magnetic flux linked with such a circuit is periodic in units of flux quantum of magnitude $h/2e$ [2.13] where h is the Planck's constant and e is the electronic charge. This flux quantization happens due to the interference effect of the electron-pair wave function. Further, the current through a Josephson junction is a function of the flux linked with the SQUID ring [2.14]. In practice, one measures voltage not current across the SQUID. The SQUID essentially works as a flux to voltage convertor. For measurement of magnetization, the sample is moved through a superconducting detection coil (see Fig. 2.9(a)). This detection coil is connected to SQUID-input coil. The whole circuit of detection coil, SQUID-input coil and connecting wires forms a closed superconducting loop. The SQUID-input coil is inductively coupled to the SQUID sensor. The motion of sample through the detection coil, changes the flux linked with the coil. As the detection coil is a part of closed superconductor circuit, any change of flux linked with it causes a persistent current to flow through the coil. This persistent current is proportional to the change in flux due to the sample motion. This persistent current changes the flux linked with the SQUID sensor. The voltage signal across the SQUID sensor varies in accordance with the persistent current in the detection coil. This voltage signal is a measure of the magnetic moment of the sample [2.13, 2.15]. We have used two commercial SQUID magnetometers (MPMS-5 and MPMS-7XL;

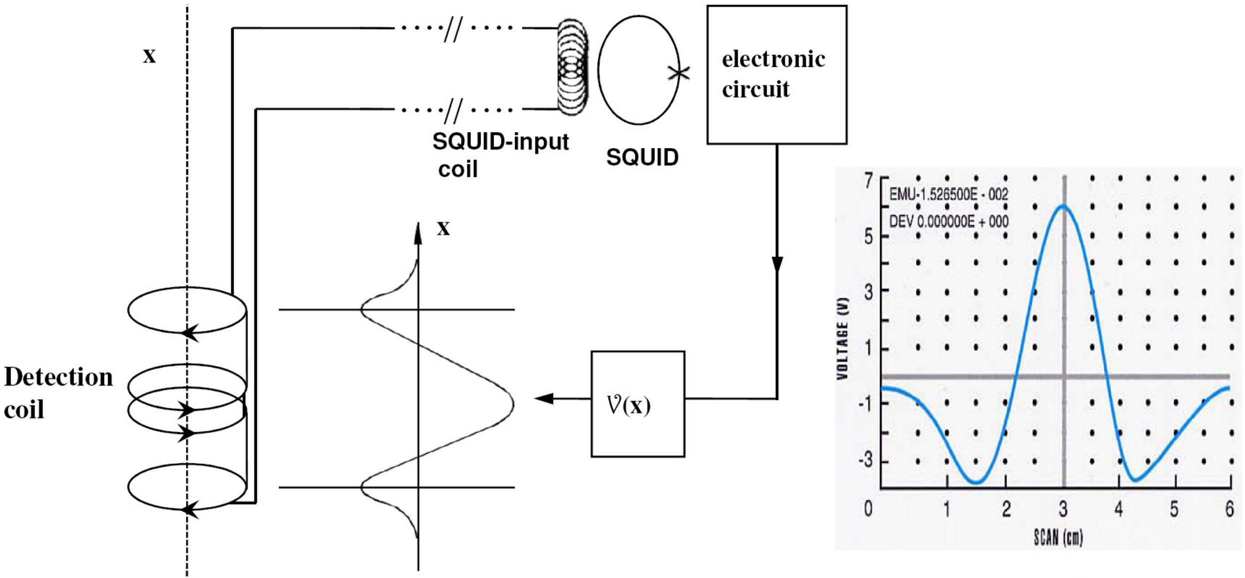

(a) (b)

Fig. 2.9: (a) Schematic of experimental configuration in SQUID magnetometer (MPMS, Quantum Design Inc.) and (b) typical signal generated by sample motion through the detection coil (Refs. 2.13 and 2.15).

Quantum Design Inc. USA) for magnetization measurements. The maximum applicable magnetic field are 50 kOe and 70 kOe in the MPMS-5 and MPMS-7 respectively. Magnetization has been measured in these magnetometers with the data steps of 5 K in temperature stabilization mode. Each temperature point has been approached with the ramp rate of 1 K/minute. The temperature has been measured with the calibrated sensors provided by the manufacture. The schematic of the experimental configuration in these magnetometers and a typical SQUID magnetometer output signal is presented in Fig. 2.9.

2.4.2 Vibrating Sample Magnetometer

It works on the Faraday's law of induction [2.16]. A periodic vibration of magnetized sample causes a periodic change in magnetic flux linked with a detection coil. This change in flux induces a periodic voltage in the detection coil. The induced periodic voltage has the same frequency as that of the sample vibration. With the use of a lock-in technique the induced voltage can be measured accurately. The magnitude of the voltage signal depends on the magnetization

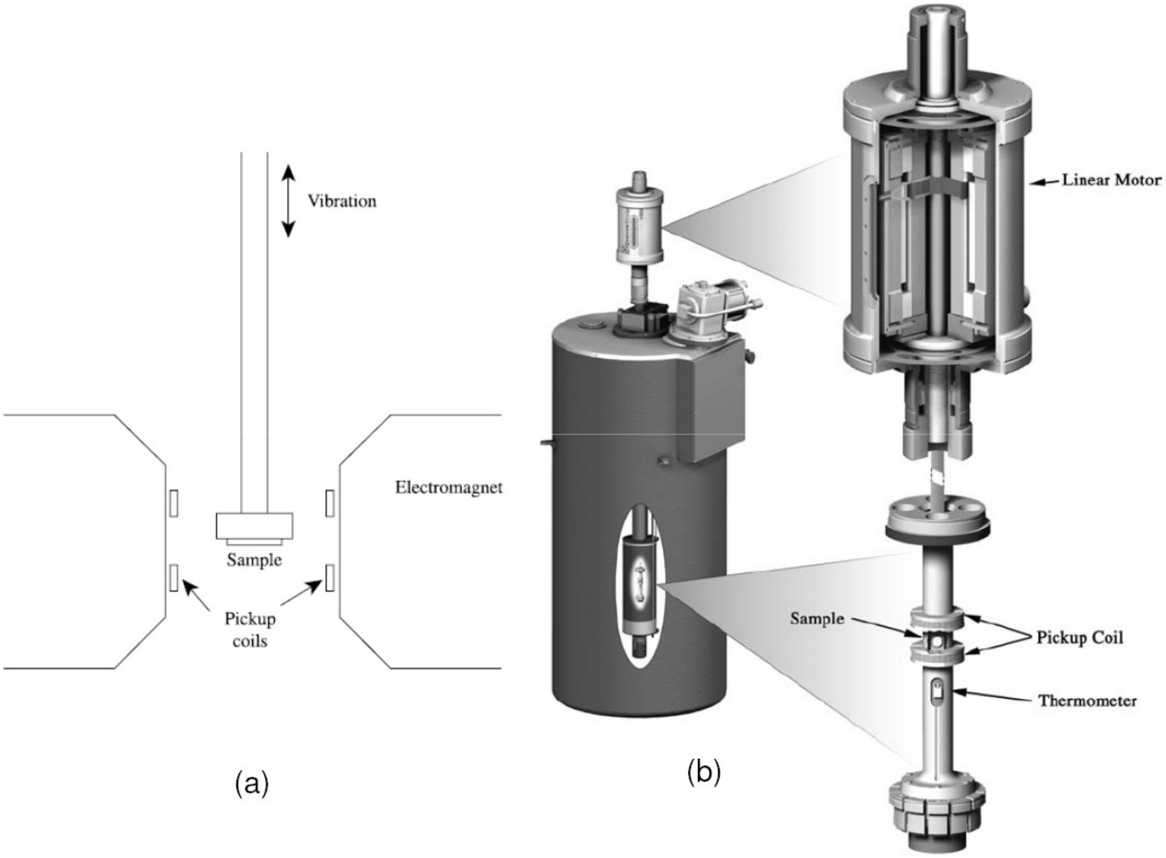

Fig. 2.10: (a) Schematic of experimental configuration in a vibrating sample magnetometer. (b) VSM (Quantum Design Inc.) working in a superconducting solenoid magnet. The oscillating sample motion is provided by linear motor (from Ref. 2.17).

of the sample, amplitude and frequency of motion, and the distance between the sample and the detection coil [2.17]. We have also used commercial vibrating sample magnetometer (VSM; Quantum design, USA) for the measurement of magnetization. The maximum applicable field is 90 kOe in this setup. Magnetization data as a function of temperature have been collected with typical ramp rate of 1 K/minute. A schematic of a VSM configuration is shown in Fig. 2.10.

2.4.3 Magnetization measurement under hydrostatic pressure

We have done magnetization measurements under hydrostatic pressure (*P*) up to 10 kbar in the MPMS-7XL using a pressure cell arrangement (Mcell-10, easyLab Technologies, UK). The pressure is varied by changing the volume of a pressure transmitting liquid in a cylindrical sample holder put inside beryllium-copper piston clamp pressure cell (see Fig. 2.11). The sample holder consists of a polytetrafluoroethylene (PTFE) plug and cap arrangement. The sample is placed in this PTFE container. This container is then filled with the pressure transmitting medium and placed into the sample space of the beryllium-copper piston clamp pressure cell. Pressure is applied at room temperature (for details of pressuring process see [2.18]). The pressure at low temperature is determined in situ by measuring the superconducting transition temperature of a small piece of high purity tin wire placed alongside the sample, in an applied magnetic field of 10 Oe.

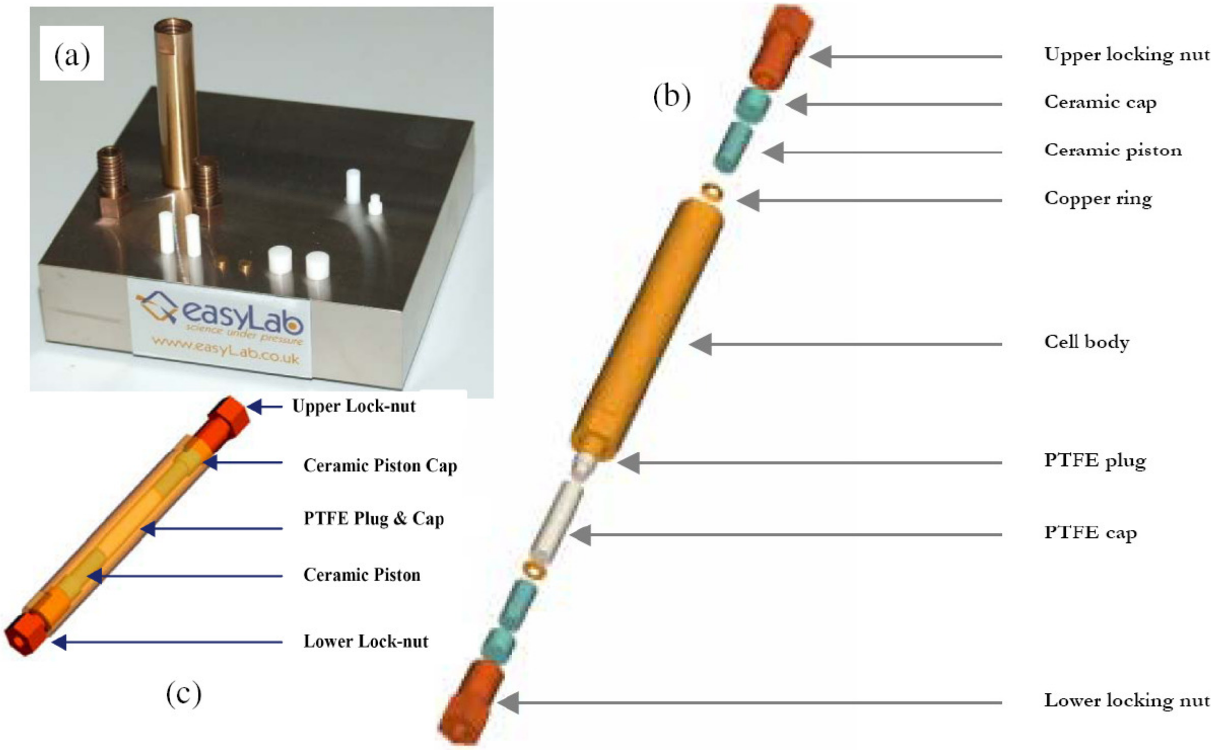

Fig. 2.11: easyLab's Mcell-10 :(a) Mcell components on the mounting platform, (b) Exploded view of Mcell-10 and (c) View of completely assembled Mcell-10 (from Ref. 2.18) (courtesy: easyLab Technologies, UK).

2.5 Thermal property measurement

The thermal response of a material provides valuable information about the material. The most basic thermal property of a material is its heat capacity. It provides insight in the lattice, electronic and sometimes magnetic properties of material. In the following sections we briefly describe the technique of heat capacity measurement we have used. Further, alloy samples investigated in this work, undergo martensitic transition. Differential scanning calorimetry (DSC) which measures heat flow from the sample is a useful method to study such a transition. We have developed a DSC setup in house during the course of this work. We also describe this DSC setup in the following sections.

2.5.1 Heat capacity measurement

Heat capacity at constant pressure is defined as $C_p = \left(\frac{dQ}{dT}\right)_p$, where dT is the rise in temperature for a given heat dQ. We have measured the heat capacity of the alloy samples using a commercial Physical Properties Measurement System (PPMS; Quantum design, USA). PPMS uses relaxation technique [2.19] for measurement of heat capacity. The sample is mounted on a sample platform using thermally conducting grease (shown in Fig. 2.12) [2.19]. The sample platform has a heater and a temperature sensor mounted on it in order to provide a known heating power to the platform and for measurement of the temperature of the platform respectively. The sample platform is supported by thin wires connected to the puck which serves as calorimetric thermal bath; these wires also act as electrical connections for platform heater and thermometer. The puck also has a thermometer for measurement of the puck temperature. The whole arrangement is covered by a thermal shield which prevents unwanted heating of the sample and the sample platform from the warmer surfaces of sample chamber. The experiment is performed in high vacuum.

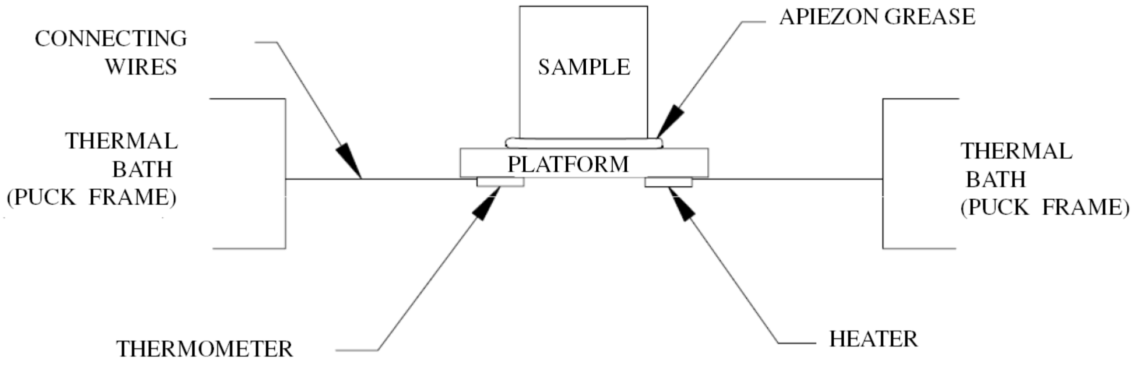

Fig. 2.12: Configuration of sample mounting in PPMS Heat Capacity option (from Ref. 2.19).

For each measurement, a certain power is generated by the platform heater. The entire temperature response of the sample platform is fitted with two models. The first is a simple model which assumes that there is a good thermal contact between the sample and the platform, and both are at the same temperature. The second model assumes that there is a temperature difference between the sample and the platform due to poor thermal contact between the two. This model accounts for both the thermal relaxation of the sample platform to the bath temperature and the relaxation between the sample platform and the sample itself. This is also known as the two-tau method. The following mathematical equations are used in the two models [2.19].

(i) Simple model: $C_{total}\frac{dT}{dt} = -K_W(T - T_b) + P_w(t)$ (2.4)

(ii) Two-tau model:

$$\left.\begin{aligned} C_{platform}\frac{dT_p}{dt} &= P_w(t) - K_W(T_p(t) - T_b) + K_g(T_s(t) - T_p(t)) \\ C_{sample}\frac{dT_s}{dt} &= -K_g(T_s(t) - T_p(t)) \end{aligned}\right\} \qquad (2.5)$$

Here C_{platform} and C_{sample} are the heat capacities of the sample platform and sample respectively. C_{total} is the total heat capacity of sample and platform. K_{W} and K_{g} are the thermal conductance of the supporting wires and grease respectively. T_s, T_p and T_b are the temperatures of sample, platform and bath (puck frame) respectively. $P_w(t)$ is the power applied by the heater. First the C_{addenda} is measured in the simple model without any sample so that $C_{\mathrm{total}} = C_{\mathrm{addenda}}$. The experimental data measured with the sample is fitted in the simple model as well the two-tau model using $C_{\mathrm{total}} = C_{\mathrm{sample}} + C_{\mathrm{addenda}}$. The heat capacity of sample is taken from the model with the smaller fit deviation.

2.5.2 Differential scanning calorimetry

A differential scanning calorimetry (DSC) measures the flow of heat to the sample as compared to a reference sample while continuously changing the temperature [2.20]. This is suitable for the measurement of latent heat associated with a first-order phase transition. There are broadly two categories of DSC [2.20]. One category called as power-compensated DSC consists of two separate heaters for the sample and the reference. The sample and reference are heated at an equal rate and the power-compensation required for maintaining the rate is measured. In the second category called heat-flow DSC both the sample and the reference are heated with the same heater, and the temperature difference between the two (which proportionate to the heat flow from the sample to the reference) is measured. We have developed a heat-flow type DSC setup during the course of the present work.

The DSC setup is designed using commercially available thermoelectric modules (TEMs). Thermoelectric modules are batteries of thermocouples. As shown in Fig. 2.13(a), a thermoelectric module consists of a series of n and p type elements of Bi_2Te_3 which are connected electrically in series but thermally in parallel. This can work as a Peltier element i.e. it can transport heat from one face plate to the other when a current is passed through it, or in inverse-Peltier configuration (Seebeck effect) to generate voltage when there is temperature

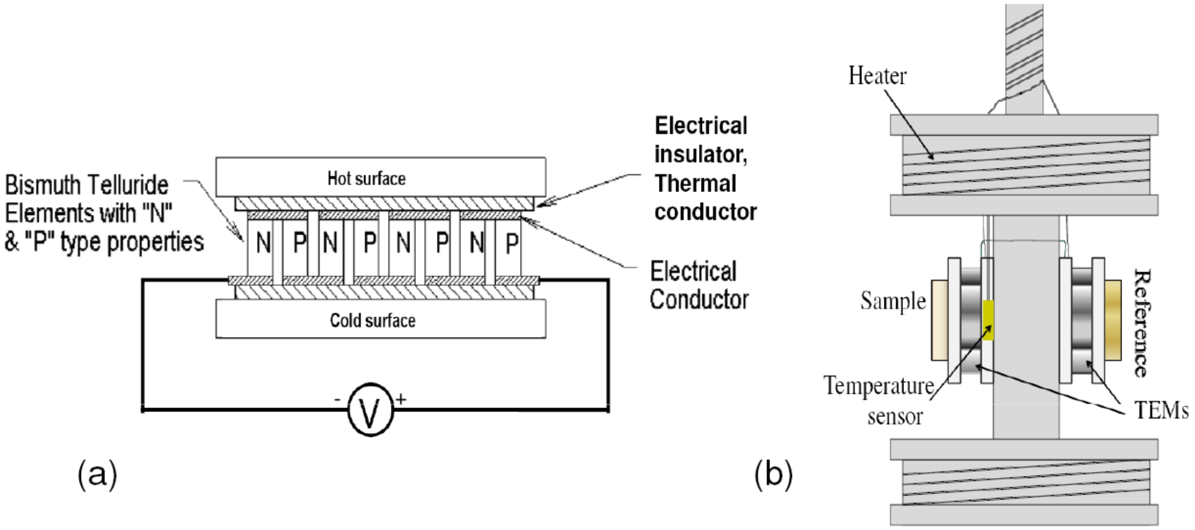

Fig. 2.13: (a) Internal structure of a thermoelectric module (TEM) and Seebeck effect [2.20]. (b) Schematic of arrangement of sample, reference and TEMs on the sample holder.

difference between the end plates. The voltage across the TEM is proportional to the temperature difference between the two plates which in turn is a measure of the heat flow through the module. The polarity of voltage changes with the direction of heat flow.

The setup basically consists of two TEMs (Melcor ET 0.8-32-F0-H1/C1) mounted on a copper spool (shown in Fig. 2.13(b)). The copper spool is attached to a variable temperature insert. The copper spool works as a thermal bath. The sample is mounted on one TEM and the reference is mounted on the second TEM. The two TEMs are connected differentially. The heat released or absorbed by the sample as compared to the reference is measured by reading the differential voltage furnished by the TEMs by using a nano-voltmeter (Keithley 2182). As the two sensors are connected differentially, the heat flow of the reference is subtracted from that of the sample, and therefore, the major contribution to the calorimetric output is the thermal power released (or absorbed) by the sample during the first-order phase transition. The sample chamber is maintained at pressure of 1 atm by connecting a He filled balloon to the sample chamber. The temperature of the sample is measured and controlled with the help of a Pt-100 temperature sensor and a heater mounted on the sample holder. The instrument works in the temperature range 80-320 K in zero magnetic field and typical temperature ramp rate used for recording DSC curve is 2 K/minute.

Calibration of DSC: The DSC output has been calibrated with resistive heating [2.21]. For calibration the sample is replaced by a manganin heater wire. The temperature dependence of resistance of this heater wire is already measured using the four-probe technique. Constant power (P_w) dissipation in the resistance due to Joule heating at a steady state gives a voltage signal (Y) (see inset (a) to Fig. 2.14). Y is found to be linear in P_w (see inset (b) to Fig. 2.14).The slope of $Y(P_w)$ curve gives the sensitivity (K_{DSC}) at that temperature. The sensitivity thus obtained is plotted in the main panel of Fig. 2.14.

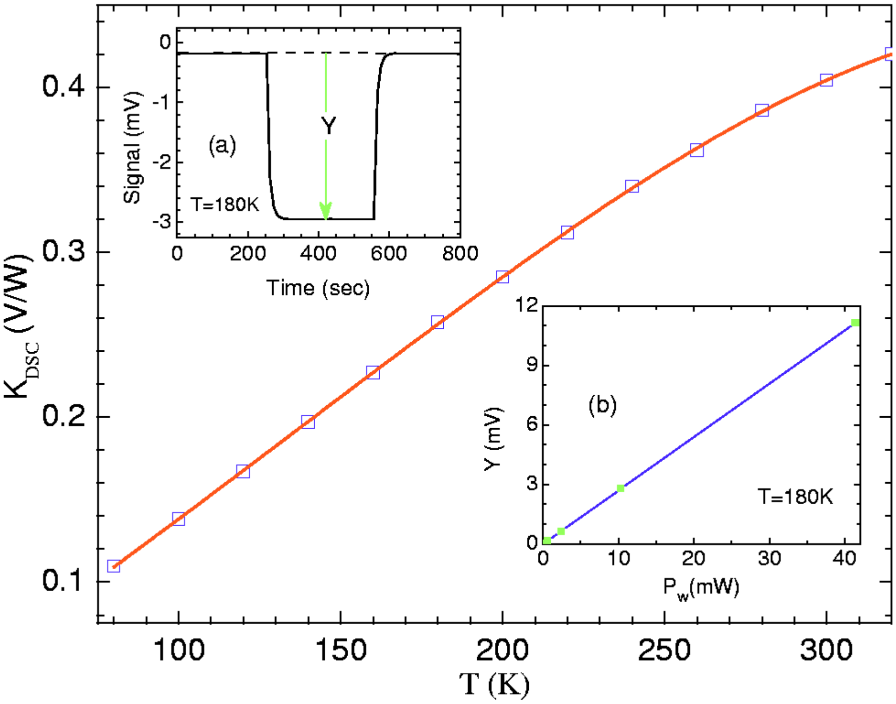

Fig. 2.14: Temperature (T) dependence of sensitivity (K_{DSC}) of the DSC set up in zero magnetic field. Points are experimental data and line is a fit to data. Inset: (a) Output voltage signal vs. time calibration curve in steady state at T = 180 K with input power (P_w) = 10.34 mW, (b) Output signal (Y) vs. power curve at T = 180 K.

The DSC signal $\mathcal{V}(T)$ is recorded while cooling/heating the sample. From $\mathcal{V}(T)$, heat flow (in watts) is calculated from $dQ/dt = \mathcal{V}(T)/K_{\mathrm{DSC}}(T)$. From the temperature ramp rate dT/dt, the calorimetric curve dQ/dT is calculated using $dQ/dT = (dQ/dt)/(dT/dt)$. From this dQ/dT vs. temperature plot the entropy change across a first-order phase transition is obtained from the following equation after base line correction.

$$\Delta S = \int_{T_1}^{T_2} \frac{1}{T}\left(\frac{dQ}{dT}\right) dT \qquad (2.6)$$

Here T_1 and T_2 are the start and finish temperatures of the transition.

Baseline: Fig. 2.15 shows typical calorimetric plot in a cooling cycle across a first-order phase transition from high temperature phase to lower temperature phase. The DSC signal shows a peak corresponding to a first-order phase transition. The start temperature of the transition is

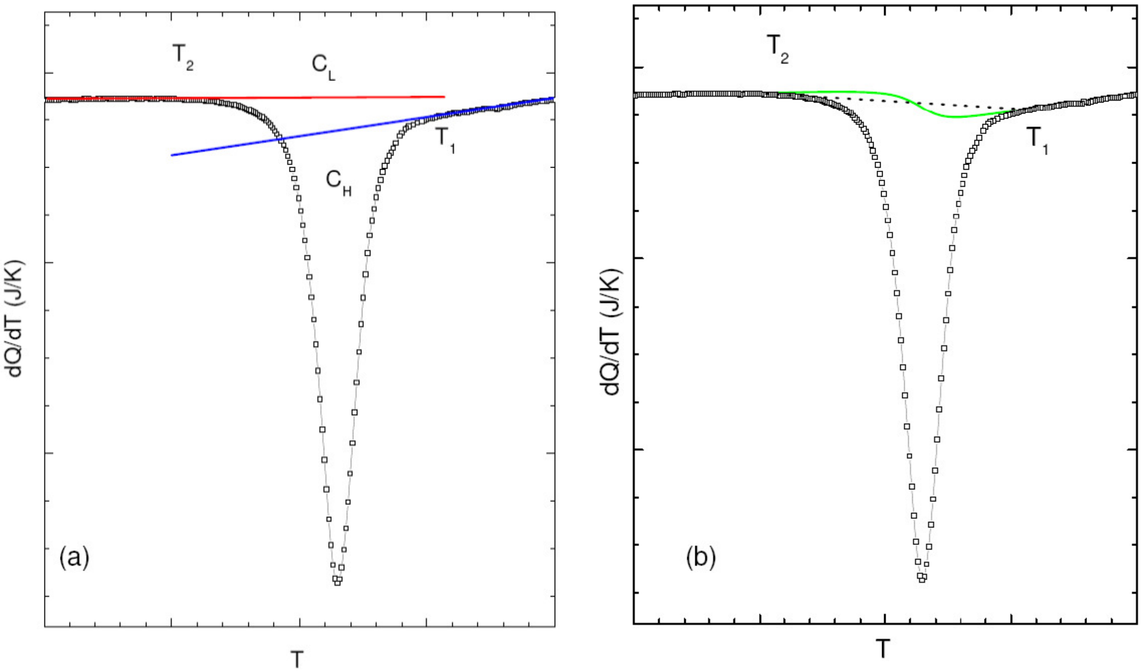

Fig. 2.15: (a) Typical peak in temperature (T) dependence of calorimetric signal (dQ/dT) across a first-order phase transition in cooling. The curves C_H and C_L are base lines at higher and lower temperatures outside the phase transition region. T_1 and T_2 are start and finish temperatures of the phase transition. (b) Baseline estimation in the phase transition region: dotted curve is a linear baseline from T_1 to T_2, and solid green curve is the baseline estimated with iterations using eqn. (2.7).

identified as the temperature where the signal starts deviating from a smooth baseline. Similarly, finish temperature of transition is the temperature where the signal again merges with the smooth baseline. The baselines at temperatures higher and lower than the transition region are marked as C_H and C_L in Fig. 2.15(a). The start and finish temperatures are marked as T_1 and T_2. The baseline is a smooth curve above and below the transition. In the phase transition region (peak) we need to estimate the baseline. The first approximation to the baseline in the peak region is a straight line connecting the signals at T_1 and T_2. However, this baseline is erroneous because during the phase transition the heat capacity of the sample also changes with phase fraction. To avoid the contribution from this changing phase fraction, we need to estimate the baseline which takes such a contribution into consideration. Any such baseline should gradually shift from curve $C_H(T)$ to curve $C_L(T)$ in cooling. We have used the method of Scott and Ramachandrarao [2.22] for estimating the baseline. In this method the first estimate to the baseline $B(T)$ in the transition region, is the line as mentioned above (see dotted line in Fig. 2.15(b)). Let $A(T)$ be area between the peak curve and baseline from T_1 to T, and A_0 is total area between the peak curve and the baseline from T_1 to T_2. Then $f_A(T) = A(T)/A_0$ is the fractional area between the peak curve and the baseline from T_1 to T. $f_A(\mathrm{T})$ is a measure of transformed phase fraction during the phase transition. In second iteration the base line is taken as

$$B(T) = \left[1 - f_A(T)\right] \; C_H(T) + f_A(T) \; C_L(T) \qquad (2.7)$$

With this new baseline, the fractional area is calculated again. In the third iteration, baseline is again corrected as per eqn. (2.7). The process is repeated until we get a consistent baseline.

2.6 Magnetocaloric effect

The magnetocaloric effect (MCE) refers to the isothermal entropy change (ΔS_M) or the adiabatic change in temperature (ΔT_{ad}) of a material as a result of exposure to an external magnetic field [2.23]. The MCE is intrinsic to all magnetic materials and is due to the coupling of the magnetic sub-lattice with the magnetic field, which changes the magnetic part of the entropy of a solid under the change of field. The MCE in a ferromagnet near the Curie temperature is shown in Fig. 2.16. At constant pressure the total entropy (S) is a function of temperature and magnetic field, and is the sum of magnetic S_M, lattice S_{Lat} and electronic S_{El} contributions [2.24]. In a given phase of the material, all these parts increase with temperature.

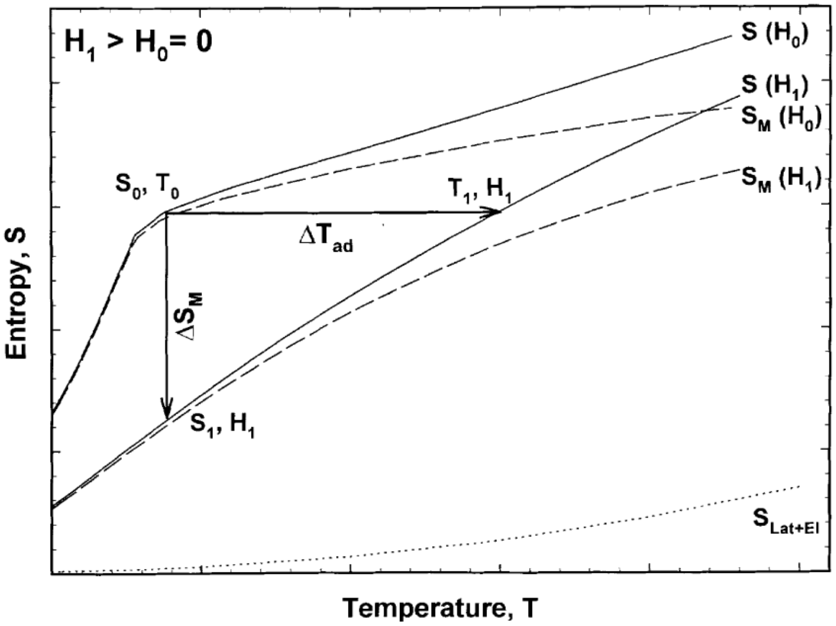

Fig. 2.16: Magnetocaloric effect near the Curie temperature of a ferromagnet illustrated with the entropy (S) - temperature (T) diagram (from ref. 2.24). The solid lines represent the total entropy in magnetic field $H_0 = 0$ and $H_1 > 0$. The dotted line shows the non-magnetic (lattice + electronic) entropy. Dashed lines show the magnetic entropy in the two fields. S_0 and T_0 are zero-field entropy and temperature, and S_1 and T_1 are entropy and temperature in magnetic field H_1. The horizontal arrow shows the adiabatic change in temperature (ΔT_{ad}) and the vertical arrow shows the isothermal magnetic entropy change (ΔS_M) when the magnetic field is changed from H_0 to H_1.

When a magnetic field is applied isothermally, the spins align with magnetic field and the entropy decreases. Conversely, when a magnetic field is removed, entropy increases as the randomness in the spin orientation increases. If the field is applied adiabatically, the magnetic part of the entropy decreases due to a increased alignment of spins. However as adiabatic process is an isentropic process, the non-magnetic part of the entropy increases to keep the total entropy constant. So the temperature of the system increases. Conversely, the adiabatic removal of the magnetic field causes the temperature of the system to decrease. These processes: decrease (increase) in entropy under isothermal application (removal) of field and increase (decrease) in temperature under adiabatic application (removal) of field, are designated as conventional MCE. In some cases the result can be the opposite and this termed as inverse MCE.

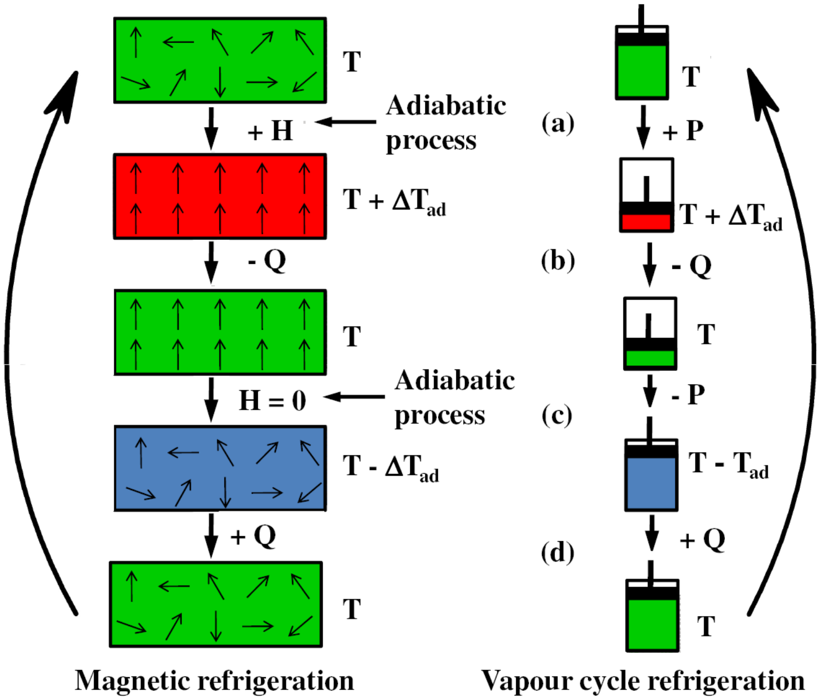

Fig. 2.17: Schematic showing analogy of magnetic refrigeration with vapor cycle refrigeration (Ref. 2.25).

A proper combination of these adiabatic and isothermal processes can be utilized for refrigeration applications. One of the methods using this idea is presented schematically in Fig. 2.17. The steps involved in such a refrigeration are also compared with those involved in a vapor cycle (gas compression) based technology. Just as the adiabatic compression of a gas, the adiabatic magnetizing of a ferromagnet increases the temperature of the system (step (a) in Fig. 2.17). Now it is brought in contact with the ambient environment, so that heat is removed from the refrigerant (step (b) in Fig. 2.17) and thermal equilibrium at T is established. In such a state the adiabatic demagnetization (which is similar to the expansion of a gas) decreases the temperature of the refrigerant (step (c) in Fig. 2.17). When it is brought in contact with the system to be cooled, it takes heat from the system [step (d) in Fig. 2.17]. This cycle can be repeated with the net result of heat removed from the system and discarded to the environment.

2.6.1 Experimental techniques of estimation of MCE

ΔT_{ad} can be estimated directly by applying/removing the magnetic field adiabatically. However, ΔS_{M} can only be measured indirectly. The change of magnetic entropy in a material due to an isothermal change of magnetic field can be estimated using the following Maxwell's equation [2.23, 2.26].

$$\left(\frac{\partial S(T,H)}{\partial H}\right)_T = \left(\frac{\partial M(T,H)}{\partial T}\right)_H \qquad (2.8)$$

which for isothermal-isobaric process yields

$$\Delta S_M(T,\Delta H) = \int_{H_1}^{H_2} \left(\frac{\partial M(T,H)}{\partial T}\right)_H dH \qquad (2.9)$$

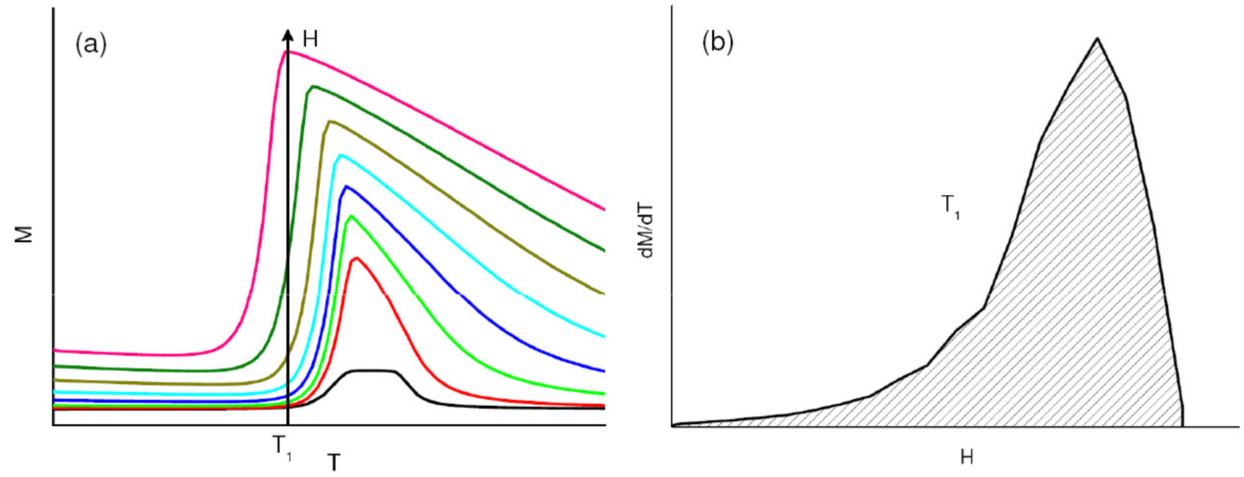

Fig. 2.18: (a) Magnetization (*M*) vs. temperature (*T*) curves in constant magnetic fields (*H*). (b) Isothermal $\frac{\partial M}{\partial T}$ vs. *H* curve at $T = T_1$ from (a). The area under isothermal $\frac{\partial M}{\partial T}$ vs. *H* curve is measure of isothermal magnetic entropy change at $T = T_1$ according to eqn. (2.9).

Isothermal $\frac{\partial M(T,H)}{\partial T}$ vs. H curve can be obtained from different isofield magnetization vs. temperature curves (see Fig. 2.18). Numerical integration of isothermal $\frac{\partial M(T,H)}{\partial T}$ vs. H curve from zero to *H* gives ΔS_M at that temperature.

ΔS_M can also be estimated from isothermal magnetization vs. field curves. For magnetization measured isothermally at discrete magnetic field intervals, equation (2.9) can be approximately written as [2.27]

$$\Delta S_M\left(T + \frac{1}{2}\Delta T\right) = \frac{1}{\Delta T}\left[\int_0^H M(T+\Delta T, H)dH - \int_0^H M(T,H)dH\right] \qquad (2.10)$$

Thus the area under the isothermal *M*(*H*) curves obtained at close temperature intervals are obtained through numerical integration of each curve from 0 to H. The area obtained for the *M*(*H*) curve at a temperature *T* is subtracted from that for the adjacent *M*(*H*) curve corresponding to the next higher temperature $T + \Delta T$ (see Fig. 2.19). The remaining area is divided by ΔT to get ΔS_M corresponding to the temperature ($T + ½\,\Delta T$). In case of a first-order phase transition, the

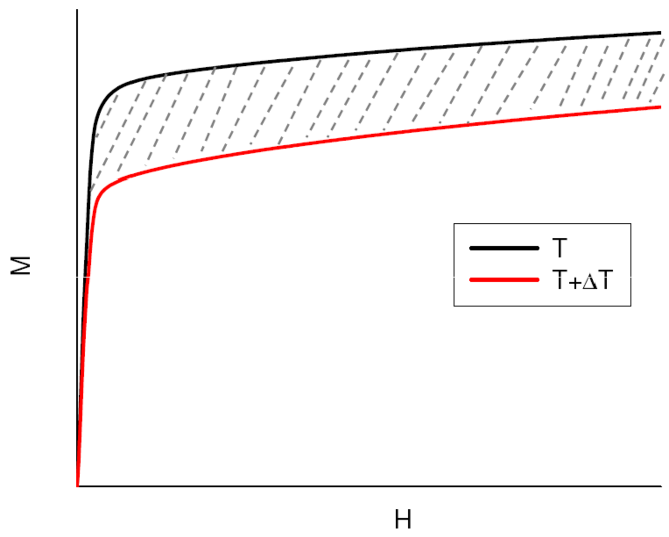

Fig. 2.19: Magnetization (*M*) vs. magnetic field (*H*) curves at constant temperatures *T* and *T+ΔT*. The area between the two curves divided by the temperature difference *ΔT* estimates the isothermal magnetic entropy change at *(T* + ½ *ΔT)* according to eqn. (2.10).

estimation of ΔS_M from isothermal M(H) curves can result in erroneous estimation [2.28, 2.29] as the phase fractions of two phases (high-*T* phase and low-*T* phase) at *T* and *T+ΔT* are different. In such a case estimation of ΔS_M from isofield *M*(*T*) curves is advisable [2.28, 2.29].

MCE can also be estimated from heat capacity measurements. The technique of heat capacity measurement is discussed in section 2.5.1 of this Chapter. If *C* is the heat capacity, then from the equations $C\mathrm{d}T = \mathrm{d}Q$ and $\mathrm{d}Q = -T\mathrm{d}S$ (when the magnetic entropy decreases the lattice heat increases) we get for infinitesimal adiabatic temperature rise [2.24].

$$dT = -\left(\frac{T}{C(T,H)}\right)_H \left(\frac{\partial M(T,H)}{\partial T}\right)_H dH \tag{2.11}$$

Integration of this equation gives

$$\Delta T_{ad}(T,H) = -\int_0^H \left(\frac{T}{C(T,H)}\right)_H \left(\frac{\partial M(T,H)}{\partial T}\right)_H dH \tag{2.12}$$

Heat capacity measurement as a function of temperature in constant magnetic field alone can be used to estimate ΔS_M and ΔT_{ad}. The entropy of magnetic solid can be calculated from heat capacity as

$$S(T)_{H=0} = \int_0^T \frac{C(T)_0}{T} dT + S_0 \qquad (2.13)$$

and

$$S(T)_H = \int_0^T \frac{C(T)_H}{T} dT + S_{0,H} \qquad (2.14)$$

where S_0 and $S_{0,H}$ are the zero temperature entropies. In a condensed system these are the same (i.e. $S_0 = S_{0,H}$) [2.23, 2.26]. Then ΔS_M and ΔT_{ad} can be estimated from following equations and as illustrated in Fig. 2.16.

$$\Delta S_M(T)_H = S(T)_H - S(T)_0 \qquad (2.15)$$

and

$$\Delta T_{ad}(T)_H = \left[T(S)_H - T(S)_0\right]_S \qquad (2.16)$$

2.7 Strain measurement

Strain is defined as the relative change in dimension of a material sample. The change in dimension can be due to some external isothermal stimulus like stress or magnetic field, or it can be due to a temperature change. Linear strain (ε) due to uniaxial stress is defined as the relative change in length of the sample along the direction of stress.

$$\varepsilon = \frac{\Delta L}{L_0} = \frac{(L - L_0)}{L_0} \qquad (2.17)$$

Where L_0 is the starting length and L is the final length along the direction of applied stress. In case of a temperature change the thermal strain ε_T is defined with respect to some reference temperature T_0.

$$\varepsilon_T = \frac{\Delta L}{L_{T_0}} = \frac{\left(L_T - L_{T_0}\right)}{L_{T_0}} \qquad (2.18)$$

Where L_T is the length at temperature T and L_{T_0} is the length at reference temperature T_0. Generally T_0 is chosen to be room temperature 293 K. For magnetic field change the magnetostrain ε_H is defined with reference to length in zero field.

$$\varepsilon_H = \frac{\Delta L}{L_0} = \frac{\left(L_H - L_{H=0}\right)}{L_{H=0}} \qquad (2.19)$$

Where L_H is the length in magnetic field H.

There are a number of techniques developed for strain measurement. These include resistance strain gauge, capacitance strain gauge, inductance method and interferometeric methods etc. Out of these, resistance strain gauge technique is the simplest yet robust. We have used this technique for measurement of temperature and magnetic field dependence of strain in our alloy samples. Details of this technique are described below.

A strain gauge is constructed by bonding, a fine electric resistance wire or photographically etched metallic resistance foil, to an electrical insulation base using an appropriate bonding material. Leads are attached to the gauge for resistance measurement. The resistance R of strain gauge varies with the strain as [2.30]

$$\frac{\Delta R}{R_0} = \frac{\left(R - R_0\right)}{R_0} = F\varepsilon \qquad (2.20)$$

here R_0 is the resistance at zero strain, F is the gauge factor which qualifies the strain sensitivity of the gauge. F can have temperature dependence. For strain measurement, the gauge is attached to the sample with an adhesive so that the gauge becomes an integral part of the sample. Strain experienced by the sample is also transferred to the gauge. Isothermal strain due to an applied stress can be estimated by measuring directly the relative change in gauge resistance and using eqn. (2.20) as

$$\varepsilon = \frac{\Delta L}{L_0} = \frac{(L - L_0)}{L_0} = \frac{1}{F}\frac{(R - R_0)}{R_0} = \frac{1}{F}\frac{\Delta R}{R_0} \tag{2.21}$$

In case of mechanical stress, the only source of change in the gauge resistance is the strain. However in case of temperature change and magnetic field change, apart from the strain in sample, the gauge resistance can also change due to inherent temperature/field dependence of the gauge resistance. For example the case of temperature change is discussed. When the gauge is not mounted on sample, there is zero strain. In this case the resistance of gauge will change under change of temperature (say from T to T+ΔT) as

$$\left(\frac{\Delta R}{R_{T_0}}\right)_G = \left(\frac{R_{T_0+\Delta T} - R_{T_0}}{R_{T_0}}\right)_G = (\beta_G \Delta T) \tag{2.22}$$

Here β_G is the temperature coefficient of gauge resistance. When the gauge is mounted on a sample and temperature is changed, the gauge resistance $\left(\frac{\Delta R}{R_0}\right)_{G/Sample}$ will change from two reasons. First, there will be a change due to the temperature dependence of the gauge resistance. Second, as the gauge and sample have different thermal expansions, the gauge will be under differential strain and this strain will change the gauge resistance. So change in gauge (mounted on the sample) resistance is

$$\left(\frac{\Delta R}{R_0}\right)_{G/Sample} = \left(\frac{\Delta R}{R_0}\right)_{Thermal} + F\left(\frac{\Delta L}{L_0}\right)_{Diferential} \tag{2.23}$$

$$\left(\frac{\Delta R}{R_0}\right)_{G/Sample} = (\beta_G \Delta T) + F\left[\left(\frac{\Delta L}{L_0}\right)_{Sample} - \left(\frac{\Delta L}{L_0}\right)_G\right] \tag{2.24}$$

Here $\left(\frac{\Delta L}{L_0}\right)_{Sample}$ and $\left(\frac{\Delta L}{L_0}\right)_G$ corresponds to the change in length of sample and gauge respectively (relative to respective length L_0 at T_0). Thus the gauge experiences a differential strain of $\left(\frac{\Delta L}{L_0}\right)_{Sample} - \left(\frac{\Delta L}{L_0}\right)_G$. Note that if the gauge has been mounted on a sample whose thermal expansion matches with that of the sample, there would be no strain in the gauge (as if gauge is free). In this case the change in gauge resistance would result from the temperature dependence only. However in general, the gauge experiences a differential strain. Further, we are interested in measuring $\left(\frac{\Delta L}{L_0}\right)_{Sample}$ so we need get rid of $\left(\frac{\Delta L}{L_0}\right)_G$ as well as $\beta_G \Delta T$ in eqn. (2.24). If an identical gauge is also mounted on a reference material, similar to eqn. (2.24) the change in gauge (mounted on reference) resistance is given by

$$\left(\frac{\Delta R}{R_0}\right)_{G/\mathrm{Re}\,f} = (\beta_G \Delta T) + F\left[\left(\frac{\Delta L}{L_0}\right)_{\mathrm{Re}\,f} - \left(\frac{\Delta L}{L_0}\right)_G\right] \tag{2.25}$$

Taking the difference of eqns. (2.24) and (2.25) we have for a differential measurement

$$\left(\frac{\Delta R}{R_0}\right)_{G/Sample} - \left(\frac{\Delta R}{R_0}\right)_{G/\mathrm{Re}\,f} = F\left[\left(\frac{\Delta L}{L_0}\right)_{Sample} - \left(\frac{\Delta L}{L_0}\right)_{\mathrm{Re}\,f}\right]$$

or

$$\left(\frac{\Delta L}{L_0}\right)_{sample} = \frac{1}{F}\left\{\left(\frac{\Delta R}{R_0}\right)_{G/sample} - \left(\frac{\Delta R}{R_0}\right)_{G/\mathrm{Re}\,f}\right\} + \left(\frac{\Delta L}{L_0}\right)_{\mathrm{Re}\,f} \tag{2.26}$$

With the known temperature dependence of $\left(\frac{\Delta L}{L_0}\right)_{\mathrm{Re}f}$ and F, the eqn. (2.26) gives

$$\left(\frac{\Delta L}{L_0}\right)_{sample}(T)=\frac{1}{F(T)}\left\{\left(\frac{\Delta R}{R_0}\right)_{G/sample}(T)-\left(\frac{\Delta R}{R_0}\right)_{G/\mathrm{Re}f}(T)\right\}+\left(\frac{\Delta L}{L_0}\right)_{\mathrm{Re}f}(T) \qquad (2.27)$$

The quantity $\left\{\left(\frac{\Delta R}{R_0}\right)_{G/sample}(T)-\left(\frac{\Delta R}{R_0}\right)_{G/\mathrm{Re}f}(T)\right\}$ can be measured either directly in a bridge configuration, or from separate measurements on the sample and reference. Similarly for change of magnetic field,

$$\left(\frac{\Delta L}{L_0}\right)_{sample}(H)=\frac{1}{F(H)}\left\{\left(\frac{\Delta R}{R_0}\right)_{G/sample}(H)-\left(\frac{\Delta R}{R_0}\right)_{G/\mathrm{Re}f}(H)\right\}+\left(\frac{\Delta L}{L_0}\right)_{\mathrm{Re}f}(H) \qquad (2.28)$$

Here L_0 is the length of sample/reference at reference field ($H = 0$) and R_0 is the gauge resistance at that field.

During the course of this work an experimental set up has been developed for the measurement of strain using the strain gauge technique. We have used strain gauges CFLA-1-350-11 [2.31]. During the measurement with the gauges used in the present work we have followed the procedure recommended by the gauge manufacturer (Tokyo Sokki Kenkyujo Co., Ltd., Tokyo) so that the gauge becomes an integral part of the sample minimizing the influence of the glue. The set up can measure temperature and magnetic field dependence of the strain in the temperature range 30-300 K and in magnetic field up to 50 kOe. A commercial cryostat-magnet (American Magnetics Inc., USA) system was used for providing the low temperature environment. A double walled sample chamber was made using two quartz tubes and aluminium flanges as shown in Fig. 2.20. The sample is mounted on a copper sample holder which constitutes the lower part of an insert. The double walled chamber with sample insert inside is lowered in the commercial cryostat. The temperature of the sample is measured and controlled with the help of a Cernox temperature sensor (LakeShore Cryotronics Inc., USA) and a heater mounted on the sample holder. Data are acquired with a typical temperature ramp rate of 1 K/minute.

We have used copper as the reference material and the data available in literature [2.32] for copper was used to calculate the temperature dependence of $\frac{\Delta L}{L}$ of the sample with reference to the length at 293 K. Our setup has a noise level of $\frac{\Delta L}{L} \approx 10^{-5}$ which corresponds to 0.001% strain.

We measured the magnetic field dependence of $\frac{\Delta R}{R}$ for a bare gauge up to a field of 80 kOe at various temperatures. No detectable change could be registered; or the change was within noise level of the setup. This ruled out any magnetic field dependence of the gauge resistance. Further magnetic field dependence of $\frac{\Delta R}{R}$ for the gauge mounted on the copper reference was also measured up to 80 kOe at various temperatures. No detectable change could be measured. Moreover, no detectable change in the length of copper under the application of a magnetic field is reported in literature. Thus any magnetic field dependence of gauge factor is ruled out. In the light of all these observations, for measurement of magnetic field dependence of $\frac{\Delta L}{L}$ for samples, the eqn. (2.28) takes the following simple form.

$$\left(\frac{\Delta L}{L_0}\right)_{sample}(H) = \frac{1}{F}\left\{\left(\frac{\Delta R}{R_0}\right)_{G/sample}(H)\right\} \qquad (2.29)$$

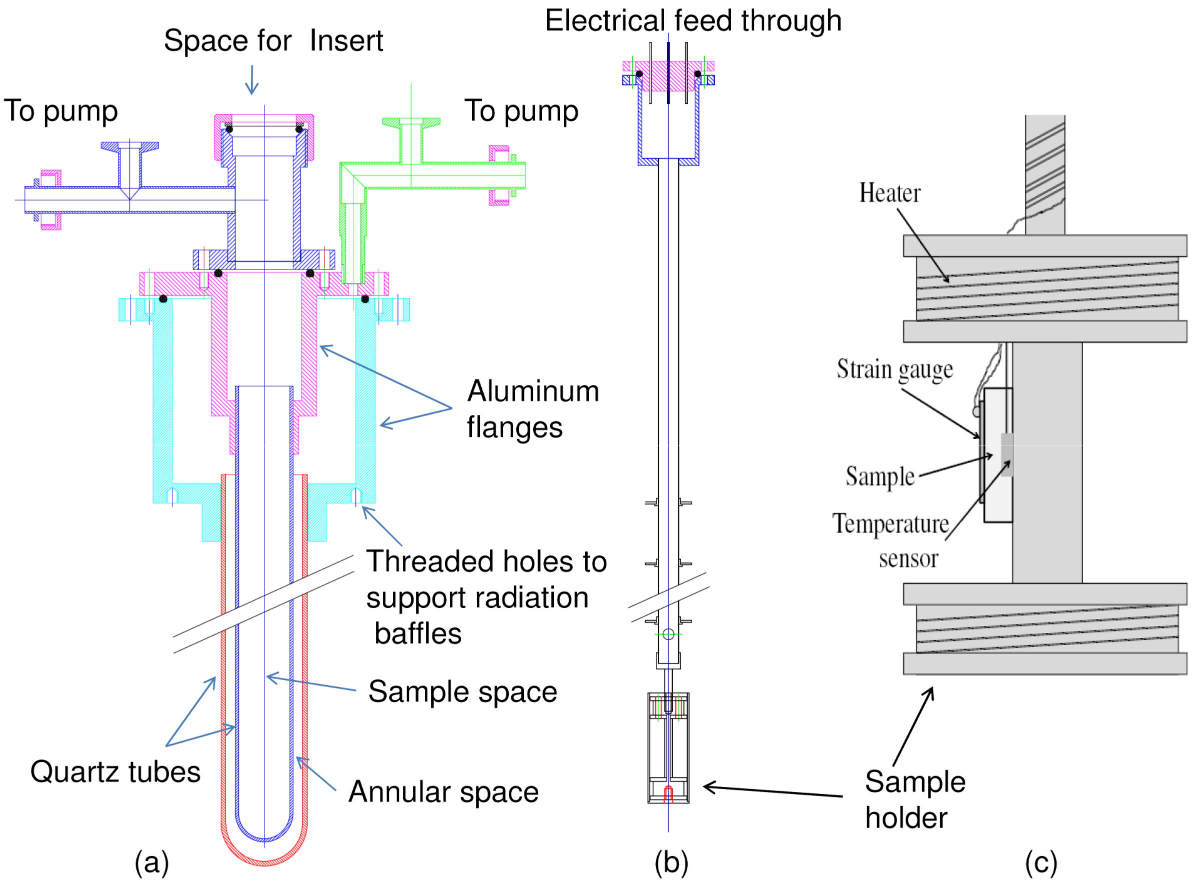

Fig. 2.20: Strain measurement set up. (a) Double walled chamber and (b) insert for temperature control. (c) Schematic details of sample mounting on the sample holder.

2.8 Magnetoresistance measurement

Magnetoresistance (MR) refers to the change in electrical resistance under application of magnetic field. MR arises due to change in scattering of charge carriers under application of magnetic field. The temperature/field dependence of MR is calculated using following equation.

$$MR(H)(\%) = \left(\frac{\rho(H)-\rho(0)}{\rho(0)}\right)\times 100 \qquad (2.30)$$

Here $\rho(H)$ is the resistivity in magnetic field H. We have performed MR measurements using two set ups. First is a commercial Oxford 16 T magnet-cryostat system. MR has been measured in this setup with typical data step of 0.5 K with ramp rate of 0.5 K/minute in magnetic field of up to 100 kOe. The second one is the set up described for strain measurement configured for measurement of the resistance of the sample. The temperature and magnetic field dependence of MR of alloy samples is calculated using eqn. (2.30) from the resistivity measured using the four probe technique.

2.9 Ac susceptibility measurement

Ac susceptibility (χ_{ac}) is a measure of the slope dM/dH of the magnetization vs. field curve in the limit of low ac magnetic field [2.33, 2.34]. The ac susceptibility measurement setup works on the principle of mutual-inductance [2.34]. A primary coil and two identical but oppositely wound secondary coils connected in series, form the main parts of the setup (see schematic in Fig.2.21). The primary coil carries an alternating current to generate an alternating magnetic field. Ideally in absence of any sample the net emf across the secondary coils, due to the alternating magnetic field in the primary, is zero. When a sample is placed at the centre of one of the secondary coils (as shown in schematic in Fig. 2.21), a magnetization is induced in the sample due to the alternating magnetic field in the primary coil. This induced magnetization results in an off-balance signal across the secondary coils. This signal is a measure of the ac susceptibility of the sample [2.34]. We have used a liquid-nitrogen based homemade setup for ac susceptibility measurements in the temperature range 78-350 K. The sample is mounted on a thin copper strip. The temperature of the sample is measured with the help of a Pt-100 temperature sensor. The temperature is controlled with a heater mounted on the copper strip. The magnetic field generated from the alternating current (frequency 333 Hz) in the primary coil is approximately 3 Oe. The signal from secondary coils is measured using a lock-in-amplifier

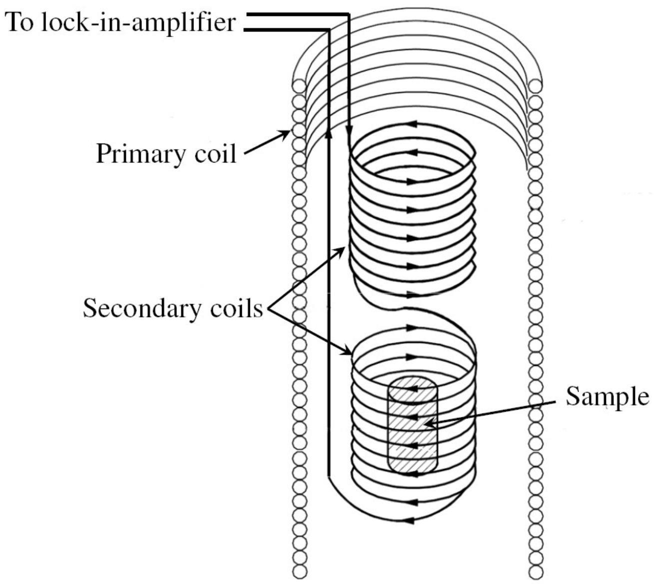

Fig. 2.21: Schematic of the primary and secondary coils arrangement in an ac susceptibility measurement setup.

(SR830, Stanford Research Systems, USA). Data acquisition is done in the temperature ramping mode with a typical temperature ramp rate of 0.5 K/minute.

2.10 Scanning Hall probe imaging

The Hall probe imaging technique utilizes the Hall-effect to image the variation of stray magnetic field near the surface of a magnetized sample. The Hall-effect is the appearance of a voltage difference (known as the Hall voltage) across a current carrying sample placed in an applied magnetic field that is perpendicular to the current direction (see Fig. 2.22). The direction of the Hall voltage is transverse to both the electric current in the sample and the applied magnetic field [2.35]. Magnitude of the Hall voltage is proportional to the magnitude of current as well as the applied magnetic field; the constant of proportionality is material specific. Thus Hall-effect can be used for measurement of the magnetic field. Very small Hall sensors can be fabricated using modern day lithographic techniques. Such sensors in combination with

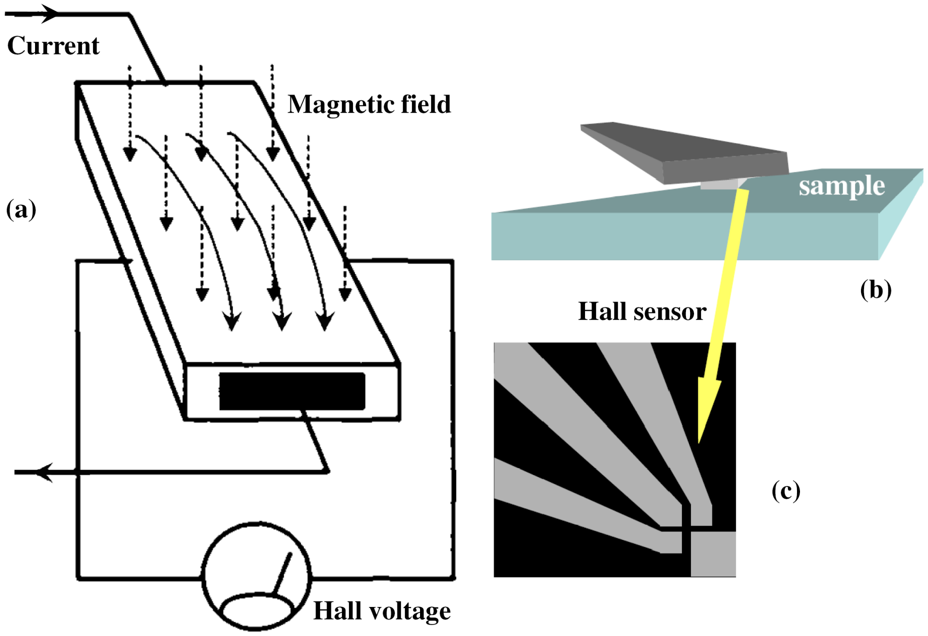

Fig. 2.22: Schematics showing (a) the Hall-effect (from Ref. 2.34), (b) a scanning Hall probe imaging arrangement and (c) a Hall sensor (Courtesy: Blackett Laboratory, Imperial College, London).

appropriate scanning mechanism can be used to image the stray magnetic field near the surface of magnetic materials. This stray magnetic field is correlated with local magnetization. We have performed scanning Hall probe imaging using a setup that was developed by Imperial College, London, UK [2.36]. This setup utilizes a 5 μm InSb Hall sensor and the spatial resolution of this sensor is 10 µm. Hall voltage is measured using lock-in technique with an alternating current (frequency 2 kHz). We have rastered (the details of the setup and the scanning mechanism can be seen in Refs. 2.36-2.37) the Hall sensor in a plane 10 µm above the polished sample surface to produce a two-dimensional profile of the magnetization component perpendicular to the surface. The Hall probe apparatus and the sample were inserted into an Oxford Instruments double-axis transverse field magnetometer capable of maximum field 40 kOe applied perpendicular to the sample plane. This setup works in the temperature range of 5-300 K.

Chapter 3

Investigations in the Ni-Mn-In and Ni-Mn-Sn alloys

In this Chapter we investigate the properties of Ni-Mn-In and Ni-Mn-Sn alloys, focusing particularly on the $Ni_{50}Mn_{34}In_{16}$ and $Ni_{50}Mn_{34}Sn_{16}$ alloys. These compositions were chosen from the phase diagram of the alloy systems published by Sutou et al. [3.1] (see Fig. 1.15 of Chapter 1) so that there is a transition from a ferromagnetic austenite (AST) phase to a ferromagnetic martensite (MST) phase as the temperature is lowered. With both the AST and MST phases being ferromagnetic, the alloys are expected to have interesting magnetic properties. Results of the measurements of the electrical resistivity (ρ), ac susceptibility (χ_{ac}), dc magnetization (M) and heat capacity (C) as a function of temperature (T) and/or magnetic field (H) are presented in this Chapter. Our results confirm the presence of a temperature induced AST to MST phase transition in $Ni_{50}Mn_{34}In_{16}$ and $Ni_{50}Mn_{34}Sn_{16}$ alloys with lowering of the temperature. Our results also show that while in $Ni_{50}Mn_{34}In_{16}$ alloy MST-AST phase transition can also be induced by magnetic field, there is only weak signatures of such a transition in $Ni_{50}Mn_{34}Sn_{16}$ alloy. This magnetic field induced transition is correlated with the detailed nature of the temperature induced martensitic transition (MT) in the respective alloy. Further we have studied various physical properties of $Ni_{50}Mn_{34.5}In_{15.5}$ and $Ni_{50}Mn_{35}In_{15}$ alloys. The results of these studies show that even in Ni-Mn-In alloys the nature of the MT is quite sensitive to the alloy composition.

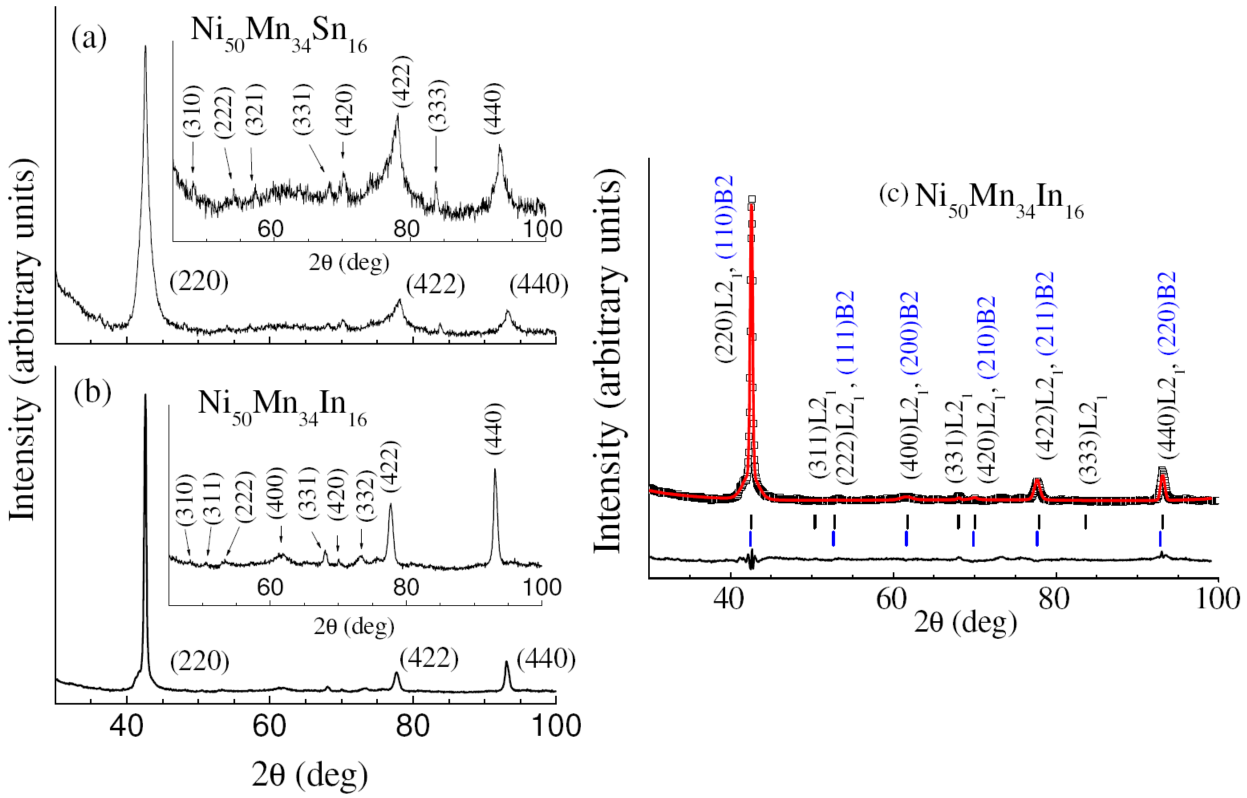

Fig. 3.1: X-ray diffraction patterns of (a) $Ni_{50}Mn_{34}Sn_{16}$ and (b) $Ni_{50}Mn_{34}In_{16}$ alloys. (c) Rietveld fit (line) of XRD pattern (points) of $Ni_{50}Mn_{34}In_{16}$ alloy. See text for details.

3.1 $Ni_{50}Mn_{34}Sn_{16}$ and $Ni_{50}Mn_{34}In_{16}$ alloys: sample preparation and characterization

The alloys were prepared using the arc melting furnace technique described in section 2.1 of Chapter 2. Energy dispersive x-ray (EDX) analysis determined the actual compositions of $Ni_{50}Mn_{34}In_{16}$ and $Ni_{50}Mn_{34}Sn_{16}$ samples to be $Ni_{49.2}Mn_{34.7}In_{16.1}$ and $Ni_{49.8}Mn_{33.5}Sn_{16.7}$ respectively. In the subsequent discussion these alloys will be referred with their nominal compositions.

Fig. 3.1(a) and 3.1(b) present the room temperature x-ray diffraction (XRD) patterns of $Ni_{50}Mn_{34}Sn_{16}$ and $Ni_{50}Mn_{34}In_{16}$ respectively obtained with Cu Kα radiation. The peaks in the XRD pattern of both the alloys can be indexed to the $L2_1$ structure. Type-I superlattice peaks, which are indicative of the presence of $L2_1$ ordering [3.2, 3.3], have been obtained along with the principal peaks. The peaks like (310), (321) and (332) observed in our data are ideally not allowed for stoichiometric composition with the $L2_1$ structure (peaks with *h*, *k*, *l* all odd or all even, only have non-zero intensity in stoichiometric $L2_1$ structure; see section 2.2.2 of Chapter 2). Their presence can be attributed to the site disorder in the samples as discussed in context with Heusler alloy structure in section 2.2.2 of Chapter 2. Average lattice constants calculated from prominent peaks are 6.011 Å and 5.999 Å for $Ni_{50}Mn_{34}In_{16}$ and $Ni_{50}Mn_{34}Sn_{16}$ respectively. These values match closely those reported for the same nominal composition of Ni–Mn–In alloy [3.4] and nearby composition of Ni–Mn–Sn alloy [3.5].

Rietveld fitting for the XRD pattern of the $Ni_{50}Mn_{34}In_{16}$ alloy using FULLPROF program [3.4] with $L2_1$ structure gives positions of the peaks correctly but does not match with the peak intensity/profile entirely. A better fit is obtained by taking into account also the possible B2 structure (see Fig. 2.7 and related discussion in section 2.2.2 in Chapter 2 for reduction of $L2_1$ structure into B2 with lattice constant half that of $L2_1$ structure). Such B2 structure may arise due to random distribution of Mn and In in this off-stoichiometric alloy. This Ritveld fitting is shown in Fig. 3.1(c). Lattice constant obtained from Rietveld fitting agrees with that obtained from the regular analysis mentioned above in the previous paragraph.

3.1.1 Temperature dependence of electrical resistivity of the $Ni_{50}Mn_{34}Sn_{16}$ and $Ni_{50}Mn_{34}In_{16}$ alloys

Fig. 3.2 presents resistivity (ρ) vs. *T* plot in the T range of 78–350 K for $Ni_{50}Mn_{34}In_{16}$ and $Ni_{50}Mn_{34}Sn_{16}$ measured in temperature ramping mode with ramp rate of 0.6 K/minute. In both the alloys there is a change in slope in ρ around 305 K with a lowering of *T*. This is related with the paramagnetic (PM) to ferromagnetic (FM) transition in these alloys (this transition is inferred from temperature dependence of ac susceptibility and magnetization discussed in sections 3.1.2

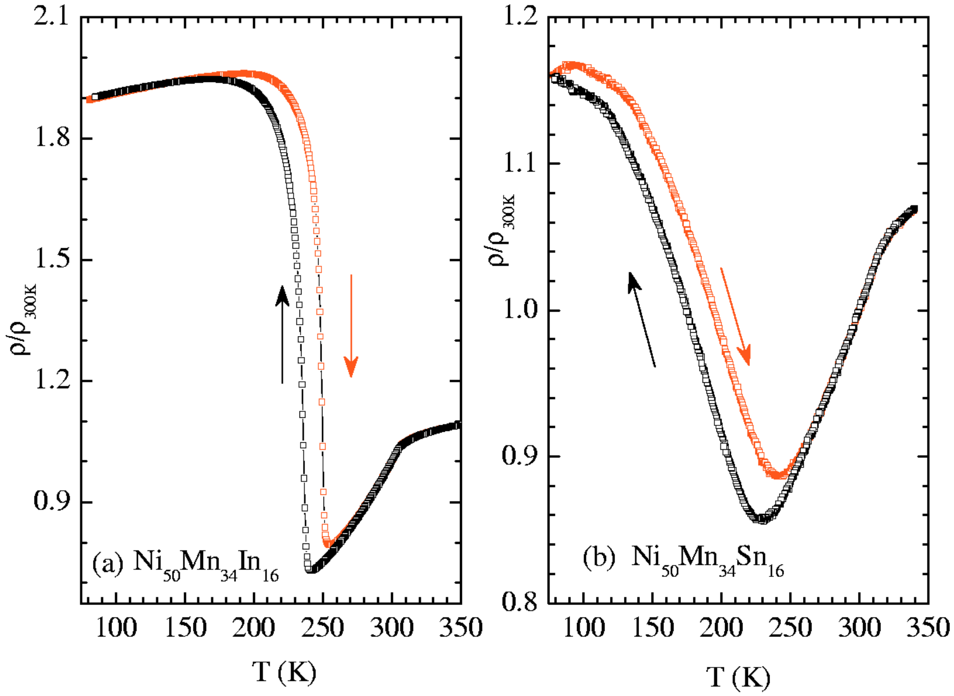

Fig. 3.2: Temperature (T) dependence of electrical resistivity (ρ) of (a) $Ni_{50}Mn_{34}In_{16}$ and (b) $Ni_{50}Mn_{34}Sn_{16}$ alloys. Resistivity is normalized to its value at 300 K.

and 3.1.3 below). As T is lowered further, ρ exhibits an anomalous rise in both the alloys. A distinct thermal hysteresis is associated with this rise in resistivity. We will see in later sections that distinct features along with thermal hysteresis are also observed in the temperature dependence of χ_{ac} and M of these alloys in the similar temperature range. Earlier, MT was reported in the same nominal composition of Ni–Mn–In alloy [3.5] and nearby composition of Ni–Mn–Sn alloy [3.6] in the same temperature range where this anomalous rise in ρ is observed. So this feature can be attributed to the MT in these alloys. The associated thermal hysteresis is a manifestation of the first-order nature of this transition. The absence of any reversible region in the ρ vs. T plot in Fig. 3.2 for $Ni_{50}Mn_{34}Sn_{16}$ in the low T side indicates that the MT is incomplete up to 78 K in this alloy. Though both the alloys undergo a MT around the similar temperature range, $\rho(T)$ shows significantly different behaviors across the MT in these alloys. While $\rho(T)$

increases over a wider T range in $Ni_{50}Mn_{34}Sn_{16}$, the change in $\rho(T)$ is sharp and the transition extends over a relatively narrow T range in $Ni_{50}Mn_{34}In_{16}$. This is indicative of a relatively broader MT in $Ni_{50}Mn_{34}Sn_{16}$.

3.1.2 Temperature dependence of ac susceptibility of the $Ni_{50}Mn_{34}Sn_{16}$ and $Ni_{50}Mn_{34}In_{16}$ alloys

Fig. 3.3 presents χ_{ac} vs. T plot in the T range of 78–330 K for $Ni_{50}Mn_{34}In_{16}$ and $Ni_{50}Mn_{34}Sn_{16}$. In both the alloys there is a sharp rise in χ_{ac} around 305 K with a lowering of T, which is indicative of PM to FM transition in these alloys. The Curie temperatures (T_C) obtained from the point of inflection in the χ_{ac} vs. T plots are 305 and 306 K for $Ni_{50}Mn_{34}In_{16}$ and $Ni_{50}Mn_{34}Sn_{16}$ respectively. As T is lowered further, χ_{ac} exhibits an anomalous drop in both the alloys. A distinct thermal hysteresis is associated with this anomalous drop in χ_{ac}. As mentioned earlier, MT has been reported in the same nominal composition of Ni–Mn–In alloy [3.5] and nearby composition of Ni–Mn–Sn alloy [3.6] in the same temperature range where this anomalous drop in χ_{ac} is observed. So this effect can be attributed to the MT in these alloys and the thermal hysteresis is related to the first-order nature of this transition. The absence of any reversible region in the χ_{ac} vs. T plot in Fig. 3.3 for $Ni_{50}Mn_{34}Sn_{16}$ in the low T side indicates that the MT is incomplete up to 78 K in this alloy. It supports the inference drawn from the results of $\rho(T)$ measurements. Though $Ni_{50}Mn_{34}In_{16}$ as well as $Ni_{50}Mn_{34}Sn_{16}$ undergo an MT around the similar temperature range, the behavior of $\chi_{ac}(T)$ differs significantly across the MT in these alloys. While χ_{ac} decreases over a wider T range in $Ni_{50}Mn_{34}Sn_{16}$, the change in χ_{ac} is sharp and the temperature hysteresis is relatively narrower in $Ni_{50}Mn_{34}In_{16}$. This supports the inference drawn from results of resistivity measurement about the broader MT in $Ni_{50}Mn_{34}Sn_{16}$. Further, in $Ni_{50}Mn_{34}In_{16}$ χ_{ac} exhibits another feature within the MT region around 220 K where it shows a

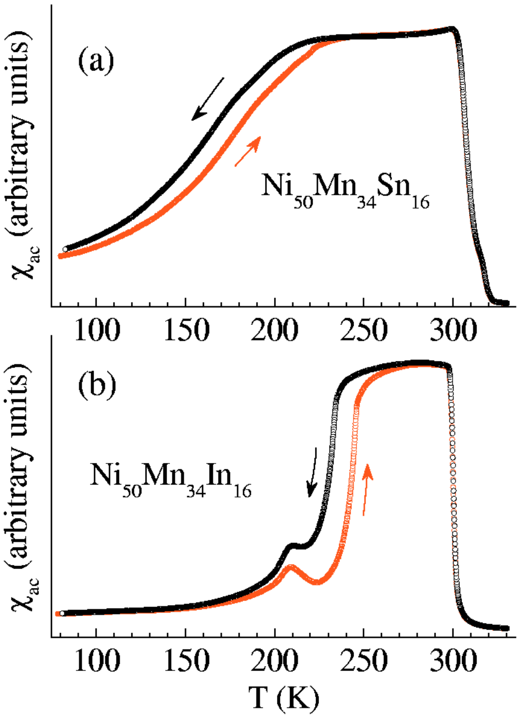

Fig. 3.3: Temperature (T) dependence of ac susceptibility (χ_{ac}) of (a) $Ni_{50}Mn_{34}Sn_{16}$ and (b) $Ni_{50}Mn_{34}In_{16}$ alloys.

local minimum followed by a local maximum with decreasing T. A possible explanation for these features in χ_{ac} is as follows. MT involves change in lattice parameters; as a result MST and AST phases may have different ferromagnetic characters and the Curie temperatures of the MST phase (T_{CM}) and of the AST phase (T_{CA}) may differ (a general discussion pertaining to T_{CM}, T_{CA} and the MT temperature, can be found in [3.7].) In the present case T_{CA} is the T_C we have estimated from our experiment above. Now if T_{CM} lies within the T regime of MT, it will lead to a local minimum in the $\chi_{ac}(T)$ plot similar to what we have seen in $Ni_{50}Mn_{34}In_{16}$ (see Fig. 3.3). At the onset of MT near 240 K in $Ni_{50}Mn_{34}In_{16}$, the MST phase formed is in the paramagnetic state, so χ_{ac} decreases rapidly with lowering of T. As T is lowered further, there is a paramagnetic to ferromagnetic transition in the MST phase within the T regime of the MT and as a result χ_{ac} starts increasing, resulting in a local minimum. Below this PM to FM transition in the MST phase, χ_{ac}

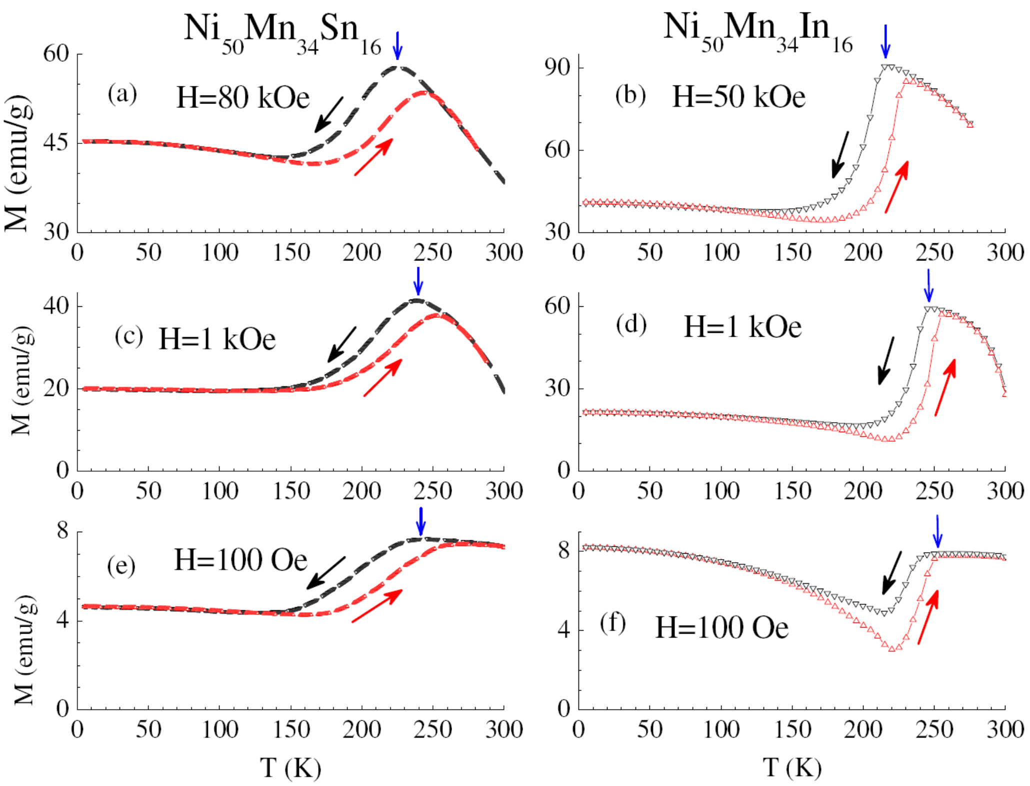

Fig. 3.4: Temperature (*T*) dependence of magnetization (*M*) of $Ni_{50}Mn_{34}Sn_{16}$ alloy ((a), (c) and (e)), and of $Ni_{50}Mn_{34}In_{16}$ alloy ((b), (d) and (f)) in various magnetic fields (H). The martensite start temperature of the austenite to martensite phase transition while cooling is indicated with vertical arrow.

decreases with decreasing *T*, which is possibly related to the difficulty in the magnetic domain rotation at low temperatures, and so χ_{ac} exhibits a local maximum. T_{CM} lying in the temperature regime of the MT has been inferred from magnetization measurements for the same nominal composition of Ni–Mn–In alloy [3.5]. The absence of such a structure in $\chi_{ac}(T)$ in $Ni_{50}Mn_{34}Sn_{16}$ indicates that T_{CM} of this alloy probably does not lie within its MT region.

3.1.3 Temperature dependence of magnetization of the $Ni_{50}Mn_{34}Sn_{16}$ and $Ni_{50}Mn_{34}In_{16}$ alloys

We have measured the temperature dependence of the magnetization in constant magnetic field for both the $Ni_{50}Mn_{34}In_{16}$ and $Ni_{50}Mn_{34}Sn_{16}$ alloys with field cooled cooling (FCC) and field cooled warming (FCW) protocols. In the FCC protocol *H* was applied at 300 K and M was measured while cooling down to the lowest temperature of measurement. After the FCC measurements, M was measured while warming up the sample in the presence of the same applied H and this protocol is called the FCW. Figure 3.4 presents M vs. T curves for $Ni_{50}Mn_{34}In_{16}$ and $Ni_{50}Mn_{34}Sn_{16}$ measured in FCC and FCW protocols in the T range 5–300 K and in various applied magnetic fields. We first discuss $M(T)$ curves in a magnetic field of 100 Oe (Figs. 3.4(e) and 3.4(f)). At T = 300 K $Ni_{50}Mn_{34}In_{16}$ and $Ni_{50}Mn_{34}Sn_{16}$ both are in the ferromagnetic phase as $T_C > 300$ K for these alloys. In the case of $Ni_{50}Mn_{34}In_{16}$, with lowering of T there is a rapid fall in M between 240 and 215 K. At 215 K there is a sharp minimum in M, which is followed by an appreciable increase in M with further lowering of T. Also there is a thermal hysteresis in M. The sharp decrease in M around 240 K and thermal hysteresis can be attributed to the MT occurring in this alloy. It is established that, depending upon the values of T_{CM}, T_{CA} and MT temperature, the M vs. T curve of a ferromagnetic Heusler alloy can exhibit quite different features [3.7]. The sharp local minimum in M around 215 K followed by a noticeable increase in M with decreasing T have the explanation that T_{CM} lies within the T regime of MT which we have already inferred from χ_{ac} data. $Ni_{50}Mn_{34}Sn_{16}$ also exhibits a decrease in M with lowering in T around 240 K and a thermal hysteresis, which can be attributed to MT occurring in this alloy. But $M(T)$ curve of $Ni_{50}Mn_{34}Sn_{16}$ shows no extra feature in the MT region like that in $Ni_{50}Mn_{34}In_{16}$. Further the increase in M with decreasing T below the MT region in $Ni_{50}Mn_{34}Sn_{16}$ is relatively small. This finds the explanation that in this alloy T_{CM} is well above the T regime of the MT. As a result there is no feature in the MT region and the increase in M with decrease in T in the MST phase is also small because this T range is far below T_{CM}. This type of relationship between T_{CM} and the MT temperature regime is reported for a nearby composition of Ni–Mn–Sn alloy [3.6]. $M(T)$ curves in higher magnetic field in both the alloys reveal that transition temperatures of the MT shift to lower *T* with increasing *H*. This shift is much larger in $Ni_{50}Mn_{34}In_{16}$ as compared that in $Ni_{50}Mn_{34}Sn_{16}$. Also *M* in the AST phase has a higher value as compared to that in the MST phase in both the alloys. The MT in both the alloys has the similarity that the MST phase has a lower value of *M* than the respective AST phase, in other words *M* has positive temperature coefficient across the MT in both the alloys. However, the change in magnetization across the martensitic transition is much larger in $Ni_{50}Mn_{34}In_{16}$ as compared to that in $Ni_{50}Mn_{34}Sn_{16}$. The probable reason for the change in spontaneous magnetization can be the change in exchange interaction across the MT because of different lattice parameters in AST and MST phases. It should be noted here that an excess of Mn in these off-stoichiometric alloys as compared with the stoichiometric Ni_2MnIn and Ni_2MnSn, leads to occupation of a number of 4(b) sites in the $L2_1$ structure by Mn atoms [3.8]. There is an incipient antiferromagnetic (AFM) coupling between the magnetic moments of these excess Mn atoms and the magnetic moments of the Mn atoms occupying sites corresponding to the stoichiometric composition. This incipient AFM coupling can be strengthened further in the MT phase [3.8, 3.9]. Also the characteristic temperatures of the MT shift towards the lower *T* side with increasing *H* in both the alloys. On the other hand the MT in these alloys is somewhat different in character. The nature of variation of *M* across the MT highlights the basic difference between the MT in these alloys. It is clear that the transition is rather broad in $Ni_{50}Mn_{34}Sn_{16}$. Also the jump in value of M across the MT is smaller in $Ni_{50}Mn_{34}Sn_{16}$ than in $Ni_{50}Mn_{34}In_{16}$. Furthermore, the shift in temperatures of the MT with *H* is substantially smaller in $Ni_{50}Mn_{34}Sn_{16}$. A smaller shift of MT temperature in Ni–Mn–Sn alloy as compared to that in Ni–Mn–In alloy has been observed for other compositions of these alloy systems [3.10].

3.1.4 Temperature dependence of heat capacity of the $Ni_{50}Mn_{34}Sn_{16}$ and $Ni_{50}Mn_{34}In_{16}$ alloys

Heat capacity has been measured for both of these alloys while warming in zero magnetic field. C vs. T data in zero magnetic field in T range 5–300 K is presented in Fig. 3.5 for $Ni_{50}Mn_{34}In_{16}$ and $Ni_{50}Mn_{34}Sn_{16}$. The peaks in $C(T)$ correspond to the MT in these alloys. $Ni_{50}Mn_{34}In_{16}$ shows a sharp peak in C while the peak in C of $Ni_{50}Mn_{34}Sn_{16}$ is much broader. This supports our earlier inference from resistivity and magnetic measurements that the MT in $Ni_{50}Mn_{34}Sn_{16}$ is relatively broad.

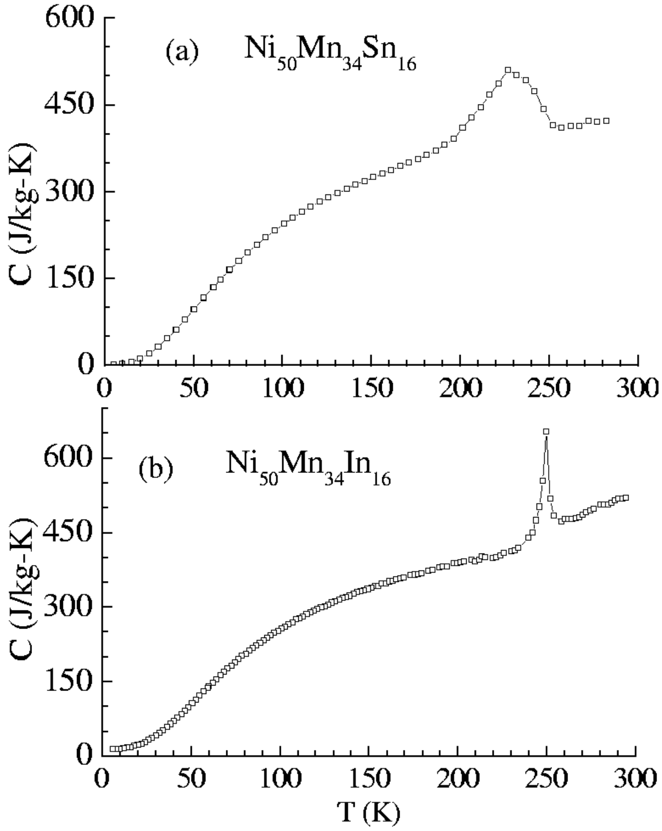

Fig. 3.5: Temperature (T) dependence of heat capacity (C) of (a) $Ni_{50}Mn_{34}Sn_{16}$ and (b) $Ni_{50}Mn_{34}In_{16}$ alloys in zero magnetic field.

3.1.5 Magnetic field induced phase transition in the $Ni_{50}Mn_{34}Sn_{16}$ and $Ni_{50}Mn_{34}In_{16}$ alloys

Fig. 3.6 presents isothermal *M*(*H*) curves up to a maximum magnetic field of 80 kOe for $Ni_{50}Mn_{34}In_{16}$ and $Ni_{50}Mn_{34}Sn_{16}$ alloys. We have performed *M*(*H*) measurements at each temperature of interest starting from an initial state, which was prepared by cooling the samples from 300 K to the target temperature in zero magnetic field. Then isothermal *M*(*H*) measurements were performed by changing *H* from zero to 80 kOe and then back to zero. Figs. 3.6(a) and 3.6(b) present isothermal *M*(*H*) curves at representative temperatures in *T* regimes well outside the MT region. Figs. 3.6(c) and 3.6(d) present M(H) curves within the MT region. Isothermal *M*(*H*) curves are reversible in the *T* regime away from the MT region in both the alloys. This indicates the soft ferromagnetic character of the MST phase as well as the AST phase of these alloys. In the crossover regime of AST to MST phase transition, the isothermal *M*(*H*) curves exhibit a marked hysteresis. This hysteresis is not related to the ferromagnetic character of MST and AST phases but is a result of the magnetic field-induced first-order phase transition from MST phase to AST phase. In a ferromagnetic material the hysteresis arises due to domain wall pinning and/or anisotropy and has maximum width at $H = 0$. In such a case the width of the hysteretic region increases with the lowering of temperature. But in the present case the hysteresis is almost zero at $H = 0$. Further in the present case the hysteresis vanishes both on the lower and higher temperature sides of the MT regime. The distinct rise in *M* with increasing *H* and the associated hysteresis mentioned above are typical signatures of a magnetic field-induced first-order phase transition [3.11]. Such hysteresis related to magnetic field-induced phase transition is reported in other magnetic systems [3.12, 3.13] and also in Ni–Mn–In [3.5] and some Ni–Mn– Sn [3.14] alloys. Presence of magnetic field induced MST to AST phase transition in Ni-Mn-In alloy has been verified from neutron diffraction measurements in increasing magnetic field [3.9]. In $Ni_{50}Mn_{34}In_{16}$, the magnetic field induced phase transition leads to change in magnetization to the extent of the difference in the magnetization between the MST and the AST phases. However, in $Ni_{50}Mn_{34}Sn_{16}$ the magnetic field induced phase transition is not able to change magnetization to the extent of difference in the magnetization between the MST and the AST phases. Thus the magnetic field-induced phase transition is much weaker in $Ni_{50}Mn_{34}Sn_{16}$ than in $Ni_{50}Mn_{34}In_{16}$. In $Ni_{50}Mn_{34}In_{16}$ at certain temperatures the magnetic field induced MST to AST phase transition is completed in a magnetic field of 80 kOe. However, in $Ni_{50}Mn_{34}Sn_{16}$ it appears that the magnetic field induced MST to AST phase transition is not completed up to magnetic field of 80 kOe.

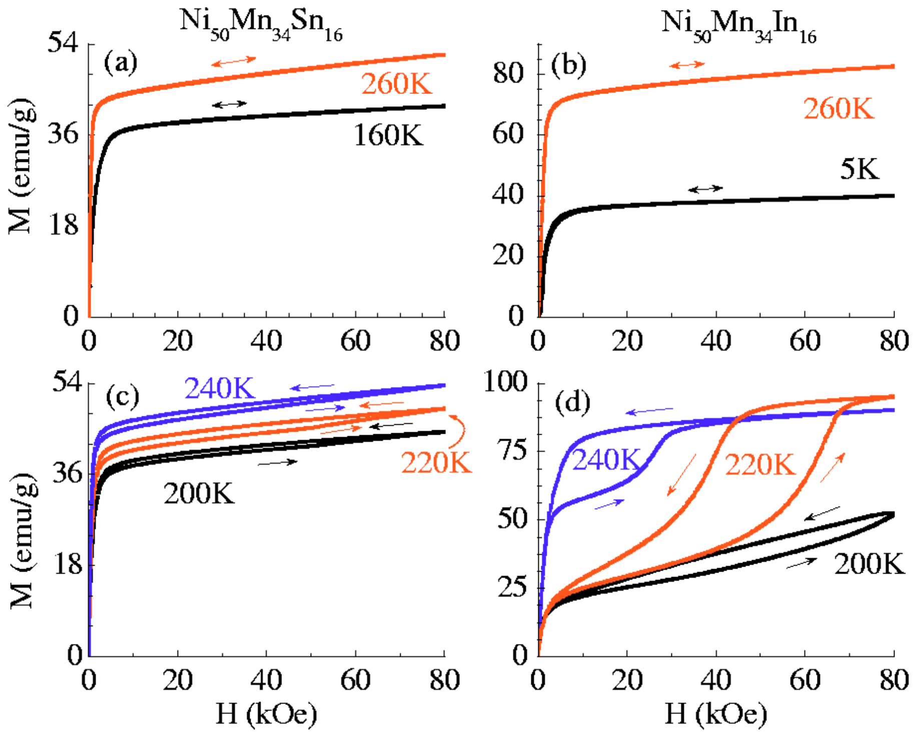

Fig. 3.6: Representative isothermal magnetization (*M*) vs. magnetic field (*H*) curves of $Ni_{50}Mn_{34}Sn_{16}$ alloy ((a) and (c)) and of $Ni_{50}Mn_{34}In_{16}$ alloy ((b) and (d)) at constant temperatures. *M*(*H*) curves in (a) and (b) are in the temperature regime well away from martensitic transition region while those in (c) and (d) are within the temperature regime of the martensitic transition.

3.1.6 Possible reason for the difference in magnetic field induced martensite to austenite phase transition in the $Ni_{50}Mn_{34}Sn_{16}$ and $Ni_{50}Mn_{34}In_{16}$ alloys

We have noticed that while $Ni_{50}Mn_{34}Sn_{16}$alloy shows only a weak signature of magnetic field induced MST to AST phase transition, this transition is quite prominent in $Ni_{50}Mn_{34}In_{16}$ alloy. This difference can be correlated with the character of the phase transition in the respective alloy. First we recall from Chapter 1 (see section 1.4.2) that the MT is characterized by four characteristic temperatures: MST start temperature T_{MS}, MST finish temperature T_{MF}, AST start temperature T_{AS} and AST finish temperature T_{AF}. In the present case the magnetization in MST phase is smaller as compared to that in AST phase. Hence, T_{MS} can be determined as the temperatures where magnetization starts decreasing while cooling the sample and T_{MF} can be taken as the temperature where the thermal hysteresis in magnetization goes to zero in the low temperature side. Similarly, T_{AS} can be taken as the temperatures where the magnetization starts increasing while warming the sample and T_{AF} can be taken as the temperature where the temperature hysteresis in magnetization ceases to exist in the higher temperature side. T_{MF} (T_{AF}) will be the limit of supercooling (superheating) in terms of standard phenomenology of a first-order phase transition [3.15]. It is worthwhile noting here that the AST to MST phase transition while cooling the sample as well as the MST to AST phase transition while warming the sample takes place over a finite width of temperature. This suggests the disorder-influenced nature of the transition [3.16, 3.17] (as discussed in section 1.3.4 of Chapter 1). Further, it is observed in Fig. 3.4 that T_{MS} is greater than T_{AS}. This indicates the presence of a landscape of transition onsets in the present alloy [3.18]. We will explore this issue further in Chapter 5.

From the temperature dependence of the electrical resistivity, ac susceptibility, magnetization and heat capacity, we note the following points about the transition in these $Ni_{50}Mn_{34}Sn_{16}$ and $Ni_{50}Mn_{34}In_{16}$ alloys.

(i) The MT in $Ni_{50}Mn_{34}Sn_{16}$ alloy is quite broad as compared to that in $Ni_{50}Mn_{34}In_{16}$ alloy so the temperature span of T_{MS} to T_{MF} (also T_{AS} to T_{AF}) is relatively larger in $Ni_{50}Mn_{34}Sn_{16}$ (see Figs. 3.2-3.5).

(ii) The temperature regime of MT as well reverse MT in both the alloys shifts to lower temperature side with increasing magnetic field. Thus the characteristic temperatures T_{MS}, T_{MF}, T_{AS} and T_{AF} shift to lower temperature side with increasing magnetic field (see Fig. 3.4). However this shift in $Ni_{50}Mn_{34}In_{16}$ alloy is much larger. Fig. 3.7 shows schematic variation of these temperatures with magnetic field. The magnetic field dependence of these characteristic temperatures will be discussed in detail in Chapter 5.

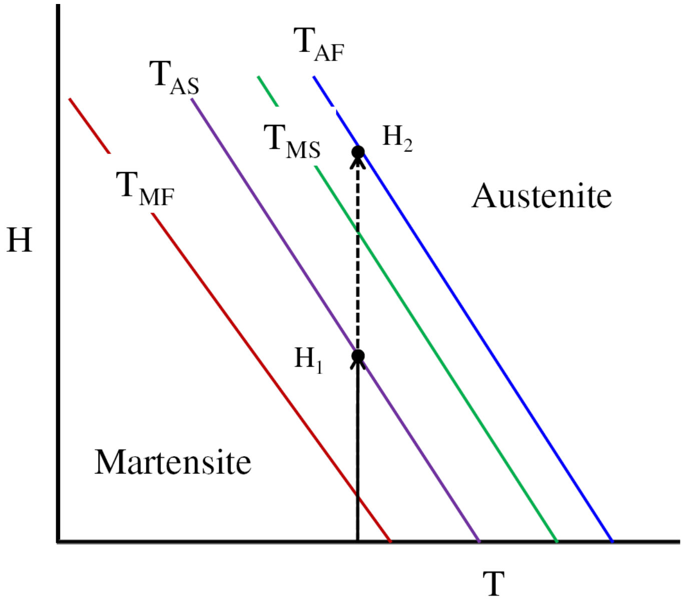

Fig. 3.7: Schematic showing magnetic field induced martensite to austenite phase transition in systems where characteristic temperature decrease with increasing field. Phase transition starts at magnetic field value H_1 and finishes at H_2.

The above two points help to understand qualitatively why there is a prominent magnetic field induced MST to AST phase transition in $Ni_{50}Mn_{34}In_{16}$, while this magnetic field induced transition in $Ni_{50}Mn_{34}Sn_{16}$ is quite weak. Consider the schematic shown in Fig. 3.7. When magnetic field is increased from zero isothermally, at certain magnetic field value H_1, T_{AS} line is crossed resulting in the start of the MST to AST phase transition. At a certain higher magnetic field H_2, the T_{AF} line is crossed resulting in the finish of the MST to AST phase transition. Such a transition is observed in Fig. 3.6. It is obvious from the schematic that a larger shift in characteristic temperatures with magnetic field and a smaller width of transition, will facilitate the magnetic field induced MST to AST phase transition. If the shift of characteristic temperatures is too small, a larger magnetic field is required to start the magnetic field induced transition. Over and above this, if the width of transition is also large, a still larger magnetic field is required to complete this transition. As noted above $Ni_{50}Mn_{34}In_{16}$ has a larger shift of characteristic temperature and a smaller width of transition as compared to that in $Ni_{50}Mn_{34}Sn_{16}$ which helps the magnetic field induced MST to AST phase transition in $Ni_{50}Mn_{34}In_{16}$ alloy. On the other hand, $Ni_{50}Mn_{34}Sn_{16}$ alloy with a smaller shift of characteristic temperature with magnetic field and a larger width of transition will require a much higher magnetic field than 80 kOe.

3.2 Sensitivity of the magnetic field induced phase transition in the Ni-Mn-In alloys to the composition

The above discussion on the experimental results suggests that Ni-Mn-In alloys are likely to exhibit a prominent magnetic field induced transition. In this direction we have investigated two more members of Ni-Mn-In family with nominal compositions: $Ni_{50}Mn_{34.5}In_{15.5}$ and

$Ni_{50}Mn_{35}In_{15}$. The results of this investigation show that in Ni-Mn-In family the transition is also more sensitive to composition than indicated in the previously reported phase diagram (Fig. 1.15 of Chapter1).

3.2.1 $Ni_{50}Mn_{34.5}In_{15.5}$ and $Ni_{50}Mn_{35}In_{15}$ alloys: sample preparation and characterization

These alloys were also prepared in an arc melting furnace and given similar heat treatments as $Ni_{50}Mn_{34}In_{16}$. It was found that the samples with the nominal compositions $Ni_{50}Mn_{35}In_{15}$ and $Ni_{50}Mn_{34.5}In_{15.5}$ had the average compositions of $Ni_{49.7}Mn_{35.1}In_{15.2}$ and

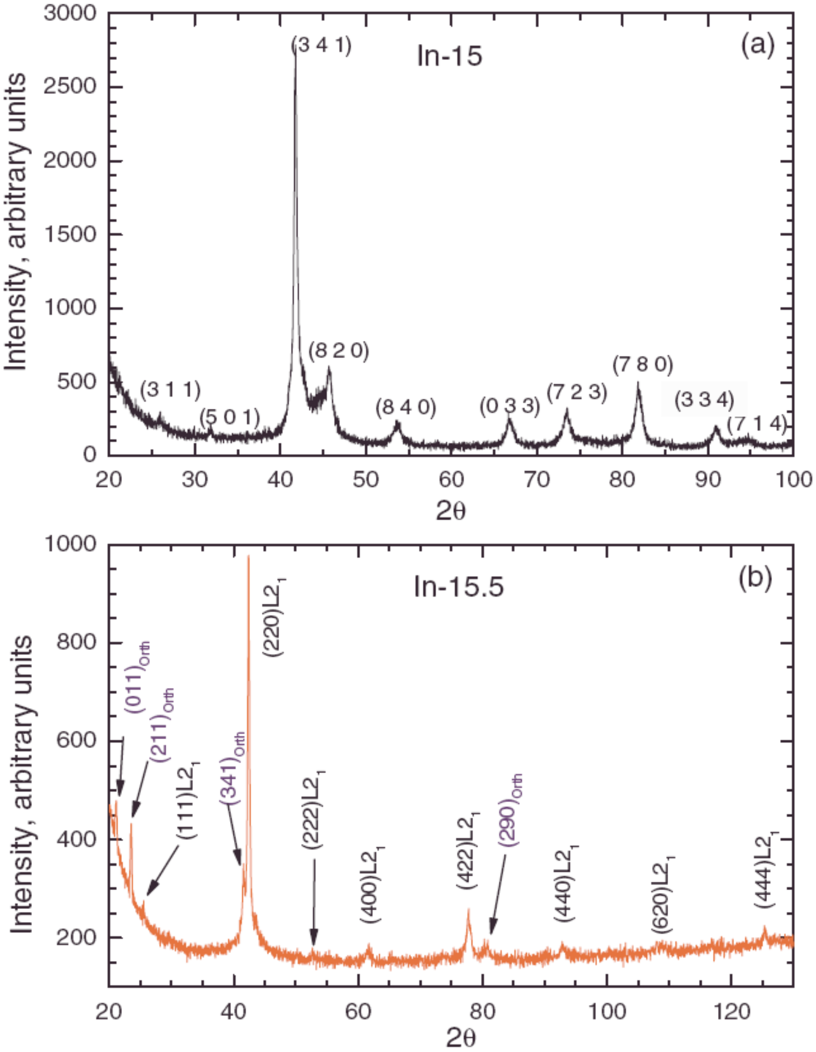

Fig. 3.8: The x-ray diffraction patterns for the (a) $Ni_{50}Mn_{35}In_{15}$ and (b) $Ni_{50}Mn_{34.5}In_{15.5}$ alloy samples at room temperature.

$Ni_{48.6}Mn_{35.1}In_{16.3}$ respectively as determined with EDX analysis. These EDX analyses were performed at nearly twenty locations on the samples. However, EDX may not be a suitable tool for resolving the very small composition differences in the Ni, Mn, and In concentrations as the error bar for EDX is of the order of 3 at. % for this alloy system. The chemical compositions of the samples were also determined through x-ray fluorescence (XRF) studies using a homemade spectrometer [3.19]. According to the XRF results, the samples with the nominal compositions $Ni_{50}Mn_{35}In_{15}$ and $Ni_{50}Mn_{34.5}In_{15.5}$ had the actual compositions of $Ni_{50.1}Mn_{34.9}In_{15.1}$ and $Ni_{49.3}Mn_{35.2}In_{15.6}$ respectively. The error bar for XRF is of the order of 0.2 at. % for these alloys. We will henceforth refer to these alloy samples as In-15 and In-15.5, respectively, based on the nominal composition alone.

The XRD pattern obtained for the In-15 sample is shown in Fig. 3.8. All the XRD peaks for this sample could be indexed for an orthorhombic crystal structure. Six XRD peaks (Nos. 1, 3, 4, 5, 6, and 7, starting from the left of the figure) in the 2θ range of 20°–80° match well with those observed by Pathak et al. [3.20], obtained for a sample of the same nominal composition. The positions of some of the peaks of our sample (Fig. 3.8(a)), appear to match with an unindexed XRD pattern reported by Bhobe et al. [3.21] for a sample of the same nominal composition. In spite of the matching of the most intense XRD peak, the XRD pattern presented in Fig. 3.8(a) looks quite different from that of Bhobe et al [3.21]. This difference is probably because of the fact that the actual composition (determined from EDX study) of the sample of Bhobe et al. [3.21] was $Ni_{50.17}Mn_{34.59}In_{15.24}$. The lattice parameters for our In-15 sample are found to be a = 17.678 Å, b = 10.66 Å, and c = 4.632 Å, which are closer to the parameters reported by Pathak et al. [3.20] for the same nominal composition. Bhobe et al. [3.21], however, have attempted to fit their XRD pattern to a B2 structure with a lattice parameter of 3.02 Å. The orthorhombic crystal structure derived from the XRD pattern of our sample indicates that the sample is in the MST phase at room temperature. Figure 8(b) shows the XRD pattern obtained for the In- 15.5 sample. The XRD peaks corresponding to both the $L2_1$ and the orthorhombic structures were found in this pattern, indicating that both the AST and the MST phases are present in the sample at room temperature. The lattice parameters obtained from the analysis of the XRD results are a = 6.020 Å for the $L2_1$ phase, and a = 18.156 Å, b = 10.786 Å , and c = 4.555 Å for the orthorhombic phase. The lattice parameter for the $L2_1$ phase is quite close to that of our $Ni_{50}Mn_{34}In_{16}$ sample studied earlier (see section 3.1 of this Chapter). On the other hand, the lattice parameters for the orthorhombic phase are close to that of our In-15 sample mentioned above.

3.2.2 Temperature dependence of electrical resistivity of the $Ni_{50}Mn_{34.5}In_{15.5}$ and $Ni_{50}Mn_{35}In_{15}$ alloys

Fig. 3.9(a) shows the temperature dependence of electrical resistivity $\rho(T)$ of In-15.5 in zero magnetic field. The temperature dependence of $\rho(T)$ depicted in Fig. 3.9(a) is quite similar to that of our $Ni_{50}Mn_{34}In_{16}$ alloy reported earlier. In zero magnetic field, a change in slope in the $\rho(T)$ curve is observed at around 312 K while cooling. A very similar kink in the temperature dependence of electrical resistivity was earlier observed in $Ni_{50}Mn_{34}In_{16}$ at the Curie temperature of that alloy. The kink in the present $\rho(T)$ curve could thus be the signature of the Curie temperature of the In-15.5 sample. On further cooling, a sharp rise in the electrical resistivity is observed near 250 K, which is also associated with distinct thermal hysteresis. As discussed earlier, in context with $Ni_{50}Mn_{34}In_{16}$, the sharp change in resistivity and the associated thermal hysteresis is attributed to the first-order AST–MST phase transition in the present sample. It is

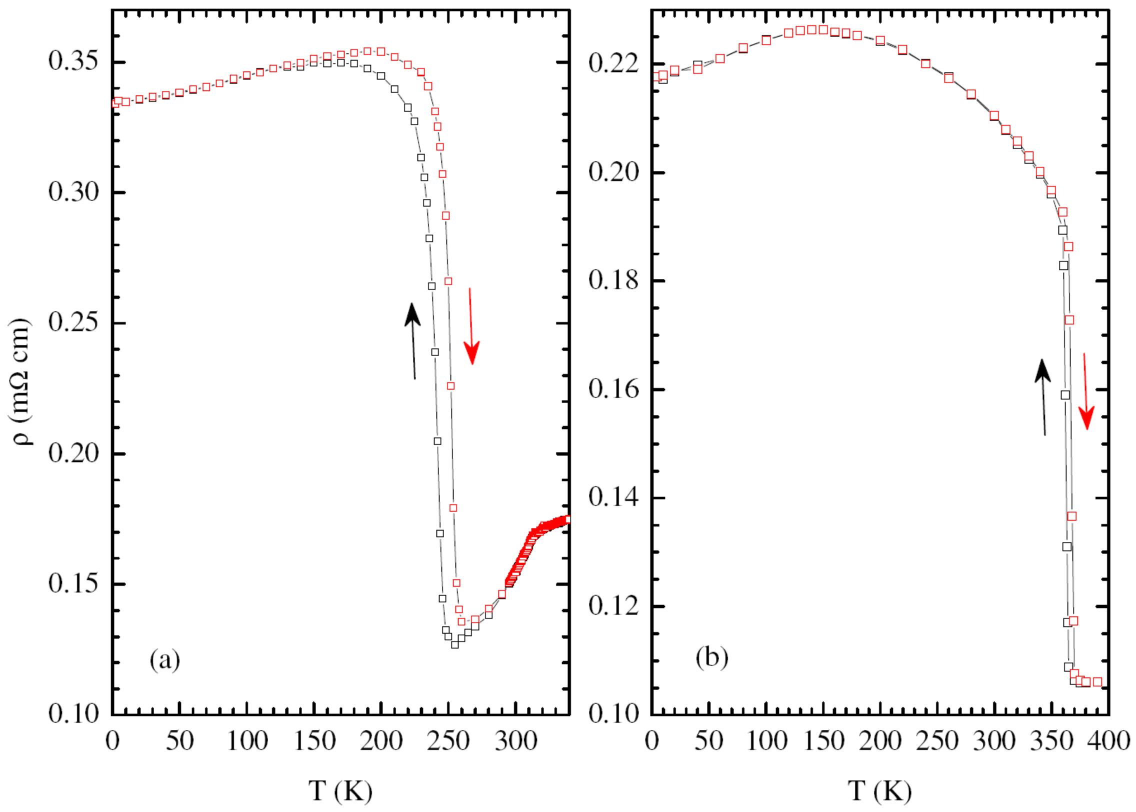

Fig. 3.9: Temperature (*T*) dependence of resistivity (*ρ*) of the (a) $Ni_{50}Mn_{34.5}In_{15.5}$ and (b) $Ni_{50}Mn_{35}In_{15}$ alloys in zero magnetic field.

noted that outside this phase transition regime the temperature coefficient of electrical resistivity is positive, commensurate with the metallic nature of the present sample.

Figure 9(b) shows the electrical resistivity of In-15 as a function of temperature in zero magnetic field. In the zero magnetic field measurement, there is a sharp increase in resistivity below 365 K during cooling. Below 350 K, the resistivity continues to increase gradually until 150 K below which it decreases with the lowering of temperature. There is a clear thermal hysteresis in resistivity between 350 and 375 K. There is no signature of thermal hysteresis in any other temperature regime of measurement. As discussed for Ni-Mn-In alloys above, these off-stoichiometric Heusler alloys are known to undergo a first-order AST to MST phase transition with the lowering of temperature. It has been inferred from the XRD data in section

3.2.1 that the In-15 sample is in the MST phase at room temperature. Thermal hysteresis of an experimental observable is usually a signature of a first-order phase transition [3.15]. We, therefore, attribute the sharp rise in resistivity near 365 K, and the associated thermal hysteresis to the first-order nature of the AST–MST phase transition in the sample. As discussed earlier, the end points of the thermal hysteresis demarcate the limits of metastability (supercooling and superheating) [3.15] of this first-order AST–MST phase transition. It is clear from Fig. 3.9(b) that below 350 K the sample is certainly in the MST phase, a finding supported by XRD measurements as well. In Fig. 3.9(b) it is observed that within this MST phase the In-15 sample has a negative temperature coefficient of resistivity between 350 and 150 K. This is quite anomalous since metallic samples are expected to have a positive temperature coefficient of resistivity arising from electron–phonon scattering [3.22]. The resistivity maximum observed in Fig. 3.9(b) at around 150 K is quite interesting. The ρ vs. T results on a $Ni_{50}Mn_{35}In_{15}$ (nominal composition) sample has been recently reported by Bhobe et al. [3.23] Their sample exhibits a sharp rise in resistivity below 300 K (nearly 365 K in our case), which has been interpreted as an indication of the AST–MST phase transition. A broad maximum is also seen in their $\rho(T)$ curve close to 165 K, though its significance is not clear from their work. Clearly, the characteristic features observed in the $\rho(T)$ for the sample of Bhobe et al., occurs at temperatures different from those of the In-15 alloy. Furthermore, thermal expansion measurements reported by Pathak et al. [3.20] show a MT near 310 K for the same In-15 composition. This apparent mismatch between the results obtained by various authors highlights the need of characterizing the Ni–Mn–In family of alloys with a technique that can resolve very small differences in the actual composition. The effect of the anti-site disorder involving Ni and Mn also needs to be investigated, which could be important in deciding the nature of magnetic interaction in these samples. Recently, a sharp rise in resistivity near and above 300 K and a broad maximum in $\rho(T)$ at a lower temperature has also been observed in some $Ni_{50}Mn_{25+x}Sb_{25-x}$ alloys [3.24] and $Ni_{50}Mn_{35}In_{14}X$ (X = Si,Ge,Al) alloys [3.25]. While the sharp rise in resistivity has been interpreted as the indication of the AST–MST phase transition, the reason for the broad maximum was not stated. On the other hand, a somewhat similar broad maximum in $\rho(T)$ observed earlier in a Co_2NbSn shape memory alloy has been interpreted as the signature of the Curie temperature of that material [3.26]. We will see in later discussion that in the temperature regime between 350 and 250 K there is no magnetic ordering in zero magnetic field. We have performed the temperature dependent resistivity measurement in presence of 80 kOe magnetic field and found that there is almost no effect of magnetic field on the resistivity in the temperature regime between 350 and 250 K. This indicates the absence of any kind of magnetic ordering in this temperature regime even in the presence of magnetic field. We conjecture that the negative temperature coefficient of resistivity between 350 and 250 K may be related to the strain and disorder present in the system. The In-15 alloy being in the MST phase below 350 K, it is quite likely to be strained with respect to the AST phase. The effect of strain in the presence of twin boundaries in the MST phase could probably enhance the scattering of electrons and lead to such anomalous resistivity.

3.2.3 Temperature dependence of magnetization of the $Ni_{50}Mn_{34.5}In_{15.5}$ and $Ni_{50}Mn_{35}In_{15}$ alloys

Fig. 3.10(a) shows the M vs. T curve (measured in FCW protocol) of the In-15.5 sample for H = 100 Oe. Qualitatively similar M vs. T curve has been observed previously in the $Ni_{50}Mn_{34}In_{16}$ alloy. The rise in M around 312 K indicates a PM-FM transition in the alloy. This feature can be correlated with the kink on the $\rho(T)$ curve of the same sample observed at

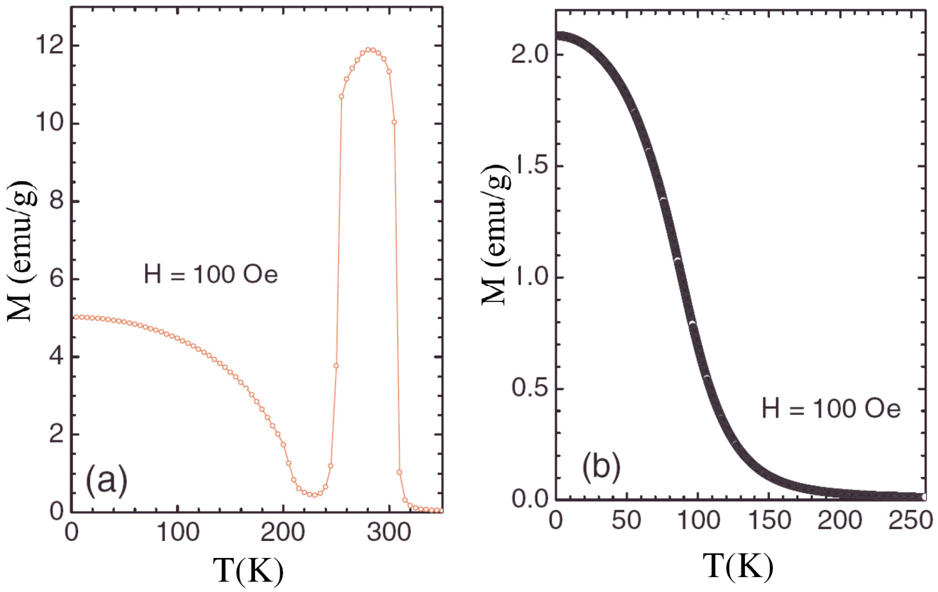

Fig. 3.10: Temperature (*T*) dependence of magnetization (*M*) of the (a) $Ni_{50}Mn_{34.5}In_{15.5}$ and (b) $Ni_{50}Mn_{35}In_{15}$ alloy samples in magnetic field (*H*) of 100 Oe in FCW protocol.

around 312 K, and supports our earlier conjecture that this kink indicates the Curie temperature of the AST phase of In-15.5. The sharp drop in *M* around 260 K has an associated thermal hysteresis (not shown in the Fig. 3.10), and this is correlated with the first-order nature of AST-MST phase transition.

Fig. 3.10(b) shows the *M* vs. *T* curve of the In-15 sample for *H* = 100 Oe obtained using the FCW protocol. The rise in M near 150 K indicates PM to FM transition in the alloy. We have already inferred that in this temperature regime the sample is in MST phase. The magnetic character of AST phase (in In-15 alloy, AST phase appears at *T*>375 K) could not be investigated because the high temperature range is not available in vibrating sample magnetometer (VSM) used for these investigations.

3.2.4 Magnetic field induced phase transition in $Ni_{50}Mn_{34.5}In_{15.5}$ and $Ni_{50}Mn_{35}In_{15}$ alloys

Like $Ni_{50}Mn_{34}In_{16}$ alloy, isothermal *M*(*H*) curves at temperatures away from the MST-AST phase transition in In-15.5 alloy show characteristics of a soft ferromagnet and within the temperature regime of transition exhibit signature of magnetic field induced MST to AST phase transition. For example, Fig. 3.11(a) shows the isothermal *M* vs. *H* curve of the In-15.5 sample for *T* = 230 K starting from zero field cooled state. There is a clear signature of a magnetic field induced phase transition at about 25 kOe on the virgin magnetization curve. As discussed earlier in context of $Ni_{50}Mn_{34}In_{16}$ alloy, this transition is associated with a hysteresis which is quite different in nature compared to the hysteresis observed in the M(H) curves of a ferromagnet. The magnetic field hysteresis associated with this transition is attributed to the first-order nature of this magnetic field induced phase transition.

Fig. 3.11(b) shows the *M* vs. *H* curves for In-15 alloy obtained at 80, 120, 170, and 350 K. The *M* vs. *H* curves obtained above 150 K do not exhibit any signature of technical saturation. Absence of any spontaneous magnetization above *T* = 150 K has been confirmed using M^2 vs. *H*/*M* plot or Arrott plot [3.27] constructed from the isothermal *M*(*H*) curves.

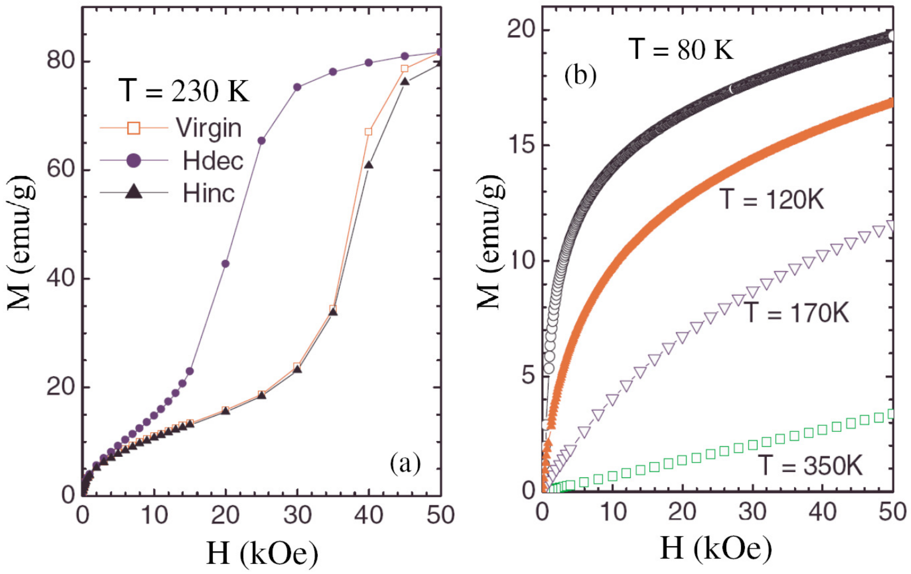

Fig. 3.11: Isothermal magnetic field (*H*) dependence of magnetization (*M*) of the (a) $Ni_{50}Mn_{34.5}In_{15.5}$ and (b) $Ni_{50}Mn_{35}In_{15}$ alloy samples.

3.2.5 Possible reason for contrasting magnetic behavior of the $Ni_{50}Mn_{34.5}In_{15.5}$ and $Ni_{50}Mn_{35}In_{15}$ alloys

Our observations in $Ni_{50}Mn_{50-y}In_y$ (y = 15.5 and 15) show that the Ni-Mn-In alloy system is more sensitive to the composition in this regime of y (In-content) than what is apparent from the earlier phase diagram [3.1]. A concentration differences as low as 0.5 at. % causes a drastic difference in the properties of the alloy. While in case of y = 15.5 a magnetic field induced transition is clearly observed, there is no detectable signature of any magnetic field induced phase transition in the y = 15 alloy even up to magnetic fields as high as 80 kOe. The reason behind such extreme dependence of the functional properties of the alloys on the composition is not understood at present. However, it is known that the Ni–Mn–In off-stoichiometric Heusler alloys In is partially replaced by Mn at the 4(b) site of the stoichiometric compound [3.9], and the magnetic and structural transitions in this alloy system are sensitive to this off-stoichiometry [3.1]. We speculate that the sharp contrast of magnetic behavior between the y = 15.5 and y = 15 alloys may be related to the random distribution of Mn and In at the 4(b) site, though we had followed the same well documented preparation technique for both the alloys [3.5]. As discussed earlier, in Ni-Mn-X alloys, the Mn atoms occupying sites corresponding to the stoichiometric composition Ni_2MnX, are coupled ferromagnetically. On the other hand, in the off-stoichiometric alloys there is an incipient antiferromagnetic coupling between these Mn atoms (occupying proper Mn sites) and the excess Mn atoms (occupying In sites in present case). This incipient antiferromagnetic coupling might get strengthened in the MST phase [3.8, 3.9]. The excess Mn atoms can also have some magnetic coupling among themselves which will depend on their distribution at In sites. In Chapter 6 we will see that the magnetic properties strongly affect the AST-MST phase transition in these alloys. Recently, the effects of random distribution of Mn and Fe in the 4(b) site of the $Co_2Mn_{1-x}Fe_xSi$ Heusler alloys were probed by ^{55}Mn nuclear magnetic resonance (NMR) [3.28, 3.29]. Such NMR studies could also be very informative in the present systems. .

3.3 Conclusion

From the various experimental studies on the Heusler alloys $Ni_{50}Mn_{34}Sn_{16}$ and $Ni_{50}Mn_{34}In_{16}$ alloys, it is found that both the alloys undergo a martensitic transition from an austenite phase to a martensite phase with decreasing temperature in a similar temperature regime. Thermal hysteresis associated with a first-order phase transition has been observed in the temperature dependence of the physical properties. It has been found that the transition in $Ni_{50}Mn_{34}Sn_{16}$ alloy takes place over a comparatively broader temperature regime. Further we observed that the AST phase has larger value of magnetization as compared to that in the MST phase in both the alloys. It is also found that in both the alloys the transition shifts to lower temperature with increasing magnetic field. However, this shift is much larger in $Ni_{50}Mn_{34}In_{16}$ alloy. Further, isothermal magnetization measurements as a function of applied magnetic field show a prominent magnetic field induced MST to AST phase transition in $Ni_{50}Mn_{34}In_{16}$ alloy, while there is only weak signature of such magnetic field induced phase transition in $Ni_{50}Mn_{34}Sn_{16}$ alloy. The magnetic field induced phase transition has been correlated with the width of the transition and the shift of characteristic temperatures of the AST-MST phase transition in these alloys. Moreover, results of investigations on $Ni_{50}Mn_{34.5}In_{15.5}$ and $Ni_{50}Mn_{35}In_{15}$ alloys show that while $Ni_{50}Mn_{34.5}In_{15.5}$ alloy also undergoes magnetic field induced MST-AST phase transition, $Ni_{50}Mn_{35}In_{15}$ alloy exhibit no detectable signature of magnetic field induced transition up to magnetic field of 80 kOe. This dependence of field induced transition in the off-stoichiometric Ni-Mn-In Heusler alloys on the small change in the composition may have origin in the random distribution of Mn and In atoms at 4(b) lattice site.

Publications based on this Chapter:

1. Magnetocaloric effect in Heusler alloys $Ni_{50}Mn_{34}In_{16}$ and $Ni_{50}Mn_{34}Sn_{16}$. *J. Phys.: Condens. Matter* **19**, 496207 (2007).

   Sharma V. K., Chattopadhyay M. K., Kumar R., Ganguli T., Tiwari P., and Roy S. B.

2. Contrasting magnetic behavior of $Ni_{50}Mn_{35}In_{15}$ and $Ni_{50}Mn_{34.5}In_{15.5}$ alloys. *J. Appl. Phys*. **108,** 073909 (2010).

   Chattopadhyay M. K., Manekar M. A., **Sharma V. K.**, Arora P., Tiwari P., Tiwari M. K., and Roy S. B.

Chapter 4

Functional properties of the $Ni_{50}Mn_{34}In_{16}$ alloy

In Chapter 3 we have observed that the $Ni_{50}Mn_{34}In_{16}$ alloy undergoes a first-order martensite (MST)-austenite (AST) phase transition which can be induced by temperature (*T*) as well as magnetic field (*H*). First-order magnetostructural transition is known to give rise to large magnetoresistance (MR) in FeRh [4.1], GdSiGe [4.2] and MnAs [4.3] based alloys. A number of material systems have also been reported to be showing a large magnetocaloric effect (MCE) associated with a first-order magnetostructural transition. $Gd_5(Ge,Si)_4$ [4.4-4.6], $MnFeP_{0.45}As_{0.55}$ [4.7], $MnAs_{1-x}Sb_x$ [4.8], MnAs [4.9], Ni-Mn-Ga [4.10], manganese oxide compounds [4.11], FeRh [4.12] and doped $CeFe_2$ alloys [4.13] are examples of such systems. A large magnetic field induced strain has been reported in NiCoMnSn [4.14] and NiCoMnIn [4.15] alloys, which owes its origin to a first-order magnetostructural transition. We have seen in the earlier Chapter that the MST and AST phases of the $Ni_{50}Mn_{34}In_{16}$ alloy differ substantially in their properties (resistivity, magnetization etc.). We anticipate that the temperature and magnetic field induced martensitic transition (MT) in this alloy is likely to give rise to interesting functionalities viz. large MR, large MCE etc. In this Chapter we present results of our investigations on the possibility of such functionalities in $Ni_{50}Mn_{34}In_{16}$ alloy. It has been found that this alloy indeed shows large MR of the order of 64%, large MCE with isothermal magnetic entropy change of nearly 18 J/kg-K and large strain of the order of 0.06% in magnetic field of 50 kOe.

4.1 Large magnetoresistance in the $Ni_{50}Mn_{34}In_{16}$ alloy

To investigate the magnetoresistance in $Ni_{50}Mn_{34}In_{16}$ alloy we have measured the temperature dependence of resistivity (ρ) of the alloy between 5 and 300 K for various constant magnetic fields (H) in field cooled cooling (FCC) and field cooled warming (FCW) protocols. These results are presented in Fig. 4.1. Near 300 K, the resistivity decreases with decreasing temperature for all magnetic field values. At a lower temperature (the value of this temperature depends on the applied magnetic field) there is a sharp rise in resistivity with decreasing temperature. We have discussed in the previous Chapter that the sharp rise in resistivity which has an associated thermal hysteresis, is related to a first-order AST-MST phase transition in the alloy. At temperatures lower than this phase transition region, the resistivity again decreases with decreasing temperature. It is observed that temperatures of both the AST to MST phase transition and the reverse transition from MST phase to AST phase, shift towards lower T with increasing H. The width of the transitions and the width of the thermal hysteresis are found to increase with increasing H. The overall resistivity of the alloy decreases with increasing H between 5 and 300 K (see Fig. 4.1).

MR has been calculated using the following equation (as described in the section 2.8 of Chapter 2).

$$MR(H)(\%) = \left(\frac{\rho(H) - \rho(0)}{\rho(0)} \right) \times 100 \qquad (4.1)$$

The temperature dependence of MR for magnetic field of 10 kOe and 50 kOe is presented in Fig. 4.2. The value of MR in the MST phase as well as in the AST phase is negative. Both the AST and MST phases are ferromagnetic in nature and the negative MR in both the phases is probably because of the decrease in spin disorder scattering with applied magnetic field. A relatively large MR is observed in the MT region (see Fig. 4.2). This MR arises from the shift of the temperature

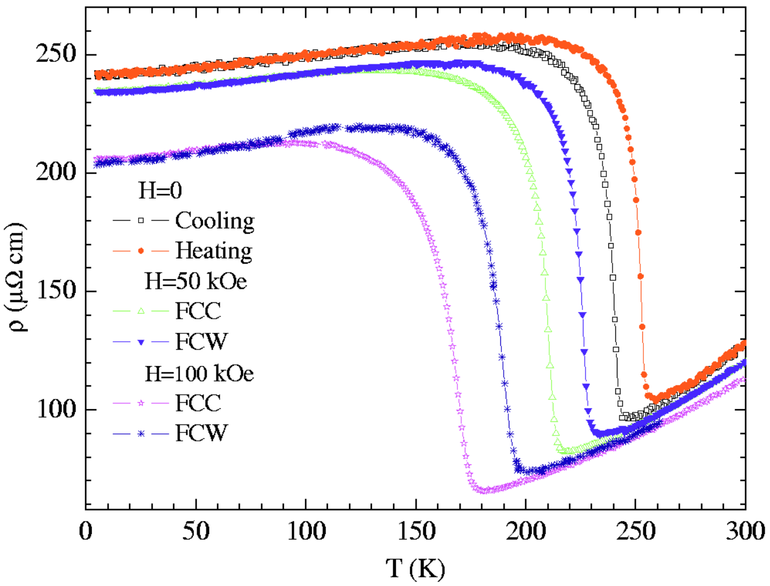

Fig. 4.1: Temperature (T) dependence of resistivity (ρ) of the $Ni_{50}Mn_{34}In_{16}$ alloy in different constant magnetic fields (H).

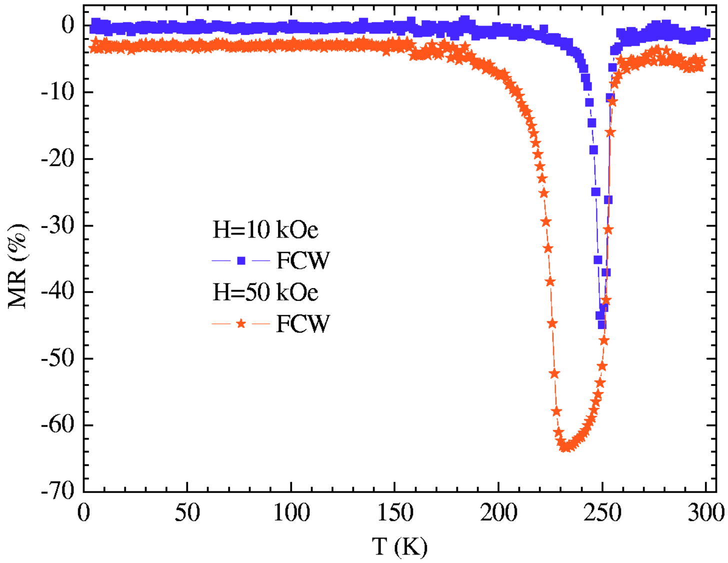

Fig. 4.2: Temperature (T) dependence of magnetoresistance (MR) of the $Ni_{50}Mn_{34}In_{16}$ alloy in different constant magnetic fields (H).

regime of the AST-MST phase transition under applied magnetic field. For H = 10 kOe, an MR of about 46% is obtained at 250 K. This MR increases with magnetic field, and for 50 kOe magnetic field 64% MR is observed at 230 K. On increasing the applied magnetic field to 100 kOe, an MR of 75% is obtained at 180 K.

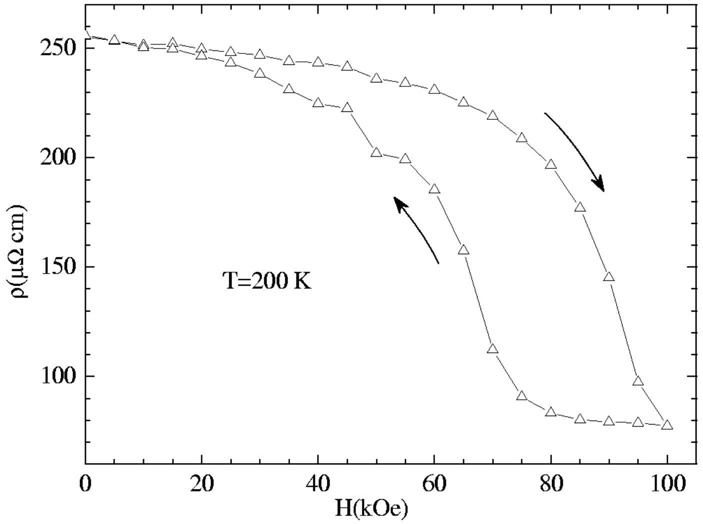

Fig. 4.3: Isothermal magnetic field (*H*) dependence of resistivity (*ρ*) of the $Ni_{50}Mn_{34}In_{16}$ alloy at 200 K indicating negative magnetoresistance.

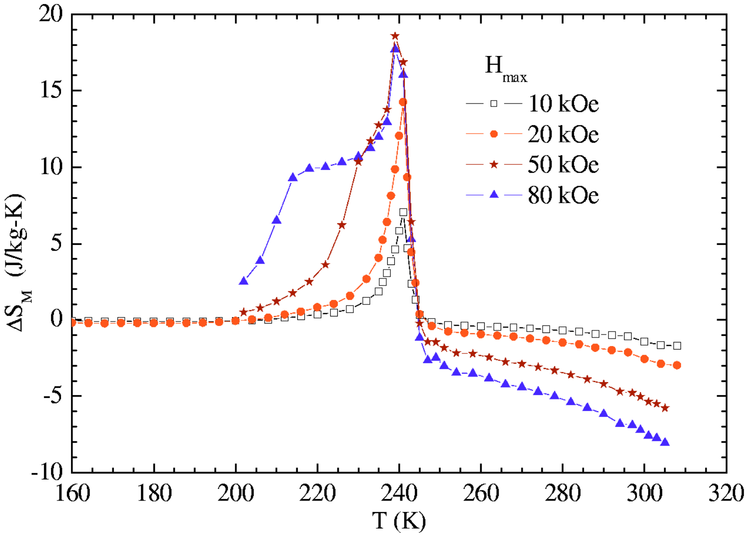

Fig. 4.4: Isothermal change in magnetic entropy (ΔS_M) as a function of temperature (*T*) across the austenite-martensite phase transition in $Ni_{50}Mn_{34}In_{16}$ for various magnetic field excursions.

The shift of temperature regime of the AST-MST phase transition with magnetic field, suggests the possibility of large change in resistivity under isothermal application of magnetic field. This large change has indeed been observed in isothermal magnetic field dependent resistivity measurement. The result of such an isothermal measurement at 200 K is presented in Fig. 4.3. The temperature has been approached by cooling the sample from 300 K in zero magnetic field. The sharp change in resistivity and the magnetic field hysteresis in Fig. 4.3 are related with the first-order nature of the magnetic field induced MST to AST phase transition. Such MR under isothermal application of magnetic field has been reported in FeRh [4.1], GdSiGe [4.2] and MnAs [4.3] based alloys which also undergo a first-order phase transition. Further, large MR as observed in the present study has also been reported in an alloy with similar nominal composition as that of present alloy [4.16]. Similar MR has been observed in our $Ni_{50}Mn_{34.5}In_{15.5}$ alloy.

4.2 Large magnetocaloric effect in the $Ni_{50}Mn_{34}In_{16}$ alloy

The MCE is estimated from isothermal change of magnetic entropy ($\mathit{\Delta}S_M$) and/or adiabatic change of temperature ($\mathit{\Delta}T_{ad}$). The isothermal change of magnetic entropy in a material due to an isothermal change of magnetic field can be estimated from the experimentally obtained isothermal magnetization (M) vs. H curves as described in section 2.6 of Chapter 2. For magnetization measured isothermally at temperatures T and $T+\mathit{\Delta}T$ at discrete magnetic field intervals, following equation (discussed in section 2.6 of Chapter 2) was used.

$$\Delta S_M\left(T+\frac{1}{2}\Delta T\right)=\frac{1}{\Delta T}\left[\int_0^H M(T+\Delta T,H)dH-\int_0^H M(T,H)dH\right] \tag{4.2}$$

The magnitude of $\mathit{\Delta}S_M$ as a function of temperature estimated for different magnetic field excursions from zero to H_{max} is shown in Fig. 4.4. The $\mathit{\Delta}S_M(T)$ peaks around the AST–MST phase transition regime of $Ni_{50}Mn_{34}In_{16}$, and its sign is positive in contrast to the ΔS_M observed in conventional MCE. In the literature such a positive sign of ΔS_M is associated with an inverse MCE [4.17]. With the increase in temperature above the AST–MST phase transition regime $\Delta S_M(T)$ changes sign and becomes negative as expected in the conventional MCE. The maximum in $\mathit{\Delta}S_M$ gets enhanced in magnitude as H_{max} is increased from 10 to 20 kOe. A further increase in H_{max} beyond 20 kOe does not seem to cause much enhancement of $\mathit{\Delta}S_M$. However, there is a change in character of ΔS_M in the temperature regime below the peak in $\Delta S_M(T)$. In this temperature regime $\Delta S_M(T)$ obtained with higher H_{max} drops less rapidly. This is possibly correlated with the magnetic field induced MST to AST phase transition in this temperature regime. Although the critical magnetic field for the onset of the AST phase increases rapidly with the decrease in temperature (see Fig. 3.6 of Chapter 3), this critical magnetic field remains below 80 kOe approximately down to 210 K. Hence, while the enhancement in ΔS_M is not quite as large in higher magnetic fields, the drop in ΔS_M with temperature is less rapid. The maximum of $\Delta S_M \approx 19$ J/kg-K in the magnetic field of 50 kOe around 240 K is comparable to those observed in manganese oxide systems in the temperature regime 10–30 K [4.18, 4.19]. The change in entropy in the $Ni_{50}Mn_{34}In_{16}$ alloy is also higher than the $\Delta S_M \approx 10$ J/kg-K found in the well-known MCE material Gd around 295 K [4.20]. The change in entropy in the present $Ni_{50}Mn_{34}In_{16}$ alloy in magnetic field of 50 kOe is larger than that 13 J/kg-K reported in $Ni_{46}Mn_{41}In_{13}$ alloy near 190 K for field change of 90 kOe [4.21]. However, it is smaller than $\Delta S_M = 28$ J/kg-K in $Ni_{45}Co_5Mn_{36.7}In_{13.3}$ alloy at 292 K for field change of 70 kOe [4.15]. It is well recognized that systems undergoing a temperature and magnetic field induced first-order phase transition often give rise to a large magnetic entropy change, $Gd_5(Si_xGe_{1-x})_4$ with $0\leq$ x 0.5 being a classic example of such systems [4.4- 4.6]. In these alloys ΔS_M (20–70 J/kg-K) was found to be much higher than that found in the materials like Gd and $Gd_{0.73}Dy_{0.27}$ [4.5, 4.6] with reversible second-order phase transition. However, it should be noted that the thermomagnetic hysteresis is a characteristic of a first-order phase transition process, and this might reduce the effectiveness of the MCE of the material. Also a first-order phase transition is often quite sharp in nature, and that narrows down the effective temperature range of large MCE. One remedy for this situation possibly is to broaden the first-order phase transition with the introduction of quenched disorder, but without making it a reversible second-order phase transition. Indeed it is observed that with the introduction of iron impurities the hysteresis loss in $Gd_5(Ge,Si)_4$ can be reduced considerably [4.22]. In the light of the discussion above, the suitability of H–T regime for a practical application needs to be judged cautiously after taking the hysteresis losses of the material into consideration. This can be done with the proper estimation of the refrigerant capacity [4.22, 4.23] of the system. The refrigerant capacity provides an estimate of heat transfer between cold and hot sinks in one ideal refrigeration cycle [4.23, 4.24]. While making a comparison between different materials to be used in the same refrigeration cycle, the material with higher refrigerant capacity is preferred since it would support transport of a greater amount of heat in a real refrigeration cycle [4.24]. The refrigerant capacity (RC) is defined for a magnetic field change of ΔH as

$$RC = \int_{T_{cold}}^{T_{hot}} \left(\Delta S_M\left(T\right)\right)_{\Delta H} dT \tag{4.3}$$

which indicates how much heat can be transferred from the cold end (T_{cold}) to the hot end (T_{hot}) of the refrigerator in one thermodynamic cycle. The RC of $Ni_{50}Mn_{34}In_{16}$ has been calculated by the method proposed by Gschneidner et al. [4.23, 4.24]. In Fig. 4.5, the crossed area under the ΔS_{M} vs. T plot measures the refrigerant capacity of the material within the framework proposed in [4.23]. The upper and lower temperature limits of the shaded area represent the temperatures of the hot and cold reservoirs (T_{hot} and T_{cold} respectively) of the refrigerant cycle in which $Ni_{50}Mn_{34}In_{16}$ is assumed to be used as the working medium. These limiting temperatures are obtained from the temperatures at the half maximum of the peak value in the $\Delta S_{\mathrm{M}}(T)$ curve. For calculating the effective refrigerant capacity (RC_{EFF}), first the average hysteresis losses are estimated from the isothermal $M(H)$ curves in the relevant H–T regimes. These are then subtracted from the calculated RC. The effective refrigerant capacity thus obtained for $Ni_{50}Mn_{34}In_{16}$ is plotted as a function of H in Fig. 4.6. Table 4.1 summarizes the results

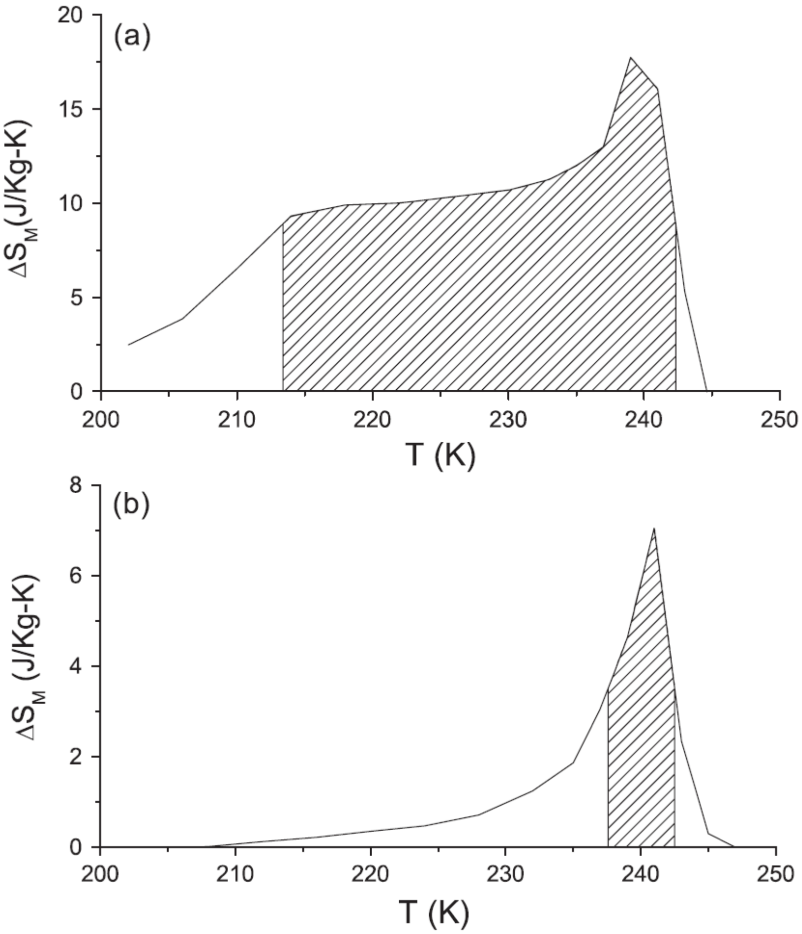

Fig. 4.5: Estimation of refrigerant capacity (RC) of $Ni_{50}Mn_{34}In_{16}$. Crossed area under full width at half maximum of $\Delta S_M(T)$ measures the RC of the material. The maximum magnetic field for magnetic field excursion from zero to H_{max} is 80 kOe in (a) and is 10 kOe in (b).

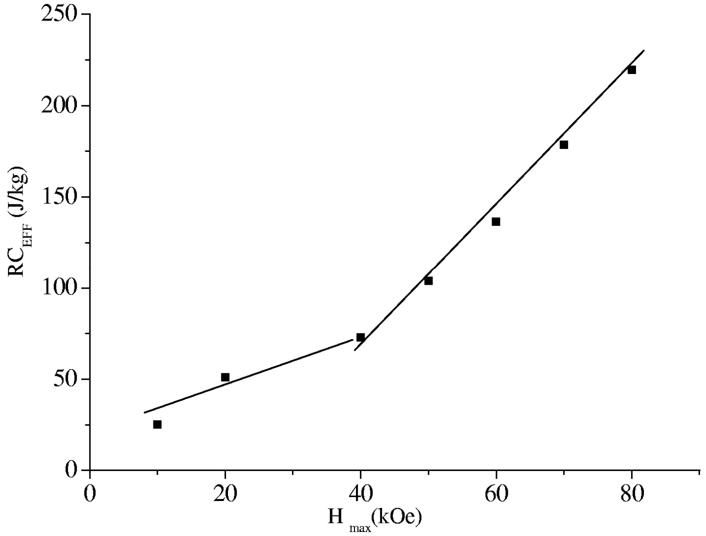

Fig. 4.6: Effective refrigerant capacity (RC_{EFF}) of $Ni_{50}Mn_{34}In_{16}$ as a function of the magnetic field excursion from zero to H_{max}. Points are experimental data points. Lines are given as guides to the eyes.

Table 4.1: Useful temperature range, refrigerant capacity, hysteresis loss and effective refrigerant capacity estimated for $Ni_{50}Mn_{34}In_{16}$ alloy.

Maximum field excursion H_{max} (kOe)	T_{cold} (K)	T_{hot} (K)	Refrigerant capacity (J/kg)	Average hysteresis loss (J/kg)	Effective refrigerant capacity RC_{EFF} (J/kg)
10	236.8	242.8	25.38	0.42	24.96
20	236.5	242.7	53.26	2.16	51.1
40	233.2	242.5	132.84	60.03	72.81
50	229.9	242.3	180.8	77.01	103.79
60	224.5	242.4	227.09	90.49	136.6
70	218.9	242.4	279.67	101.23	178.44
80	214	242.3	328.47	108.96	219.51

concerning the refrigerant capacity in $Ni_{50}Mn_{34}In_{16}$. A large RC_{EFF} is observed for this alloy over a wide temperature interval in a relatively high temperature regime. The highest RC_{EFF} value of 219 J/kg obtained in a magnetic field of 80 kOe, however, is lower than that of 305 J/kg in $Gd_5Ge_2Si_2$ obtained in a magnetic field of 50 kOe [4.22]. $RC_{EFF}(H)$ plotted in Fig. 4.6 shows a change in the slope around 40 kOe. This may be related to the qualitative change in the temperature dependence of $\Delta S_M(T)$ obtained with higher H_{max} (see Fig. 4.4) due to the magnetic field induced MST to AST phase transition. This change in the character of $\Delta S_M(T)$ in turn increases the span of T_{hot} and T_{cold} significantly for applied magnetic fields above 40 kOe (see table 4.1). Fig. 4.4 also shows a substantially large change of ΔS_M (with usual negative sign) in $Ni_{50}Mn_{34}In_{16}$ around 300 K, which is associated with the paramagnetic to ferromagnetic transition of this alloy. Due to the experimental constraint with our magnetometer, the temperature regime above 305 K could not be explored. But even in this limited temperature regime the magnitude of ΔS_M reached a value 8 J/kg-K, which is quite comparable to that of Gd in the similar temperature regime. Our isothermal magnetic field dependence study of magnetization (up to a maximum magnetic field of 80 kOe) revealed no magnetic hysteresis in this temperature regime.

Whereas the magnitude of ΔS_M is indicative of the potential of a material for MCE, estimation of the ΔT_{ad} is needed for a final conclusion about the magnitude of MCE [4.24]. We have estimated ΔT_{ad} using the results of heat capacity measurements in conjunction with magnetization data. For an estimation of ΔT_{ad}, the value of entropy (S) as a function of T in zero magnetic field and in the magnetic field of interest is needed. Zero-field entropy was estimated from heat capacity (C) data measured in zero magnetic field (presented in Fig. 3.5(b) of Chapter 3). $S(T)$ in zero field as a function of temperature can be calculated using zero-field heat capacity data with the following equation [4.25, 4.26]

$$S(T)_0 = \int_0^T \frac{C(T)_0}{T} dT + S_0 \tag{4.4}$$

where $S(T)_0$ and $C(T)_0$ are entropy and heat capacity at temperature T in zero field and S_0 is zero temperature entropy. In a solid-state system S_0 is independent of magnetic field and so can be taken as a constant, say zero [4.25, 4.26]. We have estimated S from C data with the numerical method available in the literature [4.25, 4.26]. $\Delta S_M(T)_H$ calculated from isothermal magnetization curves was combined with this zero-field entropy to calculate S at constant magnetic field as a function of temperature

$$S(T)_H = S(T)_0 + \Delta S(T)_H \tag{4.5}$$

From S vs. T curves we estimated ΔT_{ad} as a function of temperature. To estimate ΔT_{ad} an iso-entropic path was followed from the zero-field S curve to the curve for magnetic field H such that $S(T)_0$ equals $S(T + \Delta T_{ad})_H$ and ΔT_{ad} was obtained as (see Fig. 2.16 of Chapter 2) [4.25, 4.26]

$$\Delta T_{ad}(T)_H = [T(S)_H - T(S)_0]_S \tag{4.6}$$

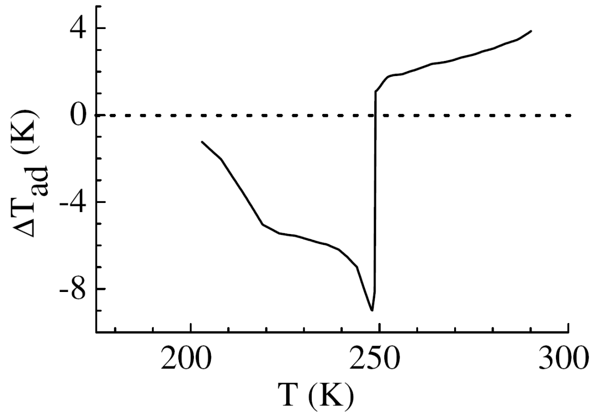

Fig. 4.7: Temperature (*T*) dependence of the adiabatic temperature change (ΔT_{ad}) for the $Ni_{50}Mn_{34}In_{16}$ alloy for a magnetic field change of 80 kOe.

We have estimated ΔT_{ad} for a magnetic field change of 80 kOe. Fig. 4.7 presents ΔT_{ad} vs. *T* data for a magnetic field change of 80 kOe for $Ni_{50}Mn_{34}In_{16}$ alloy. As expected, the shape of ΔT_{ad} vs. *T* curve is like inverted ΔS_M vs. *T* curve of the alloy. A negative ΔT_{ad} corresponding to an inverse MCE around the martensitic transition region and a positive ΔT_{ad} corresponding to a conventional MCE away from this temperature regime is observed. ΔT_{ad} attains a maximum value of 9 K around 248 K in the alloy. This magnitude of ΔT_{ad} is comparable to $\Delta T_{ad} \approx 12$ K reported for Gd [4.26] and $Gd_5(Si_2Ge_2)$ [4.27] for a magnetic field change of 50 kOe. Furthermore, the magnitude of ΔT_{ad} peak corresponding to conventional MCE is ≈ 4 K at 290 K for a magnetic field change of 80 kOe for this alloy.

4.3 Large temperature and magnetic field induced strain in the $Ni_{50}Mn_{34}In_{16}$ alloy

We have measured temperature and magnetic field induced strain in $Ni_{50}Mn_{34}In_{16}$ alloy using the strain gauge techniques described in section 2.7 of Chapter 2. The temperature dependence of the strain is measured as the relative length change ($\Delta L/L$) with respect to length at 293 K (as defined in section 2.7 of Chapter 2). The magnetic field dependence of the strain is measured as the relative length change ($\Delta L/L$) with respect to length in zero field (see section 2.7

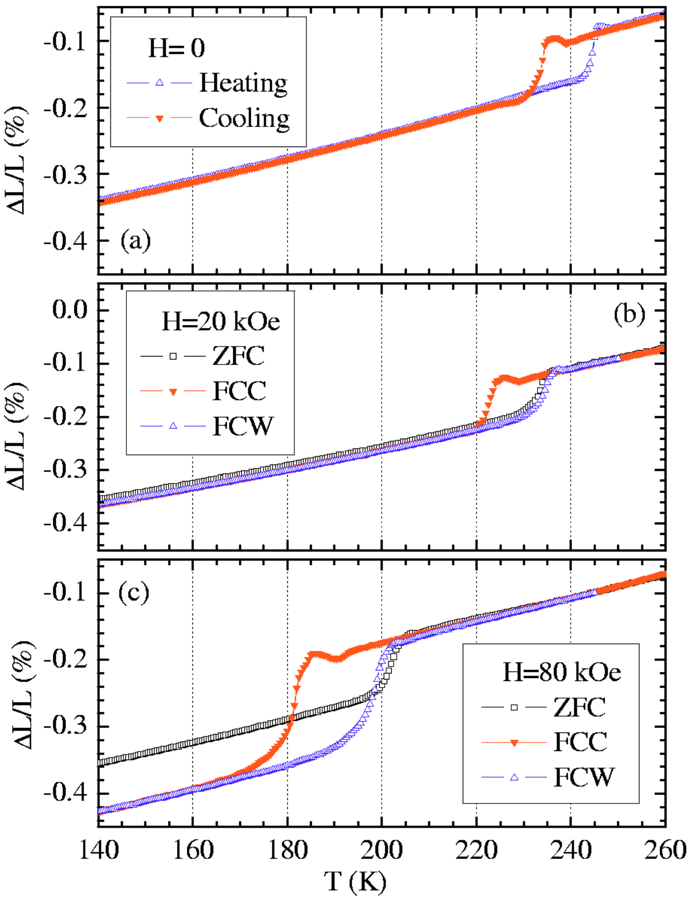

Fig. 4.8: Temperature (*T*) dependence of strain (*ΔL/L*) in (a) zero magnetic field, (b) magnetic field of 20 kOe and (c) magnetic field of 80 kOe for $Ni_{50}Mn_{34}In_{16}$ alloy.

of Chapter 2). Figs. 4.8(a)–4.8(c) present the results of temperature dependent strain measurement under zero field cooled (ZFC), FCC and FCW protocols in *H* = 0, 20 and 80 kOe. In the ZFC protocol the sample is cooled in zero field from 300 K to the lowest temperature of measurement. An external magnetic field is applied at this lowest temperature and the measurement is performed while warming the sample in the same applied magnetic field. FCC and FCW protocols have been explained earlier in section 3.1.3 of Chapter 3. Starting from well inside the AST phase in zero magnetic field (see Fig. 4.8(a)), *ΔL/L* decreases with decreasing temperature. Near 240 K, *ΔL/L*(*T*) first forms a small hump and then exhibits a sharp drop of about 0.08%. Then *ΔL/L* shows a subtle dip (visible in magnified view) and thereafter it continues to decrease smoothly with further lowering of temperature. A very similar behaviour is seen on increasing the temperature from well inside the MST phase, but there is distinct thermal hysteresis between 230 and 250 K. This sharp change in $\Delta L/L(T)$ and the associated thermal hysteresis occur in the same temperature regime where our studies of magnetization, resistivity and specific heat measurements indicated the presence of AST-MST phase transition in $Ni_{50}Mn_{34}In_{16}$. Accordingly, the observed features (namely the hump, sharp drop and dip) in $\Delta L/L(T)$ can be correlated with the process of AST-MST phase transition. Further, the hump like feature in $\Delta L/L(T)$ observed around the AST-MST phase transition region has also been reported in Ni–Mn–Ga alloys [4.28, 4.29] and is expected to be originating from the dynamics around the AST-MST phase transition, but the origin of this feature is not yet understood. Figs. 4.8(b) and 4.8(c) show $\Delta L/L(T)$ in the presence of a magnetic field. These $\Delta L/L(T)$ curves exhibit behaviour similar to that in a zero magnetic field, but the transition temperatures are decreased. This is related with the shift of MST-AST phase transition with magnetic field as observed in magnetization and resistivity measurements. Interestingly, the ZFC curve lies above the FCC and FCW curves in the MST phase. In fact the ZFC curves in 20 and 80 kOe magnetic field overlap up to 180 K. Further the difference in $\Delta L/L(T)$ between AST and MST phases across the transition increases to about 0.09% and 0.15% in 20 kOe and 80 kOe, respectively. The difference in $\Delta L/L(T)$ across the transition in zero magnetic field is comparable to that reported in polycrystalline samples of $Ni_{49.8}Mn_{34.7}Sn_{15.5}$ [4.30] and $Ni_{50.3}Mn_{33.7}In_{16.0}$ [4.31] alloys. The negative strain from AST phase to MST phase in $Ni_{50}Mn_{34}In_{16}$ polycrystalline sample indicates that MST phase has lower volume as compared to AST phase in this alloy. Further the increased negative strain from AST phase to MST phase with increasing magnetic field indicates that some short axis of MST is the easy axis of magnetization [4.30]. We have also measured the magnetic

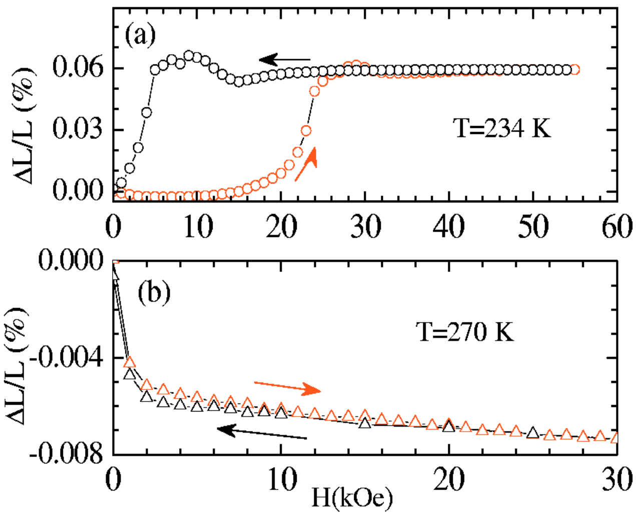

Fig. 4.9: Isothermal magnetic field (*H*) dependence of strain (*ΔL/L*) for $Ni_{50}Mn_{34}In_{16}$ alloy at temperature (*T*) (a) 234 K and (b) 270 K.

field induced strain in $Ni_{50}Mn_{34}In_{16}$ alloy. Fig. 4.9(a) shows results of isothermal *ΔL/L*(*H*) measurements performed at 234 K by increasing the magnetic field and decreasing it back to zero. With the increase in the magnetic field, *ΔL/L*(*H*) shows a sharp rise close to 20 kOe and then saturates around the 40 kOe magnetic field. However, before reaching saturation *ΔL/L*(*H*) shows a hump like feature similar to that seen in the temperature induced transition in Fig. 4.8. Further the complete H cycle reveals a large magnetic field hysteresis in the *ΔL/L*(*H*)curve. We assign all these features in isothermal *ΔL/L*(*H*) data to the magnetic field induced transition from the MST phase to the AST phase. The magnetic field induced strain is comparable to that across the temperature induced transition. In the decreasing magnetic field cycle, *ΔL/L* remains nearly constant down to *H* ≈ 20 kOe and decreases after exhibiting the hump like feature. The hump like feature in the magnetic field induced strain, as observed here, has also been reported in Ni–Mn–Ga [4.29] and similar composition of Ni–Mn–In alloy [4.31]. The isothermal Δ*L*/*L*(H) curves at temperatures outside the temperature regime of MST-AST phase transition show quite different behaviour. As an example, in Fig. 4.9(b) we present the isothermal *ΔL/L*(*H*)curve measured at 270 K. Here *ΔL*/*L*(*H*) decreases with the increase in magnetic field which signifies the negative magnetostriction of the AST phase. Within the experimental uncertainty in our measurement setup no significant magnetic field induced strain was observed well inside the MST phase. This shows that the twin boundaries in the MST twin variants are not very mobile. This is consistent with the observation that the ZFC curves for 20 and 80 kOe magnetic fields overlap in the temperature regime below the MST to AST phase transition in the 80 kOe magnetic field (see Fig. 4.8).

4.4 Conclusion

The magnetic field induced martensite-austenite phase transition in $Ni_{50}Mn_{34}In_{16}$ alloy imparts interesting functional properties to this alloy. It has been found that the alloy shows a peak magnetoresistance of nearly 45 % near 240 K in magnetic field of 10 kOe, which increases to 65% in a magnetic field of 50 kOe. The alloy also shows a large inverse magnetocaloric effect around the temperature regime of the martensite-austenite phase transition and a conventional magnetocaloric effect around the paramagnetic-ferromagnetic transition. It has been found that the peak value of the isothermal magnetic entropy change (estimated from isothermal magnetization vs. magnetic field curves at various temperatures using Maxwell's equation) occurs near 240 K with value of 14 J/kg-K for magnetic field excursion of 20 kOe. This increases to 18 J/kg-K for magnetic field excursion of 50 kOe. In spite of the finite hysteresis losses (associated with the martensitic transition) in the high magnetic fields, a large effective refrigerant capacity is possible in this alloy over a wide temperature interval around the martensitic transition. This alloy also shows a large strain across the temperature and magnetic field induced martensite-austenite phase transition. We found strain of 0.06% across the temperature induced transition in zero magnetic field. A similar order of magnitude of strain has also been observed across the magnetic field induced martensite to austenite phase transition in this alloy. Our studies in $Ni_{50}Mn_{34}In_{16}$ alloy reveal the potential of this alloy for magnetic refrigeration, magnetic field controlled actuation and magnetoresistance related application.

Publications based on this Chapter:

1. Large magnetoresistance in $Ni_{50}Mn_{34}In_{16}$ alloy.

   Appl. Phys. Lett. **89**, 222509 (2006).

   Sharma V. K., Chattopadhyay M. K., Shaeb K. H. B., Chouhan A., and Roy S. B.

2. Large inverse magnetocaloric effect in $Ni_{50}Mn_{34}In_{16}$.

   J. Phys. D: Appl. Phys. **40**, 1869 (2007).

   Sharma V. K., Chattopadhyay M. K., and Roy S. B.

3. Magnetocaloric effect in Heusler alloys $Ni_{50}Mn_{34}In_{16}$ and $Ni_{50}Mn_{34}Sn_{16}$.
   J. Phys.: Condens. Matter **19**, 496207 (2007).

   Sharma V. K., Chattopadhyay M. K., Kumar R., Ganguli T., Tiwari P., and Roy S. B.

4. Temperature and magnetic field induced strain in $Ni_{50}Mn_{34}In_{16}$ alloy.

   J. Phys. D: Appl. Phys. **42**, 185005 (2009).

   Sharma V.K., Chattopadhyay M.K., Chouhan A., Roy S.B.

Chapter 5

Disorder-influenced first-order phase transition and thermomagnetic history dependence of functional properties in the $Ni_{50}Mn_{34}In_{16}$ alloy

In earlier Chapters it has been discussed that the key to multifunctional properties observed in $Ni_{50}Mn_{34}In_{16}$ alloy is a temperature (T) and magnetic field induced first-order martensite (MST)-austenite (AST) phase transition. Traditionally, Arrott plots (isothermal M^2 vs. H/M plots, where H is the applied magnetic field and M is the measured magnetization of a sample) are used to analyse the ferromagnetic character of a material [5.1]. It has also been shown theoretically [5.2] that the sign of the slope of the H/M vs. M^2 isotherms may be used to distinguish between the first- and second-order magnetic phase transitions. It was found that a positive slope of the H/M vs. M^2 isotherm is related to the second-order magnetic phase transition, while a negative slope corresponds to the first-order magnetic phase transition. This criterion [5.2] has been employed for the identification of the order of the magnetic transitions in MnAs [5.2], Ru-doped $CeFe_2$ [5.3] and various other manganite systems [5.4-5.8]. The same criterion has also been used to investigate the magnetic transitions in the ferromagnetic shape memory alloy system Ni-Mn-Ga [5.9]. In the present Chapter, we perform a detailed investigation of the magnetic field-induced MST to AST phase transition in $Ni_{50}Mn_{34}In_{16}$ by studying H/M vs. M^2 isotherms. We show that, though the martensitic transition (MT) in this alloy is first-order in nature, the criterion of negative slope of the H/M vs. M^2 isotherms is not strictly applicable here. It is found that, instead of a negative slope, a decrease of slope is observed in some of the isothermal H/M vs. M^2 curves in the temperature regime of the magnetic field-induced MST to AST phase transition. This has been correlated with the disorder-influenced nature of the first-order magnetic transition. Phase coexistence and thermomagnetic hysteresis is a generic feature of a disorder-influenced first-order phase transition and has been observed in various classes of magnetic systems undergoing a first-order magneto-structural phase transition [5.10]. In this Chapter we also probe the magnetic field induced MST to AST phase transition in $Ni_{50}Mn_{34}In_{16}$ alloy using scanning Hall probe imaging experiments. The scanning Hall probe images clearly show the coexistence of the MST and AST phases across this magnetic field induced MST to AST phase transition and provide visual evidence of thermomagnetic hysteresis, implying that the phase transition is indeed first-order in nature. The magnetic field dependence of the volume fraction of the AST phase fits with an equation representing the Kolmogorov–Johnson–Mehl– Avrami (KJMA) relation [5.11] (originally proposed for study of crystallization of solids from melts), which suggests an underlying nucleation and growth mechanism of the phase transition. The local $M(H)$ loops constructed from the Hall images indicate the presence of a landscape of critical magnetic fields (for the MST–AST phase transition) distributed over the sample volume and thus confirm the disorder-influenced nature of the phase transition. In addition, the present results suggest that the functional properties (magnetoresistance (MR) and magnetocaloric effect (MCE) etc.) of $Ni_{50}Mn_{34}In_{16}$ will depend on the thermomagnetic history of the sample. In the present Chapter we also show from experimental results that the magnitude and reversibility of the functional properties under application of a magnetic field, depend on the thermomagnetic history of the sample.

5.1 Influence of disorder on the martensite-austenite phase transition in $Ni_{50}Mn_{34}In_{16}$ alloy

In the following discussion we explore the disorder broadened first-order nature of the temperature and magnetic field induced MST -AST phase transition in $Ni_{50}Mn_{34}In_{16}$ alloy.

5.1.1 Temperature dependence of magnetization in the $Ni_{50}Mn_{34}In_{16}$ alloy

In section 3.1.3 of Chapter 3 it was mentioned that in $Ni_{50}Mn_{34}In_{16}$ alloy the onset temperature of AST to MST phase transition (T_{MS}) while cooling is higher than the onset temperature of MST to AST phase transition (T_{AS}) while heating the sample. This can also be seen in Fig. 5.1, which presents the temperature (T) dependence of magnetization (M) of $Ni_{50}Mn_{34}In_{16}$ alloy measured in a magnetic field (H) of 10 kOe in the field-cooled cooling (FCC) and field-cooled warming (FCW) protocols. The temperatures T_{MF} and T_{AF} are respectively the

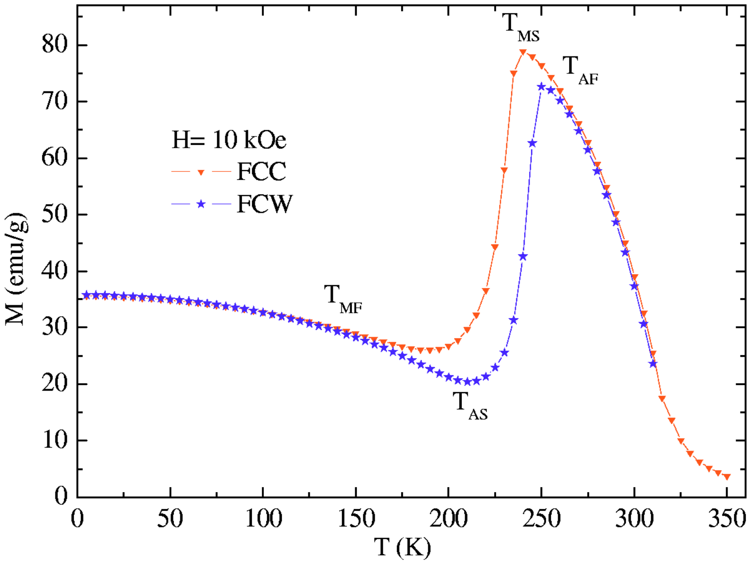

Fig. 5.1: Temperature (T) dependence of magnetization (M) for the $Ni_{50}Mn_{34}In_{16}$ alloy in 10 kOe magnetic field.

limits of supercooling (of the AST phase) and superheating (of the MST phase) and are identified as the temperature where the thermal hysteresis ceases to exist in the cooling and warming temperature path. These characteristic temperatures of the MST-AST phase transition in the alloy are marked in Fig. 5.1. In H = 10 kOe clearly $T_{MS}>T_{AS}$. This is true for all magnetic field values (Fig. 3.4 of Chapter 3).

5.1.2 Magnetic field dependence of magnetization in the $Ni_{50}Mn_{34}In_{16}$ alloy

Fig. 5.2 presents selected isothermal *M* vs. *H* curves for the $Ni_{50}Mn_{34}In_{16}$ alloy. For each isothermal *M*(*H*) measurement, the respective temperature was approached from 300 K in zero field. As discussed earlier (section 3.1.5 of Chapter 3), away from the temperature regime of the MT, the isothermal *M*(*H*) curves are that of a soft ferromagnet. But the isothermal *M*(*H*) curves

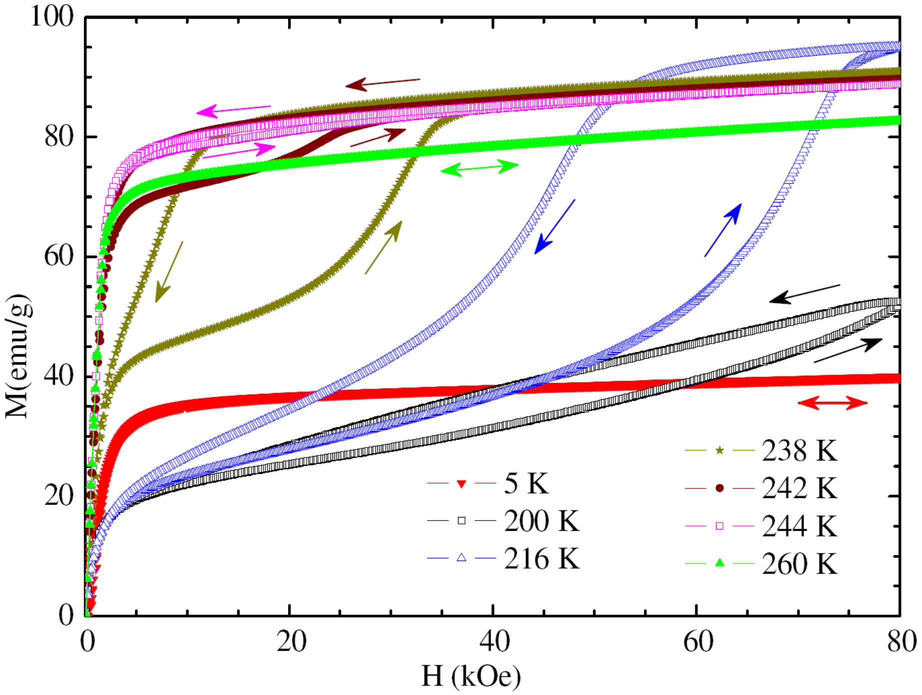

Fig. 5.2: Isothermal magnetization (*M*) vs. magnetic field (*H*) curves of the $Ni_{50}Mn_{34}In_{16}$ alloy at representative temperatures.

in the temperature regime of the MT show an additional rise in *M* above a critical *H*. The distinct rise in *M* with increasing *H* and the associated magnetic field-hysteresis signify a magnetic field induced first-order phase transition from the MST phase to the AST phase. The signatures of the magnetic field induced MST to AST phase transition mentioned above are observed more clearly in the *M*(*H*) curves in the T-regime 200-242K.

5.1.3 *H*/*M* vs. M^2 plots in the $Ni_{50}Mn_{34}In_{16}$ alloy

Fig. 5.3 shows representative *H*/*M* vs. M^2 curves of the $Ni_{50}Mn_{34}In_{16}$ alloy across the AST to MST phase transition (200-244 K). The *H*/*M* vs. M^2 curves were drawn using the increasing magnetic field portions of the isothermal *M*(*H*) curves. The negative slope region in the *H*/*M* vs. M^2 curves in the temperature range 200-238 K corresponds to the portion of *M*(*H*)

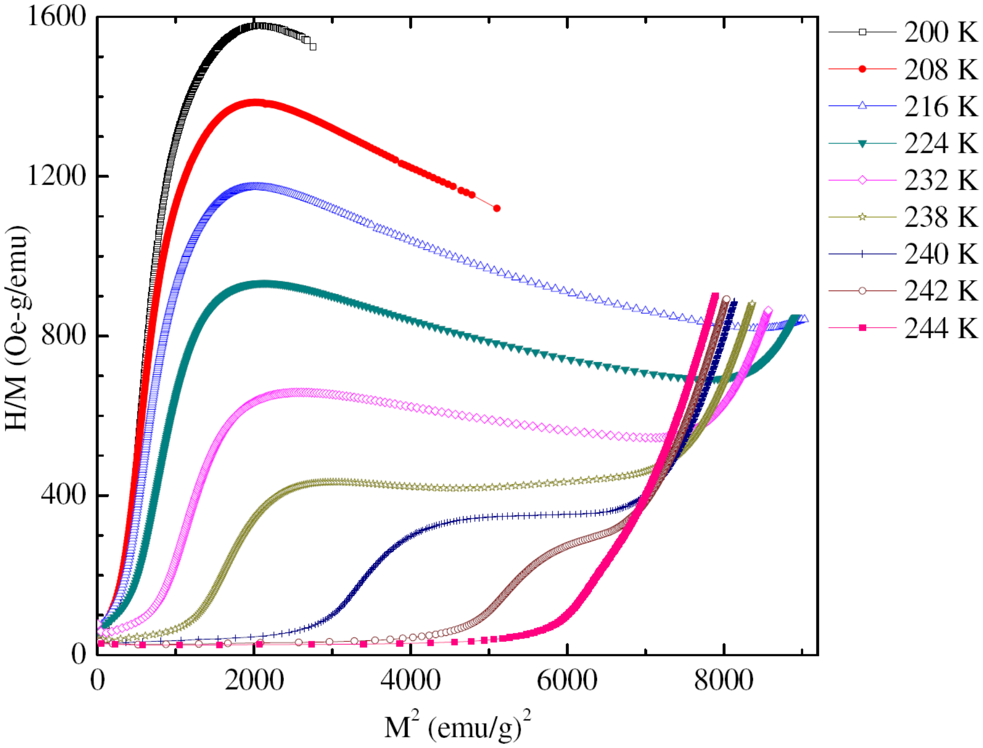

Fig. 5.3: Isothermal *H*/*M* vs. M^2 plots at representative temperatures across the martensitic transition in the $Ni_{50}Mn_{34}In_{16}$ alloy.

curves that represent a magnetic field induced first-order MST to AST phase transition. But in the temperature range 240-244 K, though the isothermal $M(H)$ curves show the signatures (explained in the preceding sub-section) of a first-order magnetic field induced MST to AST phase transition, the H/M vs. M^2 isotherms do not exhibit any negative slope. In this temperature regime, a decrease of slope of the H/M vs. M^2 curves is found to correspond to the magnetic field induced first-order MST to AST phase transition.

It has been shown theoretically that in systems undergoing a magnetic field induced first-order paramagnetic to ferromagnetic phase transition, the slope of the H/M vs. M^2 curves should be negative [5.2]. The negative slope of H/M vs. M^2 isotherms in such systems is found to decrease gradually as T approaches the zero-field transition temperature [5.4-5.8]. Such decrease in the magnitude of the negative slope of H/M vs. M^2 isotherms is also observed across the magnetic field induced first-order antiferromagnetic to ferromagnetic phase transition [5.3]. On the other hand, the absence of negative slope of H/M vs. M^2 isotherms across a magnetic field induced first-order magnetic transition, as observed here, is also reported in certain compositions of ferromagnetic shape memory alloy Ni-Mn-Ga [5.9], and in another composition of the Ni-Mn-In alloy system viz. $Ni_{50}Mn_{35}In_{15}$ [5.12]. In Ni-Mn-Ga, as the temperature approaches a characteristic temperature, the negative slope of the H/M vs. M^2 curves changes to a decrease of slope with an overall positive value across a paramagnetic to ferromagnetic phase transition (see Ref. 5.9, and Fig. 5(a) therein) as well as a ferromagnetic to ferromagnetic phase transition (see Ref. 5.9, and Fig. 3(a) therein).

5.1.4 Characteristic magnetic fields and temperatures of the field-induced martensite to austenite phase transition in the $Ni_{50}Mn_{34}In_{16}$ alloy

Instead of using the H/M vs. M^2 plots, the first-order AST-MST phase transition in the $Ni_{50}Mn_{34}In_{16}$ alloy may be investigated in another way: We examine the temperature and magnetic field dependence of various characteristic parameters related to the first-order AST-MST phase transition in $Ni_{50}Mn_{34}In_{16}$ alloy. The width of the transition (see Fig. 5.1) suggests that the transition is broadened by quenched disorder (see section 1.3.4 of Chapter 1 for a discussion on this topic), probably created during alloy formation. The disorder-influenced broadening of a first-order phase transition leads to a distribution of transition temperatures over the sample volume [5.13]. As a result, the phase transition line then broadens into a band [5.14-5.16]. The AST to MST phase transition region in $Ni_{50}Mn_{34}In_{16}$ alloy with the lowering of temperature (see Fig. 5.1) extends from the temperature of MST start (T_{MS}) to the MST finish temperature (T_{MF}). As T decreases from T_{MS} to T_{MF}, the MST phase fraction increases from 0 to 1 and the AST phase fraction decreases from 1 to 0 [5.17]. Similarly the MST to AST phase transition with increasing temperature extends from the temperature of AST start (T_{AS}) to the temperature of AST finish (T_{AF}). Coexistence of MST and AST phases is observed in the temperature ranges T_{MS} - T_{MF} and T_{AS} - T_{AF}. The temperatures T_{MF} and T_{AF} are respectively the limits of supercooling (of the AST phase) and superheating (of the MST phase) [5.18]. In section 3.1.3 of Chapter 3 we have noted that in the $Ni_{50}Mn_{34}In_{16}$ alloy T_{MS}, T_{MF}, T_{AS} and T_{AF} decrease with increasing magnetic field.

Similar to the case of a temperature driven transition, the magnetic field driven transition will also have a band of transition fields in the presence of disorder leading to a region of phase

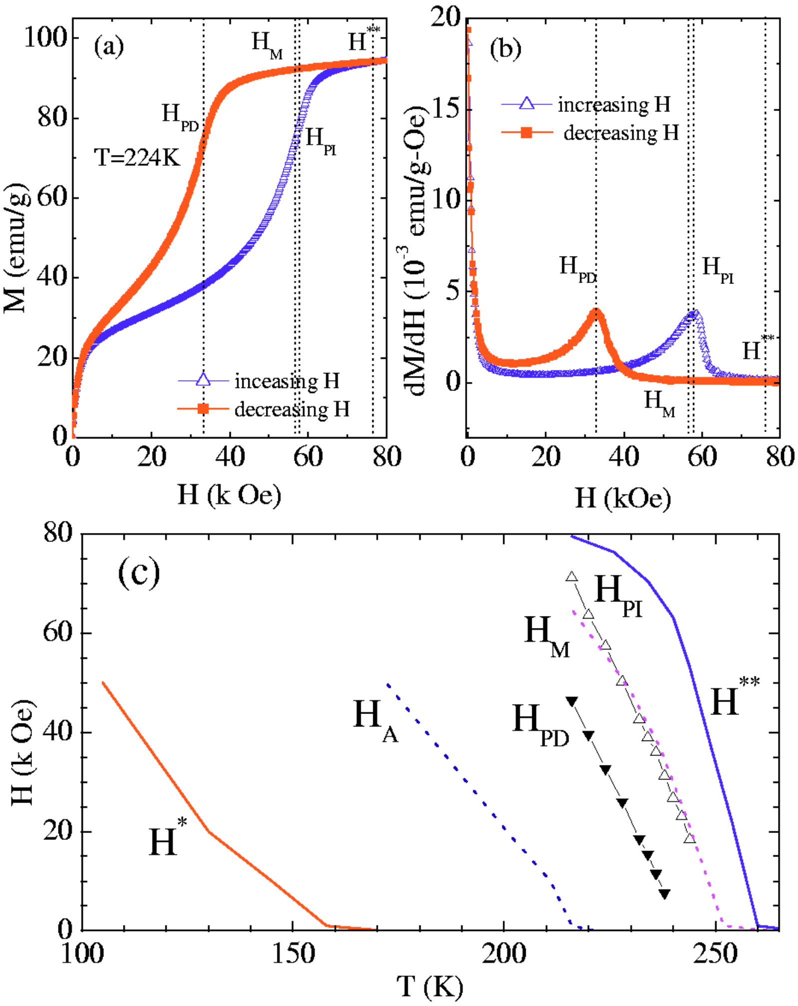

Fig. 5.4: (a) Isothermal magnetization (*M*) vs. magnetic field (*H*) plot at 224 K for $Ni_{50}Mn_{34}In_{16}$ alloy and (b) the corresponding d*M*/d*H* vs. *H* plot. The dotted lines denote the value of the characteristic magnetic field values on the magnetic field axis. (c) Temperature dependence of various characteristic magnetic fields across the martensitic transition in the alloy.

coexistence [5.16]. This is visible in Fig. 5.2 where the MST-AST phase transition occurs isothermally over a width of applied magnetic field. We therefore characterize the magnetic field induced disorder-broadened first-order magnetic transition in $Ni_{50}Mn_{34}In_{16}$ alloy by defining the characteristic magnetic fields of the transition. Figs. 5.4(a) and 5.4(b) present the *M* vs. *H* curve and the corresponding d*M*/d*H* vs. *H* curve at a representative temperature 224 K. When 224 K is approached from 300 K in zero field, both the MST and AST phases are present in the sample as this temperature is lower than T_{MS} but higher than T_{MF} in zero field. Now, as the magnetic field increases M increases towards saturation due to domain alignment (MST and AST phases are ferromagnetic in nature) and dM/dH decreases. Further increase in magnetic field leads to the transformation of the initial MST phase to the AST phase and as a result M as well as dM/dH increases (it has been discussed earlier that the AST phase has higher M value than the MST phase). At a certain magnetic field, the rate of the MST to AST phase transformation is maximum. This gives rise to a peak in dM/dH, and this magnetic field value is marked as H_{PI}. At sufficient high magnetic field, the MST to AST phase transition is complete and $M(H)$ reaches saturation. Above this field value, $M(H)$ and dM/dH for the increasing magnetic field cycle are indistinguishable from those for the decreasing magnetic field cycle. This field value is marked as H^{**} and is the limit of metastability (superheating [5.18]) of the MST phase at this temperature. As the field is now decreased, the AST phase is stable up to a field marked as H_M where the start of the AST to MST phase transition is accompanied by a decrease in M and a corresponding increase in dM/dH. At certain lower field value, the rate of transformation from the AST to MST phase is maximum. This produces a peak in dM/dH and this field value is marked as H_{PD}. As the field decreases to zero we are back in the phase coexistence regime because the AST to MST phase transition is not completed in zero field at T > 170K (this temperature has been estimated from low field M-T results; see Fig. 3.4(f) of Chapter 3). It may be observed that Fig. 5.4(a) or 5.4(b) cannot give the estimate of the magnetic field H_A corresponding to the start of MST to AST phase transition with increasing magnetic field because in zero field, in the beginning of the field increasing experiment, we are already in the phase coexistence region (see Fig. 3.4(f) of Chapter 3). Similarly at the end of the field decreasing experiment, in zero field, the sample is again in the phase coexistence region and we cannot reach the magnetic field H^*, the limit of metastability (supercooling [5.18]) of the AST phase. H_A and H^* can be estimated from the $M(H)$ curves for temperatures below 170 K where only the MST phase exits in zero field. However, the characteristic magnetic fields H_M, H^*, H_A and H^{**} can also be estimated from the $M(T)$ results obtained in various constant applied magnetic fields as the curves $H_M(T)$, $H^*(T)$, $H_A(T)$ and $H^{**}(T)$ should be identical with the curves $T_{MS}(H)$, $\mathrm{T_{MF}(H)}$, $T_{AS}(H)$ and $T_{AF}(H)$ respectively. The temperature dependence of the characteristic magnetic fields H_M, H^*, H_A and H^{**}, or the magnetic field dependence of the characteristic temperatures T_{MS}, T_{MF}, T_{AS} and T_{AF}, constitute the H-T phase diagram of the alloy. In Fig. 5.4(c) we present the temperature dependence of the characteristic field values of the first-order phase transition in $Ni_{50}Mn_{34}In_{16}$ alloy, determined from the isothermal $M(H)$ curves and the isofield $M(T)$ results. It is observed in Fig. 5.4(c) that while the H_{PI} curve is closer to H^{**} as compared to the H_A curve, the H_{PD} curve lies closer to H_M as compared to H^*. This is related to the shape of $M(H)$ curves with increasing and decreasing magnetic fields across the transition (see Fig. 5.2).

We note in Fig. 5.4(c) that H_{PI} and H_{PD} have approximately linear T dependence. Earlier, while analyzing the magnetic field induced first-order magnetic transitions with the help of the negative slope of the H/M vs. M^2 curves [5.2], the characteristic magnetic field H_{PI} was predicted to increase with temperature [5.8]. Such temperature dependence of the characteristic magnetic fields was observed in the first-order paramagnetic-ferromagnetic phase transitions in various systems like manganites [5.8], Ni-Mn-Ga [5.9], MnAs [5.19], $Gd_5Si_{1.7}Ge_{2.3}$[5.20] and also in the ferromagnetic-ferromagnetic phase transition in Ni-Mn-Ga [5.9]. But H_{PI} as well as all the other characteristic magnetic fields of $Ni_{50}Mn_{34}In_{16}$ alloy exhibit a totally different T dependence, e.g. they have a negative slope. The negative slope of the characteristic magnetic field in $Ni_{50}Mn_{34}In_{16}$ alloy is related to the fact that transition temperature in $Ni_{50}Mn_{34}In_{16}$ alloy shifts towards lower T with increasing magnetic field. Similar T dependence of the characteristic magnetic fields has been observed across the antiferromagnetic-ferromagnetic transition in Ru doped $CeFe_2$ alloys [5.21].

5.1.5 Analysis of the slope of the H/M vs. M^2 plots and the temperature dependence of the characteristic magnetic fields

The possible explanation for the above observations in the $Ni_{50}Mn_{34}In_{16}$ alloy is as follows. It is worthwhile to note that the criterion of negative slope in the H/M vs. M^2 isotherms was inferred from the theory of first-order magnetic phase transitions, where spontaneous magnetization is the appropriate order parameter. In the case of Ni-Mn-Ga [5.9], spontaneous magnetization is the relevant order parameter for the first-order paramagnetic-ferromagnetic transition. But spontaneous magnetization is not the suitable order parameter for the first-order transition from one ferromagnetic to another ferromagnetic phase in $Ni_{50}Mn_{34}In_{16}$ alloy. However, irrespective of this difference, an ideal first-order magnetic transition should exhibit a discontinuity in magnetization [5.22]. If M increases discontinuously (or very sharply) across the transition with increasing H, the slope of H/M vs. M^2 curves would become negative. In the case of a disorder broadened first-order transition this discontinuity smears out [5.13]. The present experimental data and similar results on Ni-Mn-Ga [5.9] suggest that even in the case of broadened first-order transition the increase of M with increasing H becomes relatively faster in the transition region. This results in a decrease in the slope of the H/M vs. M^2 curves, and the decrease may or may not lead to a negative slope in the H/M vs. M^2 isotherm. In $Ni_{50}Mn_{34}In_{16}$, starting from a temperature (300 K in the protocol adopted for measurement of isothermal M-H curves) well above the martensitic transition region, as the temperature is decreased the phase fraction of MST (AST) phase increases (decreases) from 0 to 1 (1 to 0) as the temperature decreases from T_{MS} to T_{MF} [5.17]. This MST phase transforms back to AST phase under the application of magnetic field. The increase in M with increasing H because of this magnetic field induced phase transition would depend upon the amount of initial MST phase (at $H = 0$) as well as the difference in M between the MST and AST phases. We have noted earlier that the MST and AST phases in the $Ni_{50}Mn_{34}In_{16}$ alloy have a large difference in M. Also the amount of MST phase formed, in the temperature region T_{MF} - T_{MS}, decreases with increasing temperature (see Fig. 5.4(c)). At lower temperatures (within the T range T_{MF} - T_{MS}), the initial amount of MST phase formed is larger and the magnetic field induced MST to AST phase transition gives larger change in M with increasing H and this effectively makes the slope of H/M vs. M^2 isotherm negative. Closer is the temperature to T_{MS}, relatively smaller is the amount of MST phase formed initially. With smaller initial MST phase fraction, the magnetic field induced phase transition becomes less effective in changing the slope of the H/M vs. M^2 isotherms. Thus the absence of a negative slope in H/M vs. M^2 isotherms in the temperature regime where isothermal $M(H)$ curves depict clear signatures of a first-order magnetic transition, is correlated with the disorder broadened nature of the first-order phase transition.

Now we investigate the possible cause of negative slope in temperature dependence of the characteristic magnetic fields H_{M}, H_{PD}, H^*, H_{A}, H_{PI} and H^{**} in $Ni_{50}Mn_{34}In_{16}$. In systems where the characteristic magnetic field increases with temperature [5.8, 5.9, 5.19, 5.20], the higher temperature phase has a lower magnetization value. On the other hand in $Ni_{50}Mn_{34}In_{16}$ the lower temperature phase (MST) has a lower magnetization. Similarly in the case of the first-order antiferromagnetic-ferromagnetic phase transition in Ru doped $CeFe_2$ [5.3, 5.21, 5.23] the lower temperature antiferromagnetic phase has a lower magnetization, and therefore the characteristic magnetic fields have a negative slope in the *T* dependence. In fact these results are in accord with the Clausius-Clapeyron equation for a first-order magnetic transition [5.19]:

$$\left(\frac{dT}{dH}\right)_P = -\frac{T\Delta M}{L_Q} \qquad (5.1)$$

Here $L_Q = T\Delta S$, ΔS being the entropy change during the transition. Applying eqn. (5.1) in the case of a magnetic field induced first-order magnetic transition we find that if the higher (lower) temperature phase has higher (lower) magnetization value, then the transition temperature will decrease with increasing magnetic field, and as a result the characteristic magnetic fields for the isothermal transition will have negative temperature dependence. Moreover, eqn. (5.1) gives only single value of d*T*/d*H*, while from Fig. 5.4 it is clear that the various characteristic temperatures of MST-AST phase transition in present alloy have different values of d*T*/d*H*. From present work it appears that in the case of the disorder broadened first-order phase transitions, though the Clausius– Clapeyron equation predicts the nature of the slope of the phase transition lines, an exact quantitative result is rather difficult to obtain.

5.2 Imaging the magnetic field induced martensite-austenite phase transition in the $Ni_{50}Mn_{34}In_{16}$ alloy

In the previous sections it has been discussed that the MST-AST phase transition in $Ni_{50}Mn_{34}In_{16}$ alloy is a disorder-influenced first-order phase transition. Thermomagnetic hysteresis is a generic feature of a disorder-influenced first-order phase transition and has been observed in various classes of magnetic systems undergoing a first-order magneto-structural transition [5.10]. Scanning Hall probe imaging experiments have been very useful in the investigation of such magnetic systems, revealing clear phase coexistence and metastability across the first-order phase transition [5.24, 5.25]. To get the visual evidence of phase coexistence across the MST-AST phase transition in $Ni_{50}Mn_{34}In_{16}$ alloy implying that the transition is indeed disorder broadened first-order phase transition in nature, we have performed scanning Hall probe imaging of the magnetic field induced MST–AST phase transition in $Ni_{50}Mn_{34}In_{16}$ alloy.

5.2.1 Scanning Hall probe imaging study of the magnetic field induced phase transition

We have chosen 236 K as the most appropriate temperature to capture images of the phase transition as this temperature is within the MST-AST phase coexistence regime (see Fig. 5.5 which is a part of H-T phase diagram of Fig. 5.4(c) and is presented separately for clarity). Also, the maximum magnetic field that can be applied in our scanning Hall probe imaging experimental set-up is 40 kOe. At 236 K, the magnetic field induced transition is nearly completed in 40 kOe magnetic field. Two different protocols were adopted to reach the temperature 236 K:

(i) In the protocol P1, the sample was cooled from 300 K in zero magnetic field down to 236 K without undershooting the target temperature. The scanning Hall probe imaging experiments were performed at constant temperature first in the increasing magnetic field cycle (up to 40 kOe) and then in the decreasing magnetic field cycle (down to zero).

(ii) In the protocol P2, the sample was cooled in zero magnetic field from 300 K to 30 K. Then the sample was warmed up to 236 K without overshooting the target temperature, and subsequently the scanning Hall probe imaging was performed at constant temperature in the increasing and decreasing magnetic field cycles .

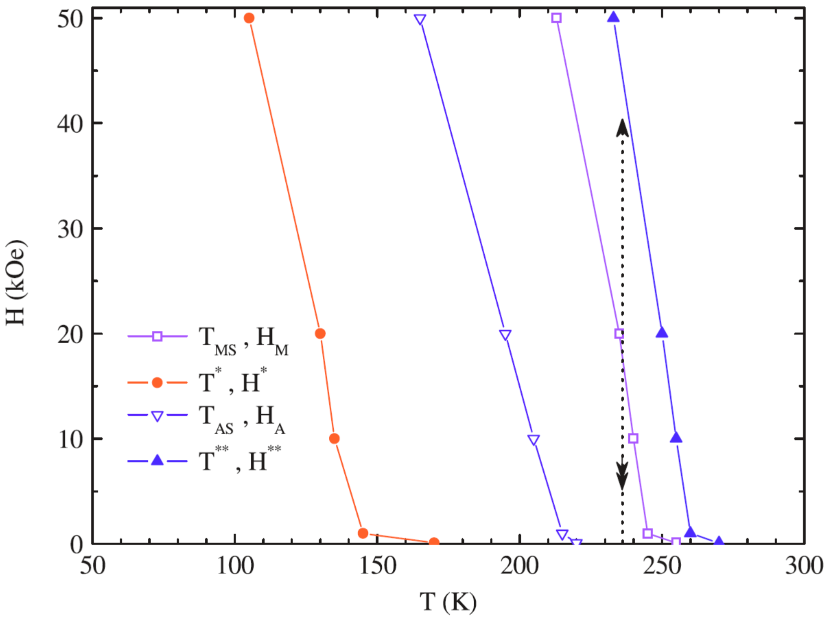

Fig. 5.5: The magnetic field (*H*)–temperature (*T*) phase diagram of the $Ni_{50}Mn_{34}In_{16}$ alloy. The dotted line in the *H–T* phase diagram depicts the path on which the scanning Hall probe imaging experiments were performed in the increasing and decreasing magnetic field cycles at 236 K. The single arrowhead shows the increasing magnetic field path and the double arrowhead shows the decreasing magnetic field path.

We have already seen that the magnetization of the MST phase is lower than that of the AST phase (see Fig. 5.1). To differentiate between the MST and AST phases in Hall voltage profile, we have chosen a voltage threshold such that the voltages below this threshold represent the MST phase, and the voltages higher than this threshold represent the AST phase. Since the magnetic field induced MST to AST phase transition is nearly complete in 40 kOe magnetic field at 236 K (see Fig. 5.5), we have taken the whole sample to be in the AST phase in 40 kOe field at this temperature. We have taken the Hall voltage threshold at 50% of the maximum in Hall voltage profile in 40 kOe magnetic field. The same voltage threshold has been used in both the protocols P1 and P2. The colour figures thus obtained in both the protocols in the increasing (H↑) and decreasing magnetic field (H↓) cycles are shown in Fig. 5.6. Here, the yellow regions represent the AST phase, and the black regions represent the MST phase. The field of view for imaging was larger than the sample size. Once the background (due to the applied magnetic

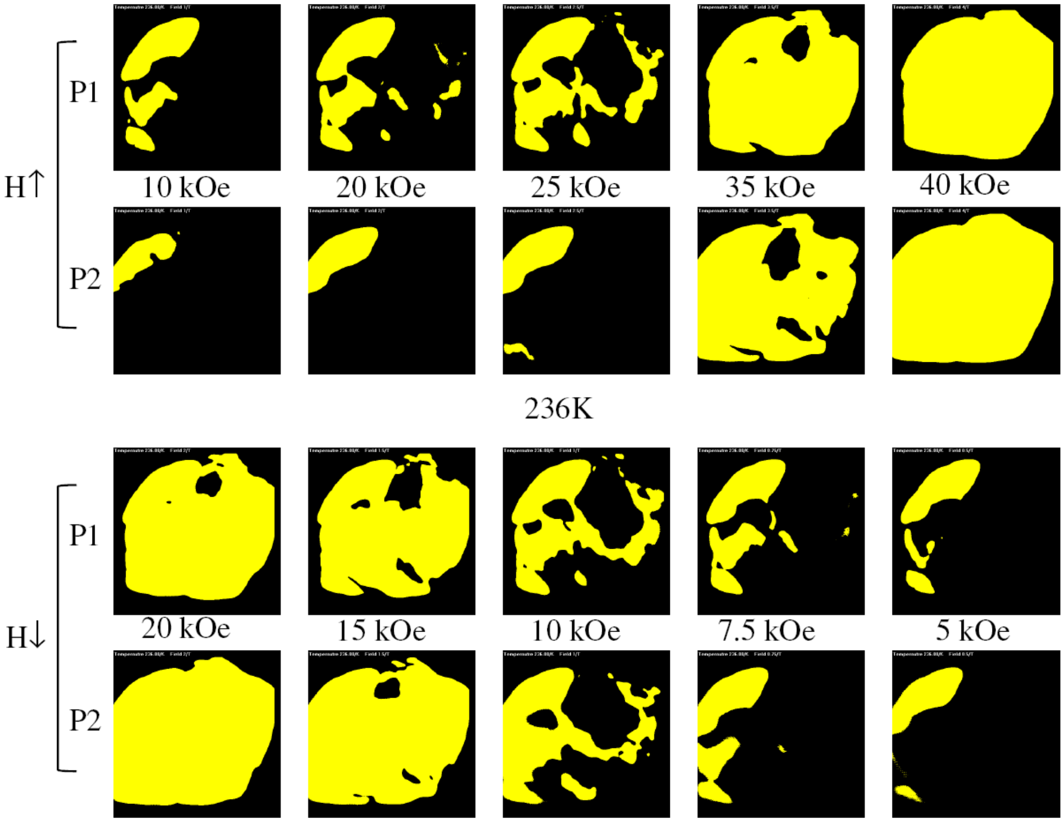

Fig. 5.6: Scanning Hall probe images of the $Ni_{50}Mn_{34}In_{16}$ alloy in different magnetic fields at 236 K in two different protocols, P1 and P2. The Hall images were taken in increasing (H↑) and decreasing (H↓) magnetic field cycles. In the Hall images, the yellow regions represent the austenite phase and the black regions represent the martensite phase. The region beyond the sample edges is also black.

field) was removed, this also produced a black region around the periphery of the sample which simply defines the edge of the sample.

As the magnetic field is increased from zero to 10 kOe at 236 K, some portions of the images show yellow colour indicating that the MST to AST phase transition has started in these regions of the sample. From Fig. 5.6 it is clearly seen that the amount of the AST phase in H = 10 kOe is larger in protocol P1. With increasing magnetic field, newer yellow patches appear and the existing yellow patches grow in area indicating the nucleation and growth of the AST phase. Finally the entire sample is yellow in 40 kOe magnetic field for both the protocols P1 and P2. However, the nucleation and growth kinetics of the MST to AST phase transformation is slower in the protocol P2 for magnetic fields up to 25 kOe. Above this field, the MST to AST phase transformation is much faster in the protocol P2 as compared to the protocol P1. In the decreasing field cycle, the MST phase appears as black spots and the nucleation and growth of the MST phase is clearly seen in the lower panel of Fig. 5.6. The nucleation and growth kinetics of the AST to MST phase transition in both the protocols P1 and P2 appear to be quite similar as the field is decreased from 40 kOe to zero. The transition becomes quite slow in the low fields and some AST phase remains un-transformed in fields down to 5 kOe in both the protocols. Thus Fig. 5.6 actually shows the snap-shots of the coexistence of MST and AST phases on the length scale of tens of micrometers, extended over a very wide regime of magnetic field. Comparison of the top and bottom panels of Fig. 5.6 also confirms the magnetic field hysteresis associated with this magnetic field induced phase transition (for example compare the Hall images taken in 20 kOe magnetic field, in the increasing and decreasing magnetic field cycles). It is also observed in Fig. 5.6 that the region of sample where the MST to AST phase transition starts first (last) in increasing magnetic field cycle, is also the region where AST to MST phase transition starts at last (first) in decreasing magnetic field cycle. This shows that the hysteresis associated with the magnetic field induced MST-AST phase transition is influenced by microscopic characteristics (disorder, strain, etc.) specific to particular microscopic regions of the sample.

To investigate further into the magnetic field induced MST–AST phase transition, we estimate the volume fractions of the AST and MST phases as a function of magnetic field in both the protocols. In Fig. 5.6, the area of the yellow region in the images is a measure of the volume of the AST phase (VF_{AST}). To calculate VF_{AST}, we normalize the area of yellow region in an image with the area of the yellow region in the scanning Hall probe image obtained in 40 kOe magnetic field. The volume fraction of the MST phase (VF_{MST}) is related to the VF_{AST} through the relation: VF_{AST} (%) + VF_{MST} (%) = 100. The volume fraction thus calculated is not an exact quantitative estimate since the MST and AST micro-regions beneath the surface of the sample also contribute to the Hall voltage profile in varying amounts depending on their depth. Hence the VF_{AST} estimated from Hall images is only representative of the actual phase distribution in the bulk sample. The contribution from the MST/AST regions to Hall voltage profile also depends on their length scale relative to the resolution of Hall probe. If the length scale of MST-AST phase coexistence is smaller than the resolution of scanning Hall probe (nearly 10 μm in present case), the probe will sense effective magnetization averaged over a pixel. This also contributes to the uncertainty in the estimated VF_{AST}. Moreover, at low magnetic fields the local magnetization may not be fully aligned with the field due to anisotropy and/or domain wall pinning, and our scanning Hall probe senses the component of local magnetic induction perpendicular to the sample surface. Nevertheless we are able to make qualitative measure of the behaviour across this magnetic field induced transition.

The magnetic field dependence of the volume fractions of AST and MST phases is presented in Fig. 5.7. As indicated by Hall images in 10 kOe magnetic field in the increasing magnetic field cycle, the amount of AST phase is larger in protocol P1. The difference in the kinetics of the MST to AST phase transition in the protocols P1 and P2 with increasing magnetic field is clearly seen in Fig. 5.7. With decreasing magnetic field there is very little change in VF_{AST} till 20 kOe, and below this magnetic field the rate of change of VF_{AST} is enhanced appreciably. The magnetic field dependence of VF_{AST} with decreasing magnetic field for the two protocols P1 and P2 are qualitatively similar, which is in contrast with the increasing field cycle discussed above.

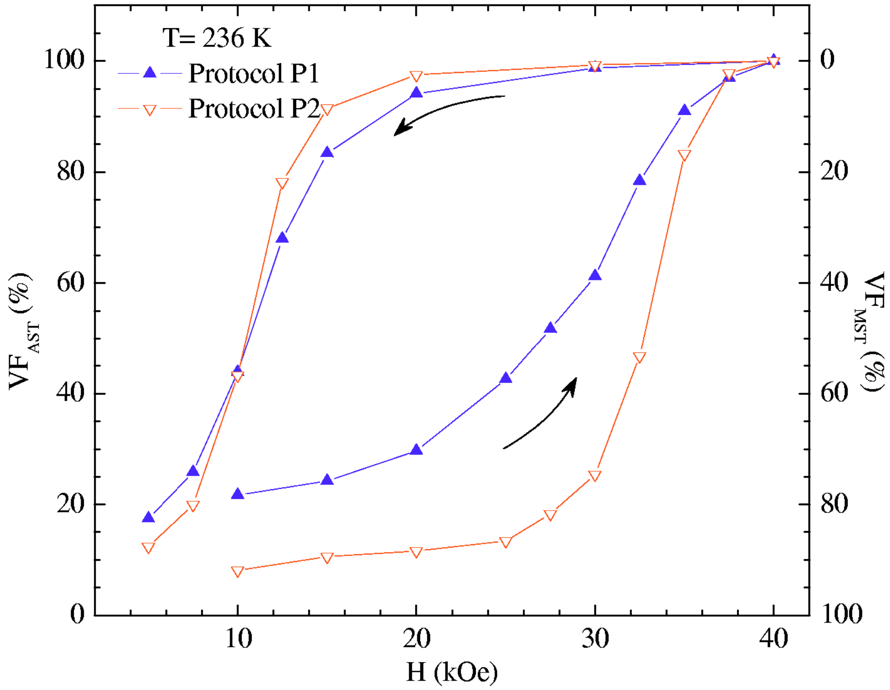

Fig. 5.7: Isothermal magnetic field (*H*) dependence of the volume fraction of the austenite (VF_{AST}) and martensite (VF_{MST}) phases in the $Ni_{50}Mn_{34}In_{16}$ alloy at 236 K in two different protocols.

We will see in the next section (section 5.3) that the *M*(*H*) behaviour of $Ni_{50}Mn_{34}In_{16}$ across the AST-MST phase transition and the functional properties exhibited by this alloy sample across this phase transition are strongly dependent on the experimental protocol. These observations suggest that the kinetics of the magnetic field induced MST to AST phase transition in the $Ni_{50}Mn_{34}In_{16}$ alloy is affected by the thermomagnetic history of the sample. The protocols P1 and P2 were adopted to investigate, the effects of such thermomagnetic history on the magnetic field induced transition in this alloy. In the protocol P2, 236 K is reached after crossing the T_{AS} or H_A line. As this line is crossed, the MST to AST phase transformation is initiated. At 236 K, the AST phase is the equilibrium configuration at $H = 0$, and the MST phase is metastable (superheated) [5.18]. As the field is raised above 30 kOe under the protocol P2, the system goes very close to the limit of superheating [5.18] T^{**} or H^{**}. The rate of the MST to AST transformation is very high in this field regime and this is in harmony with our earlier finding that the rate of a first-order magnetic phase transformation increases rapidly when the system goes close to the spinodal limit [5.16, 5.26]. This phenomenon has earlier been observed across the first-order antiferromagnetic-ferromagnetic phase transition in 4% Ru doped $CeFe_2$ alloy [5.16] and across a magnetic field induced first-order phase transition in vortex matter [5.26]. In the protocol P1, on the other hand, 236 K is reached after crossing the T_{MS} or H_M line. At $H = 0$ and $T = 236$ K in the protocol P1, part of the sample is in the equilibrium MST phase and the remaining part is in the supercooled (metastable) [5.18] AST phase. As the field is increased, however, the situation is changed altogether. The system now moves towards the limit of superheating [5.18] of the MST phase. In this route the AST phase is the equilibrium state, and the MST phase is metastable. The field increasing path in protocol P1 causes a kind of reversal of the kinetics of the phase transition, and thus probably introduces a large disturbance in the system. This kinetics is different from that of protocol P2, and accordingly, the behaviour of the system in protocol P1 is different from that of P2 in the field increasing cycle. In both the protocols P1 and P2, the system is very close to the limit of superheating (T^{**} or H^{**}) at $H = 40$ kOe. When the field is decreased from 40 kOe, there is no path difference (in the H-T phase space) between the two protocols and accordingly the kinetics of the phase transition is similar in both the protocols (Figs. 5.6 and 5.7). The AST to MST phase transition is initiated below 20 kOe when the system crosses the T_{MS} or H_M line in both the protocols. The present scanning Hall probe microscopy images suggests that the functional properties of the alloy will depend on the protocol used for changing the field and temperature because of the relative volume fractions of the MST and AST phases present in the alloy. It is clear from Fig. 5.6 and 5.7 that these volume fractions are strongly dependent on the path traversed by the system in the *H-T* phase space.

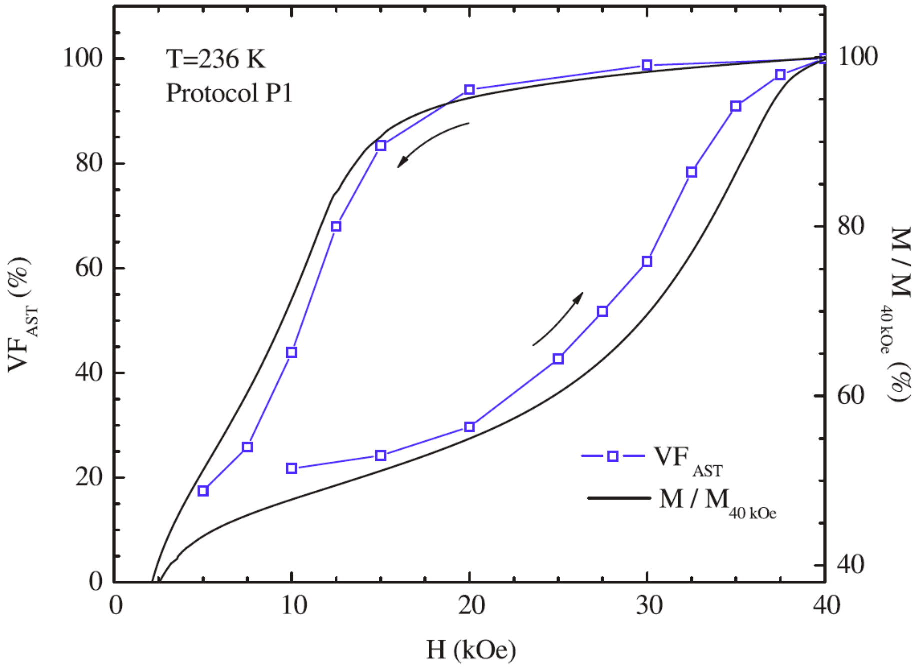

Fig. 5.8: Comparison of the isothermal magnetic field (*H*) dependence of the volume fraction of the austenite phase ($\mathrm{VF_{AST}}$) and the normalized magnetization ($M/M_{40\ \mathrm{kOe}}$) of $\mathrm{Ni_{50}Mn_{34}In_{16}}$ alloy at 236 K in protocol P1.

It is observed in Fig. 5.7 that the magnetic field dependence of volume fractions of the AST and MST phases exhibits a distinct magnetic hysteresis with increasing and decreasing magnetic fields. To compare it with the hysteresis observed in the magnetic field dependence of global magnetization, $\mathrm{VF_{AST}}$ was plotted along with the normalised $M(H)$ curve obtained in the protocol P1 at $T = 236$ K. The $\mathrm{VF_{AST}}\,(H)$ curve is qualitatively similar to the $M(H)$ curve (see Fig. 5.8 for protocol P1; magnetization is normalized with the magnetization at 40 kOe magnetic field). The data for the protocol P2 is not presented here for conciseness. The observation that $\mathrm{VF_{AST}}$ and normalized M have similar magnetic field dependence confirms that the width of the magnetic field induced MST–AST phase transition observed in the global field dependence of magnetization (and other bulk observables) is due to the nucleation and growth kinetics of this disorder broadened phase transition. It also confirms that the defined threshold voltage used to construct the scanning Hall probe images is realistic.

5.2.2 Nucleation and growth mechanism of the martensite-austenite phase transition in the $Ni_{50}Mn_{34}In_{16}$ alloy

We further attempt a quantitative analysis of the evolution of volume fraction of the AST phase as a function of magnetic field. The "S" shape of the magnetic field dependence of volume fraction of the AST phase in Fig. 5.7 resembles the transformation-time curve predicted by Avrami model [5.27] proposed for crystallization of solids. The central assumption of the Avrami model is that the product phase is nucleated by the germ nuclei which are already present in the parent phase. The density of these germ nuclei decreases in two ways. In the first way some of them become active growth nuclei of the product phase. The second way is the swallowing of other germ nuclei by these growth nuclei in the process of growth. The nucleation events are taken to be totally random. The time dependence of phase fraction (f) of the product phase is given by the Kolmogorov–Johnson–Mehl–Avrami (KJMA) relation

$$f = 1 - \exp\left(-kt^{n}\right) \tag{5.2}$$

where k is related to the activation energy and the Avrami exponent n depends on geometrical factors. Originally the model was proposed for isothermal time dependence of evolution of product phase in crystallization from liquid. The model has been extended to temperature and magnetic field dependence of the phase fraction of the product phase for first-order phase transition in doped Fe-Rh alloy [5.28] and following relationship was found suitable for description of the transition.

$$f = 1 - \exp\left(-k\left(T - T_0\right)^{n}\right) \tag{5.3}$$

where for temperature driven transition T_0 is the onset temperature of transition. Similarly, for a magnetic field driven transition the observable T in equation (5.3) can be replaced by H [5.28]. We now check whether the KJMA behaviour is observed in the magnetic field dependence of volume fraction of the AST phase (here the volume fraction is used as the phase fraction). In the original Avrami model or in that used in the Ref. 5.28, there is an onset point of transition i.e. a value of control variable (time/temperature/magnetic field) up to which the phase fraction of product phase is zero. However in the present case even at the minimum value of magnetic field the volume fraction of product AST phase is non-zero as the sample is already in the phase coexistence region at T = 236 K. So we can not apply the Avrami model directly. We have modified the KJMA relation so as to have a finite value of volume fraction of the product phase at zero magnetic field. The modified KJMA equation is:

$$f = 1 - A_1 \exp\left(-kH^n\right) \qquad (5.4)$$

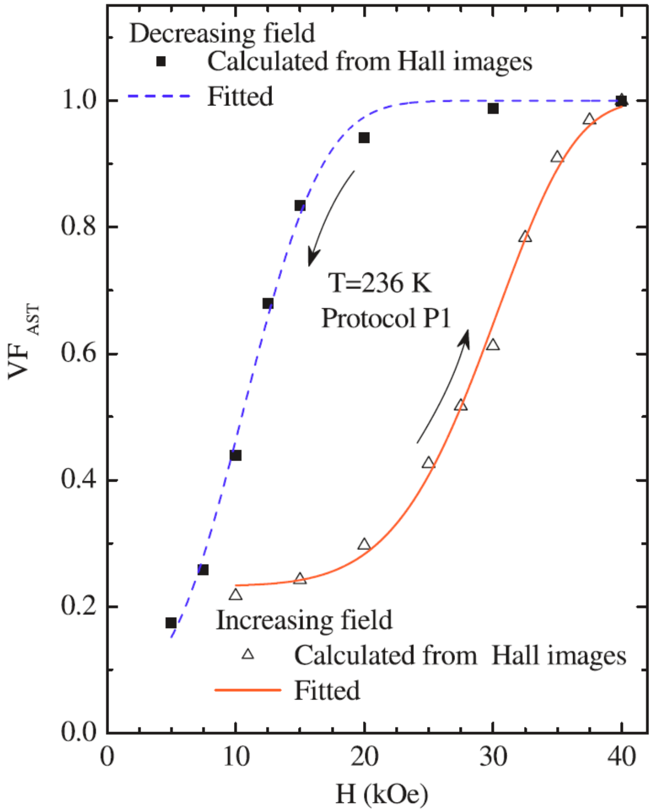

Fig. 5.9: Fitting of the magnetic field (H) dependence of the volume fraction of the austenite phase (VF_{AST}) across the H induced martensite–austenite phase transition at 236 K in protocol P1, using equation (5.4).

where the factor A_1 is included to allow finite non-zero value of phase fraction of AST phase in zero magnetic field. The fitting of equation (5.4) with the magnetic field dependence of VF_{AST} in protocol P1 is presented in Fig. 5.9. Clearly, equation (5.4) fits well with the magnetic field dependence of the volume fraction of the AST phase. The values of A_1 and n (obtained as fitting parameters) on the increasing field cycle are 0.767 and 6.018 respectively. Similarly the values of A_1 and n obtained on the decreasing field cycle are 0.920 and 2.730 respectively. The value of n in decreasing field cycle is comparable to that obtained for the structural transition in doped Fe-Rh alloy in increasing/decreasing field cycle [5.28], but the value of n in increasing field cycle is larger as compared to that in doped Fe-Rh alloy. Recently a similar large value of n (exponent of the control variable) in a KJMA type fit was reported for the temperature driven structural transition in uranium [5.29]. In the present case, the very different values of n in increasing and decreasing field cycle are due to the different shapes of the $VF_{AST}(H)$ curves in increasing and decreasing magnetic field cycles. This may be related with the intrinsic asymmetry between supercooling and superheating in the first-order phase transitions [5.16]. The observation that the volume fraction of AST phase across the magnetic field induced phase transition in the present alloy can be fitted with a KJMA type relation confirms a nucleation and growth mechanism in this magnetic field induced phase transition.

5.2.3 Landscape of transition field across the magnetic field induced martensite-austenite phase transition

We now analyze the Hall images further to explore the local magnetic behaviour of the sample across the magnetic field driven MST-AST phase transition. This is done by tracking the Hall voltage signal coming from the individual pixels which corresponds to 10 μm × 10 μm sample area approximately. The magnetic field dependence of such a voltage signal produces a

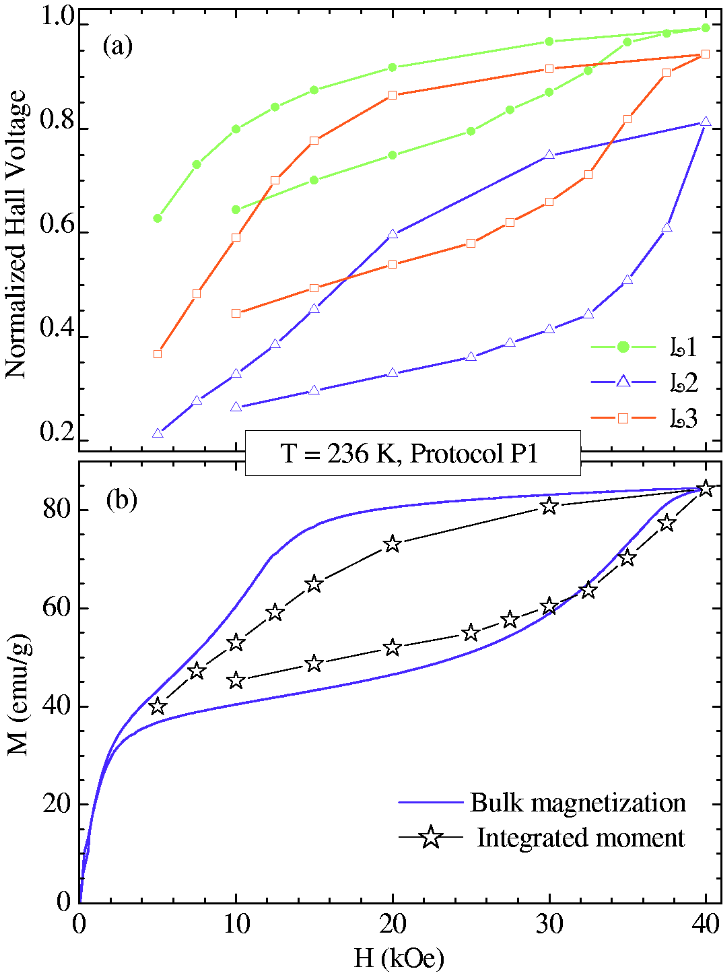

Fig. 5.10: (a) Local Hall voltage vs. magnetic field (*H*) loops at representative sites (ℒ1, ℒ2 and ℒ3) in Hall images at 236 K in protocol P1. The Hall voltage is normalized with its value in a magnetic field of 40 kOe at site ℒ1. (b) Comparison of the *H* dependence of bulk magnetization (*M*) measured using the VSM with the integrated moment calculated from Hall images at 236 K in protocol P1. The integrated moment is normalized with the value of M in a magnetic field of 40 kOe.

local Hall voltage loop. Fig. 5.10(a) presents the local Hall voltage loops corresponding to three representative sites (pixels, named as ℒ1, ℒ2, and ℒ3) on the sample. The Hall voltages in the local loops are normalized to the Hall voltage at the site L1 in 40 kOe magnetic field. It is interesting to observe in Fig. 5.10(a) that while the magnetic field induced MST to AST phase transition is completed well below 40 kOe at the site ℒ1, the transition is probably not completed at the site ℒ2 at $H = 40$ kOe. On the other hand, the transition is very near to completion at the site ℒ3 in the same field value. Further it can be seen that among the three chosen sites, the MST to AST phase transition is completed first in increasing magnetic field cycle for the site ℒ1. But the AST to MST transition at this site starts at the last in the decreasing magnetic field cycle. This sequence is just the reverse for the site ℒ3. The characteristics exhibited by the local Hall voltage loops indicate the presence of a landscape of critical magnetic field for MST-AST phase transition across the sample. This kind of disorder induced landscape of transition temperatures or magnetic fields had been envisaged earlier theoretically by Imry and Wortis [5.13], and observed experimentally in vortex matter [5.30] and various magnetic systems [5.24, 5.25]. Thus it confirms the disorder-influenced nature of this magnetic field induced MST-AST phase transition in $Ni_{50}Mn_{34}In_{16}$.

The integrated moment is the summation of the Hall voltage signals from all the pixels across the sample. Fig. 5.10(b) shows the comparison of the bulk magnetization measured in the vibrating sample magnetometer (VSM) and the integrated moments calculated from the Hall images. Though the integrated moments calculated from the Hall images follow the bulk magnetization behaviour, there is a visible difference between the two curves. We attribute this difference to the demagnetization factor [5.31]. While the sample used for the measurements in the VSM is distorted needle shaped of length approximately 1 mm, the sample used for scanning Hall probe imaging experiments is of the shape of a distorted circular plate of diameter approximately 2 mm. The shape of the field dependence of the integrated moments seems to be somewhat different from the individual local loops.

5.3 Thermomagnetic history dependence of the functional properties

We have seen that the interesting functional properties observed in $Ni_{50}Mn_{34}In_{16}$ alloy arise from the first-order MST-AST phase transition. In the previous discussion it is established that the MST-AST phase transition in $Ni_{50}Mn_{34}In_{16}$ alloy is a disorder-influenced first-order phase transition. Thermomagnetic history dependence of the volume fractions of AST and MST phases has been verified from Hall images of the sample across the transition. The functionalities in the alloy obviously are expected to depend on the volume fractions and so are expected to be dependent on the thermomagnetic history of the sample. Such history dependence is explored in the present section.

5.3.1 Thermomagnetic history dependence of magnetoresistance in the $Ni_{50}Mn_{34}In_{16}$ alloy

Fig. 5.11 shows isothermal magnetic field dependence of resistivity (ρ) of the $Ni_{50}Mn_{34}In_{16}$ alloy at 250 K measured in two protocols. In the first protocol the sample was cooled monotonically from 300 K, without undershooting, in zero field down to the target temperature. In the second protocol the sample was first cooled from 300 K in zero field down to 5 K. It was then warmed up monotonically without overshooting to the target temperature (in zero field). These protocols are equivalent to the protocols P1 and P2 respectively discussed in section 5.2.1.

In both the protocols the MR is negative. However, there is a substantial difference between the MR measured in the two protocols. In first protocol the MR is comparatively smaller and totally reversible. On the other hand MR is not only relatively larger but also irreversible in the second protocol. It is clear that the magnitude as well as the reversibility of MR depend on the history of the sample.

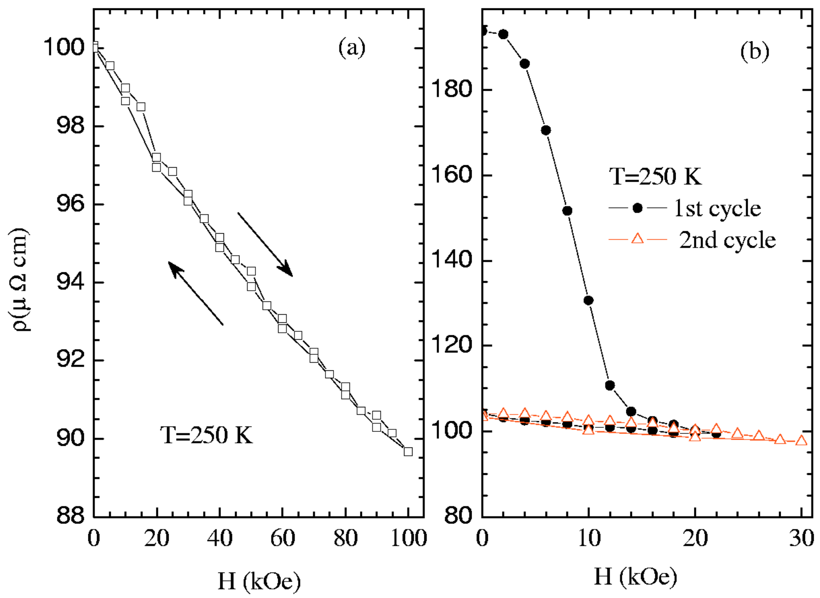

Fig. 5.11: (a) Isothermal magnetic field (*H*) dependence of resistivity (*ρ*) of the alloy at 250 K, reached by cooling in zero magnetic field from 300 K. In the first cycle *H* is increased from 0 to 100 kOe and then reduced back to 0. Then in the second cycle *H* is again increased from 0 to 100 kOe. (b) Isothermal magnetic field dependence of resistivity of the alloy at 250 K reached directly from 300 K in zero magnetic field.

5.3.2 Thermomagnetic history dependence of magnetocaloric effect in the $Ni_{50}Mn_{34}In_{16}$ alloy

We have estimated isothermal magnetic entropy change (ΔS_M) in $Ni_{50}Mn_{34}In_{16}$ alloy using isothermal M(H) curves measured in three different protocols P1, P2 and P3. The *M*(*H*) thus measured at 242 K is shown in Fig. 5.12(a) for example. In P1 the sample is first zero field cooled to 150 K and then gradually warmed up to 242 K ; in P2 protocol $T = 242$ K is reached by zero field cooling the sample from 305 K; in P3 the sample is first cooled down to 30 K before warming up to 242 K.

The magnitude of ΔS_M as a function of temperature estimated for a magnetic field excursion from zero to H_{max} = 80 kOe is shown in Fig. 5.12(b). It is clearly seen that the maximum obtainable value of MCE depends on the protocol of the measurement. The highest value of ΔS_M =24 J/kg-K is obtained under protocol P1. We have also calculated the effective refrigerant capacity (RC_{EFF}) for the three protocols. Table 5.1 summarizes the results concerning the refrigerant capacity obtained under the three different experimental protocols P1, P2, and P3. We find that the RC_{EFF} obtained under the protocol P2 has the largest value of 226 J/kg.

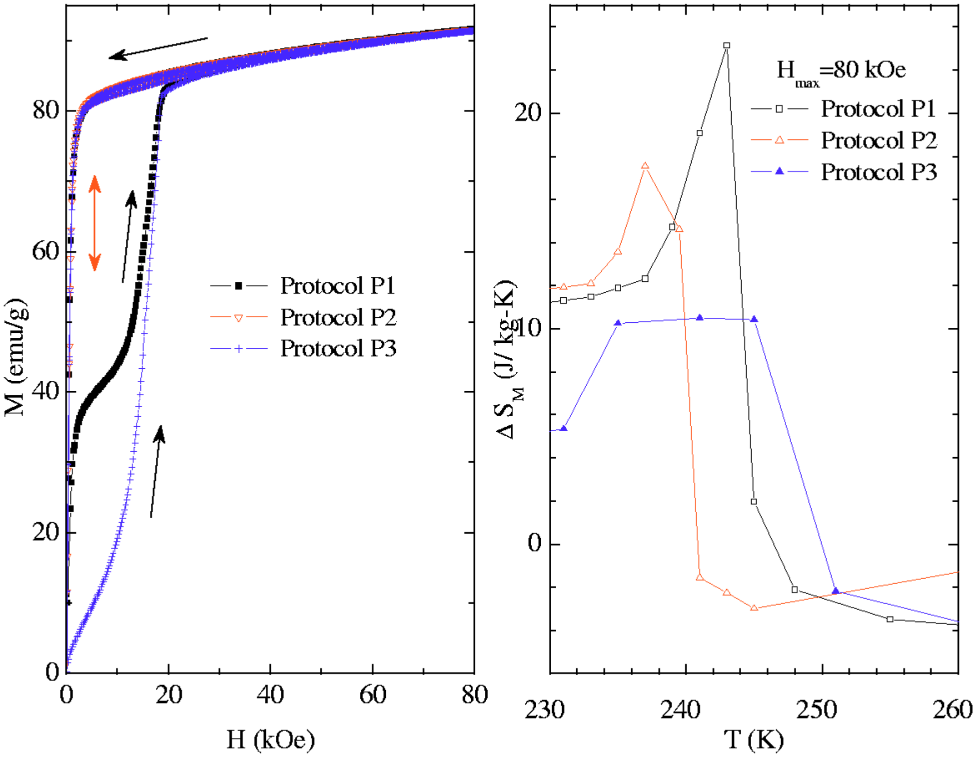

Fig. 5.12: (a) Isothermal magnetization (*M*) vs. magnetic field (*H*) plots at T = 242 K in $Ni_{50}Mn_{34}In_{16}$, measured under three different experimental protocols P1, P2, and P3. (b) Isothermal change in magnetic entropy (ΔS_M) as a function of temperature (*T*) across the austenite-martensite phase transition in $Ni_{50}Mn_{34}In_{16}$, measured under these three protocols.

Table 5.1: Useful temperature range, refrigerant capacity, average hysteresis loss, and effective refrigerant capacity RC_{EFF} estimated for $Ni_{50}Mn_{34}In_{16}$ measured under the three different protocols.

Experimental protocol	T_{cold} (K)	T_{hot} (K)	Refrigerant capacity (J/kg)	Average hysteresis loss (J/kg)	Effective refrigerant capacity RC_{EFF} (J/kg)
P1	233.6	244.1	163	103	60
P2	208.6	240	367	141	226
P3	230.7	247.4	156	119	37

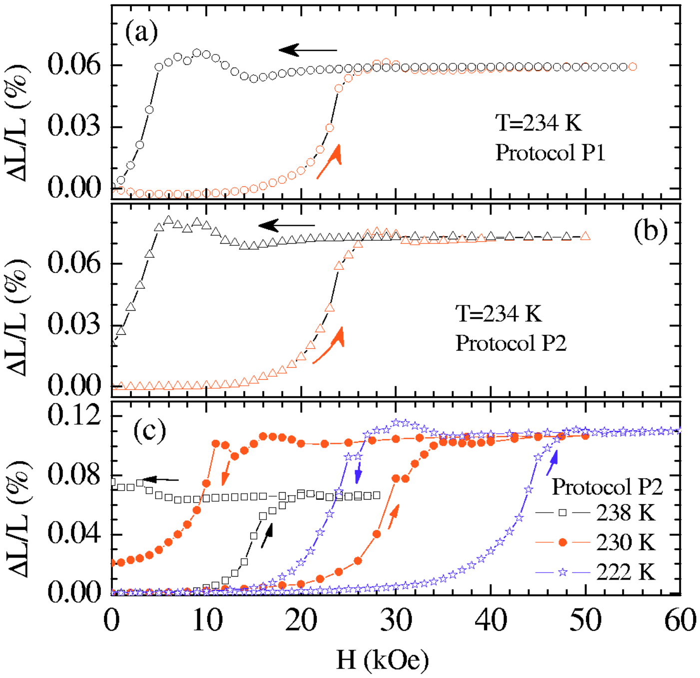

Fig. 5.13: Isothermal magnetic field (*H*) dependence of strain (*ΔL/L*) for $Ni_{50}Mn_{34}In_{16}$ alloy at a representative temperature 234 K in (a) protocol P1 and (b) protocol P2.

5.3.3 Thermomagnetic history dependence of the magnetic field induced strain in the $Ni_{50}Mn_{34}In_{16}$ alloy

We have measured the magnetic field induced strain in the temperature regime of the MST–AST phase transition using two different experimental protocols. For example, the isothermal magnetic field dependence of relative length change (*ΔL/L*) measured at 234 K, is presented in Fig. 5.13. In protocol P1 the sample was cooled from 300 K in a zero magnetic field without undershooting the target temperature 234 K. The subsequent isothermal *ΔL/L*(*H*) measurements were performed at 234 K by increasing the magnetic field and decreasing it back to zero (see Fig 5.13(a)). In protocol P2 the sample was first cooled to 50 K in a zero magnetic field before warming it up to 234 K without overshooting the target temperature. The isothermal *ΔL/L*(H) measurements were performed at this temperature (see Fig 5.13(b)). With the increase in the magnetic field, in both the protocols *ΔL/L*(H) shows a sharp rise close to 20 kOe and then saturates around the 40 kOe magnetic field. However, before reaching saturation $\Delta L/L(H)$ shows a hump like feature similar to that seen in the temperature induced transition (see Fig. 4.8 of Chapter 4). Further the complete H cycle reveals a large magnetic field hysteresis in the $\Delta L/L(H)$ curve in both the protocols. All these features in isothermal $\Delta L/L(H)$ are related to the magnetic field induced transition from the MST to the AST phase. The magnetic field induced strain is larger in protocol P2. In decreasing the magnetic field cycle $\Delta L/L(H)$ remains nearly constant down to $H \approx 20$ kOe and decreases after exhibiting the hump like feature (Figs. 5.13(a) and 5.13(b)). Further, on reducing the magnetic field isothermally from the state with saturated H-induced strain, the zero-field strain value is completely recoverable in protocol P1 while it is only partially recoverable in protocol P2. Fig. 5.13(c) presents isothermal $\Delta L/L(H)$ curves in protocol P2, at various temperatures within the temperature regime of MST–AST phase transition. At all these temperatures, $\Delta L/L(\mathrm{H})$ exhibits features of magnetic field induced transition similar to that at 234 K, i.e. it shows a sharp rise at certain critical magnetic field and exhibits a field hysteresis. The magnetic field value, at which a sharp rise in $\Delta L/L(H)$ occurs, increases with the decrease in temperature. Further, as the temperature decreases, the residual strain in zero magnetic field decreases and at some temperature the magnetic field induced strain can be totally recoverable (with zero residual value) even in protocol P2 (see the $\Delta L/L(H)$ curve at $T = 222$ K in Fig. 5.13(c)). The observations in Figs. 5.13(a)–(c) signify that in the present alloy the H-induced strain can be recoverable or non-recoverable depending on the temperature and the experimental protocol.

As mentioned earlier thermomagnetic history dependence of the functional properties of $Ni_{50}Mn_{34}In_{16}$ alloy arises from the history dependence of the AST and MST volume fractions. In the temperature regime of phase-coexistence, these volume fractions depend on the path followed in *H-T* phase space to reach a specific point (*H*,*T*). For example, in Fig. 5.7 VF_{AST} at (236 K, H = 0) at start in protocol P2 not similar to that in P1. Application of field of 40 kOe causes a larger change in VF_{AST} in protocol P2. Further, in the *H-T* phase diagram (in Fig. 5.5) increasing temperature and increasing field paths are equivalent as both cause an MST to AST phase transition. Also a decreasing field path is equivalent to a decreasing temperature path. The point (236 K, H = 0) at the start and the point (236 K, H = 0) after field cycling are expected to have similar VF_{AST} in protocol P1 but not in P2. Hence, while in protocol P1 no hysteresis is expected, P2 is expected to have a field hysteresis as has been observed in isothermal magnetic field dependence of resistivity (Fig. 5.11(b)) and strain (Fig. 5.13(b)).

5.4 Conclusion

Summarizing, the isothermal M vs. H curves of $Ni_{50}Mn_{34}In_{16}$ show the signatures of a magnetic field-induced first-order martensite to austenite phase transition in the temperature range 200–250 K. The isothermal H/M vs. M^2 curves, however, do not exhibit a negative slope at certain temperatures within this temperature range. This suggests that the criterion of relating the negative slope of the H/M vs. M^2 isotherms to the first-order magnetic transitions is not applicable for all the magnetic transitions. On the other hand, a decrease in slope of the H/M vs. M^2 isotherm is found to characterize the first-order magnetic transition in the present case. Such a decrease in slope might lead to a negative slope of the H/M vs. M^2 isotherms if there is a large change of magnetization because of the magnetic field-induced magnetic phase transition. The isothermal $M(H)$ curves and the temperature dependence of the characteristic fields of the first-order martensite–austenite phase transition can be explained within the framework of disorder broadened first-order transition. The nature of the temperature dependence of the characteristic magnetic fields is found to follow the Clausius–Clapeyron relation for a first-order phase transition. Further, the scanning Hall probe imaging experiments on $Ni_{50}Mn_{34}In_{16}$ alloy provide clear visual evidence of the coexistence of the martensite and austenite phases across the magnetic field induced martensite –austenite phase transition in this alloy. This highlights the disorder broadened first-order nature of the phase transition. Thermomagnetic history effects are found to play an important role in the evolution of this phase transition. The relative volume fractions of the martensite and austenite phases in the phase coexistence regime are found to depend strongly on the path chosen in the field–temperature phase space for varying the temperature and magnetic field. Quantitative analysis of the Hall images suggests nucleation and growth dynamics of phases across the magnetic field induced phase transition. Also the local Hall voltage loops constructed from the Hall images suggest a landscape of the critical magnetic field of the MST–AST phase transition, thus confirming the disorder-influenced nature of the transition. The magnitude and reversibility of the functional properties of the alloy under application of magnetic field, have been found to depend on the experimental path traversed in the *H*–*T* phase space to prepare the starting point of measurements.

Publications based on the present Chapter:

1. Large magnetoresistance in $Ni_{50}Mn_{34}In_{16}$ alloy.

   Appl. Phys. Lett. **89**, 222509 (2006).

   Sharma V. K., Chattopadhyay M. K., Shaeb K. H. B., Chouhan A., and Roy S. B.

2. Studies on the field-induced martensite to austenite phase transition in $Ni_{50}Mn_{34}In_{16}$.

   J. Phys.: Condens. Matter. **20**, 425210 (2008).

   Sharma V. K., Chattopadhyay M. K., and Roy S. B.

3. Thermomagnetic history dependence of magnetocaloric effect in $Ni_{50}Mn_{34}In_{16}$. *Appl. Phys. Lett.* **92**, 022503 (2008).

   Chattopadhyay M. K., **Sharma V.K.**, and Roy S. B.

4. A scanning Hall probe imaging study of the field induced martensite-austenite phase transition in $Ni_{50}Mn_{34}In_{16}$ alloy.

   J. Phys.: Condens. Matter. **22**, 016008 (2009).

   Sharma V.K., Moore J. D., Chattopadhyay M.K., Morrison K., Cohen L. F., and Roy S.B.

5. Temperature and magnetic field induced strain in $Ni_{50}Mn_{34}In_{16}$ alloy.

   J. Phys. D: Appl. Phys. **42**, 185005 (2009).

   Sharma V.K., Chattopadhyay M.K., Chouhan A., Roy S.B.

Chapter 6

Tuning the useful temperature regime of functional properties in the Ni-Mn-In alloy

In earlier Chapters it has been shown that the $Ni_{50}Mn_{34}In_{16}$ alloy undergoes a paramagnetic (PM)-ferromagnetic (FM) transition near 305 K during cooling. On further cooling, the alloy undergoes a martensitic transition (MT) around 220 K. The martensite (MST) to austenite (AST) phase transition in this alloy can be induced both by temperature (T) and magnetic field (H). The multi-functional properties observed in this alloy are related to the magnetic field induced MST-AST phase transition and are exhibited around the temperature regime of MST-AST phase transition. The functional properties of the alloy will have more technological importance if the temperature range of the martensitic transition can be shifted towards the room temperature. There are two reported mechanisms affecting the martensitic transition temperature in the Ni-Mn-X (X = In,Sn etc.) alloys [6.1]: (i) the number of valence electrons per atom (e/a) taken as the concentration weighted sum of s, p and d electrons and (ii) the atomic volume effect. Accordingly, two methods are reported in literature to increase the martensitic transition temperature in the Ni-Mn-X alloys: (i) increasing the e/a ratio by varying the relative compositions of Ni, Mn, and X [6.2], (ii) applying external pressure [6.3].

The pressure can be either applied externally or the effect of applying pressure can be simulated by substituting the atoms in Ni-Mn-X alloy by some smaller atom. The chemical pressure so generated is equivalent to externally applied physical pressure.

Therefore the substitution of an atom in Ni-Mn-X alloy by relatively smaller isoelectronic atom is expected to shift the martensitic transition towards the higher temperature side. Further if the substituted and substituent atoms are not isoelectronic, the e/a ratio will also change. Moreover, as discussed earlier, in the off-stoichiometric Ni-Mn-X alloys (e.g. $Ni_{50}Mn_{34}In_{16}$) an incipient antiferromagnetic coupling appears between the extra Mn atoms partially occupying the X sites. This antiferromagnetic coupling becomes stronger in the MST phase [6.4]. The pressure either external or generated through chemical substitution is likely to affect the inter-atomic separation and, as a result, the magnetic interactions are likely to be modified. This is also expected to influence the functional properties in this alloy system.

To explore the possibility of tuning the useful temperature regime with the chemical substitution, we have chosen to substitute Mn in $Ni_{50}Mn_{34}In_{16}$ alloy with its periodic table neighbours Cr and Fe. We have substituted 1% and 2% (nominal) of Mn by Cr, and 1% and 3% (nominal) of Mn by Fe to form $Ni_{50}(Mn,x\%Cr)_{34}In_{16}$ ($x = 1, 2$) and $Ni_{50}(Mn,y\%Fe)_{34}In_{16}$ ($y = 1, 3$) alloys. Both Cr and Fe have comparatively smaller atomic radii as compared to that of Mn [6.5]. However, Cr atom has one electron less, and Fe atom has one electron more as compared to Mn atom (Cr, Mn and Fe have outer electronic configurations as $3d^5 4s^1$, $3d^5 4s^2$ and $3d^6 4s^2$ respectively). Through the substitutions described above, in the present Chapter we study the combined effect of chemical pressure and change in *e/a* ratio on the martensitic transition in these alloys through ac susceptibility (χ_{ac}), electrical resistivity (ρ) and magnetization (M) measurements. We find that while the martensitic transition temperature increases with Cr substitution (in the $Ni_{50}(Mn,x\%Cr)_{34}In_{16}$ ($x = 1, 2$) alloys), it decreases with Fe substitution (in the

$Ni_{50}(Mn,y\%Fe)_{34}In_{16}$ (y = 1, 3) alloys) as compared to the parent $Ni_{50}Mn_{34}In_{16}$ alloy. The magnetocaloric effect (MCE) increases with increasing Cr concentration and the temperature regime of MCE increases from near 240 K in parent $Ni_{50}Mn_{34}In_{16}$ alloy to near 294 K in $Ni_{50}(Mn,2\%Cr)_{34}In_{16}$ alloy.

A deeper insight in the martensitic transition in $Ni_2Mn_{1+x}Sn_{1-x}$ has been obtained in a recent study with the help of x-ray photoelectron spectroscopy and a first-principles density functional calculation [6.6]. An abrupt decrease in the peak associated with Ni 3*d* e_g states is observed at the martensitic transition for the alloys with composition x = 0.36–0.42. It was argued that the energy shift of the Ni minority spin e_g state in the AST phase took place due to the hybridization with the antiferromagnetically coupled Mn in the Sn site [6.6]. It was further stated that the Jahn-Teller splitting of the Ni 3*d* e_g states played an important role in driving the instability of the cubic AST phase for $x \geq 0.36$ (Ref. 6.6). This idea of the important role of hybridization of Ni 3*d* states and 3*d* states of antiferromagnetically coupled Mn atoms at the Sn sites, has motivated us to study the effect of substitution of Cu atoms at the Ni site of Ni-Mn-In alloys exhibiting the martensitic transition. The $3d^{10}$ states of Cu atoms are likely to enhance the extent of the hybridization in such alloy systems. In the present Chapter, we also show that a small amount (2 at. %) of Cu substitution for Ni atoms indeed causes a large shift of martensitic transition in $Ni_{50}Mn_{34}In_{16}$ from 240 to 295 K. This martensitic transition in turn leads to large MCE, large magnetoresistance (MR) and a field-temperature induced strain in this Cu-doped $Ni_{50}Mn_{34}In_{16}$ alloy.

Further, in the present Chapter, we also study the effect of hydrostatic pressure on the MST-AST phase transition and MCE associated with the phase transition in the

$Ni_{50}Mn_{34}In_{16}$ alloy. We show that the temperature regime of the MCE in this alloy increases towards room temperature with increasing pressure. The temperature dependence of the isothermal magnetic entropy change under different pressures is found to follow a universal curve for a particular magnetic field change.

6.1 Substitution of Mn by Fe and Cr in $Ni_{50}Mn_{34}In_{16}$ alloy

The nominal alloy compositions $Ni_{50}(Mn, 1\%Cr)_{34}In_{16}$, $Ni_{50}(Mn, 2\%Cr)_{34}In_{16}$, $Ni_{50}(Mn, 1\%Fe)_{34}In_{16}$ and $Ni_{50}(Mn, 3\%Fe)_{34}In_{16}$ were prepared in an arc melting furnace (see section 2.1 of Chapter 2). The samples were encapsulated in quartz tubes under argon gas and were annealed at 900^0C for 24 hours, and subsequently quenched in ice water. Energy dispersive x-ray (EDX) analysis determined the compositions of $Ni_{50}(Mn, 1\%Cr)_{34}In_{16}$, $Ni_{50}(Mn, 2\%Cr)_{34}In_{16}$, $Ni_{50}(Mn, 1\%Fe)_{34}In_{16}$ and $Ni_{50}(Mn, 3\%Fe)_{34}In_{16}$ alloys to be $Ni_{49.2}Mn_{33.8}Cr_{0.6}In_{16.4}$, $Ni_{48.5}Mn_{34.4}Cr_{1.2}In_{16.0}$, $Ni_{48.6}Mn_{33.1}Fe_{1.5}In_{16.8}$ and $Ni_{47.2}Mn_{34.2}Fe_{1.8}In_{16.8}$ respectively within the error bar of 3%. However, henceforth in most of the discussion the $Ni_{49.2}Mn_{33.8}Cr_{0.6}In_{16.4}$, $Ni_{48.5}Mn_{34.4}Cr_{1.2}In_{16.0}$, $Ni_{48.6}Mn_{33.1}Fe_{1.5}In_{16.8}$, $Ni_{47.2}Mn_{34.2}Fe_{1.8}In_{16.8}$ and earlier studied $Ni_{50}Mn_{34}In_{16}$ alloys will be denoted as Ni(Mn, 1%Cr)In, Ni(Mn, 2%Cr)In, Ni(Mn, 1%Fe)In, Ni(Mn, 3%Fe)In and NiMnIn respectively following the nominal composition.

6.1.1 Structural analysis of the Ni(Mn,x%Cr)In (x = 1, 2) and Ni(Mn,y%Fe)In (y = 1, 3) alloys

Fig. 6.1 shows the x-ray diffraction (XRD) patterns for the alloys near 290 K. As for the NiMnIn alloy, the XRD patterns of the Ni(Mn,y%Fe)In (y = 1, 3) alloys can be indexed to the $L2_1$ structure with a lattice constant of 6.01±0.02 Å. This indicates that the presence of AST phase of the alloys at 290 K. The XRD patterns of Ni(Mn,x%Cr)In (x = 1, 2) alloys can also be indexed to $L2_1$ structure with lattice constant of 6.01±0.02 Å. However, there are some extra

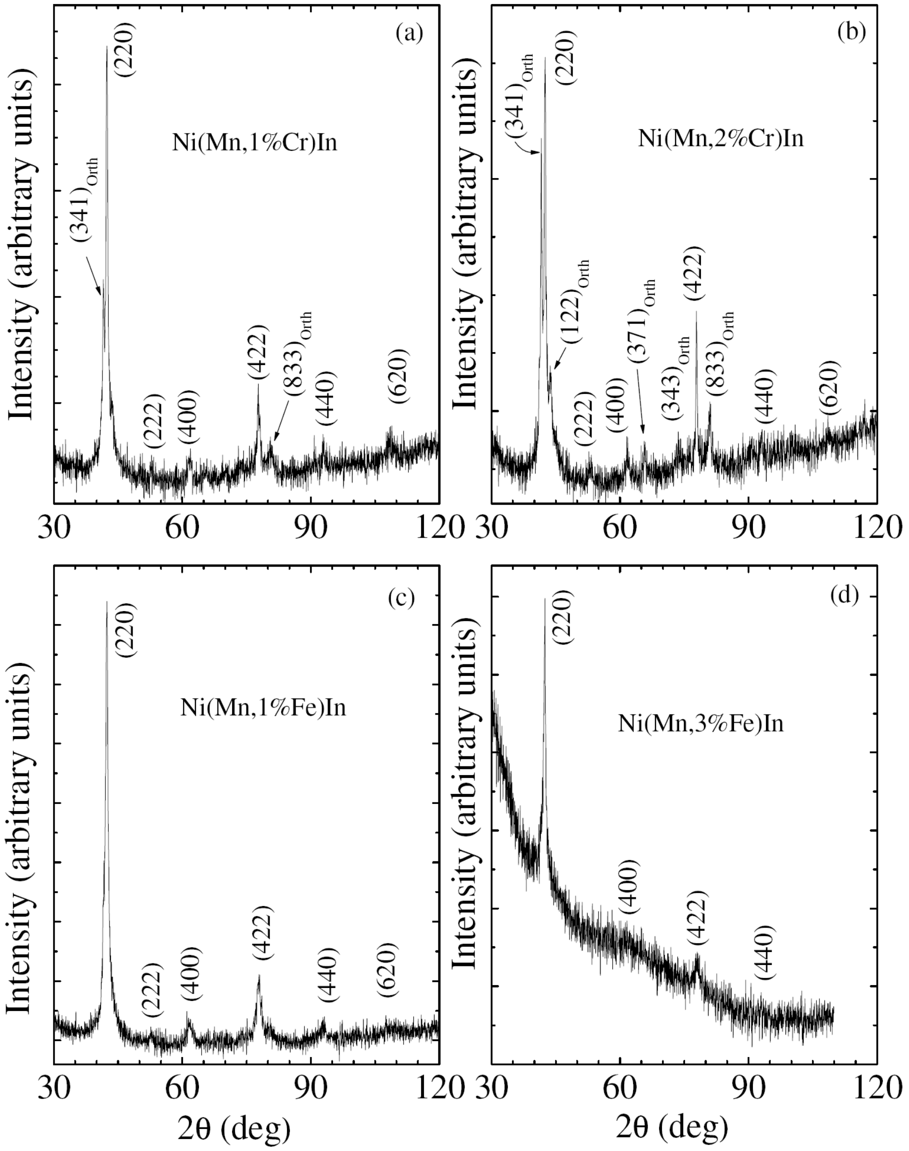

Fig. 6.1: X-ray diffraction (XRD) patterns of Cr and Fe substituted Ni-Mn-In alloys near 290 K. The XRD peaks are indexed to the $L2_1$ structure. The XRD peaks of Cr substituted alloys with subscript 'Orth' in (a) and (b) are indexed to the orthorhombic structure of the MST phase of the alloys.

peaks in the XRD patterns of Ni(Mn,x%Cr)In (x = 1, 2) alloys, which can be indexed to an orthorhombic structure. It will be discussed later in this Chapter that this second phase with orthorhombic structure is actually the MST phase of these alloys. The lattice constants of the orthorhombic phase of Ni(Mn,1%Cr)In alloy are a = 18.16 Å, b = 10.78 Å and c = 4.55 Å respectively. The lattice constants of the orthorhombic phase of Ni(Mn,2%Cr)In alloy are a =

18.16 Å, b = 10.78 Å and c = 4.52 Å respectively. The lattice constants of Ni(Mn,x%Cr)In (x = 1, 2) and Ni(Mn,y%Fe)In (y = 1, 3) alloys in the AST phase are comparable to that of NiMnIn alloy. Peaks corresponding to the orthorhombic structure are more prominent in the XRD pattern of Ni(Mn,2%Cr)In as compared to that of Ni(Mn,1%Cr)In. This suggests the presence of a relatively large amount of orthorhombic phase at 290 K in the Ni(Mn,2%Cr)In alloy as compared that in the Ni(Mn,1%Cr)In alloy.

6.1.2 Ac susceptibility, resistivity and magnetization study of the Cr substituted alloys

Figs. 6.2(a) and 6.2(b) present the temperature dependence of ac susceptibility and resistivity of the Ni(Mn,1%Cr)In and the Ni(Mn,2%Cr)In alloys. In the Ni(Mn,1%Cr)In (Ni(Mn,2%Cr)In) alloy, with decreasing temperature, there is a sharp rise in χ_{ac} near 305 K (300 K) indicating a PM to FM transition in the alloy. The Curie temperature of the AST phase (T_{CA}) for the Ni(Mn,1%Cr)In (Ni(Mn,2%Cr)In) alloy estimated from the inflection point of $\chi_{ac}(T)$ is approximately 303 K (296 K). With a further decrease in temperature, the $\chi_{ac}(T)$ of the Ni(Mn,1%Cr)In alloy first decreases near 300 K and then increases slowly again. It then shows a large drop near 275 K and then becomes almost flat. This is in sharp contrast with the Ni(Mn,2%Cr)In alloy where $\chi_{ac}(T)$ exhibits a large drop near 295 K (below T_{CA}) and then becomes flat with further lowering of T. As T is decreased to still lower values, the $\chi_{ac}(T)$ of the Ni(Mn,1%Cr)In (Ni(Mn,2%Cr)In) alloy rises again around 240 K and forms a shoulder near 230 K (210 K) and a peak near 210 K [195 K]. Upon warming up, a distinct thermal hysteresis is observed in χ_{ac} of Ni(Mn,1%Cr)In (Ni(Mn,2%Cr)In) alloy near 275 K (290 K).

In the Ni(Mn,1%Cr)In alloy, $\rho(T)$ also shows the signature of T_{CA} in the form of a change of slope in $\rho(T)$ near 305 K. However in the Ni(Mn,2% Cr)In alloy, $\rho(T)$ shows no signature corresponding to the PM-FM transition in this alloy. In the Ni(Mn,1%Cr)In (Ni(Mn,2%Cr)In) alloy, there is a sharp rise in $\rho(T)$ near 275 K (295 K) with decreasing temperature. $\rho(T)$ shows a broad hump around 210 K (195 K) and then decreases with decreasing temperature. During the temperature increasing cycle, there is a distinct thermal hysteresis near 275K (290 K) in $\rho(T)$ as well.

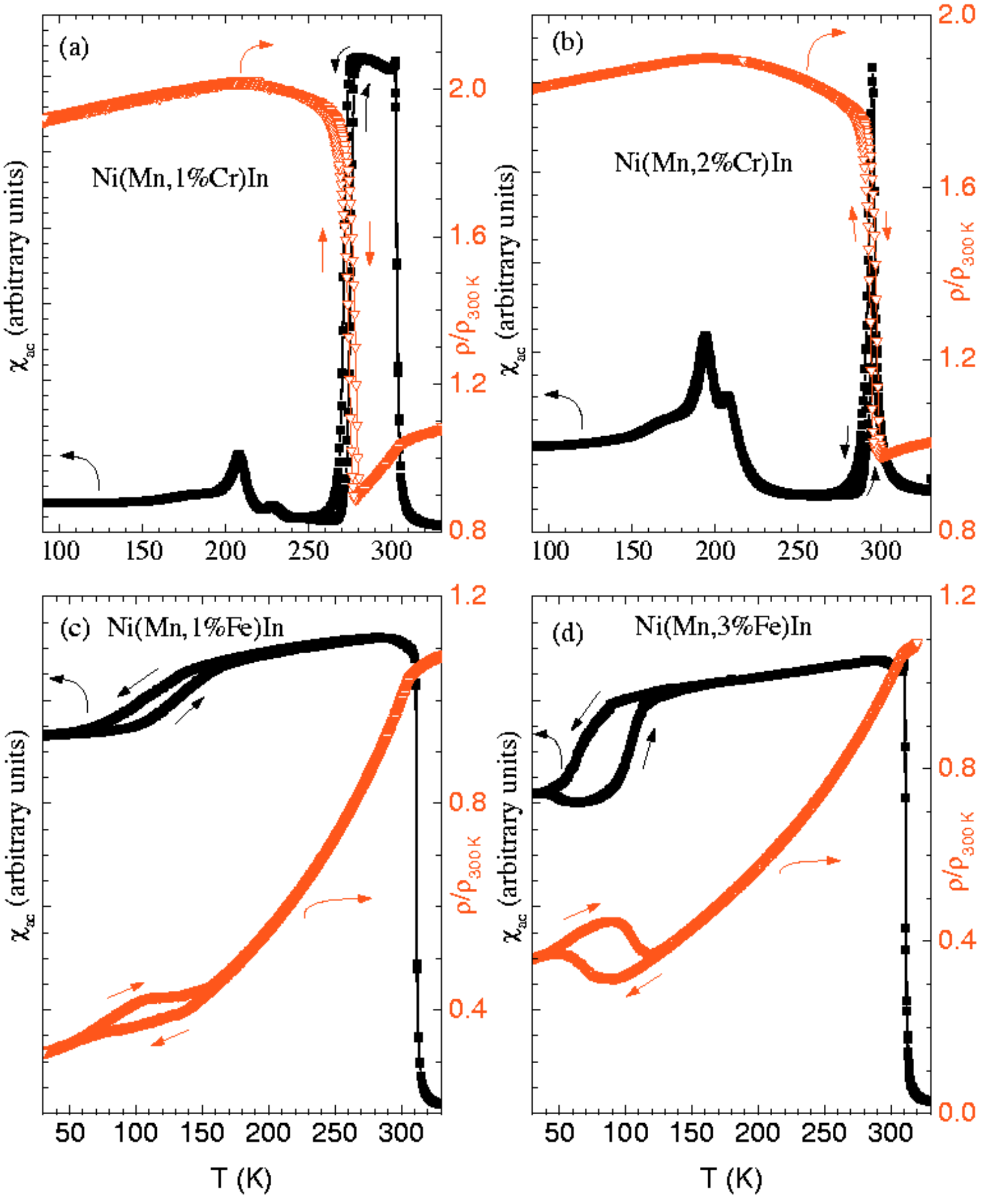

Fig. 6.2: Temperature (T) dependence of ac susceptibility (χ_{ac}) and dc resistivity (ρ) for Cr and Fe substituted Ni-Mn-In alloys. Resistivity is normalized to its value at 300 K.

The χ_{ac}(T) and $\rho(T)$ of Ni(Mn,1% Cr)In exhibit features very similar to those observed earlier in the NiMnIn alloy (see section 3.1.2 of Chapter 3) in a slightly different temperature range. The hysteresis in χ_{ac}(T) and $\rho(T)$ of the Ni(Mn,1%Cr)In alloy can be attributed to the first-order nature of the MT in this alloy system. The peak in $\chi_{ac}(T)$ of Ni(Mn,1%Cr)In near 210 K denotes the PM-FM transition in the MST phase of the alloy (see Chapter 3 and Ref. 6.7). The hump in $\rho(T)$ near 210K can thus be related with this PM-FM transition in the MST phase of the alloy. Similarly in the Ni(Mn,2% Cr)In alloy, the thermal hysteresis in $\chi_{ac}(T)$ and $\rho(T)$ near 290 K can be attributed to the martensitic transition in this alloy. The signature of PM-FM transition (near 295 K) in $\rho(T)$ of this alloy is probably masked by the much larger change in ρ associated with the onset of martensitic transition in the temperature regime immediately below. The peak in $\chi_{ac}(T)$ and the hump in $\rho(T)$ near 195 K in the Ni(Mn,2%Cr)In alloy indicates the PM-FM transition in the MST phase of the alloy (see Chapter 3 and Ref. 6.7). The small shoulder in $\chi_{ac}(T)$ near 230 K in the Ni(Mn,1%Cr)In and near 210 K in the Ni(Mn,2%Cr)In, might be due to presence of small amount of second magnetic phase which goes undetected in resistivity and XRD. Moreover, it can be noted from $\chi_{ac}(T)$ and $\rho(T)$ of Ni(Mn, x%Cr)In (x = 1, 2) alloys that the hysteresis due to the MST to AST phase transition extends nearly up to 290 K in Ni(Mn,1%Cr)In alloy, and this temperature lies amid the temperature regime of the martensitic transition in the Ni(Mn,2%Cr)In alloy. This suggests the presence of some amount of the MST phase near this temperature in these alloys. The MST phase of the Ni-Mn-In alloys is reported to have the orthorhombic structure [6.8]. Thus the orthorhombic second phase indicated in the XRD patterns of the Ni(Mn,x%Cr)In (x = 1, 2) alloys is due to the presence of the MST phase of the alloys at 290 K. This is supported by the observation in the XRD pattern of Ni(Mn,2%Cr)In alloy that suggests the presence of relatively larger amount of orthorhombic phase in the alloy at

290 K as compared to that in Ni(Mn,1%Cr)In alloy, and that is because the temperature 290 K lies well within the temperature regime of AST-MST phase transition in the Ni(Mn,2%Cr)In alloy.

The main panel of Fig. 6.3(a) shows a comparison of the temperature dependence of resistivity $\rho(T)$ of Ni(Mn,1%Cr)In and Ni(Mn,2%Cr)In with that of the parent NiMnIn alloy highlighting the martensitic transition. In the Ni(Mn,1%Cr)In alloy the martensitic transition temperature is increased nearly by 35 K as compared to that of the NiMnIn alloy. In the Ni(Mn,2%Cr)In alloy the martensitic transition further increases nearly by 20 K. The inset to Fig. 6.3(a) shows comparison of $\chi_{ac}(T)$ near the T_{CA} of the three alloys. The T_{CA} of the NiMnIn alloy

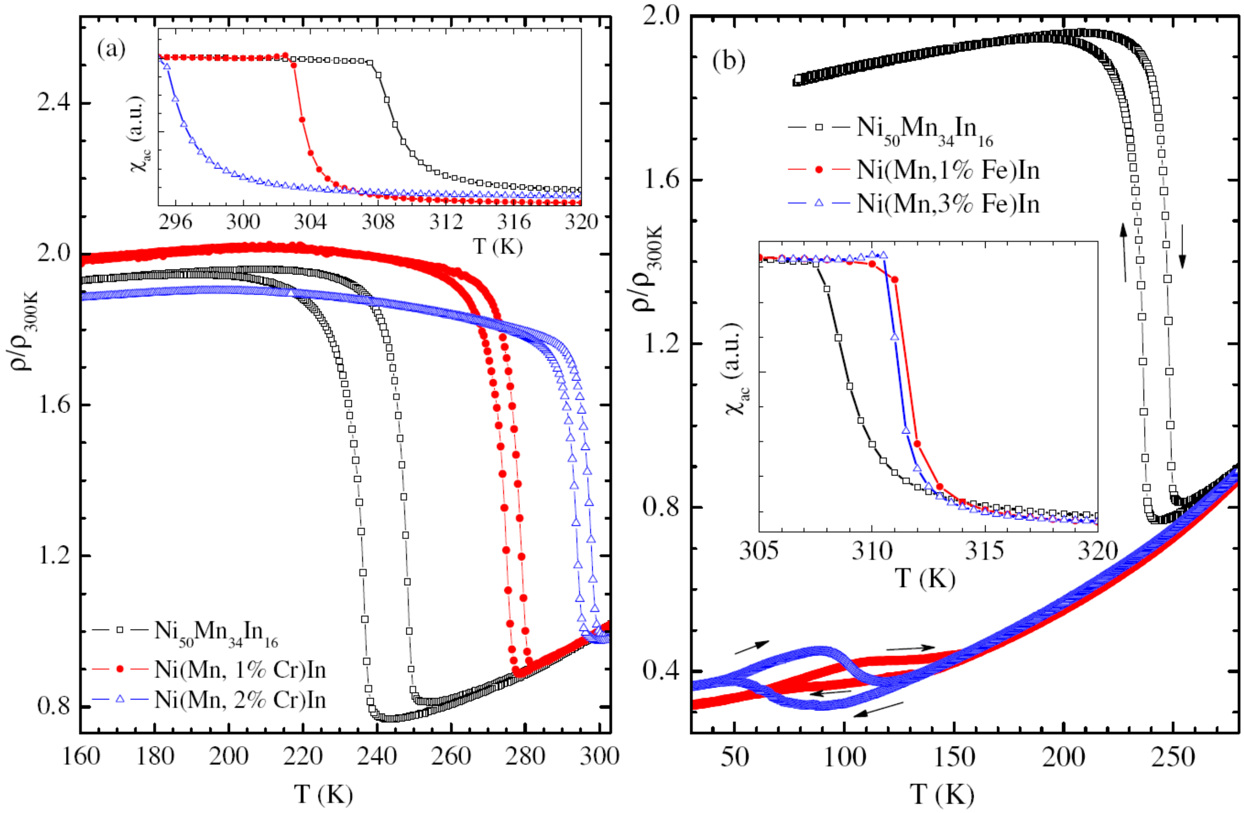

Fig. 6.3: Comparison of temperature (T) dependence of dc resistivity (ρ) of (a) Cr substituted alloys, and (b) Fe substituted alloys, with that of parent $Ni_{50}Mn_{34}In_{16}$ alloy around the martensitic transition. Resistivity is normalized to its value at 300 K. The inset shows comparison of the T dependence of ac susceptibility (χ_{ac}) of the alloys near the Curie temperature of the austenite phase.

determined from the inflection point of $\chi_{ac}(T)$ is approximately 308 K. The comparison of T_{CA} of the three alloys (see inset to Fig. 6.3(a)) indicates that there is a small decrease in T_{CA} with the substitution of Mn by Cr in the NiMnIn system. In the Ni-Mn-Sn alloy, substituting Mn by Cr causes the martensitic transition to shift towards lower temperature [6.8]. Thus the direction of shift in the martensitic transition temperature of the Ni(Mn,x% Cr)In (x = 1, 2) alloys is opposite to that observed for substitution of Mn by Cr in the Ni-Mn-Sn alloy [6.8]. It is also observed that the shift in T_{CA} is much smaller as compared to the shift in martensitic transition temperature in the present system of alloys. This is in accordance with the report in the literature which suggests that in the Ni-Mn-X alloys T_{CA} is not as sensitive to the change in composition as the martensitic

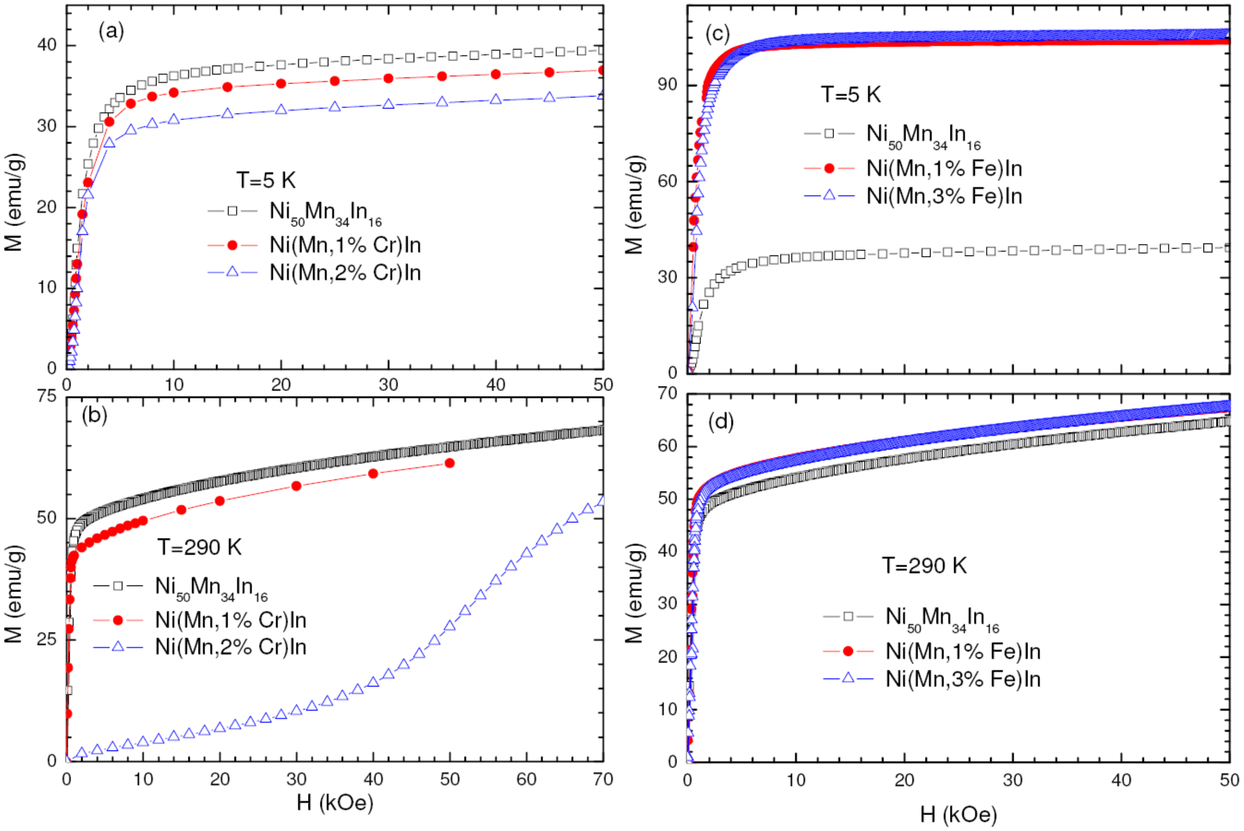

Fig. 6.4: Comparison of magnetic field (*H*) dependence of magnetization (*M*) of Cr substituted alloys with that of parent $Ni_{50}Mn_{34}In_{16}$ alloy at (a) 5 K and (b) 290 K. Comparison of *H* dependence of *M* of Fe substituted alloys with that of parent $Ni_{50}Mn_{34}In_{16}$ alloy at (c) 5 K and (d) 290 K.

transition [6.9].

To compare the magnetization in the Ni(Mn,x% Cr)In (x = 1, 2) alloys with that of the NiMnIn alloy, the isothermal *H* dependence of *M* at 5 and 290 K has been measured in these alloys and is presented in Figs. 6.4(a) and 6.4(b). The *M*(*H*) curves indicate ferromagnetic ordering in the AST and MST phases of these alloys. The presence of spontaneous magnetization in the AST as well MST phase of the alloys has been confirmed by drawing Arrott plots. The rise in the *M*(*H*) of the Ni(Mn, 2%Cr)In at 290 K near 40 kOe is related to the magnetic field induced MST to AST phase transition in this alloy at this temperature. The decrease in the saturation magnetization in the Ni(Mn, 1%Cr)In and the Ni(Mn, 2%Cr)In alloys as compared to that of the NiMnIn, suggests a decrease in the ferromagnetic interaction with the substitution of Mn by Cr in the NiMnIn alloy.

6.1.3 Ac susceptibility, resistivity and magnetization of the Fe substituted alloys

Figs. 6.2(c) and 6.2(d) present the $\chi_{ac}(T)$ and $\rho(T)$ curves for the Ni(Mn,1%Fe)In and Ni(Mn,3%Fe)In alloys measured in the temperature range 30-350 K. With decreasing temperature both the alloys exhibit a sharp rise in χ_{ac}(T) near 315 K indicating a PM to FM transition in the AST phase of these alloys. The T_{CA} estimated from the inflection point of $\chi_{ac}(T)$ is approximately 311 K for both the alloys. At lower temperatures, in both the alloys $\chi_{ac}(T)$ decreases slowly with decreasing temperature. In the Ni(Mn,1%Fe)In (Ni(Mn,3%Fe)In) alloy, $\chi_{ac}(T)$ shows a change in slope near 140 K (90 K) and decreases with further decrease in temperature. It is observed that χ_{ac} show a distinct thermal hysteresis in the temperature range 75-160 K (50-130 K) in Ni(Mn,1%Fe)In (Ni(Mn,3%Fe)In) alloy. Both the alloys exhibit a change in slope in $\rho(T)$ near 311 K indicating the PM to FM transition in these alloys. With decreasing temperature, $\rho(T)$ for the Ni(Mn,1%Fe)In alloy shows a change in slope around 140

K, which is also associated with a distinct thermal hysteresis in the same temperature regime as the thermal hysteresis in $\chi_{ac}(T)$. The change in slope of $\chi_{ac}(T)$ and $\rho(T)$ near 140 K, and the hysteretic behaviour in $\chi_{ac}(T)$ and $\rho(T)$ can be related to the martensitic transition in Ni(Mn,1%Fe)In alloy. The Ni(Mn,3%Fe)In alloy also exhibits qualitatively similar behaviour of $\rho(T)$ and $\chi_{ac}(T)$ with thermal hysteresis in the temperature range 50-130 K.

The main panel of Fig. 6.3(b) shows a comparison of the temperature dependence of resistivity $\rho(T)$ of Ni(Mn,y%Fe)In (y = 1, 3) with that of the NiMnIn alloy focussing on the martensitic transition. In the Ni(Mn,1%Fe)In alloy the martensitic transition temperature is decreased nearly by 100 K as compared to that of NiMnIn alloy. In Ni(Mn,3%Fe)In there is further decrease in martensitic transition temperature to 90 K. Inset to Fig. 6.3(b) shows comparison of $\chi_{ac}(T)$ near T_{CA} for these three alloys with decreasing temperature. The comparison of T_{CA} of Ni(Mn,y%Fe)In (y = 1, 3) and NiMnIn alloys indicates that there is only a marginal increase in T_{CA} with substitution of Mn with Fe. In Ni-Mn-Sn alloy, substitution of Mn by Fe causes martensitic transition to shift to lower temperature [6.10]. Thus the direction of shift in martensitic transition temperature in Ni(Mn,y% Fe)In (x = 1, 3) alloys is same as observed for substitution of Mn by Fe in Ni-Mn-Sn alloy.

Figs. 6.4(c) and 6.4(d) present the isothermal magnetic field dependence of magnetization at 5 K and 290 K for Ni(Mn, 1%Fe)In, Ni(Mn, 3%Fe)In and N_IMnIn alloys. Comparison of $M(H)$ at 5 K and 290 K suggest that the saturation magnetizations in Ni(Mn, 1%Fe)In and Ni(Mn, 3%Fe)In alloys are comparable at both the temperatures, and are higher than that in NiMnIn alloy at the respective temperatures, indicating an enhancement of the ferromagnetic interaction.

6.1.4 The shift of martensitic transition temperature in the Ni-Mn-X alloys

Though the Cr and Fe doped alloys are expected to have higher degree of disorder as compared to parent alloy, the shift in the martensitic transition temperature in our Cr and Fe doped alloys can not be attributed to the increased disorder. While the transition temperature shifts to higher temperature with Cr substitution, the temperature shift is towards lower temperature for Fe substitution. Further, as discussed in the section 1.3.4 of Chapter 1, the effect of disorder on the phase transition is to broaden it. On the contrary the transition in Cr substituted alloys is sharper as compared to that in the parent alloy (see Fig. 6.3). In the literature, the shift in the martensitic transition temperature of Ni-Mn-X alloys is reported to be affected by two parameters as discussed in the starting of this Chapter: it increases with the increase in the valence electron concentration *e*/*a* [6.2], and with the increase of external pressure [6.3]. Moreover, as discussed earlier that magnetism in the Ni-Mn-X alloys is predominantly due to the magnetic moment of Mn sub-lattice. In the stoichiometric Ni-Mn-X Heusler alloys there is a ferromagnetic coupling between the Mn atoms. In the off-stoichiometric Ni-Mn-X Heusler alloys (like $Ni_{50}Mn_{34}In_{16}$), the extra Mn atoms partially occupy the sites, which otherwise would have been occupied by the X atoms [6.4, 6.11]. An incipient antiferromagnetic coupling between these extra Mn atoms and those occupying sites corresponding to the stoichiometric composition has been suggested, which might strengthen in the MST phase [6.4, 6.11]. Note that there still exists ferromagnetic coupling between the Mn atoms occupying sites corresponding to stoichiometric composition, resulting in an overall ferromagnetic character of MST phase.

The atomic radii of Cr and Fe are smaller as compared to that of Mn [6.5]. Substitution of Mn by Cr or Fe is equivalent to positive external pressure. This should cause an increase in the martensitic transition temperature in the Ni(Mn, x%Cr)In (x = 1, 2) and Ni(Mn, y%Fe)In (y = 1,

3) alloys as per the observed pressure dependence of this transition temperature [6.3]. Further the *e*/*a* ratio calculated as per the composition determined with EDX analysis is 7.81, 7.80, 7.79, 7.76 and 7.83 for Ni(Mn, 1%Cr)In , Ni(Mn, 2%Cr)In, Ni(Mn, 1%Fe), Ni(Mn, 3%Fe)In and NiMnIn alloys respectively. Thus e/a ratios of both the Ni(Mn, x%Cr)In (x = 1, 2) and Ni(Mn, y%Fe)In (y = 1, 3) system of alloys are smaller than that of the NiMnIn alloy. Hence the martensitic transition should shift towards lower temperature in these alloys as compared to that in the NiMnIn alloy [6.2]. On the other hand, the substitution of Mn by Cr or Fe in the off-stoichiometric NiMnIn alloy will result in occupation of some of the Mn sites and some In sites (corresponding to the stoichiometric composition) also, by Cr or Fe. This will result in the decrease in Mn-Mn distance owing to the smaller size of Cr and Fe atoms as compared to Mn and In atoms. This can strengthen the incipient antiferromagnetic coupling between the Mn atoms occupying In sites and those occupying proper sites in MST phase. Also the same effect may decrease the ferromagnetic coupling between the Mn atoms occupying sites corresponding to stoichiometric composition [6.12] in the Ni(Mn, x%Cr)In (x = 1, 2) and Ni(Mn, y%Fe)In (y = 1, 3) alloys. Now our earlier study in NiMnIn alloy (see Chapter 3) has shown that the martensitic transition in NiMnIn alloy is suppressed by magnetic field, which suggests that ferromagnetism helps to stabilize AST phase in NiMnIn alloys. This observation along with the *M*(*H*) curves (see Fig. 6.4) provides a plausible explanation for the shift in martensitic transition in Ni(Mn, x%Cr)In (x = 1, 2) and Ni(Mn, y%Fe)In (y = 1, 3) alloys as compared to that of NiMnIn alloy as follows. The *M*(*H*) curves of Ni(Mn, x%Cr)In (x = 1, 2) alloys taken at 290 K and 5 K (see Figs. 6.4(a) and 6. 4(b)) indicate lower saturation magnetic moment in these alloys as compared to that in NiMnIn alloy. This suggests that the ferromagnetic interaction is reduced in Ni(Mn, x%Cr)In (x = 1, 2) alloys as compared to NiMnIn alloys. Hence, the MST phase is

stabilized as compared to AST phase and the martensitic transition shifts to higher temperature side. The $M(H)$ curves of Ni(Mn, y%Fe)In (y = 1, 3) alloys at 290 K and 5 K are indicative of higher saturation magnetic moment in these alloys as compared to that in NiMnIn. This suggests increased ferromagnetic interaction in these alloys as compared to NiMnIn alloy, which causes a decrease in the martensitic transition temperature in these alloys. The increase in ferromagnetic interaction in the Ni(Mn, y%Fe)In (y = 1, 3) alloys as compared to NiMnIn, might also be related to the larger magnetic moment of Fe as compared to Mn [6.10]. Another important aspect related to the substitution of Mn in the off-stoichiometric alloy $Ni_{50}Mn_{34}In_{16}$ by Fe/Cr is that substitution is likely to result in a random distribution of Fe/Cr at Mn sites as well as In sites (corresponding to stoichiometric composition). Such random distribution of atoms can also affect the martensitic transition in Ni-Mn-In alloys very significantly (see case of $Ni_{50}Mn_{34.5}In_{15.5}$ and $Ni_{50}Mn_{35}In_{15}$ alloys in Chapter 3). Another perspective of the martensitic transition in Ni-Mn-Sn alloy has been revealed by a recent photo electron spectroscopy study and first principle calculations of electronic structure [6.6]. An abrupt decrease in peak associated with the Ni 3*d* e_g states have been observed across the martensitic transition. Further the energy shift in Ni minority spin e_g states was argued to be originating from hybridization of Ni 3*d* states and with 3*d* states of antiferromagnetically coupled Mn atoms occupying Sn site due to off-stoichiometry [6.6]. The spatial extension of 3*d* orbitals in Cr atom is larger than that of 3*d* orbitals of Mn atom and the spatial extension of 3*d* orbital of Fe atom is smaller than that of 3*d* orbitals in Mn [6.13]. Thus the substitution of Mn by Cr and Fe is expected to affect the hybridization of 3*d* states of Ni states in opposite sense as compared to that NiMnIn, and thus to shift the martensitic transition in the alloy in opposite direction of temperature. It will be interesting to probe the effect of substitution of Mn by Cr and Fe in NiMnIn alloy with photo electron spectroscopy.

6.2 Magnetocaloric effect in the Cr substituted alloys

It has been discussed in earlier sections that the Cr substituted alloys have temperature regime of the MST-AST phase transition shifted to higher temperatures as compared to that of parent alloy. In the following sub-sections we discuss the MCE in these alloys.

6.2.1 Magnetocaloric effect in the Ni_{50}(Mn, 1%Cr)$_{34}In_{16}$ alloy

From the temperature dependence of the resistivity and the ac susceptibility we have seen that this alloy undergoes a AST to MST phase transition near 275 K. Fig. 6.5(a) presents the *T* dependence of *M* of this alloy in *H* = 100 Oe in the T regime 5 K ≤T ≤300 K. In the field cooled

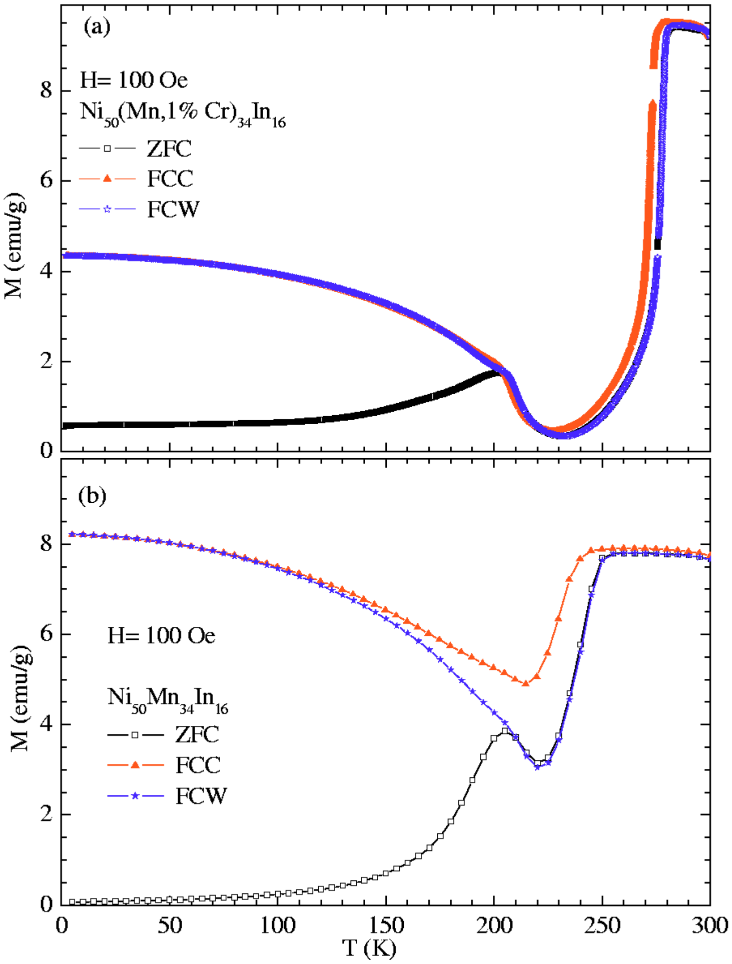

Fig. 6.5: Temperature (*T*) dependence of magnetization (*M*) in 100 Oe magnetic field (*H*) for (a) Ni_{50} (Mn,1%Cr)$_{34}In_{16}$ alloy and (b) parent $Ni_{50}Mn_{34}In_{16}$ alloy.

cooling (FCC) protocol M increases with decreasing *T* at high *T* near 300 K (as discussed earlier, ac-susceptibility studies show that this alloy actually undergoes a PM to FM transition near 305 K). With further lowering of *T*, *M*(*T*) shows a sharp drop near 275 K, and then increases again below 225 K. *M*(*T*) shows a similar behaviour in the field cooled warming (FCW) protocol. However, there is a distinct thermal hysteresis between the FCC and FCW curves. Fig. 6.5(b) shows *M*(*T*) curves obtained in zero field cooled (ZFC), FCC and FCW protocols for the parent $Ni_{50}Mn_{34}In_{16}$ alloy in H = 100 Oe for comparison. As discussed in earlier chapters, the *M* of $Ni_{50}Mn_{34}In_{16}$ alloy also increases with decreasing *T* near 300 K in the FCC protocol. *M*(*T*) shows a sharp drop near 240 K and again increases with decreasing *T* at temperatures below 215 K. A clear thermal hysteresis is observed below 250 K between the *M*(*T*) curves of $Ni_{50}Mn_{34}In_{16}$ obtained in the FCC and FCW protocols. A sharp change in M and associated thermal hysteresis characterize the first-order nature [6.14, 6.15] of MST-AST phase transition in $Ni_{50}Mn_{34}In_{16}$. The *M*(*T*) curves of the $Ni_{50}(Mn,1\%Cr)_{34}In_{16}$ alloy are qualitatively very similar to that of $Ni_{50}Mn_{34}In_{16}$. We assign the sharp changes in *M*(*T*) and associated thermal hysteresis in $Ni_{50}(Mn,1\%Cr)_{34}In_{16}$ to an MST-AST phase transition. Comparing Figs. 6.5(a) and 6.5(b) we find that the MST-AST phase transition in the $Ni_{50}(Mn,1\%Cr)_{34}In_{16}$ alloy has been shifted to higher temperature as compared to the $Ni_{50}Mn_{34}In_{16}$ alloy. This supports the inference drawn from resistivity and ac susceptibility studies.

Figure 6.6(a) presents isothermal *M*(*H*) curves for the $Ni_{50}(Mn,1\%Cr)_{34}In_{16}$ alloy at various representative temperatures. Comparing with Fig. 6.5(a) we observe that in the *T*-regime above and below the hysteretic region in *M*(*T*), the *M*(*H*) curves are that of a soft ferromagnet with negligible hysteresis (see *M*-*H* curves at 200 K and 290 K). A clear signature of a magnetic

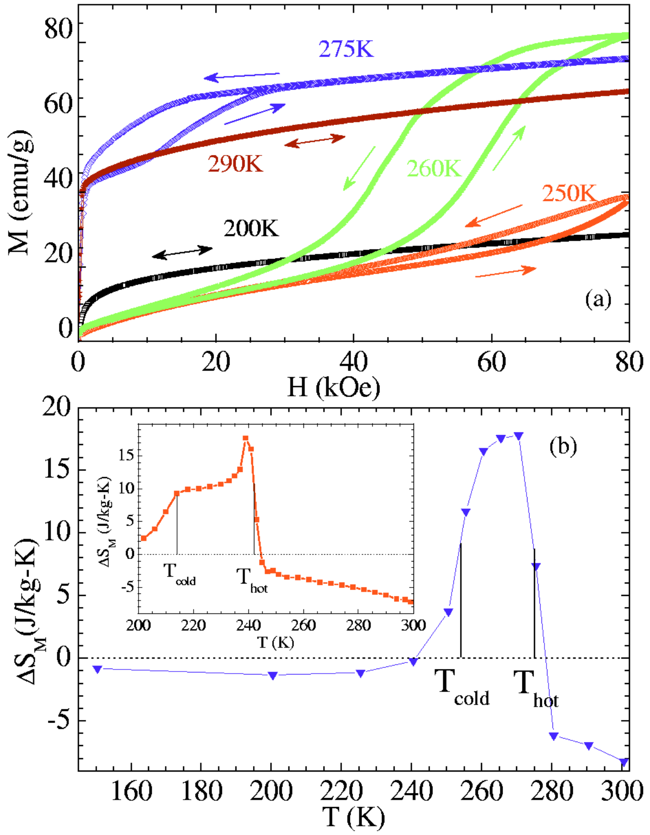

Fig. 6.6: (a) Isothermal magnetic field (*H*) dependence of magnetization (*M*) for $Ni_{50}(Mn,1\%Cr)_{34}In_{16}$ alloy at various temperatures. (b) Temperature (*T*) dependence of isothermal magnetic entropy change (ΔS_M) of the alloy for a field change of 80 kOe. The inset to (b) shows *T* dependence of ΔS_M for parent $Ni_{50}Mn_{34}In_{16}$ alloy for a magnetic field change of 80 kOe. The area enclosed by ΔS_M(T) curve between the temperatures T_{cold} and T_{hot} is a measure of refrigerant capacity of the alloy.

field induced MST-AST phase transition is observed in the *M*(*H*) curves in the *T*-regime where the *M*(*T*) curves exhibit thermal hysteresis (see *M*-*H* curves at 250K-275K). This magnetic field induced MST-AST phase transition is also associated with a field-hysteresis which is attributed to the first-order nature [6.14, 6.15] of the MST-AST phase transition in $Ni_{50}(Mn,1\%Cr)_{34}In_{16}$ alloy that can be driven both by *T* and *H* as observed in $Ni_{50}Mn_{34}In_{16}$ alloy.

We have estimated isothermal entropy change (ΔS_M) as a function of *T* from isothermal *M*(*H*) curves using the integrated Maxwell's relation (see Chapter 2 and Ref. 6.16). Fig. 6.6(b) presents the *T*-dependence of ΔS_M for the present alloy. The negative value of ΔS_M at temperatures away from the MST-AST phase transition, is consistent with the negative value of d*M*/d*T* in this temperature regime, as is observed in ferromagnetic materials. However, in the *T*-regime of MST-AST phase transition ΔS_M shows a positive peak (inverse MCE). The peak value of ΔS_M is 17.7 J/kg-K near 270 K for the field change of 80 kOe. This peak ΔS_M value for the present alloy is larger than the $\Delta S_M \approx$ 10 J/kg-K observed in Gd around 295K [6.17]. The peak value of ΔS_M in the present alloy is comparable to that in the $Ni_{50}Mn_{34}In_{16}$ alloy for the same field change (see Chapter 4). However, the peak position is shifted to near 270 K in the present alloy as compared to near 240 K in the $Ni_{50}Mn_{34}In_{16}$ alloy (see Fig. 6.6(b) and inset therein).

We have also estimated refrigerant capacity (RC), which is the amount of heat transferred between cold and hot reservoirs in an ideal refrigeration cycle, for the present alloy. RC was calculated using the method available in literature (see Chapter 4 and Ref. 6.18) (see Fig. 6.6(b)). In order to estimate the effective refrigerant capacity (RC_{EFF}) the average hysteresis loss was calculated from *M*(*H*) curves in the relevant T-range and was subtracted from RC. RC_{EFF} thus calculated is 254 J/kg for field change of 80 kOe. This RC_{EFF} is somewhat smaller as compared to 305 J/kg reported for Gd_5 (Si_2Ge_2) alloy for field change of 50 kOe [6.19]. However it is larger than that of the $Ni_{50}Mn_{34}In_{16}$ alloy, where it is approximately 220 J/kg for a field change of 80 kOe (see Table 4.1 of Chapter 4). Further the temperatures of cold and hot reservoirs of the ideal refrigeration cycle of the present alloy are 253.8 K and 274.8K respectively, as compared to 214 K and 242.3 K respectively for the parent $Ni_{50}Mn_{34}In_{16}$ alloy.

6.2.2 Magnetocaloric effect in the $Ni_{50}(Mn, 2\%Cr)_{34}In_{16}$ alloy

From the resistivity and ac susceptibility studies it was inferred that this alloy undergoes a MST-AST phase transition near room temperature. The main panel of Fig. 6.7 presents the temperature dependence of the magnetization of the $Ni_{50}(Mn,2\%Cr)_{34}In_{16}$ alloy in 100 Oe magnetic field, in the temperature regime 5-340 K. The rise in M near 300 K with decreasing temperature in the FCC protocol indicates PM to FM transition in the AST phase of this alloy. The T_{CA} estimated from the point of inflection on the $M(T)$ curve is 296 K approximately. With further lowering of temperature, $M(T)$ shows a sharp drop below 295 K and becomes almost temperature independent, and then increases again below 240 K. $M(T)$ shows a similar behaviour in the FCW protocol as well. However, there is a distinct thermal hysteresis between the FCC and FCW curves. This sharp change in magnetization and the associated thermal hysteresis is ascribed to the first-order MST-AST phase transition observed in the off-stoichiometric Ni-Mn-In alloys [6.9]. Comparison of the $M(T)$ curve of the present alloy with those of the parent $Ni_{50}Mn_{34}In_{16}$ and sister $Ni_{50}(Mn,1\%Cr)_{34}In_{16}$ alloys reveal that the MST-AST phase transition in the present alloy has been shifted to 294 K as compared to near 240 K and 270 K in the $Ni_{50}Mn_{34}In_{16}$ and $Ni_{50}(Mn,1\%Cr)_{34}In_{16}$ alloys respectively.

As discussed earlier, the MST to AST phase transition in the $Ni_{50}Mn_{34}In_{16}$ and $Ni_{50}(Mn,1\%Cr)_{34}In_{16}$ alloys can be induced by magnetic field as well. This magnetic field induced MST to AST phase transition is the key behind the large MCE observed in these alloys. To check whether the MST to AST phase transition in the present alloy can be induced by magnetic field, we have measured the isothermal field dependence of magnetization across the temperature regime of MST-AST phase transition in the present alloy. One such isothermal $M(H)$ curve at T = 290 K is presented in an inset to Fig. 6.7. The rise in magnetization near 40 kOe in the field increasing cycle and the field hysteresis are indicative of a magnetic field-induced first-order MST to AST phase transition (see Chapter 5) in this alloy. Since the MST to AST phase transition is associated with a large change in magnetization (see Fig. 6.7), and is induced both by temperature and magnetic field, the alloy is likely to exhibit a large MCE.

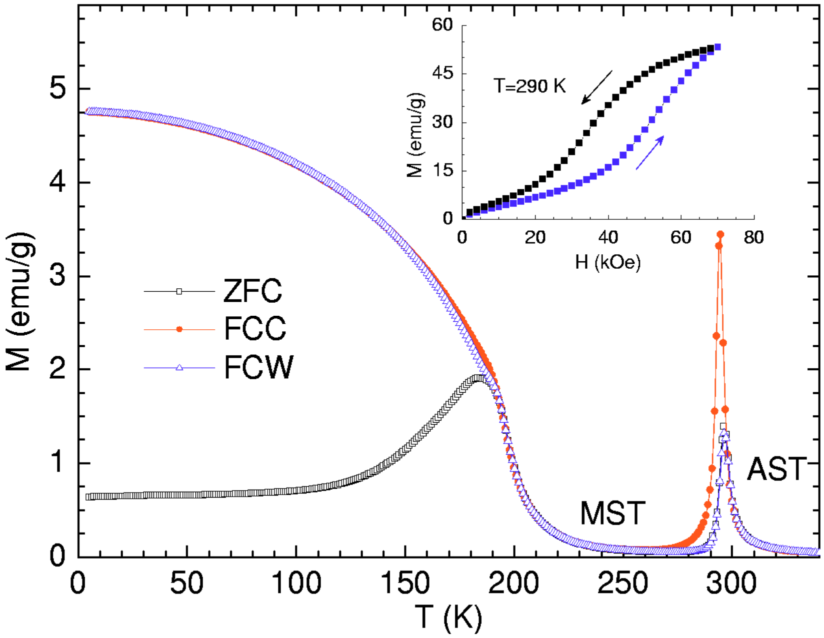

Fig. 6.7: Temperature (*T*) dependence of magnetization (*M*) of $Ni_{50}(Mn,2\%Cr)_{34}In_{16}$ alloy in applied magnetic field (*H*) of 100 Oe in ZFC, FCC and FCW protocols. AST and MST denote austenite and martensite phases respectively. Inset shows isothermal *M* vs. *H* curve at T = 290 K.

Earlier in the $Ni_{50}Mn_{34}In_{16}$ and $Ni_{50}(Mn,1\%Cr)_{34}In_{16}$ alloys, ΔS_M for a given change of magnetic field was determined from the isothermal M(H) curves using the approximate integral form of the Maxwell's relation (see Chapter 2 and Ref. 6.16). However, it has been suggested in the literature that this method can result in a somewhat erroneous estimation of ΔS_M across a first-order phase transition [6.20, 6.21]. In the light of this information, we have estimated the ΔS_M for $Ni_{50}(Mn,2\%Cr)_{34}In_{16}$ alloy from the constant field *M*(*T*) curves as discussed in section 2.6 of Chapter 2.

The *M* vs. *T* measurements were performed in the ZFC mode starting each time from a temperature well inside the MST phase. Fig. 6.8 presents the temperature dependence of ΔS_M for $Ni_{50}(Mn,2\%Cr)_{34}In_{16}$ alloy calculated in the method mentioned above for a magnetic field change of 10 kOe, 20 kOe and 50 kOe. The ΔS_M has a negative value at temperatures away from MST-AST phase transition. This is consistent with the negative value of d*M*/d*T* in this *T*-regime

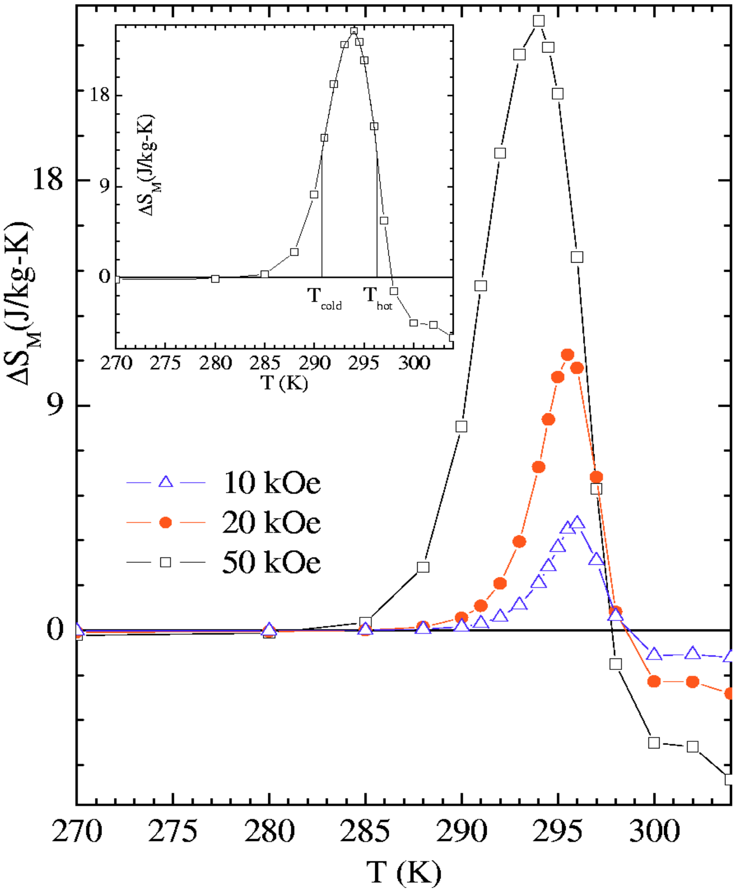

Fig. 6.8: Temperature (*T*) dependence of isothermal magnetic entropy change (ΔS_M) in $Ni_{50}(Mn,2\%Cr)_{34}In_{16}$ alloy estimated for a field change of 10 kOe, 20 kOe and 50 kOe. Inset shows estimation of refrigerant capacity of ideal refrigeration cycle using this alloy as working medium, for a field change of 50 kOe. T_{cold} and T_{hot} represent the end temperatures of the refrigeration cycle. The area under ΔS_M(T) curve between these two temperatures is a measure of refrigerant capacity of the alloy.

and is related with the ferromagnetic nature of AST and MST phases of the alloy. However, in the temperature regime of MST-AST phase transition ΔS_M shows a positive peak (inverse MCE). The peak values of ΔS_M are 4.3 J/kg-k and 11.1 J/kg-K for the field changes of 10 kOe and 20 kOe respectively. The peak value of ΔS_M increases to 24.4 J/kg-K near 294 K for a field change of 50 kOe. The peak ΔS_M value 11.1 J/kg-K for the present alloy in 20 kOe of applied field is larger than that of Gd ($\Delta S_M \approx$ 10 J/kg-K observed around 295K in 70 kOe magnetic field [6.17]), while the peak ΔS_M value of 24.4 J/kg-K in 50 kOe field is large than some of the $Gd_5Si_2Ge_2$

alloys ($\Delta S_M \approx$ 19 J/kg-K observed close to 276 K in 50 kOe magnetic field [6.22]). This peak value of ΔS_M for a field change of 50 kOe in the present alloy is considerably larger than the $\Delta S_M \approx$19 J/Kg-K value obtained in the parent $Ni_{50}Mn_{34}In_{16}$ alloy around 240 K for the same field change, but may be compared with the case of $Ni_{45}Co_5Mn_{36.7}In_{13.3}$ where a ΔS_M value of 28.4 J/Kg-K is observed near 292 K for a much higher change of magnetic field (70 kOe) [6.23]. It is also larger than the $\Delta S_M \approx$ 19 J/Kg-K value observed in the $Ni_{50}(Mn,1\%Cr)_{34}In_{16}$ alloy for a field change of 50 kOe. It is to be noted that the peak in MCE in $Ni_{50}Mn_{34}In_{16}$ and $Ni_{50}(Mn,1\%Cr)_{34}In_{16}$ alloys appears near 240 K and 270 K respectively, whereas the peak in the isothermal entropy change appears near 294 K in the present alloy. This highlights the significantly higher potential of present alloy for practical use in terms of magnetic refrigeration near ambient temperature. It is worth noting here that ΔS_M in the $Ni_{50}Mn_{34}In_{16}$ and $Ni_{50}(Mn,1\%Cr)_{34}In_{16}$ alloys as well as in $Ni_{45}Co_5Mn_{36.7}In_{13.3}$ alloy [6.23] was estimated from isothermal *M*(*H*) curves. In order to estimate ΔS_M in the $Ni_{50}Mn_{34}In_{16}$ alloy from the isothermal *M*(*H*) curves, the sample was cooled down unidirectionally from 300 K to the temperature of measurement in zero magnetic field. The *M* vs *H* measurement was initiated from this zero field cooled state. This measurement protocol is similar to the 'loop process' described by Caron et al. [6.24]. This method gives a value $\Delta S_M \approx$ 28 J/kg-K in the present case. This value is considerably higher than the 24.4 J/kg-K value obtained from the constant field *M*(*T*) curves for magnetic fields up to 50 kOe.

We have also estimated the entropy change across the martensitic transition in the present alloy from differential scanning calorimetry (DSC) experiments (see section 2.5.2 of Chapter 2). Fig. 6.9 presents the temperature dependence of the DSC signal of the present alloy in zero magnetic field. The shoulder in the temperature range 300-296 K on the cooling curve is due to

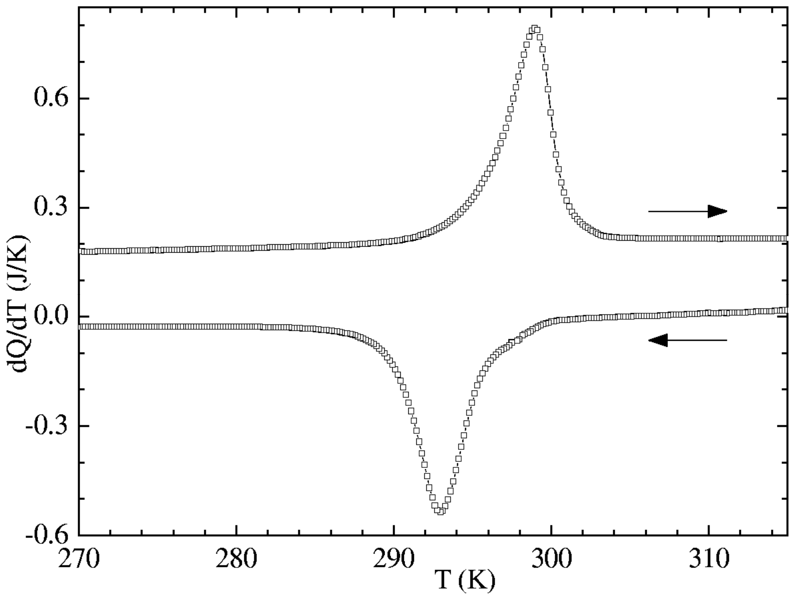

Fig. 6.9: Differential scanning calorimetric signal (dQ/dT) vs. temperature (T) plot of the $Ni_{50}(Mn,2\%Cr)_{34}In_{16}$ alloy in zero applied magnetic field.

the PM to FM transition (see Fig. 6.7) in AST phase of this alloy. This shoulder tends to overlap with the peak in the DSC signal due to the AST to MST phase transition in the alloy. On the heating curve the signature of this PM-FM transition is inseparable from the peak due to MST to AST phase transition. Because of the closeness of the PM-FM transition in the AST phase to the martensitic transition in present alloy the estimation of the change of entropy across the martensitic transition from DSC signal is likely to be erroneous. We have however estimated the approximate entropy change from the area under the peak using the following equation

$$\Delta S = \int_{T_1}^{T_2} \frac{1}{T}\left(\frac{dQ}{dT}\right) dT \tag{6.1}$$

Where T_1 and T_2 are the start and end points of the peak. These are MST (AST) start and MST (AST) finish temperatures on the cooling (heating) curve of the DSC experiment. The entropy change estimated from the peak in cooling and heating DSC curves after base line correction comes out to be 38.3 and 38.7 J/kg-K respectively with an experimental error bar of 3 J/kg-K.

When an approximate correction is made for the shoulder due to PM-FM transition in the cooling curve, the entropy change comes out to be 34.4±3 J/kg-K. However, such estimation is not at all possible for heating curve because of the reasons mentioned above.

It is observed that ΔS_M estimated (from isothermal $M(H)$ curves) for a field change of 50 kOe increases from 18.6 J/kg-K in the $Ni_{50}Mn_{34}In_{16}$ alloy (see Chapter 4) to 28.4 J/kg-K in the present $Ni_{50}(Mn,2\%Cr)_{34}In_{16}$ alloy. The peak value of ΔS_M obtained across a magnetic field induced first-order phase transition depends on the shift of the transition temperature achieved in a particular field [6.21], and the maximum of ΔS_M is limited to the transition entropy i.e. the entropy difference between the two phases (MST and AST in this case) [6.21]. The increase in the peak value of ΔS_M in the $Ni_{50}(Mn,2\%Cr)_{34}In_{16}$ alloy as compared to the $Ni_{50}Mn_{34}In_{16}$ alloy indicates to an increase in the entropy difference between the AST and MST phases because of the substitution of Mn by Cr in $Ni_{50}Mn_{34}In_{16}$ alloy. To find a possible explanation for the above observation we recall that in a ferromagnetic material, the spin disorder entropy increases as the temperature increases towards the Curie temperature of the material. In the parent $Ni_{50}Mn_{34}In_{16}$ alloy the magnetic state of MST phase becomes paramagnetic in the temperature regime very close to the MST to AST phase transition (see Chapter 3). The entropy of the MST phase due to spin disorder is therefore almost saturated in the temperature regime of the MST to AST transition, while the entropy of AST phase due to spin disorder continues to increase with temperature below $T_{CA.}$ Thus the entropy difference between AST and MST phases is expected to increase if it is possible to shift the MST to AST phase transition towards higher temperature. This seems to be the case in the present $Ni_{50}(Mn,2\%Cr)_{34}In_{16}$ alloy. We have shown in section 6.1.4 of this Chapter that the ferromagnetic interaction in the $Ni_{50}Mn_{34}In_{16}$ system decreases as Mn is substituted by Cr, and this causes the martensitic transition to shift towards higher temperature and closer to T_{CA}. The magnetic state of MST phase in $Ni_{50}(Mn, x\%Cr)_{34}In_{16}$ (x = 1, 2) alloys becomes paramagnetic at temperature well below the temperature regime of AST-MST phase transition (see Figs. 6.5(a) and 6.7 of this Chapter). The spin disorder entropy of MST phase field is saturated well below martensitic transition. The higher martensitic transition temperature in this alloy now results in increased transition entropy. Temperature dependence of the lattice and electronic entropies also add to the above change in magnetic entropy.

In order to judge the potential of the $Ni_{50}(Mn,2\%Cr)_{34}In_{16}$ alloy as a magnetic refrigerant we have also estimated the refrigerant capacity of the alloy (see the inset to Fig. 6.8). For the estimation of RC_{EFF} the average hysteresis loss was calculated from isothermal *M*(*H*) curves in the relevant temperature range and was subtracted from the RC. The value of RC_{EFF} comes out to be 90 J/kg for a field change of 50 kOe. The temperatures of the cold and hot reservoirs of the ideal refrigeration cycle for the present alloy are 290.7 K and 296.3 K respectively, as compared to 214 K and 242.3 K respectively for the parent $Ni_{50}Mn_{34}In_{16}$ alloy, and 253.8 K and 274.8K respectively for $Ni_{50}(Mn,1\%Cr)_{34}In_{16}$. This RC_{EFF} is somewhat smaller as compared to nearly 100 J/kg of the $Ni_{50}Mn_{34}In_{16}$ alloy for the same magnetic field change (see Chapter 4). However, the fact that working temperature regime in $Ni_{50}(Mn,2\%Cr)_{34}In_{16}$ alloy is at ambient temperature as compared to around 240 K in parent $Ni_{50}Mn_{34}In_{16}$ alloy, makes the $Ni_{50}(Mn,2\%Cr)_{34}In_{16}$ alloy a better potential candidate for practical application.

6.3 Substitution of Ni by Cu in the $Ni_{50}Mn_{34}In_{16}$ alloy

A polycrystalline sample with nominal composition of $Ni_{49}CuMn_{34}In_{16}$ was prepared by arc melting under argon atmosphere. The sample was found to be homogeneous with average composition $Ni_{48.3}Cu_{0.9}Mn_{33.9}In_{16.9}$ as determined from energy dispersive x-ray (EDX) analysis.

In the rest of the discussion this alloy will be presented as NiCuMnIn. The parent alloy $Ni_{50}Mn_{34}In_{16}$, with which the present alloy is compared, will be continued to be termed as NiMnIn. Room-temperature XRD pattern (shown in inset (a) to Fig. 6.10) shows presence of two phases in the NiCuMnIn alloy, which arises due to an admixture of AST and MST phases (the study of various physical properties described below indeed shows evidence of a AST to MST phase transition around room temperature). The AST phase with $L2_1$ ordering has a lattice constant of 6.01 Å. The MST phase with orthorhombic structure has lattice constants a = 17.67 Å, b = 10.78 Å and c = 4.62 Å respectively.

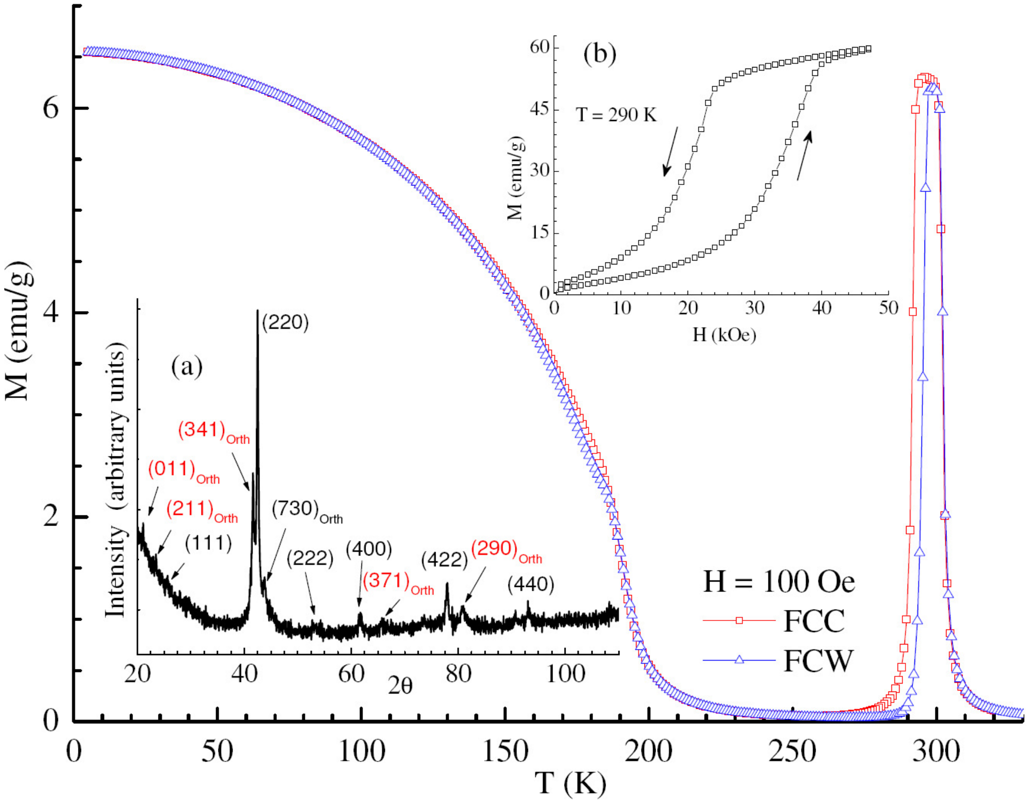

Fig. 6.10: Magnetization (M) vs. temperature (T) plot for $Ni_{49}CuMn_{34}In_{16}$ alloy obtained with an applied magnetic field (H) of 100 Oe in FCC and FCW protocols. The inset (a) shows room temperature XRD pattern of the alloy indexed to the $L2_1$ structure. The XRD peaks with subscript 'Orth' are indexed to the orthorhombic structure of the MST phase of the alloy. The inset (b) shows the isothermal magnetization vs. magnetic field plot for the alloy at 290 K.

6.3.1 Martensite-austenite phase transition in the $Ni_{49}CuMn_{34}In_{16}$ alloy

The main frame of Fig. 6.10 presents M vs. T plots for NiCuMnIn obtained in FCC and FCW protocols in an applied magnetic field of $H = 100$ Oe. The sharp rise in $M(T)$ while cooling down with a point of inflection around 300 K, is attributed to the PM to FM transition. Around 295 K, $M(T)$ undergoes a very sharp drop and this marks the onset of martensitic transition in this alloy system. This martensitic transition is accompanied by distinct thermal hysteresis between $M_{\mathrm{FCC}}(T)$ and $M_{\mathrm{FCW}}(T)$, which highlights the first-order nature of this martensitic transition. On the other hand, the PM to FM transition (which takes place entirely within the AST phase) is second-order in nature, as is evidenced by the absence of any thermal hysteresis. The magnetization acquires a very low value in the MST phase in the T regime just below the martensitic transition point. This is suggestive of the paramagnetic or antiferromagnetic nature of the MST phase in this T regime. M increases with lowering in T and inverse dc susceptibility (H/M) in the T regime 245–215 K shows a linear T dependence. Such a behavior is usually a characteristic of paramagnetic phase in a material and not expected in the antiferromagnetic phase. With further decrease in T a ferromagnetic transition takes place in the MST phase around 190 K. The existence of the spontaneous magnetization in the T-regime below 190 K has been confirmed through the study of Arrott plots. In the inset (b) to Fig. 6.10, we show isothermal M vs H plot at 290 K. This M-H plot shows a clear evidence of magnetic field- induced reverse martensitic transition. This in turn suggests the potential of this system for large MCE, large magnetoresistance and field-induced strain. Further, from $M(H)$ curve at 5 K, it has been found that saturation magnetization of this NiCuMnIn alloy is smaller than that of parent $Ni_{50}Mn_{34}In_{16}$ alloy at the same temperature and probably indicates decrease in ferromagnetic interaction as compared to the parent alloy. This is in consonance with the observation made in alloys prepared by substituting Mn by Cr and Fe (see Fig. 6.4 and sections 6.1.2 and 6.1.3) regarding shift of MST-AST phase transition and change in ferromagnetic interaction.

6.3.2 Functional properties of the $Ni_{49}CuMn_{34}In_{16}$ alloy

The main frame of Fig. 6.11 presents *M* vs *T* plots for the NiCuMnIn alloy in various applied *H* up to 45 kOe concentrating mainly on the martensitic transition. These *M* vs *T* plots were obtained in the ZFC protocol starting each time from a temperature well inside the MST phase. With the increase in *H* the martensitic transition temperature is clearly lowered. Isothermal entropy change *ΔS* induced by applied H is determined using a set of *M* vs *T* plots obtained with different applied *H* of closely spaced values (see Fig. 6.11). Fig. 6.12 shows the estimated *ΔS* as a function of *T* in an applied *H* of 45 kOe. The inverse MCE peaks around 292 K with a value of 25.8 J/kg-K. This is considerably larger than peak value of 19 J/kg-K observed in

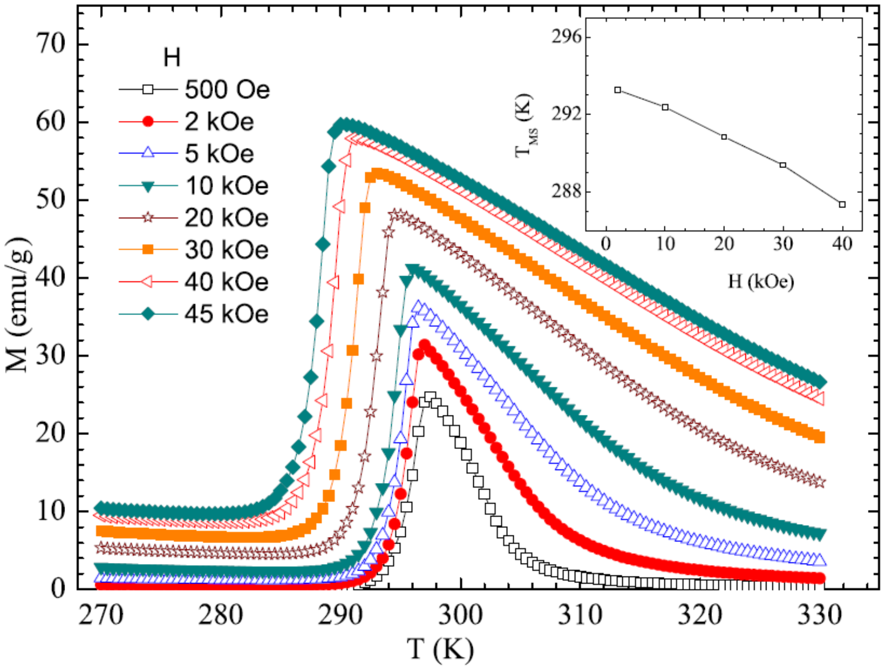

Fig. 6.11: Magnetization (*M*) vs. temperature (*T*) plot for the $Ni_{49}CuMn_{34}In_{16}$ alloy at various temperatures obtained in the ZFC protocol. The inset shows the onset temperature of martensitic transition (T_{MS}) while cooling as a function of applied magnetic field.

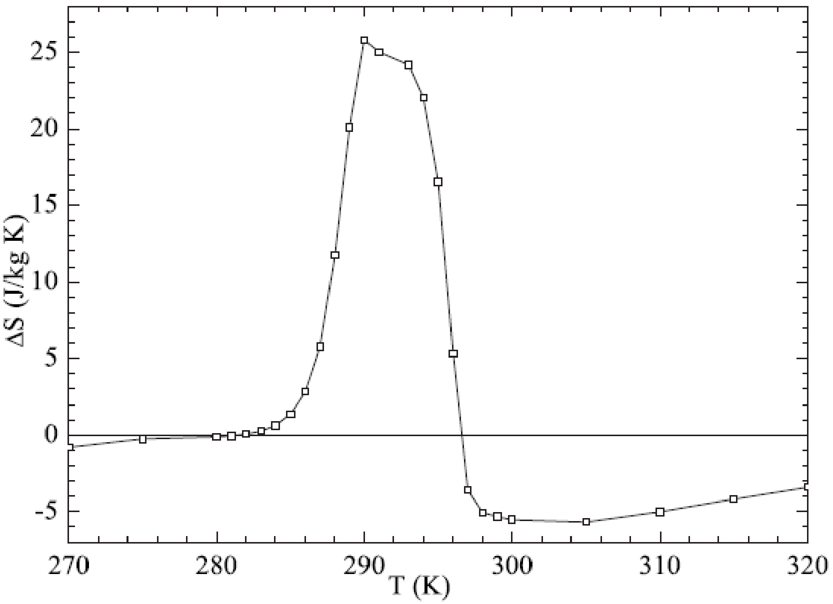

Fig. 6.12: Change in entropy (*ΔS*) vs. temperature (*T*) plot in the $Ni_{49}CuMn_{34}In_{16}$ sample obtained with an applied field of 45 kOe.

the parent alloy NiMnIn around 240 K in an applied field of 80 kOe. We have further crosschecked the value of *ΔS* in NiCuMnIn alloy by estimating it from the martensitic transition temperature T_{MS} vs. *H* plot (see inset of Fig. 6.11) using Clausius-Clapeyron equation. Here we identify T_{MS} from the *M*(*T*) plots as the temperature of onset of the MST phase while cooling. Taking the difference between magnetizations of AST and MST phases at *H* = 45 kOe *ΔM* = 50 emu/gm and the value of slope (as deduced from the T_{MS} vs. *H* plot) d*H*/d*T* = 5.3 kOe/K, the estimated value of *ΔS* = 26.5 J /kg K. This peak value of MCE in the present NiCuMnIn alloy can be compared with the *ΔS* = 28.4 J /kg K in $Ni_{45}Co_5Mn_{36.7}In_{13.3}$ alloy observed around 292 K [6.23]. This value in the later case was estimated from Maxwell's equation using the isothermal M(H) curves with a maximum applied field of 70 kOe.

Fig. 6.13 shows the temperature dependence of electrical resistance between 50 and 300 K obtained in the ZFC and FCC protocol in applied *H* of 0 and 50 kOe. The sharp rise in the

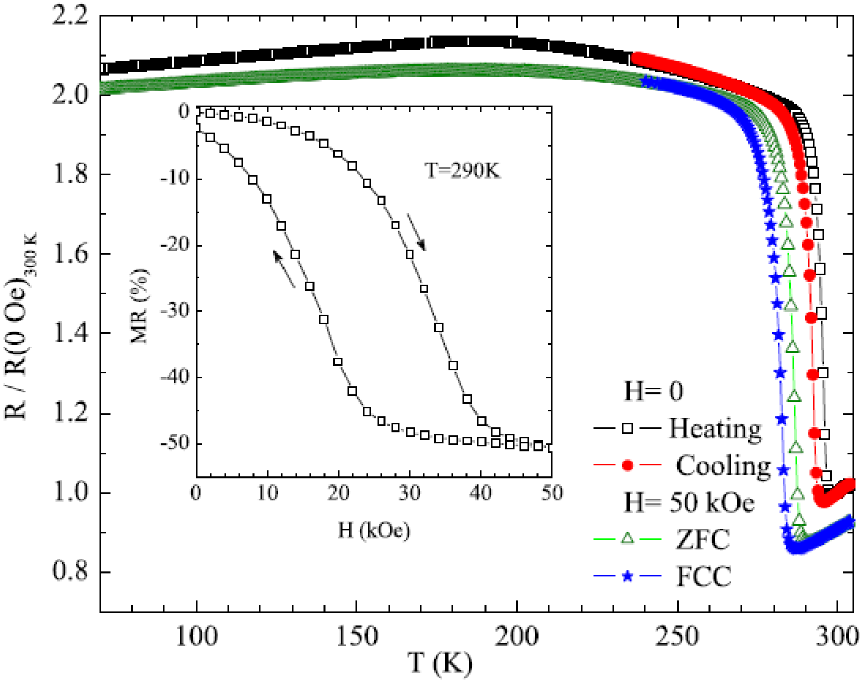

Fig. 6.13: Resistance (*R*) vs. temperature (*T*) plot of $Ni_{49}CuMn_{34}In_{16}$ alloy in 0 and 50 kOe magnetic field (*H*) obtained in the ZFC and FCC protocols. The value of resistance is normalized with respect to the resistance in zero *H* at 300 K. The inset shows isothermal magnetorsistance (MR) vs. *H* plot at $T = 290$ K.

resistance around 295 K while cooling, marks the onset of martensitic transition, which agrees well with that determined from magnetization measurements. The distinct thermal hysteresis between the heating and cooling resistance curves again emphasizes the first-order nature of the martensitic transition. The applied *H* causes the martensitic transition to take place at a lower *T* and this gives rise to large negative magnetoresistance. The inset of Fig. 6.13 shows the magnetoresistance as a function of *H* at $T = 290$ K. The magnetoresistance reaches a maximum value of 50%. This can be compared with the peak value of MR = 64% observed in the parent NiMnIn alloy around 230 K with same maximum applied *H* of 50 kOe (see section 4.1 of Chapter 4).

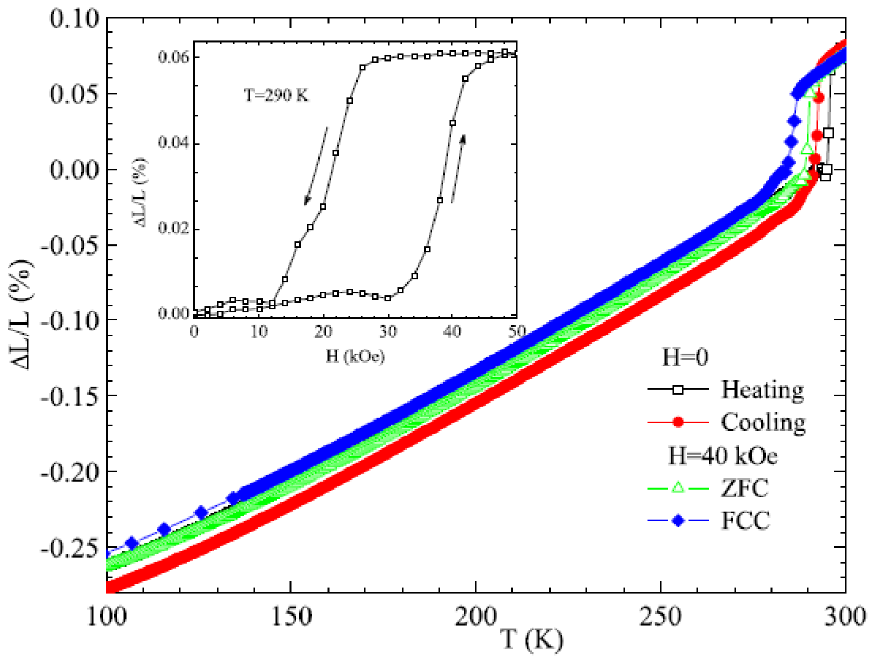

Fig. 6.14: Strain (*ΔL/L*) vs. temperature plot of Ni$_{49}$CuMn$_{34}$In$_{16}$ alloy in 0 and 40 kOe magnetic field obtained in the ZFC and FCC protocols. The inset shows isothermal strain *ΔL/L* vs. magnetic field plot at *T* = 290 K.

Fig. 6.14 presents the results of temperature and magnetic field dependent strain measurement in NiCuMnIn alloy in H = 0 and 40kOe. The temperature dependent strain is defined as relative length change *ΔL/L* with respect to length at 293 K and the isothermal magnetic field dependent strain is taken as the relative length change *ΔL/L* with respect to length in zero field. *ΔL/L* increases with increasing *T* starting from well inside the MST phase in zero magnetic field and shows a small dip at 293 K followed by a sharp rise of about 0.08% at 296 K. Thereafter it continues to increase smoothly with further increase in *T*. A similar behavior is seen on decreasing *T* from well inside the AST phase with a distinct thermal hysteresis between 292 and 298 K. In line with the results of magnetization and resistance measurements we attribute this sharp change in *ΔL/L* and the associated thermal hysteresis with the martensitic transition in NiCuMnIn alloy.

In an earlier study on various Ni-Mn-based Heusler alloys it was observed that the martensitic transition temperature increased linearly with the increase in the valence electron concentration (*e/a*) [6.2]. The actual composition of the present NiCuMnIn alloy is $Ni_{48.3}Cu_{0.9}Mn_{33.9}In_{16.9}$ and accordingly the *e*/*a* ratio of this alloy composition is 7.81. This value is slightly lower than the estimated value of *e/a* = 7.86 for the parent $Ni_{50}Mn_{34}In_{16}$. Accordingly the martensitic transition temperature in this NiCuMnIn alloys should have been marginally lower, which is in contradiction to the observed experimental results. On the other hand, in line with the recent study on the Ni-Mn-Sn alloys [6.6], the increased martensitic transition temperature can be attributed to the enhanced hybridization of 3*d* states at the Ni sites and 3*d* states of antiferromagnetically coupled Mn atoms at the In sites. Accordingly we suggest that the enhanced hybridization originating from the Cu doping at the Ni site is probably the primary cause of the increase in the martensitic transition temperature from 240 K in the parent NiMnIn alloy to near room temperature in the present NiCuMnIn alloy. Further, the change in ferromagnetic interaction as observed in this alloy along with that observed in Cr and Fe substituted alloys provide evidences that magnetism plays a crucial role in the MST-AST phase transition in Ni-Mn-In alloys.

6.4 Effect of external pressure

As mentioned earlier the temperature of MST-AST transiton in Ni-Mn-X alloys is affected by pressure also. We have measured the magnetization of $Ni_{50}Mn_{34}In_{16}$ alloy using a pressure cell arrangement under different values of the hydrostatic pressure (*P*), up to a maximum pressure of 10 kbar (see section 2.4.3 of Chapter 2). The results of these measurements are presented here.

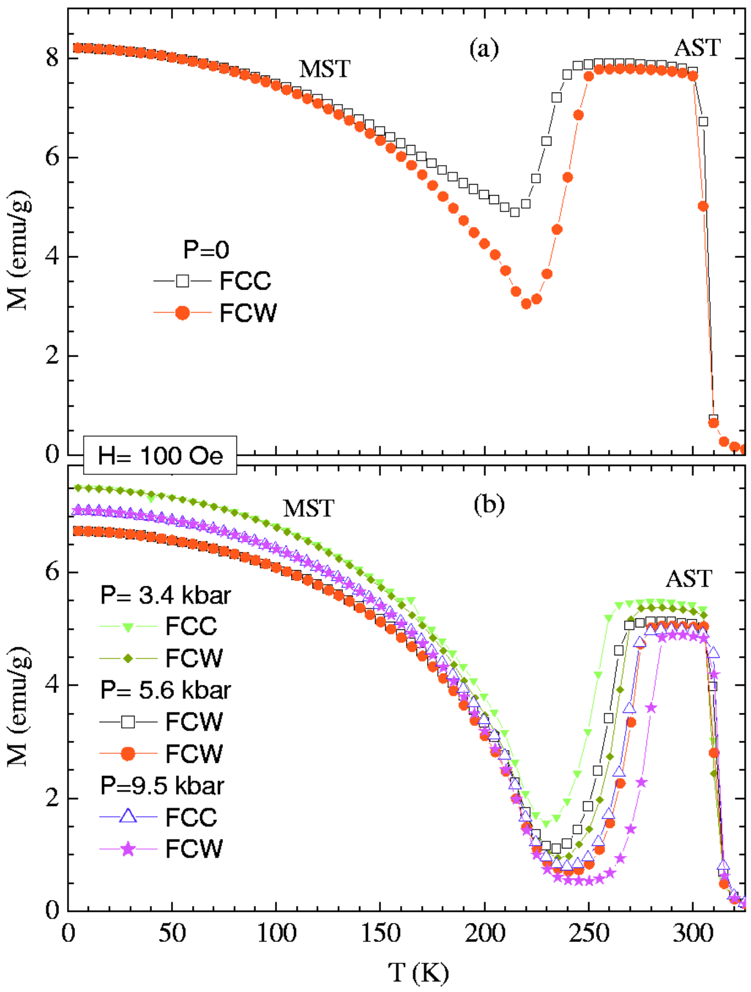

Fig. 6.15: Temperature (*T*) dependence of magnetization (*M*) of $Ni_{50}Mn_{34}In_{16}$ alloy in field cooled cooling (FCC) and field cooled warming (FCW) protocols in applied magnetic field (*H*) of 100 Oe (a) at ambient pressure ($P = 0$) and (b) under various applied pressures.

6.4.1 Effect of pressure on the martensite-austenite phase transition in the $Ni_{50}Mn_{34}In_{16}$ alloy

Fig. 6.15(a) presents the temperature dependence of magnetization of $Ni_{50}Mn_{34}In_{16}$ alloy in the temperature range of 5-325 K in 100 Oe magnetic field at ambient pressure (designated $P = 0$). At $P = 0$ the rise in M around 300 K with decreasing temperature is related with a paramagnetic to ferromagnetic phase transition in the AST phase of the alloy (see Chapter 4). As discussed earlier the sharp drop in *M* around 240 K with decreasing temperature and the associated thermal hysteresis in *M* are attributed to the first-order nature [6.14, 6.15] of the AST to MST phase transition in the alloy. Fig. 6.15(b) presents the temperature dependence of magnetization of the $Ni_{50}Mn_{34}In_{16}$ alloy in the temperature range of 5-325 K in 100 Oe magnetic field, under *P* = 3.4 , 5.6 and 9.5 kbar pressure. The comparison of the *M*(*T*) curves in Fig. 6.15(a) and 6.15(b) indicates that the application of external pressure has negligible effect on the PM-FM transition in the AST phase of the alloy. However, the MST-AST phase transition temperature shifts towards higher temperature with increasing pressure.

Fig. 6.16 presents the temperature dependence of magnetization in the FCC and FCW protocols in the representative magnetic fields of 10 kOe and 50 kOe, under applied pressures of 0, 3.4, 5.6 and 9.5 kbar. In all values of the applied pressures the magnetization in the AST phase is larger as compared to that in the MST phase. Under a constant pressure, the MST-AST phase transition in the $Ni_{50}Mn_{34}In_{16}$ alloy shifts towards lower temperature with increasing magnetic

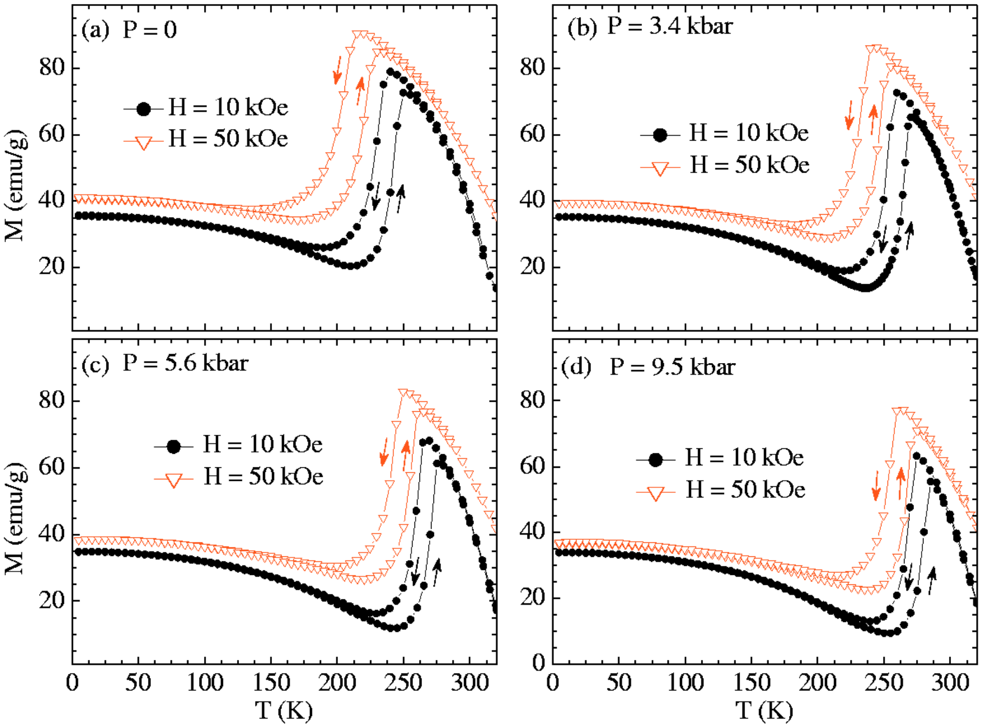

Fig. 6.16: Temperature (*T*) dependence of magnetization (*M*) of $Ni_{50}Mn_{34}In_{16}$ alloy in applied magnetic field (*H*) of 10 kOe and 50 kOe (a) at ambient pressure (*P* = 0), (b) under *P* = 3.4 kbar, (c) under *P* = 5.6 kbar and (d) under *P* = 9.5 kbar.

field. From the *M*(*T*) curves in various applied magnetic fields under constant pressures, we have determined the magnetic field and pressure dependence of the four characteristic temperatures; MST start (T_{MS}), MST finish (T_{MF}), AST start (T_{AS}) and AST finish (T_{AF}) for the martensitic transition in the present alloy (the method of determination of these temperatures from isofield *M*(*T*) curves has been discussed earlier (see section 3.1.6 of Chapter 3 and section 5.1.4 of Chapter 5).

Table 6.1 presents the magnetic field dependence of the four characteristic temperatures T_{MS}, T_{MF}, T_{AS} and T_{AF} obtained under $P = 0$, 3.4, 5.6 and 9.5 kbar respectively. This table shows the combined effect of magnetic field and pressure on the MST-AST phase transition in $Ni_{50}Mn_{34}In_{16}$ alloy. Further, Table 6.1 shows that all the four characteristic temperatures decrease with increasing magnetic field under all pressures applied in the present set of experiments. We have also estimated the pressure dependence of the four characteristic temperatures of the martensitic transition in constant magnetic fields and the same is presented in

Table 6.1: Magnetic field (*H*) dependence of the four characteristic temperatures MST start (T_{MS}), MST finish (T_{MF}), AST start (T_{AS}) and AST finish (T_{AF}) under different pressures (*P*) in $Ni_{50}Mn_{34}In_{16}$ alloy.

	$P = 0$				$P = 3.4$ kbar				$P = 5.6$ kbar				$P = 9.5$ kbar			
T(K) *H* (kOe)	T_{MS}	T_{MF}	T_{AS}	T_{AF}	T_{MS}	T_{MF}	T_{AS}	T_{AF}	T_{MS}	T_{MF}	T_{AS}	T_{AF}	T_{MS}	T_{MF}	T_{AS}	T_{AF}
0.1	255	170	220	270	275	210	235	280	280	220	240	285	285	230	255	290
1	245	145	215	260	270	185	235	275	275	210	240	280	280	220	255	290
10	240	135	205	255	260	165	234	272	270	185	235	280	275	200	250	290
20	235	130	195	250	…	…	…	…	…	…	…	…	…	…	…	…
50	215	105	165	235	245	110	210	255	250	140	220	265	265	155	235	275
70	205	80	150	225	230	95	190	245	245	125	205	255	255	135	225	270

Table 6.2: Pressure (P) dependence of the four characteristic temperatures MST start (T_{MS}), MST finish (T_{MF}), AST start (T_{AS}) and AST finish (T_{AF}) in various magnetic fields (H) in $Ni_{50}Mn_{34}In_{16}$ alloy.

	H = 100 Oe				H = 10 kOe				H = 50 kOe				H = 70 kOe			
T(K) P (kbar)	T_{MS}	T_{MF}	T_{AS}	T_{AF}	T_{MS}	T_{MF}	T_{AS}	T_{AF}	T_{MS}	T_{MF}	T_{AS}	T_{AF}	T_{MS}	T_{MF}	T_{AS}	T_{AF}
0	255	170	220	270	240	135	205	255	215	105	165	235	205	80	150	225
3.4	275	210	235	280	260	165	234	272	245	110	210	255	230	95	190	245
5.6	280	220	240	285	270	185	235	280	250	140	220	265	245	125	205	255
9.5	285	230	255	290	275	200	250	290	265	155	235	275	255	135	225	270

Table 6.2. In a constant magnetic field, all the four characteristic temperatures increase with increasing pressure. The average rate of shift of T_{MS} in H = 100 Oe with pressure is nearly 3.5 K/kbar and it increases to 5.5 K/kbar in H = 70 kOe. The rate of shift of T_{MF} is approximately 6 K/ kbar in all fields. The rate of shift of T_{AS} varies from 3.5 K/kbar in H = 100 Oe to 7.7 K/kbar in H = 70 kOe. The rate of shift of T_{AF} also increases from 2 K/kbar in H = 100 Oe to 4.5 K/kbar in H = 70 kOe. The value of rate of shift of transition temperature with pressure is comparable with the value reported in literature for an alloy with the same nominal composition [6.3] but is larger than that observed in Ni-Mn-Sn alloy [6.25]. Table 6.1 reveals that magnetic field and external pressure have opposite effects on the MST-AST phase transition in the present alloy (it is more clearly seen from Fig. 6.16 and Table 6.2). While magnetic field shifts the MST-AST phase transition towards the lower temperature side, application of pressure shifts the same towards higher temperature. The increase in the MST-AST phase transition temperature with increasing pressure in the alloy is correlated to the decrease in volume across AST to MST phase transition (inferred from decreases in strain from AST to MST; see section 4.3 of Chapter 4) through the Clausius–Clapeyron equation for a first-order phase transition [6.3]. Using the actual composition of present alloy as determined with EDX analysis, and the lattice constant of unit

cell as determined from XRD study (see section 3.1 of Chapter 3), the specific volume of alloy comes out to be 1.23 x10^{-4} m^3/kg. Considering the decrease in volume in AST to MST phase transition to be 0.3% as reported for alloy with same nominal composition [6.3] and taking the value of $dT/dP \approx 3.5$ K/kbar (this is the average rate of shift of T_{MS} and T_{AS} for $H = 100$ Oe) the change in entropy, across the MST-AST phase transition employing Clasius-Clapeyron equation, is estimated to be 10.5 J/kg-K. The decrease in transition temperature with increasing magnetic field is related with the higher value of magnetization in the AST phase of the alloy. Thus the opposite effects of increasing pressure and magnetic field on the MST-AST phase transition in the present alloy are related to the fact that while pressure stabilizes the MST phase for its lower volume, magnetic field stabilizes the AST phase due to the larger magnetization in the AST phase. Further, from *M*(*H*) curve at 5 K, it has been found that saturation magnetization of the alloy decreases with increasing pressure and probably indicates decreasing ferromagnetic interaction with increasing pressure. This is in consonance with the observation made in alloys prepared by substituting Mn by Cr and Fe(see Fig. 6.4, and sections 6.1.2 and 6.1.3) and substitution of Ni by Cu (see section 6.3.1) regarding the shift of MST-AST phase transition and the change in ferromagnetic interactions.

6.4.2 Effect of pressure on the magnetocaloric effect in the $Ni_{50}Mn_{34}In_{16}$ alloy

As discussed earlier, the magnetism in Ni-Mn-X (X = In,Sn etc.) alloys arises mainly because of the magnetic moment on the Mn sub-lattice. The magnetic properties of the Ni-Mn-X alloys are dependent on the inter-atomic distance between the Mn atoms [6.12, 6.26]. The applied pressure affects the inter-atomic separation, and as a result the magnetic interactions are modified. Therefore the magnetocaloric properties of the alloy are also expected to change with pressure. The isothermal change in magnetic entropy was estimated from the constant field $M(T)$ curves obtained at constant pressures using the following equation (as discussed in Chapter 2):

$$\Delta S_M(T,H,P) = \int_0^H \left[\frac{\delta M(T)}{\delta T}\right]_{H,P} dH \qquad (6.2)$$

Each of these iso-field $M(T)$ measurements was performed starting from a zero field cooled state at a temperature well inside the MST phase. The temperature dependence of ΔS_M (calculated in the method described above) for the present alloy under various pressures, and for the magnetic field changes of 20 and 50 kOe, is presented in Fig. 6.17. The ΔS_M has a negative value at temperatures away from the MST-AST phase transition at each pressure. This is consistent with

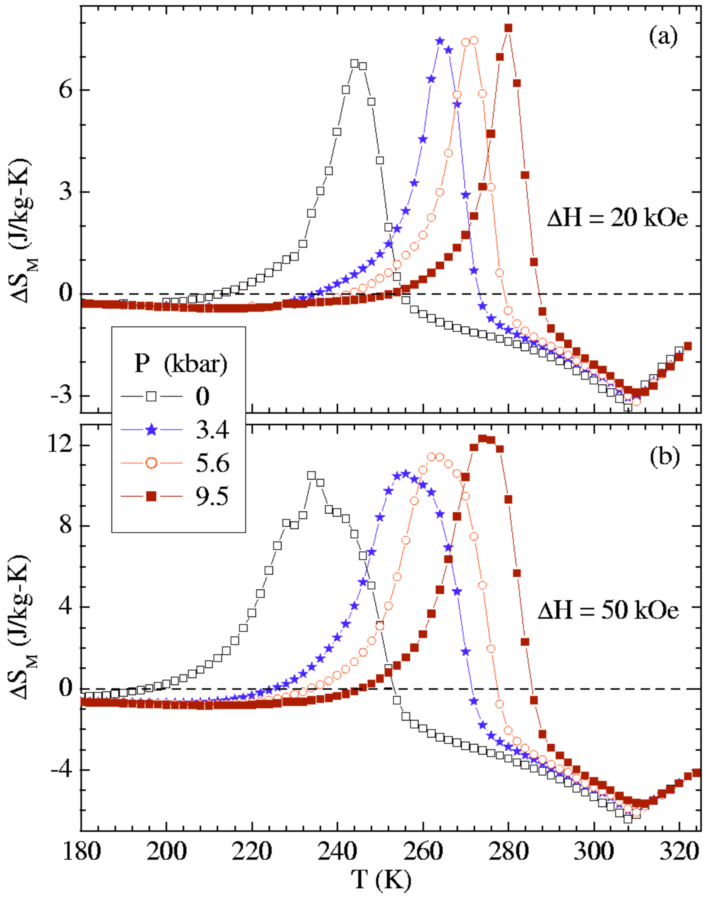

Fig. 6.17: (a) Temperature (T) dependence of isothermal magnetic entropy change (ΔS_M) in $Ni_{50}Mn_{34}In_{16}$ alloy under various applied pressures (P) estimated for a magnetic field change of (a) 20 kOe and (b) 50 kOe.

the negative value of dM/dT (see eqn. 6.2 which shows that ΔS_M will be negative for negative dM/dT) at temperatures away from the MST-AST phase transition where the material is ferromagnetic. However, in the temperature regime of MST-AST phase transition ΔS_M shows a positive peak (inverse MCE). For a magnetic field change of 20 kOe (see Fig. 6.17(a)), ΔS_M peaks at 6.8 J/kg-K near 244 K at ambient pressure which increases to 7.8 J/kg-K at 280 K under pressure of 9.5 kbar. There is another peak in ΔS_M(T) near 310 K which corresponds to conventional MCE due to PM to FM transition in the AST phase of the alloy. This peak value changes from -3.3 J/kg-K at ambient pressure to -2.9 J/kg-K under P = 9.5 kbar. For a magnetic field change of 50 kOe (see Fig. 6.17(b)), ΔS_M peaks near 234 K, 256 K, 264 K and 274 K under zero, 3.4, 5.6, 9.5 pressure respectively. The peak value of ΔS_M increases from 10.4 J/kg-K under zero pressure to 12.3 J/kg-K under a pressure of 9.5 kbar. The isothermal entropy change at ambient pressure matches closely with that estimated using the Clasius-Clapeyron equation. The peak ΔS_M value corresponding to conventional MCE near 310 K changes form -6.5 J/kg-K at ambient pressure to -5.6 J/kg-K under P = 9.5 kbar. The peak ΔS_M values for inverse MCE in the present alloy sample for field change of 20 kOe are comparable with that of Gd (nearly 10 J/kg-K near 292 K) for a field change of 70 kOe [6.17] and the peak ΔS_M values for a field change of 50 kOe are larger than the same. This peak value of ΔS_M for a field change of 50 kOe at all pressures, is smaller than the case of $Ni_{45}Co_5Mn_{36.7}In_{13.3}$ alloy where a ΔS_M value of 28.4 J/kg-K is observed near 292 K for a magnetic field change of 70 kOe [6.23]. This is also smaller than $\Delta S_M \approx$ 19 J/kg-K of $Gd_5Si_2Ge_2$ alloy observed close to 276 K in 50 kOe magnetic field [6.22]. However, these ΔS_M values for Gd, $Ni_{45}Co_5Mn_{36.7}In_{13.3}$ and $Gd_5Si_2Ge_2$ alloys were calculated from isothermal $M(H)$ curves. In the present case, ΔS_M calculated from isothermal $M(H)$ curves for a field change of 50 kOe under 3.4, 5.6 and 9.5 kbar pressure, comes out to be nearly 16.5 J/kg-K, 19.2 J/kg-K and 20 J/kg-K respectively. These values are comparable to the ΔS_M = 18.5 J/kg-K obtained for this alloy at $P = 0$ using the isothermal $M(H)$ curves (see Chapter 4). Fig 6.17 shows that in $Ni_{50}Mn_{34}In_{16}$ alloy the peak value of ΔS_M as determined using isofield $M(T)$ curves increases with pressure. In Co doped Ni-Mn-Sb alloy [6.27] and some compositions of the Ni-Mn-Ga alloy [6.28], the peak value of ΔS_M decreases with pressure. In some other compositions of Ni-Mn-Ga, the peak ΔS_M is also reported to increase with pressure [6.28]. The ΔS_M(T) curve for $Ni_{50}Mn_{34}In_{16}$ for field change of 50 kOe at ambient pressure shows an anomalous feature near the peak (at about 225 K, see Fig. 6.17(b)). The origin of this feature is not quite clear. However, from the experimental data it appears to be related to the change of slope (dM/dT) of the iso-field $M(T)$ curves at these temperatures (near T_{AS} and T_{AF}) for magnetic fields in excess of 20 kOe. A shoulder has also been observed in the $\Delta S_M(T)$ curve estimated from the isothermal $M(H)$ curves obtained at these temperatures (see Chapter 4). We tend to believe that this shoulder is a feature associated with the magnetic field induced MST to AST phase transition in the present alloy and probably is not an experimental artefact. However, this anomaly is not observed in the $\Delta S_M(T)$ curves obtained under externally applied pressure. This may be because of the fact that the MST to AST phase transition (and hence respective temperature of ΔS_M peak ($T_{MCE\text{-}peak}$)), under pressures applied in present set of experiments, is shifted to significantly higher temperatures. In this higher temperature regime the above mentioned change of slope (dM/dT) of the iso-field $M(T)$ curves is not observed near T_{AS} and T_{AF} for any value of applied magnetic field.

We now investigate the effect of pressure on the refrigerant capacity (RC) of the $Ni_{50}Mn_{34}In_{16}$. In order to estimate the effective refrigerant capacity (RC_{EFF}), the average hysteresis loss was calculated from isothermal $M(H)$ curves at different pressures in the relevant

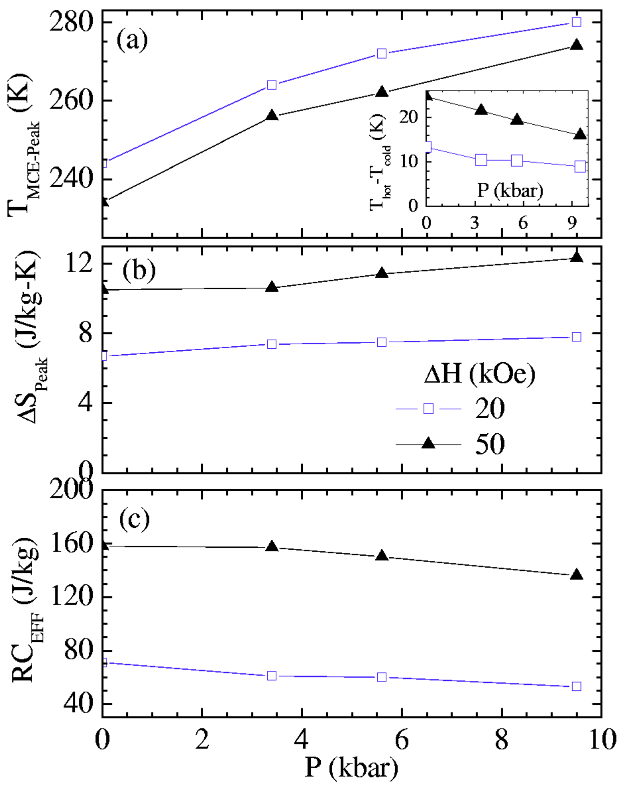

Fig. 6.18: Pressure (*P*) dependence of (a) temperature of peak in isothermal magnetic entropy change ($T_{\text{MCE-peak}}$), (b) peak value of isothermal magnetic entropy change (ΔS_{peak}), and (c) effective refrigerant capacity (RC_{EFF}) for field change (ΔH) of 20 kOe and 50 kOe for $Ni_{50}Mn_{34}In_{16}$ alloy. Inset to (a) shows *P* dependence of temperature difference between temperature of the cold reservoir (T_{cold}) and temperature of the hot reservoir (T_{hot}).

temperature range and was subtracted from the respective RC. Fig. 6.18 compares the value of $T_{\text{MCE-peak}}$, peak value of ΔS_M(ΔS_{peak}) and RC_{EFF} in $Ni_{50}Mn_{34}In_{16}$ alloy under various pressures for field changes of 20 and 50 kOe. As pointed out in the earlier discussion, ΔS_{peak} increases slowly with increasing pressure for both the field changes. Moreover, in harmony with Fig. 6.17, the temperature $T_{\text{MCE-peak}}$ increases with increasing pressure. The rate of increase of $T_{\text{MCE-peak}}$ with pressure is near 3.8 K/kbar for a field change of 20 kOe, and 4 K/kbar for a field change of 50 kOe. This matches with rate of shift of T_{MS} with pressure obtained from Table 6.2. It is worth noticing that for a pressure change from zero to 9.5 kbar the $T_{\text{MCE-peak}}$ increases from 244 K to 280 K for a field change of 20 kOe and from 234 K to 274 K for a field change of 50 kOe.

Though $\mathrm{RC_{EFF}}$ decreases slowly but remains near 60 J/kg and 150 J/kg for field changes of 20 kOe and 50 kOe respectively. The decrease in $\mathrm{RC_{EFF}}$ can be correlated with the narrowing of the temperature range T_{hot}-T_{cold} with increase in pressure (see inset to Fig. 6.18(a)). Here T_{cold} and T_{hot} are the temperatures of the cold and the hot reservoirs respectively in an ideal refrigeration cycle using the alloy under a particular pressure as a working medium. The temperatures of the cold and hot reservoirs of the ideal refrigeration cycle for the present alloy increases with pressure. These temperatures increase to 265.7 K and 281.7 K respectively under 9.5 kbar pressure, as compared to 223 K and 247.7 K respectively for magnetic field excursion of 50 kOe for $P = 0$. Thus the temperature regime of MCE in $\mathrm{Ni_{50}Mn_{34}In_{16}}$ alloy increases towards room temperature with increasing pressure while the $\mathrm{RC_{EFF}}$ remains nearly constant. The observation that the working temperature regime in $\mathrm{Ni_{50}Mn_{34}In_{16}}$ alloy increases to 280 K with pressure as compared to around 240 K in parent $\mathrm{Ni_{50}Mn_{34}In_{16}}$ alloy, suggests that the temperature regime can be further increased to room temperature with still higher pressure. This also gives a direction for tuning the temperature regime of MCE in $\mathrm{Ni_{50}Mn_{34}In_{16}}$ alloy with the chemical pressure generated by the substitution of atoms in the alloy. An isoelectronic elemental substitution with a smaller atom is equivalent to external pressure, Such a substitution is expected to elevate the AST to MST phase transition temperature as has been reported for elemental substitution of In by Ga [6.7].

6.4.3 Universal scaling function for the $\Delta S_{\mathrm{M}}(T)$ curves under different pressure

It has been observed here that though the pressure dependence of $T_{\mathrm{MCE\text{-}peak}}$ follows that of T_{MS}, the pressure dependences of ΔS_{peak} and $\mathrm{RC_{EFF}}$ do not really follow the pressure dependence of any of the characteristic temperatures of the MST-AST phase transition in any field. It is therefore important here to find out whether the magnetic field-temperature dependence of MCE continues to exhibit the same qualitative behaviour (as it were for $P = 0$) when external pressure is applied. This is done by investigating whether the temperature dependence of isothermal magnetic entropy change, corresponding to a particular change of field, follows the same universal functional form (curve) both in the presence and absence of externally applied pressure. Following the procedure described in literature [6.29, 6.30], first the Y-axis in the Fig. 6.17 is normalized with respective ΔS_{peak} value. Then the temperature axis is in Fig. 6.17 is rescaled for a new variable θ as

$$\theta = \begin{cases} -(T-T_{peak})/(T_{r1}-T_{peak}); & T \le T_{peak} \\ (T-T_{peak})/(T_{r2}-T_{peak}); & T > T_{peak} \end{cases} \tag{6.3}$$

where $T_{\text{peak}} = T_{\text{MCE-peak}}$ for the respective $\Delta S_M(T)$ curve. The temperatures T_{r1} and T_{r2} are the two reference temperatures above and below T_{peak} such that $\theta(T_{r1,\ r2}) = \pm 1$. Two reference temperatures are used to avoid the effect of demagnetization factor and the presence of any minority magnetic phase [6.30]. We have taken two reference temperatures such that $\Delta S_M(T_{r1,\ r2})/\Delta S_{\text{peak}} = 0.5$ for the respective $\Delta S_M(T)$curve with $T_{r1} < T_{\text{peak}} < T_{r2}$. With this criterion $T_{r1} = T_{\text{cold}}$ and $T_{r2} = T_{\text{hot}}$ for the respective $\Delta S_M(T)$ curve. The $\Delta S_M/\Delta S_{\text{peak}}\,(\theta)$ curves for field change of 20 and 50 kOe under $P = 0$, 3.4, 5.6, 9.5 kbar are presented in Fig. 6.19. In Fig. 6.19 there is a reasonable overlap between the two $\Delta S_M/\Delta S_{\text{peak}}\,(\theta)$ curves for field changes of 20 and 50 kOe within a narrow temperature range around the peak under all pressures applied in the present investigation. The difference in the $\Delta S_M/\Delta S_{\text{peak}}\,(\theta)$ curves for field change of 20 and 50 kOe at temperatures away from peak originates from the difference in peak shapes for the two magnetic field values. The lack of collapsing of the $\Delta S_M/\Delta S_{\text{peak}}\,(\theta)$ curves for different magnetic fields on to a single universal curve is observed in others systems also which undergo a first-order magnetic phase transition [6.30]. Further, the change in the shape of the $M(T)$ curves across the

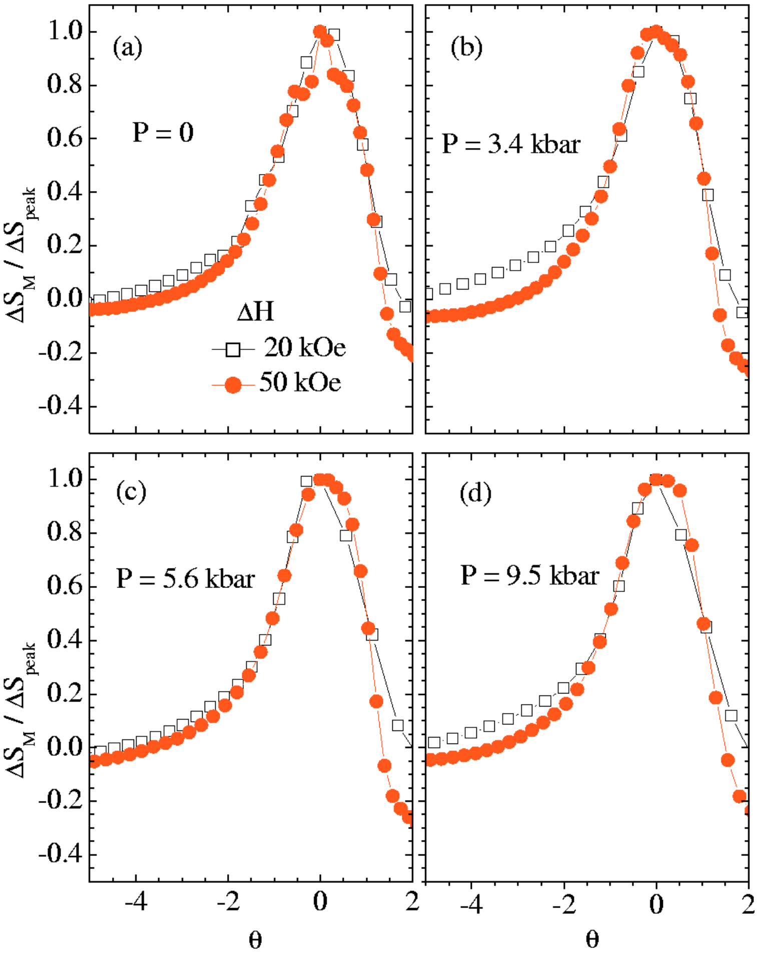

Fig. 6.19: Rescaled temperature (θ) dependence of normalized isothermal magnetic entropy change ($\Delta S_M / \Delta S_{peak}$) for field change ($\Delta H$) of 20 kOe and 50 kOe for $Ni_{50}Mn_{34}In_{16}$ alloy under (a) ambient pressure ($P = 0$), (b) P = 3.4 kbar, (c) $P = 5.6$ kbar and (d) $P = 9.5$ kbar.

MST-AST phase transition with increasing magnetic field at a constant pressure in the present alloy (see Fig. 6.16) also contributes to the difference in $\Delta S_M/\Delta S_{peak}(\theta)$ curves for different field values. However, it is interesting to investigate whether a universal $\Delta S_M/\Delta S_{peak}(\theta)$ curve, with respect to variation in pressure for a given magnetic field excursion, exists or not. $\Delta S_M/\Delta S_{peak}(\theta)$ curves under various pressures for magnetic field excursions of 20 kOe and 50 kOe are presented in Figs. 6.20(a) and 6.20(b) respectively. In Fig. 6.20(b), $\Delta S_M/\Delta S_{peak}(\theta)$ curve for field excursion of 50 kOe under $P = 0$ is not included due to the anomaly in data near the peak (see Fig. 6.17(b)). Apart from this anomaly, there is a good overlap of this $\Delta S_M/\Delta S_{peak}(\theta)$ curve (at $P = 0$) with the

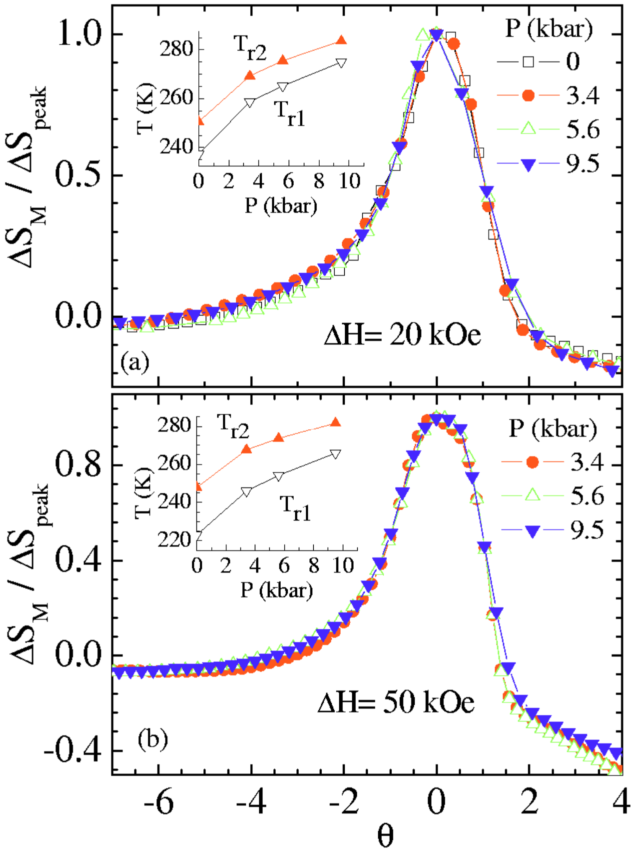

Fig. 6.20: Rescaled temperature (θ) dependence of normalized isothermal magnetic entropy change ($\Delta S_M / \Delta S_{peak}$) for $Ni_{50}Mn_{34}In_{16}$ alloy under various applied pressure (P) for field change (ΔH) of (a) 20 kOe and (b) 50 kOe. Insets to (a) and (b) shows P dependence of the two reference temperature (T_{r1} and T_{r2}) for field excursion of 20 kOe and 50 kOe respectively.

$\Delta S_M/\Delta S_{peak}(\theta)$ curves under other pressures. The collapse of the all $\Delta S_M/\Delta S_{peak}(\theta)$ curve in Fig. 6.20 to nearly a single curve, suggests existence of a universal $\Delta S_M/\Delta S_{peak}(\theta)$ scaling function at least up to 9.5 kbar pressure for a magnetic field excursions of 20 kOe and 50 kOe. Such a universal scaling function is expected in case of second-order phase transition. However, the transition in present case is of first-order and hence a universal behaviour of the curves is not obvious. One possible explanation for the observed universal behaviour can be as follows. The peak in isothermal $\Delta S_M(T)$ curves under discussion is related to the magnetic field induced MST to AST phase transition in the alloy. These isothermal $\Delta S_M(T)$ curves are estimated for a particular magnetic field excursion (ΔH = 20 kOe in Fig. 6.17(a) and ΔH = 50 kOe in Fig.

6.17(b)) under different external pressures. Further, the variation of the four characteristic temperatures T_{MS}, T_{MF}, T_{AS} and T_{AF} with magnetic field (see Table 6.1) constitutes the *H*-*T* phase diagram of the alloy. The *H*-*T* phase diagrams of the present alloy under P = 0 and 9.5 kbar (extreme values of pressure in present investigations), constructed from the data in Table 6.1, are presented in Fig. 6.21. Similar *H*-*T* phase diagrams have also been constructed for P = 3.4 kbar and 5.6 kbar (not presented here for the sake of conciseness) and the following discussion applies

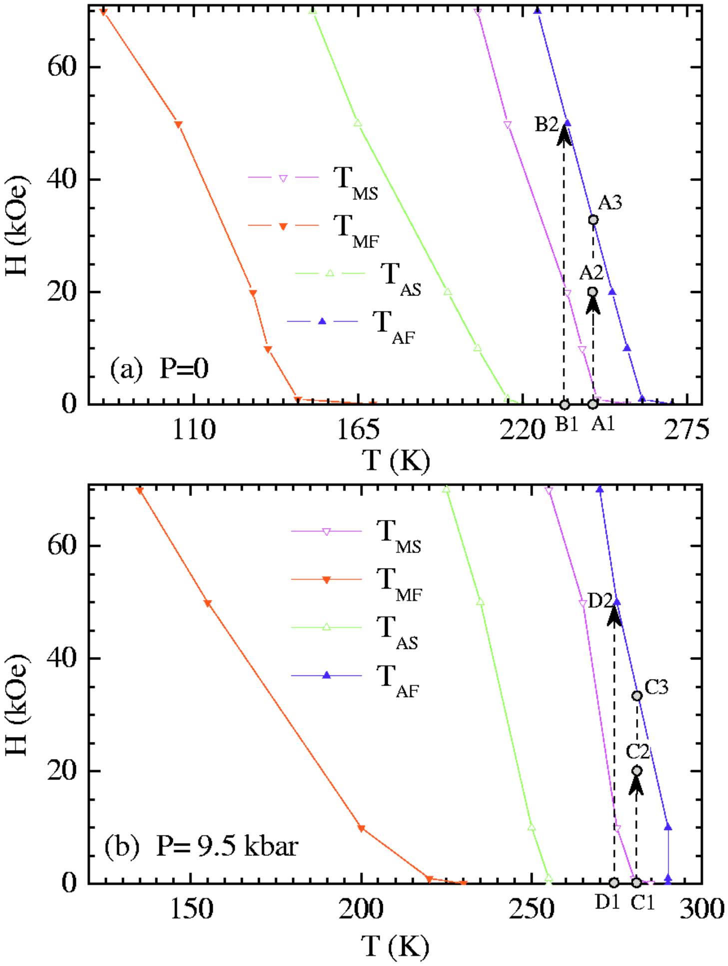

Fig. 6.21: Magnetic field (*H*) - temperature (*T*) phase diagrams of $Ni_{50}Mn_{34}In_{16}$ alloy under applied pressures (*P*) of (a) P = 0 and (b) P = 9.5 kbar. T_{MS}, T_{MF}, T_{AS} and T_{AF} are the four characteristic temperature of the austenite-martensite phase transition in the alloy. Isothermal paths A1 to A2 in (a) and C1 to C2 in (b) represent field excursion of 20 kOe at respective T_{peak}. Similarly, isothermal paths B1 to B2 in (a) and D1 to D2 in (b) represent field excursion of 50 kOe at respective T_{peak}. T_{peak} is the temperature where isothermal magnetic entropy change peaks for the particular magnetic field excursion.

to those as well. We see in the H-T phase diagrams (see Fig. 6.21) that depending on the temperature and magnitude of the magnetic field excursion, an isothermal field excursion can lead to conversion of a particular fraction of MST to the AST phase because of the magnetic field induced MST to AST phase transition at that temperature (see Chapter 5). The $\Delta S_{\mathrm{M}}/\Delta S_{\mathrm{peak}}(\theta)$ curves under different pressures have been constructed by normalising $\Delta S_{\mathrm{M}}(T)$ with respective ΔS_{peak}, and rescaling T-axis with respective T_{peak} and $T_{\mathrm{r1},\mathrm{r2}}$ as explained earlier. For a given magnetic field excursion, the locations of T_{peak} under different pressures, are equivalent in the respective H-T phase diagrams. So this field excursion at respective T_{peak}, leads to MST to AST phase transition to the same extent under all pressures. Similarly, the same field excursion at respective rescaled temperatures leads to MST to AST phase transition to the extent which is similar under all pressure but varies with rescaled temperature. For example the field excursion of 20 kOe and 50 kOe are shown in the Fig. 6.21 at their respective T_{peak} values. The field excursions of 20 kOe from point A1 to A2 at respective T_{peak} in Fig. 6.21(a) and from C1 to C2 at respective T_{peak} in Fig. 6.21(b), lead to MST to AST phase transition to similar extent as these are in equivalent positions in the respective H-T phase diagrams. The MST to AST phase transition is incomplete at point A2 in Fig. 6.21(a) as well as at point C2 in Fig. 6.21(b). To attain complete AST phase, in Fig. 6.21 (a) we need to increase the magnetic field up to the point A3 and in Fig. 6.21(b) we need to go up to the point C3. The extra field increments A2 to A3 and C2 to C3, required to complete the MST to AST phase transition, are similar in both the cases. Similarly, the field excursion of 50 kOe at respective $\mathrm{T}_{\mathrm{peak}}$ from point B1 to B2 in Fig 6.21(a) and from D1 to D2 in Fig. 6.21(b), are also equivalent. In both the cases, the magnetic field induced MST to AST phase transition is near to completion at respective T_{peak}. It is expected that for a given field excursion, similar will be the case not only at respective T_{peak} but also at respective rescaled temperatures. Thus for a constant field excursion $\Delta S_M/\Delta S_{peak}$ (θ) curves under different pressures can follow a universal curve. On the other hand different isothermal field excursions under a given pressure lead to MST to AST phase transition to different extents. For example, the field excursion path A1 to A2 (ΔH = 20 kOe) is not equivalent to the path B1 to B2 (ΔH = 50 kOe) in Fig. 6.21(a). These two field excursions lead to MST to AST phase transition to different extents as mentioned in the previous discussion. As the extent of the isothermal MST to AST phase transition depends on the temperature (see Fig. 6.21), for these different field excursions the extent of magnetic field induced MST to AST phase transition is expected to be different at the rescaled temperatures as well. Therefore such $\Delta S_M/\Delta S_{peak}$ (θ) curves do not follow a universal curve.

The universality of the $\Delta S_M/\Delta S_{peak}(\theta)$ curve with respect to pressure can be useful for estimating the temperature dependence of isothermal magnetic entropy change in the present alloy in a desired range of temperature (say at $T > T_{peak}$) under a certain pressure, without actually performing an experiment with applied pressure. This may be done using the data available at other temperatures (say at $T \leq T_{peak}$). Insets to Fig. 6.20 show pressure dependence of the two reference temperatures (T_{r1} and T_{r2}) for field changes of 20 kOe and 50 kOe. Both the temperatures increase with pressure.

6.5 Conclusion

The martensitic transition was studied in $Ni_{50}(Mn,x\%Cr)_{34}In_{16}$ (x = 1, 2), $Ni_{50}(Mn,y\%Fe)_{34}In_{16}$ (y = 1, 3) and $Ni_{49}CuMn_{34}In_{16}$ alloys. These alloys were prepared by substituting Mn by Cr and Fe and substitution of Ni by Cu in $Ni_{50}Mn_{34}In_{16}$ alloy. The partial substitutions of Mn by Cr and Ni bu Cu are found to increase the martensitic transition temperature as compared to that in $Ni_{50}Mn_{34}In_{16}$ alloy. On the other hand, with substitution of Mn by Fe in the same alloy the martensitic transition temperature is found to be decreased. The increase in martensitic transition temperature in Cr substituted alloys can be related to a decrease in ferromagnetic interaction in these alloys. In the Fe substituted alloys, the decrease in martensitic transition temperature can be related with an increase in the ferromagnetic interaction in these alloys. A similar correlation between the shift of martensitic transition temperature and the change in the ferromagnetic interaction has also been found in the Cu substituted alloy and under the effect of external pressure on $Ni_{50}Mn_{34}In_{16}$ alloy.

Moreover, the temperature regime of magnetocaloric effect which is near 240 K in $Ni_{50}Mn_{34}In_{16}$ increases to near 270 in $Ni_{50}(Mn,1\%Cr)_{34}In_{16}$ and near room temperature in $Ni_{50}(Mn,2\%Cr)_{34}In_{16}$ alloy. Thus the substitution of Mn by Cr has caused substantial improvement in the potential of $Ni_{50}Mn_{34}In_{16}$ alloy system in terms of technological application near ambient temperatures.

It is also shown that a small substitution of Cu in the Ni site of $Ni_{50}Mn_{34}In_{16}$ also raises the martensitic transition from 240 K to 295 K. This martensitic transition in the $Ni_{49}CuMn_{34}In_{16}$ alloy gives rise to multifunctional properties, namely the magnetocaloric effect, magnetoresistance and magnetic field induced strain near room temperature. We conjecture that the enhanced hybridization of 3d states at the Ni sites and 3d states of antiferromagnetically coupled Mn atoms at the In sites, is the primary cause of the increase in the martensitic transition temperature of the present Cu substituted alloy. Magnetoresistance and strain measurements on Cr substituted alloys are planned and we expect these alloys also to show multifunctional properties.

Further, the temperature regime of martensitic transition in $Ni_{50}Mn_{34}In_{16}$ alloy also shifts towards the higher temperature side under hydrostatic pressure. The temperature regime of peak magnetocaloric effectis also found to shift towards higher temperature with increasing pressure. The temperature of the peak isothermal magnetic entropy change increases to near 280 K under pressure of 9.5 kbar as compared to near 240 K at ambient pressure. The peak isothermal magnetic entropy change in the alloy also increases with pressure. The effective refrigerant capacity, however, decreases slightly with increasing pressure. But it still continues to remain close to 150 J/kg for a field change of 50 kOe as the pressure is raised from ambient to 9.5 kbar. Though the pressure-dependence of the magnitude and temperature of the peak in magnetocaloric effect, and the effective refrigerant capacity of the alloy appears to be somewhat different qualitatively, the temperature dependence of isothermal magnetic entropy change for a given field change is found to follow a universal curve under all pressures investigated.

Thus present results show that chemical substitution as well as external pressure can be used to tune the temperature regime of the magnetocaloric effect in Ni-Mn-In family of alloys.

Publications based on this Chapter:

1. Large magnetocaloric effect in $Ni_{50}Mn_{33.66}Cr_{0.34}In_{16}$ alloy.

   J. Phys. D: Appl. Phys. **43,** 225001 (2010).

   Sharma V. K., Chattopadhyay M. K., and Roy S. B.

2. The effect of substitution of Mn by Fe and Cr on the martensitic transition in the $Ni_{50}Mn_{34}In_{16}$ alloy.

   J. Phys.: Condens. Matter. **22**, 486007 (2010).

   Sharma V. K., Chattopadhyay M. K., Nath S. K., Sokhey K. J. S., Kumar R., Tiwari P., and Roy S. B.

3. Martensitic transition near room temperature and the temperature- and magnetic-field-induced multifunctional properties of $Ni_{49}CuMn_{34}In_{16}$ alloy.

   Phys. Rev. B **82**, 172411 (2010).

   Sharma V. K, Chattopadhyay M. K., Khandelwal A., and Roy S. B.

4. Elevating the temperature regime of the large magnetocaloric effect in a Ni–Mn–In alloy towards room temperature.

   J. Phys. D: Appl. Phys. **44**, 145002 (2011).

   Sharma V. K., Chattopadhyay M. K., Sharathchandra L. S., and Roy S. B.

5. The effect of external pressure on the magnetocaloric effect of Ni–Mn–In alloy.

   J. Phys.: Condens. Matter **23**, 366001 (2011)

   Sharma V. K., Chattopadhyay M. K. and Roy S. B.

Chapter 7

Non-equilibrium dynamics of the austenite to martensite phase transition in the Ni-Mn-In based alloys

In earlier Chapters we have seen that $Ni_{50}Mn_{34}In_{16}$ alloy undergoes a martensitic transition from a high temperature (*T*) austenite (AST) phase to a low temperature martensite (MST) phase that can be induced by temperature as well as magnetic field (*H*). This *H*-induced phase transition gives rise to interesting functionalities in the alloys in the form of magnetic superelasticity, large magnetocaloric effect, and large magnetoresistance. In a parallel development there has been a recent spurt of interest in the *H*,*T* induced magnetostructural phase transition in various classes of magnetic materials such as doped-$CeFe_2$ alloys [7.1,7.2], magnetocaloric material Gd_5Ge_4 [7.3], RhFe [7.4], Nd_7Rh_{13} [7.5] and manganite compounds showing colossal magnetoresistance (CMR) effect [7.6-7.9]. The observed magnetostructural transition in these different classes of magnetic systems is found to be accompanied by interesting thermomagnetic history effects [7.1-7.9]. These thermomagnetic effects are now understood to be the manifestations of phase coexistence and metastability [7.2, 7.10] associated with a disorder-influenced first-order phase transition [7.11-7.12]. It is also observed that under certain circumstances this magnetostructural transition gets kinetically arrested [7.8, 7.13], giving rise to an interesting magnetic state with a glass-like dynamical response [7.14,7.15]. In all these systems the magnetic part of the transition involves a ferromagnetic (FM) and an antiferromagnetic state (AFM). In Chapter 6 we have shown that very similar thermomagnetic history effects are associated with the magnetostructural phase transition in $Ni_{50}Mn_{34}In_{16}$ alloy. In the present Chapter we show that in this $Ni_{50}Mn_{34}In_{16}$ alloy the AST to MST phase transition gets kinetically arrested in the presence of high applied magnetic field (>40 kOe). This study of $Ni_{50}Mn_{34}In_{16}$ alloy further extends the generality of the observed phenomena, since in contrast with all other magnetic systems mentioned above, both the high-T and the low-T magnetic phases involved in this alloy are ferromagnetic in nature. Further, it is found that the substitution of Mn by Fe actually favours the kinetic arrest of the AST to MST phase transition. In this $Ni_{50}(Mn, 1\%Fe)_{34}In_{16}$ alloy a partial kinetic arrest of the AST to MST phase transition takes place even in the absence of any applied magnetic field. We show that the AST to MST phase transition in this $Ni_{50}(Mn, 1\%Fe)_{34}In_{16}$ alloy can be totally arrested by the application of an external magnetic field. In the present Chapter we also show that external pressure diminishes the kinetic arrest of the AST to MST phase transition in $Ni_{50}Mn_{34}In_{16}$ alloy.

7.1 Kinetic arrest of the austenite to martensite phase transition in the $Ni_{50}Mn_{34}In_{16}$ alloy

Fig. 7.1 presents magnetization (M) vs. temperature plots for $Ni_{50}Mn_{34}In_{16}$ obtained in zero field cooled (ZFC), field cooled cooling (FCC), and field cooled warming (FCW) protocol in the presence of applied fields H = 0.1, 1, 10, and 50 kOe (these modes of $M(T)$ measurements have already been explained in the earlier Chapters). In the H = 100 Oe measurement, the sharp rise in $M(T)$ while cooling down with a point of inflection around 304 K, is attributed to the paramagnetic (PM) to ferromagnetic (FM) transition. Further down in temperature there is a sharp drop in the $M(T)$ around 240 K, and this is due to the AST-MST phase transition in this alloy. As discussed in earlier Chapters, a distinct thermal hysteresis between $M_{FCC}(T)$ and $M_{FCW}(T)$ observed around this AST-MST phase transition indicates the first-order nature of this phase transition. The MST phase in $Ni_{50}Mn_{34}In_{16}$, although FM in nature, has lower magnetic

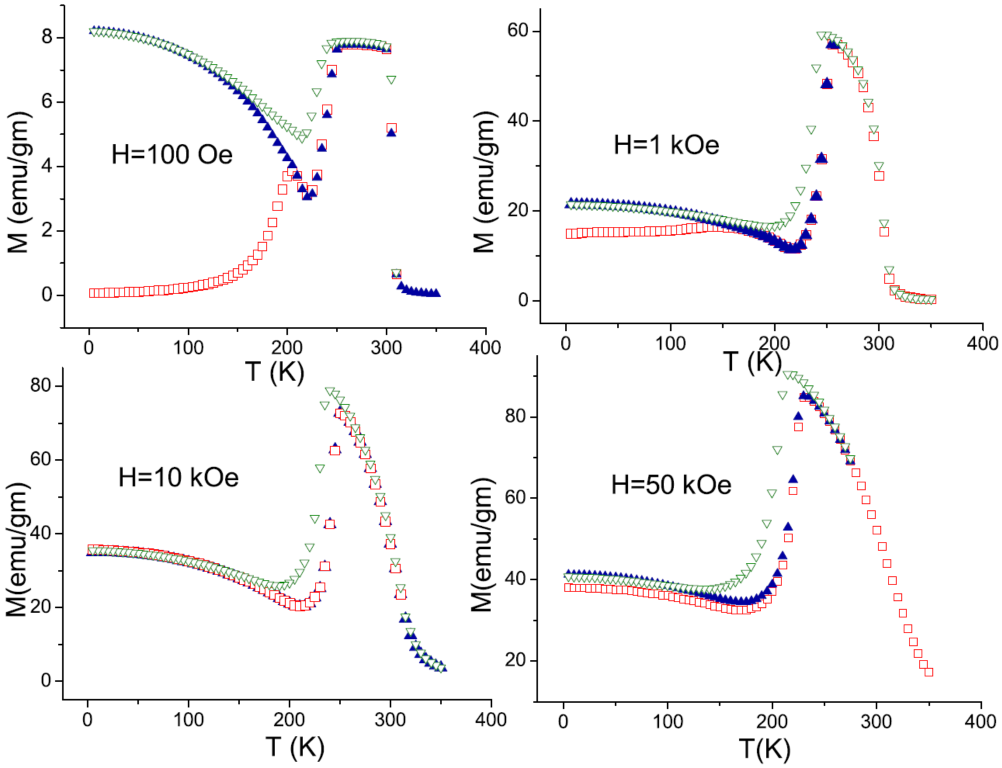

Fig. 7.1: Magnetization (M) vs. temperature (T) plots for $Ni_{50}Mn_{34}In_{16}$ in external magnetic field $H = 0.1$, 1, 10, and 50 kOe. Open square represents ZFC data and open (close) triangle represents FCC (FCW) data.

moment than the FM state of the higher temperature AST phase. This makes the AST-MST phase transition and its first-order nature clearly visible in the present T dependent magnetization study.

When the applied magnetic field $H < 5$ kOe there is a distinct difference between the $M_{ZFC}(T)$ and $M_{FCW}(T)$ below a certain temperature T_{irrv}, which decreases with the increase in H. In $H > 5$ kOe, $M_{ZFC}(T)$ and $M_{FCW}(T)$ are indistinguishable in the T range of present measurement (5 K< T < 350 K). This behaviour can be explained in terms of the hindrance of domain motion in the martensite FM phase. However, with the further increase in H above 40 kOe, $M_{ZFC}(T)$ again bifurcates from $M_{FCW}(T)$ and the degree of irreversibility (i.e., $M_{FCW}(T)$-$M_{ZFC}(T)$) actually increases with the applied H. These features are exemplified in Fig. 7.2 with M vs. T measurements performed in the presence of higher applied fields H = 70 and 80 kOe. A very similar behaviour has been observed earlier across the first-order FM to AFM phase transition in doped- $CeFe_2$ alloys [7.13], and CMR manganite compounds [7.8]. It was argued that when the applied H is beyond a certain critical value, the first-order FM to AFM transition was kinetically arrested and gave rise to a glass-like nonergodic magnetic state [7.8, 7.13]. In contrast to the canonical spin-glass (where the spin-configuration is random in nature, similar to a paramagnet frozen in time), the magnetic configuration in the magnetic-glass consisted of a phase coexistence of FM and AFM clusters frozen in time [7.13]. Importing the same arguments here we say that beyond H>40 kOe, the first-order AST to MST phase transition in $Ni_{50}Mn_{34}In_{16}$ is not completed, but is kinetically arrested. The low T state thus obtained in the FCC mode is not an equilibrium state. It consists of converted phase fractions of equilibrium MST phase coexisting with the metastable phase fractions of the higher temperature AST phase. On the other hand, the ZFC state in which the low temperature values of $M_{ZFC}(T)$ are distinctly lower than $M_{FCC}(T)$ or $M_{FCW}(T)$, is the equilibrium state with MST phase only.

7.2 Non-equilibrium nature of the arrested state in the $Ni_{50}Mn_{34}In_{16}$ alloy

To support the conjecture of kinetic arrest of AST-MST phase transition in $Ni_{50}Mn_{34}In_{16}$ leading to a low T metastable glasslike magnetic state, we first show that the low temperature FCC state is indeed metastable in nature and tends towards the ZFC state with the introduction of energy fluctuations. We do an experiment where the sample is first made to reach 5 K by following the FCC path with H = 80 kOe, and then subjected to various temperature cycling between 5 K and T_{max} inside this FCC state, where T_{max} = 60, 80, 100, and 120 K. There is a clear decrease in $M(T)$ with such T cyclings (see inset in top panel of Fig. 7.2). The same T cycling does not, however, produce any change in M in the ZFC state; this emphasizes the equilibrium

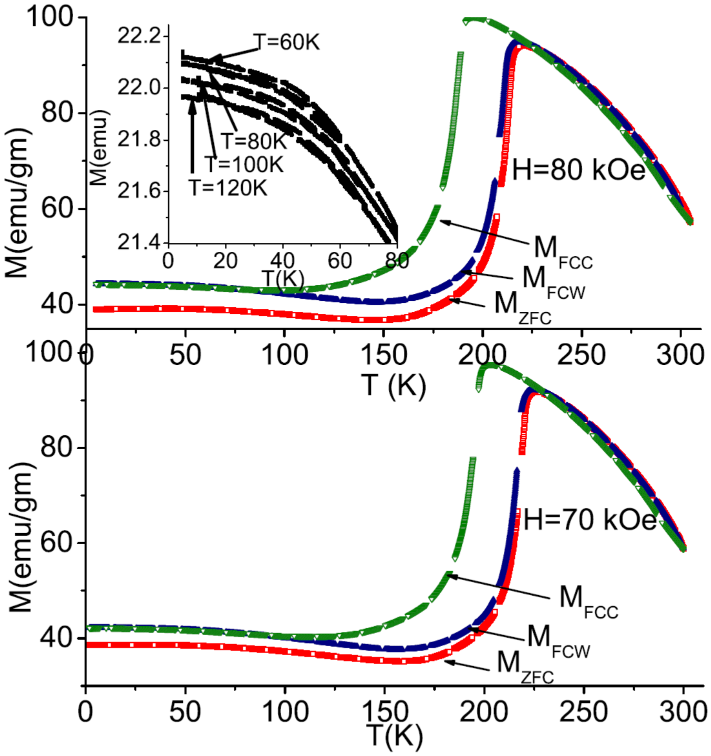

Fig. 7.2: Magnetization (*M*) vs. temperature (*T*) plots for $Ni_{50}Mn_{34}I16_6$ in external magnetic field H = 70 and 80 kOe. The inset in top panel shows the effect of thermal cycling on $M_{FCC}(T)$.

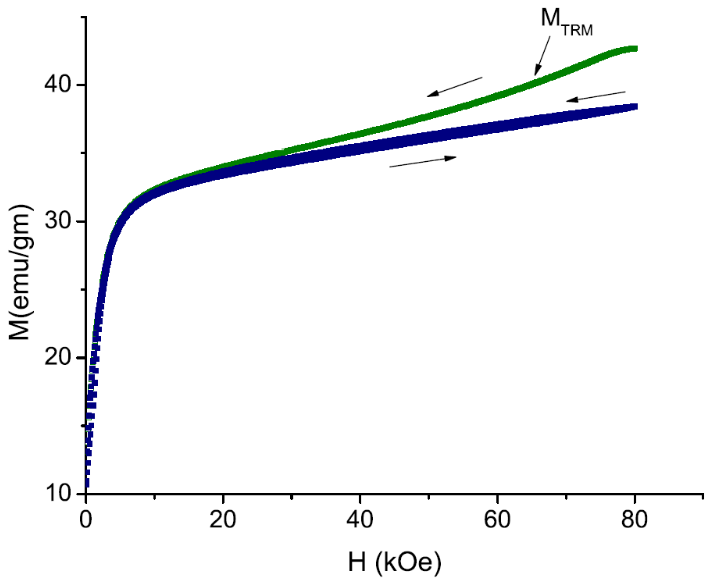

Fig. 7.3: Thermoremanent magnetization (M_{TRM}) vs. magnetic field (*H*) plot for $Ni_{50}Mn_{34}In_{16}$ at 80 K. This $M_{TRM}(H)$ is obtained by field cooling from 305 to 80 K in the presence of H = 80 kOe, and then isothermally reducing *H* to zero. Also are shown in the figure the *M*(*H*) plots obtained in the subsequent isothermal field cycling between zero and 80 kOe.

nature of the ZFC state. To add further to the evidences of metastability of the FCC state, in Fig. 7.3 we plot isothermal $M(H)$ curve at 80 K by reducing the applied H to zero after cooling the sample to 80 K in a field of 80 kOe. This $M(H)$ measurement is then followed immediately by another measurement where H was cycled isothermally between 0 to 80 kOe. The initial FCC thermoremanent magnetization (M_{TRM}) at $T = 80$ K and $H = 80$ kOe was found to be lost in this subsequent field cycle. The magnetization value reached by increasing H again to 80 kOe, is distinctly below the initial M_{TRM} (see Fig. 7.3). The distinct difference in $M(H)$ obtained through these two different measurements highlights that the FCC state is indeed metastable in nature.

Further support for the existence of the low temperature glass-like magnetic state in $Ni_{50}Mn_{34}In_{16}$ alloy is obtained from the results of magnetization relaxation study. In Fig. 7.4 we present M vs. time (t) plots at various temperatures on the FCC path across the AST-MST phase transition with H kept fixed at 80 kOe. A considerable relaxation in M is expected at 180 K due to the expected metastability (nucleation and growth) across a first-order (AST-MST) phase transition. With the decrease in temperature the relaxation rate decreases continuously. However, a distinct relaxation can be observed even down to 70 K and below. The $M(t)$ data below 150 K can be fitted with Kohlrausch-Williams-Watt (KWW) stretched exponential function $\Phi(t) \propto \exp\left[-\left(t/\tau\right)^{\beta}\right]$, where τ is the characteristic relaxation time and β is a shape parameter [7.14-7.15]. The value of β varies between 0.45 and 0.7, and it implies that the metastable state relaxes with a distribution of relaxation times [7.14-7.15]. The inset of Fig. 7.4 shows a typical example of such KWW fitting at $T = 70$ K with $\tau = 1.1\times10^{9}$ s, and $\beta = 0.65$. The same kind of glass-like magnetization relaxation has earlier been observed along the FCC path of doped-$CeFe_2$ alloys [7.13] and Gd_5Ge_4 [7.16]. In contrast the higher temperature (T>140 K) relaxation results in $Ni_{50}Mn_{34}In_{16}$ cannot be fitted with KWW stretched exponential function. As compared to the

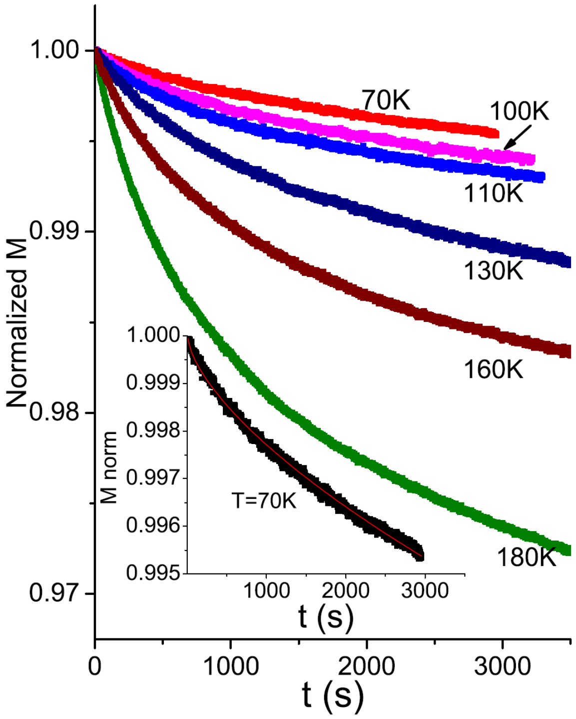

Fig. 7.4: Normalized magnetization (M_{norm}) vs. time (t) plot for $Ni_{50}Mn_{34}In_{16}$ at various temperatures (T) between T = 70 and 180 K along the FCC path in the presence of H = 80 kOe. M is normalized with respect to initial M_0 obtained 1 s after stabilizing at the respective T. The inset shows the result of the fitting of KWW stretched exponential function at T =70 K.

other systems where magnetic glass has been reported, the present $Ni_{50}Mn_{34}In_{16}$ system seems to be different in the sense that both the low-H and high-H state involved in this H-induced magnetostructural transition are FM in nature.

The possibility of a glass-like state with uncorrelated clusters of MST-like phase frozen randomly in the untransformed higher T phase has been evidenced recently in TiNi alloys [7.17] In contrast with the TiNi alloys the transformation from the high-T austenite phase to the low-T martensite phase in $Ni_{50}Mn_{34}In_{16}$ alloys is completed in zero and low applied H. It is only in the presence of an applied H greater than 40 kOe that the AST to MST phase transition process gets kinetically arrested in $Ni_{50}Mn_{34}In_{16}$ alloy.

7.3 Kinetic arrest of the austenite to martensite phase transition in the $Ni_{50}(Mn,1\%Fe)_{34}In_{16}$ alloy

Earlier in the Chapter 6 we have seen that with substitution of Mn by Fe (Cr) in $Ni_{50}Mn_{34}In_{16}$ the AST-AST phase transition temperature decreases (increases). Now we explore the possibility of kinetic arrest of AST-MST phase transition in these alloys. Fig. 7.5 shows M vs. T curves for $Ni_{50}(Mn,1\%Fe)_{34}In_{16}$ (nominal composition) alloy in H = 100 Oe, 1kOe, 10 kOe and 50 kOe in the temperature range 2 K ≤ T ≤ 300 K. Along the FCC path in 100 Oe field, M increases with decreasing temperature below 300 K. The results of dc resistivity and ac susceptibility measurements (see section 6.1.3) have shown that there is a PM to FM transition near 310 K in the present alloy. With further decrease in temperature M almost flattens out and then starts decreasing near 170 K. Magnetization starts increasing again with decreasing temperature below nearly 50 K. $M(T)$ shows similar temperature dependence in FCW mode as well. However, there is a distinct thermal hysteresis in the temperature regime where M decreases with decreasing temperature. This drop in M and the associated thermal hysteresis may be attributed to a first-order AST to MST phase transition in $Ni_{50}(Mn,1\%Fe)_{34}In_{16}$ alloy, in concurrence with the previous studies on the $Ni_{50}Mn_{34}In_{16}$ alloy. The magnitude and nature of the temperature dependence of M above and below the hysteretic region indicates that both the AST and the MST phases have ferromagnetic character (this was also suggested by $\chi_{ac}(T)$, see Fig. 6.2(c) of Chapter 6). In higher magnetic field the AST to MST phase transition shifts to lower temperature (see Fig. 7.5(b) and 5(c)). Further, the magnitude of M in the MST and the AST phases clearly indicates that the MST phase has a lower magnetization as compared to that of the AST phase. It is worth noting here that in all fields there is a distinct difference between M_{ZFC} and M_{FCW} at low temperatures. In a ferromagnetic system the difference between M_{ZFC} and M_{FCW} is related to the

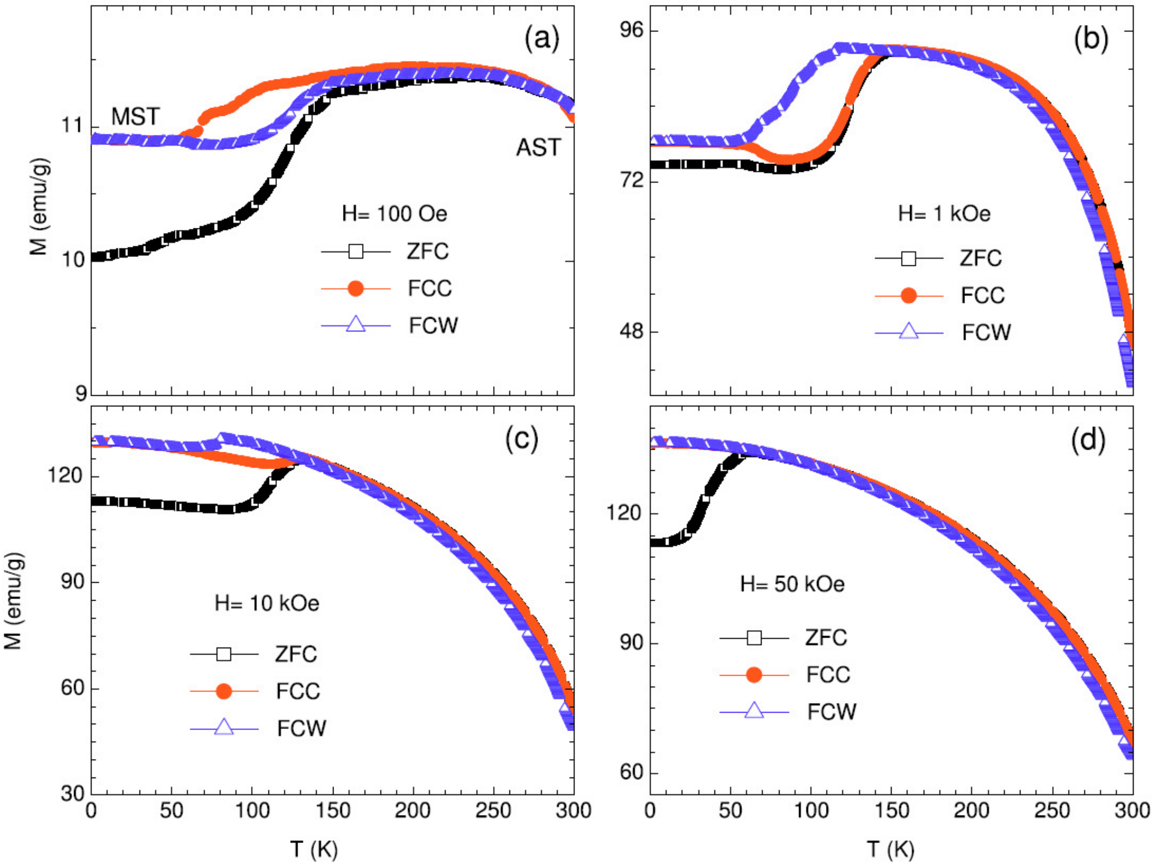

Fig. 7.5: Temperature (*T*) dependence of magnetization (*M*) of $Ni_{50}(Mn,1\%Fe)_{34}In_{16}$ alloy in various applied magnetic fields (*H*).

hindrance to domain motion at low temperatures, and this thermomagnetic irreversibility decreases with the increase in the applied magnetic field. In such a case, for magnetic fields greater than that required for saturation of magnetization, M_{ZFC} and M_{FCW} are expected to merge. In the present case, however, the difference between $M_{ZFC}(T)$ and $M_{FCW}(T)$ increases in higher applied magnetic fields (see Figs. 7.5(a)- 7.5(d)). So the difference between M_{ZFC} and M_{FCW} in the present case is not due to the hindrance to domain wall motion in a ferromagnet. Earlier, in the parent $Ni_{50}Mn_{34}In_{16}$ alloy, such difference between M_{ZFC} and M_{FCW}, which increases with applied field and was observed only in the field range $H > 40$ kOe, was argued to be due to kinetic arrest of the AST to MST phase transition for $H > 40$ kOe. Using the same argument we suggest that the (partial) kinetic arrest of AST to MST phase transition in the present

$Ni_{50}(Mn,1\%Fe)_{34}In_{16}$ alloy takes place even in the presence of an applied magnetic field as low as 100 Oe.

With the increase in the applied field to 50 kOe the $M(T)$ curve does not show any signature of the AST-MST phase transition in the FCC and FCW measurement protocol at least down to 2 K (see Fig. 7.5(d)). This behaviour suggests a complete arrest of the AST to MST phase transition in the present alloy in a field of 50 kOe. This is in contrast with the results obtained earlier in the $Ni_{50}Mn_{34}In_{16}$ alloy where the kinetic arrest of the AST to MST phase transition was possible only with applied $H > 40$ kOe and that the kinetic arrest was only partial even in an applied H of 80 kOe.

7.4 Non-equilibrium nature of the arrested state in the $Ni_{50}(Mn,1\%Fe)_{34}In_{16}$ alloy

To confirm the presence of kinetic arrest of the AST to MST phase transition in $Ni_{50}(Mn,1\%Fe)_{34}In_{16}$ alloy in $H = 100$ Oe, we have performed a temperature cycling experiment. First the sample was cooled from 300 K to 5 K in an applied field of 100 Oe in FCC protocol, then the magnetization was measured while the sample was warmed to a temperature T_1 (T_1>5 K) and cooled back to 5 K. The sample was again warmed to a temperature T_2 ($T_2 > T_1$) and cooled back to 5 K. This process was repeated for several temperatures. If the AST to MST phase transition is kinetically arrested in 100 Oe, the sample in FCC state at 5 K will have patches of AST phase frozen in the matrix of equilibrium MST phase forming a magnetic glass state [7.13, 7.16]. As the temperature is increased, the sample tends to move out of the glassy state and the frozen non-equilibrium AST phase gets gradually converted to equilibrium MST phase due to the energy fluctuation introduced with the temperature cycling. This process is akin to the recrystallization (or devitrification) of structural glass on heating [7.14]. Since the MST

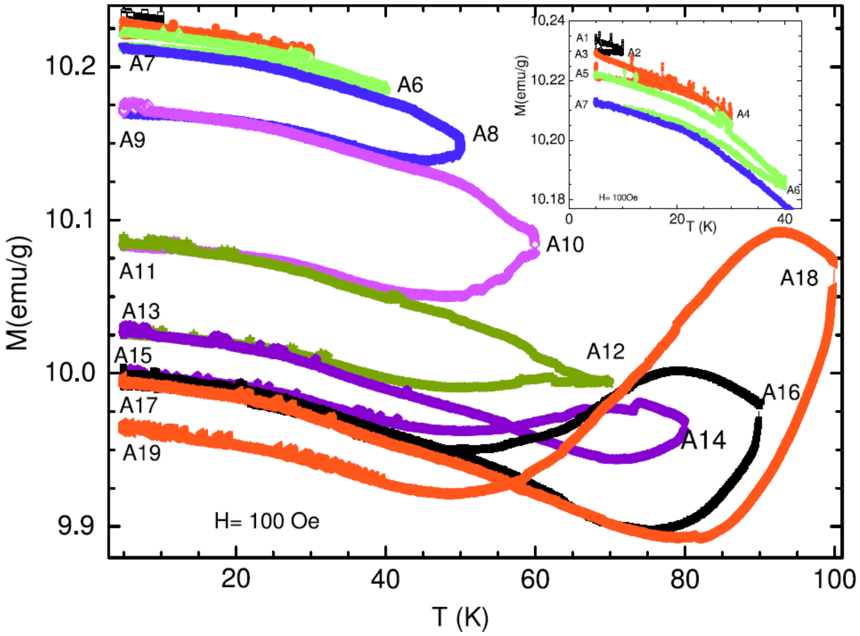

Fig. 7.6: Effect of temperature (*T*) cycling on the magnetization (*M*) of $Ni_{50}(Mn,1\%Fe)_{34}In_{16}$ alloy. The starting point at 5 K is reached from 300 K in the presence of magnetic field (*H*) of 100 Oe. Energy fluctuations due to temperature cycling devitrify the frozen non-equilibrium austenite to equilibrium martensite phase. This suggests a kinetic arrest of the austenite to martensite transition in $Ni_{50}(Mn,1\%Fe)_{34}In_{16}$ alloy in 100 Oe field. Inset shows a magnified view for the first three temperature cycles.

phase has a lower magnetization as compared to that of the AST phase (see Fig. 7.5), *M* should go on decreasing with the devitrification of frozen AST to equilibrium MST as a result of this temperature cycling. The result of such temperature cycling experiment is presented in Fig. 7.6. As sample is warmed from the starting point A1 (5 K) to A2 (10 K), *M* decreases with increasing temperature. This can be due to the *T* dependence of *M* of ferromagnetic MST (and AST). When the sample is cooled back to A3 (5 K), *M* at A3 is smaller than that at A1. M shows a similar behaviour in temperature cycling A3 (5 K)-A4 (30 K)-A5 (5 K), A5 (5 K)-A6 (40 K)-A7 (5 K), A7 (5 K)-A8 (50 K)-A9 (5 K), A9 (5 K)-A10 (60 K)-A11 (5 K), A11 (5 K)-A12 (70 K)-A13 (5 K). When the sample is warmed from A13 (5 K) to A14 (80 K), *M* first decreases with temperature and then starts increasing near 80 K. However, when the sample is cooled down to A15 (5 K), *M* at A15 is lower as compared to that at A13. A similar trend is observed for temperature cycling A15 (5 K)-A16 (90 K)-A17 (5 K), A17 (5 K)-A18 (100 K)-A19 (5 K) as well. We note from Fig. 7.5(a) that in 100 Oe field the MST to AST phase transition in FCW mode starts near 80 K. So above observation (increase in M with temperature near 80 K) is related to the temperature induced MST to AST phase transition. When the sample is cooled back, there is a temperature induced AST to MST phase transition. Also devitrification of the frozen AST phase to stable MST phase takes place due to energy fluctuation available from temperature cycling. As a result, M successively decreases from A13 to A19. Thus the temperature cycling experiment clearly provides evidence of kinetically arrested (or frozen) AST phase at 5 K in H = 100 Oe after cooling from high temperature across the AST to MST phase transition temperature.

The observation that there is a kinetic arrest of AST to MST phase transition in field of 100 Oe in $Ni_{50}(Mn,1\%Fe)_{34}In_{16}$ alloy, motivated us to explore further whether there is a kinetic arrest of this transition even in zero magnetic field. The temperature cycling experiment starting from the zero field cooled state at 5 K, also shows signatures of devitrification similar to that presented in Fig. 7.6, and confirms the presence of frozen AST at 5 K in zero field. However, it should be noted that even in the absence of an externally applied magnetic field there is always a small amount (< 5 Oe) of remnant magnetic field in the superconducting magnet. So in practice the zero applied magnetic field is only nominally zero.

A decrease in the mobility of interfaces between structurally dissimilar phases in a manganese-oxide sample was investigated through resonant ultrasonic spectroscopy measurements [7.18]. Interactions among these interfaces are mediated by elastic strain energy. Further, the motion of these interfaces is controlled by free energy difference between the parent and product phase, elastic strain energy and interfacial friction [7.18]. It has been proposed that the formation of the glassy magnetic state in material systems exhibiting quenched disorder-influenced first-order magneto-structural transitions [7.13, 7.19] is due to the freezing of the motion of this structural interface [7.18]. The $Ni_{50}(Mn,1\%Fe)_{34}In_{16}$ alloy has 1% of Mn substituted by Fe as compared to that in $Ni_{50}Mn_{34}In_{16}$ alloy. It is interesting that this small change leads to a noticeable difference in the kinetic arrest of the AST to MST phase transition in the two alloys. This is probably related to the lower temperature of AST to MST phase transition in the $Ni_{50}(Mn,1\%Fe)_{34}In_{16}$ alloy. This argument is supported by the absence of kinetic arrest of the AST to MST phase transition in $Ni_{50}(Mn,x\%Cr)_{34}In_{16}$ (x = 1, 2) (nominal composition) alloys where the transition occurs at a relatively higher temperature as compared to

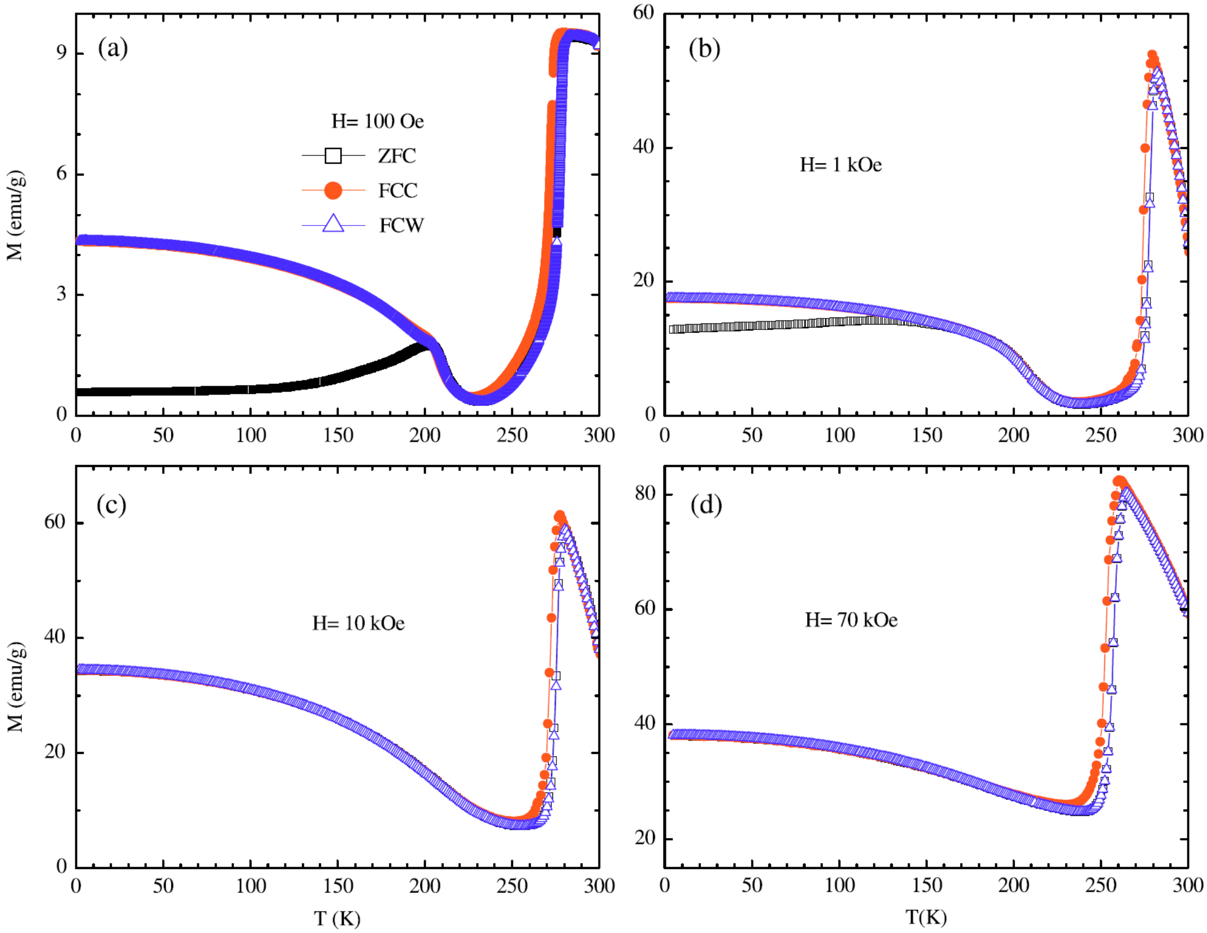

Fig.7.7. Temperature (*T*) dependence of magnetization (*M*) of $Ni_{50}(Mn,1\%Cr)_{34}In_{16}$ alloy in various applied magnetic fields (*H*).

$Ni_{50}Mn_{34}In_{16}$ alloy (see section 6.1 of Chapter 6). The *M*(*T*) curves of $Ni_{50}(Mn,1\%Cr)_{34}In_{16}$ alloy in various magnetic fields are presented in Fig. 7.7. The sharp drop in *M* near 270 K, and the associated thermal hysteresis are related with the first-order AST-MST phase transition in this alloy. With increasing magnetic field, M_{ZFC} merge with M_{FCW} in H = 10 kOe and there is no signature of bifurcation of M_{ZFC} and M_{FCW} up to H = 70 kOe. Thus there is no signature of kinetic arrest of AST to MST phase transition in $Ni_{50}(Mn,1\%Cr)_{34}In_{16}$ alloy up to H = 70 kOe. On the other hand this alloy is expected to be more disordered (like $Ni_{50}(Mn,1\%Fe)_{34}In_{16}$ alloy) than the parent alloy. These results indicate that temperature plays an important role in the process of kinetic arrest of the transition. The low temperature of the AST to MST phase transition probably makes the structural interface motion more prone to freezing. Kinetic arrest of an antiferromagnetic to ferromagnetic transition in zero magnetic field is also reported in Gd_5Ge_4 [7.16]. However in Gd_5Ge_4 there is no kinetic arrest in higher magnetic field, whereas in the present case there is a complete kinetic arrest of the first-order phase transition in higher magnetic field. This is because in Gd_5Ge_4 the low temperature equilibrium phase (ferromagnetic) has a higher magnetization as compared to the high temperature phase (antiferromagnetic), so magnetic field favours the low temperature phase.

To explore further the kinetic arrest of the AST to MST phase transition in $Ni_{50}(Mn,1\%Fe)_{34}In_{16}$ alloy, the magnetization relaxation was measured at various temperatures along the FCC path. For these measurements the temperature of interest was approached unidirectionally from 300 K in the presence of H = 1 kOe without undershooting the target temperature. After stabilizing temperature, isothermal magnetization was measured as a function of time. The main panel of Fig. 7.8 shows the magnetization relaxation data at selected temperatures. *M* is normalized to its value at the starting time i.e. t = 0. The magnetization relaxation data can be fitted with Kohlrausch-Williams-Watt (KWW) stretched exponential function $\Phi(t) \propto \exp\left[-\left(\frac{t}{\tau}\right)^{\beta}\right]$, where τ is characteristic relaxation time, and β is a shape parameter (varies between 0.8 and 0.9 in the present case). Solid lines in Fig. 7.8 represent the KWW function. The temperature dependence of the relaxation time is shown in inset to Fig. 7.8. The solid line in the inset to Fig. 7.8 shows a linear fit to the $\ln\tau$ vs. $1/T$ data indicating that relaxation time increases with decreasing temperature following an Arrhenius type of relationship. This is similar to the characteristic of a strong structural glass former like silica [7.15].

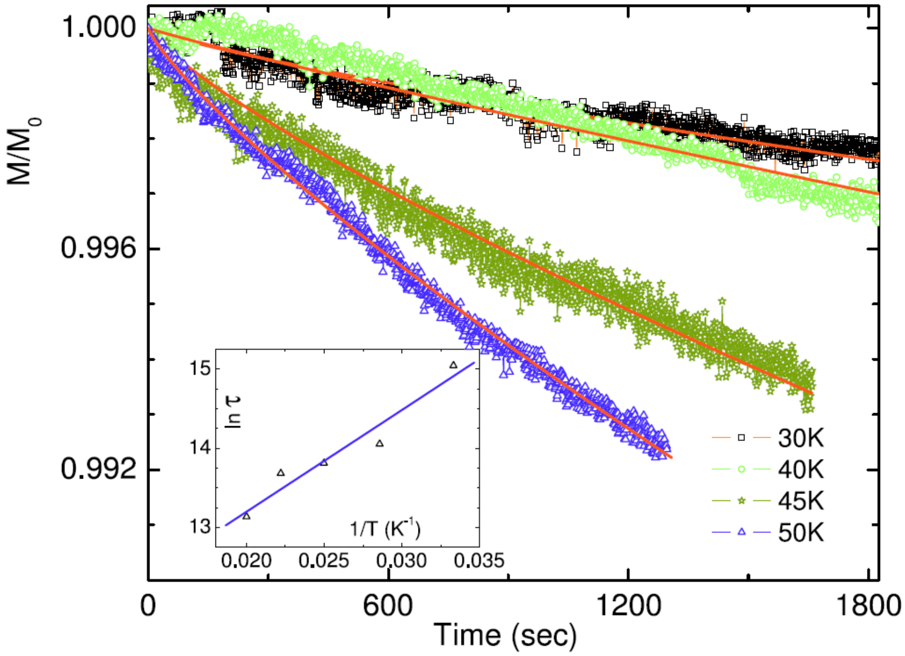

Fig. 7.8: Isothermal magnetization (*M*) vs. time curves for $Ni_{50}(Mn,1\%Fe)_{34}In_{16}$ alloy at some representative temperatures. Each temperature is reached from 300K in a field of 1 kOe and the time dependence of M is measured in the presence of the same field. M is normalized to its value at zero time. Points show the experimental data and the solid lines are curves fitted with Kohlrausch-Williams-Watt (KWW) stretched exponential function. Inset shows the temperature (*T*) dependence of the characteristic relaxation time τ (obtained from fitting the KWW function to the relaxation data).

7.5 Effect of pressure on the kinetic arrest of the austenite to martensite phase transition in the $Ni_{50}Mn_{34}In_{16}$ alloy

Earlier we have seen in section 6.4.1 of Chapter 6 that with increase in pressure the AST-MST phase transition temperature in $Ni_{50}Mn_{34}In_{16}$ increases. To explore the effect of pressure on the kinetic arrest of the AST to MST phase transition we have measured $M(T)$ curve in constant high H under different pressures. The $M(T)$ curve with H = 70 kOe is presented in Fig. 7.9. To investigate the effect of pressure on the kinetic arrest of AST to MST phase transition in the alloy we define a quantity $\left(\frac{M_{FCC}-M_{ZFC}}{M_{ZFC}}\right)_{5K}$ which is the ratio of (M_{FCC}-M_{ZFC}) with M_{FCC} at 5 K. This quantity is proportional to the degree of kinetic arrest of the AST to MST phase transition. The variation of this quantity is presented in the Table 7.1. A larger value of $\left(\frac{M_{FCC}-M_{ZFC}}{M_{ZFC}}\right)_{5K}$ signifies a higher degree of kinetic arrest of the AST to MST phase transition (for example from 50 kOe to 70 kOe under a similar pressure). Table 7.1 clearly shows that kinetic arrest of the

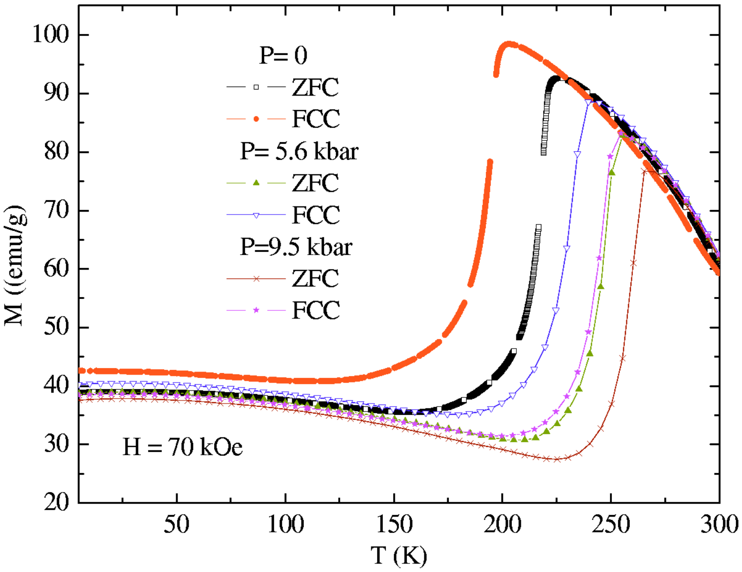

Fig. 7.9: Temperature (T) dependence of magnetization (M) of $Ni_{50}Mn_{34}In_{16}$ alloy in applied magnetic field (H) of 70 kOe under various hydrostatic pressures (P).

Table 7.1: Variation of the quantity $\left(\frac{M_{FCC}-M_{ZFC}}{M_{ZFC}}\right)_{5K}$ in $Ni_{50}Mn_{34}In_{16}$ alloy with magnetic field (*H*) and pressure (*P*).

	$\left(\frac{M_{FCC}-M_{ZFC}}{M_{ZFC}}\right)$(%)		
H(kOe)	$P = 0$	$P =$ 5.6 kbar	$P =$ 9.5 kbar
50	7.1	2.2	1.3
70	9.5	4.1	2.2

AST to MST phase transition in a given magnetic field decreases with increasing pressure. The general perception is that the pressure will help the process of glass formation (kinetic arrest). However, in the present case it is just the reverse. This might be related with the increased AST-MST phase transition temperature (as seen in Cr substituted alloy) so that higher thermal energy is available for interface motion and kinetic arrest is not possible.

7.6 Kinetic arrest of the austenite-martensite phase transition in the Ni-Mn-X (X = In and Sn) alloys: Reports in the recent literature.

Since the completion of our first study on the kinetic arrest of AST-MST phase transition in $Ni_{50}Mn_{34}In_{16}$ alloy [7.20], there have been several reports in the literature of the observation of kinetic arrest in Ni-Mn-X (X = In and Sn) alloys. We present here a brief discussion of these works.

Temperature dependent magnetization and resistivity measurements in $Ni_{45}Co_{5}Mn_{36.7}In_{13.3}$ alloy in different magnetic fields indicated that process of AST to MST phase transition in this alloy is kinetically arrested [7.21]. It was observed that the change in the magnetization and resistivity across the AST to MST phase transition in this alloy decreased with increasing magnetic field. It was also observed that if field was decreased to zero after field cooling the sample to low temperature and then the sample was warmed in zero field, the resistivity gradually approached to the zero-field value of MST phase. This was argued that in the high magnetic field the AST to MST phase transition was frozen leading to AST phase surviving at low temperatures. When the sample was field cooled to low temperature and the field was decreased to zero at low temperature, this frozen AST phase was released to stable MST phase with warming. As a result the resistivity tended to the zero-field value with the warming of sample. This conjecture was confirmed with x-ray diffraction (XRD) measurements which showed the presence of XRD peaks of AST phase in the field cooled sample at low temperature [7.21]. When the magnetic field was decreased to zero and sample was warmed in zero field, these XRD peaks gradually diminished and the XRD peaks corresponding to the MST phase increased in size. It was argued that the transition entropy across the AST-MST phase transition becomes zero in high magnetic field leading to zero driving force for the AST to MST phase transition. This decrease in transition entropy was conjectured to be arising from a magnetic entropy contribution for the AST phase. It was argued that the freezing of AST-MST phase transition is due to decrease in the mobility of the AST-MST interface. The process of kinetic arrest of the AST to MST phase transition in this alloy had been further investigated with different *H-T* paths and isothermal measurements by Ito et al. [7.22]. The transition entropy in $Ni_{50}Mn_{34}In_{16}$ alloy is also inferred to approach zero in high magnetic field [7.23]. A similar inference has also been drawn from isothermal stress-strain measurements on $Ni_{45}Co_5Mn_{36.1}In_{13.9}$ alloy [7.24]. Kustov et al. have shown that the transition entropy for $Ni_{45.0}Mn_{36.7}In_{13.3}Co_{5.0}$ alloy changed with heat treatment given to the sample [7.25]. It was shown that for a larger value of

T_C-T_M (where T_C is the Curie temperature of the austenite phase and T_M is the AST-MST phase transition temperature), the transition entropy extrapolated to zero. It was argued that for larger T_C-T_M values the lattice and magnetic parts of transition entropy might compensate in certain magnetic field, leading to zero transition entropy. The observation by Kustov et al. [7.25] suggests that for alloys with similar T_C, the process of AST to MST phase transition is likely to be kinetically arrested in alloys with lower AST-MST phase transition temperature. This is in harmony with our observation in the parent and Cr/Fe doped $Ni_{50}Mn_{34}In_{16}$ based alloys and also for $Ni_{50}Mn_{34}In_{16}$ alloy under pressure (see sections 7.3 and 7.5 of this Chapter). Recently Lee et al. [7.26] have interpreted the phenomenon of kinetic arrest of the AST to MST phase transition in high magnetic field in $Ni_{45}Co_5Mn_{36.5}In_{13.5}$ alloy with time-temperature-transformation (TTT) diagram. The model proposed interprets the kinetic arrest of the AST-MST phase transition in high magnetic field because of the shift of the nose of TTT diagram. Ni-Mn-Sn alloys are also reported to show the phenomenon of kinetic arrest of AST to MST phase transition. Resistivity measurements in $Ni_2Mn_{1.36}Sn_{0.64}$ alloy [7.27] are suggestive of kinetic arrest of AST to MST phase transition in this alloy.

7.7 Conclusion

The process of the austenite to martensite phase transition in $Ni_{50}Mn_{34}In_{16}$ alloy is not completed in the presence of high magnetic field; the transition gets kinetically arrested. This low temperature state in such a case is a non-equilibrium state, and its dynamical response is quite similar to that observed in structural glasses. Further, the austenite to martensite phase transition in $Ni_{50}(Mn, 1\%Fe)_{34}In_{16}$ alloy is also found to be kinetically arrested. Our results indicate that in the $Ni_{50}(Mn, 1\%Fe)_{34}In_{16}$ alloy, the transition is partially arrested even in zero (nominal) applied field. The process of transition in this alloy is completely arrested in a field of 50 kOe. This is in contrast with the parent $Ni_{50}Mn_{34}In_{16}$ alloy, where the signature of the kinetic arrest of austenite to martensite transition is observed only in fields greater than 40 kOe and the arrest is partial even in a field of 80 kOe. The lower temperature of the austenite to martensite phase transition in the $Ni_{50}(Mn, 1\%Fe)_{34}In_{16}$ alloys appear to make the structural interfaces (formed during the phase transition) less mobile, and thus easier to freeze. Moreover, the degree of kinetic arrest of the austenite to martensite phase transition in $Ni_{50}Mn_{34}In_{16}$ is found to decrease with the application of external pressure.

Publications based on the present chapter:

1. Kinetic arrest of the first-order austenite to martensite phase transition in $Ni_{50}Mn_{34}In_{16}$: dc magnetization studies.

   Phys. Rev. B **76**, 140401 (2007).

   Sharma V. K., Chattopadhyay M. K., and Roy S. B.

2. The effect of substitution of Mn by Fe and Cr on the martensitic transition in the $Ni_{50}Mn_{34}In_{16}$ alloy.

   J. Phys.: Condens. Matter. **22**, 486007 (2010).

   Sharma V. K., Chattopadhyay M. K., Nath S. K., Sokhey K. J. S., Kumar R., Tiwari P., and Roy S. B.

Chapter 8

Summary and future outlook

8.1 Summary and conclusion of the results

We have investigated the electrical, magnetic, thermal and mechanical properties of Ni-Mn-X (X = Sn,In) based off-stoichiometric Heusler alloys focusing on the temperature and magnetic field induced martensitic transition observed in some compositions of these alloy systems. In these investigations we have taken $Ni_{50}Mn_{34}Sn_{16}$ and $Ni_{50}Mn_{34}In_{16}$ alloys as suitable representatives of these alloy systems. The results of our study on these alloy samples, suggest that a magnetic field induced martensite to austenite phase transition in these alloys is correlated with the shift of transition temperature in applied magnetic field and also with the temperature width of the transition. It has been inferred that a larger shift of transition temperature in magnetic field along with a smaller width of the transition, are likely to facilitate this magnetic field induced phase transition. Our studies also suggest that the transition in Ni-Mn-X alloys is more sensitive to the compositional variation than anticipated from the phase diagrams reported in literature.

The magnetic field induced martensite–austenite phase transition in $Ni_{50}Mn_{34}In_{16}$ alloys is found to impart interesting functional properties to this alloy. The alloy is found to exhibit a large magnetoresistance of nearly 65%, large inverse magnetocaloric effect with an isothermal magnetic entropy change of nearly 19 J/kg-K and an effective refrigerant capacity of nearly 100 J/kg, and a magnetostriction of nearly 0.1 % in a field of 50 kOe. This present study highlights the potential of $Ni_{50}Mn_{34}In_{16}$ alloy for magnetic refrigeration, magnetic field controlled actuation and magnetoresistance based applications.

Investigations in the field induced martensite-austenite phase transition in $Ni_{50}Mn_{34}In_{16}$ alloy suggests that the criterion of relating the negative slope of the H/M vs. M^2 isotherms to the first-order magnetic phase transitions is not applicable for all the magnetic phase transitions. In case of disorder-influenced first-order phase transition a decrease in the slope of the H/M vs. M^2 isotherm is found to be useful for characterizing the first-order nature of magnetic transition. Scanning Hall probe imaging experiments on $Ni_{50}Mn_{34}In_{16}$ alloy made during the present study have provided clear visual evidence of the coexistence of the martensite and austenite phases across the magnetic field induced martensite–austenite phase transition in this alloy. This supports the disorder broadened first-order nature of the phase transition. Thermomagnetic history effects are found to play an important role in the evolution of the phase fractions across this phase transition and hence in the functional properties observed across this transition. The local magnetization loops constructed from the Hall images suggest a landscape of the critical field of the martensite-austenite phase transition, thus confirming the disorder-influenced nature of the transition.

The substitution of Mn by Cr or Ni by Cu in $Ni_{50}Mn_{34}In_{16}$ alloy as well as the application of hydrostatic pressure is found to elevate the temperature of martensitic transition towards room temperature, thus making the alloy useful for room temperature applications. On the other hand, the transition temperature decreases with substitution of Mn by Fe. The present study shows that the shift in the martensitic transition in the Ni-Mn-In alloy with chemical substitution and under hydrostatic pressure is correlated with a change in the ferromagnetic interaction in this alloy. Decreased ferromagnetic interactions are found to be related with an increase in the transition temperature and vice versa. Further, the temperature dependence of the isothermal entropy change under different pressures is found to follow a universal curve for a given magnetic field change. The existence of such a universal curve, which is not actually expected in the case of a first-order phase transition, has been understood in the framework of disorder-broadened magnetic field induced first-order phase transition.

It has been found that in the presence of high magnetic field, the process of the austenite to martensite transition in $Ni_{50}Mn_{34}In_{16}$ gets kinetically arrested. Our result suggest that in the $Ni_{50}(Mn, 1\%Fe)_{34}In_{16}$ alloy, the transition is partially arrested even in zero applied field and it gets completely arrested in field of 50 kOe. This low temperature state in such cases is a non-equilibrium state, and its dynamical response is quite similar to that observed in structural glasses. The degree of kinetic arrest of the austenite to martensite phase transition in $Ni_{50}Mn_{34}In_{16}$ is found to decrease with the application of external pressure.

8.2 Scope for future work

The present work suggests following directions for future investigations.

Studies which could provide information about the local environment at crystal sites could uncover the correlation of the martensitic transition and related functional properties in Ni-Mn-X alloys with the knowledge of distribution of atoms at crystal sites. Such studies are likely to throw light on why the martensitic transition and the associated functional properties are so sensitive to compositional change. This in turn will facilitate identification of new Heusler alloy compositions with enhanced functional properties.

In the present work the temperature regime of martensite-austenite phase transition has been elevated from around 240 K to room temperature by chemical substitution in the

$Ni_{50}Mn_{34}In_{16}$ alloy. It will be interesting to employ such chemical substitution in alloys with higher transition temperatures (say $Ni_{50}Mn_{35}In_{15}$ where transition temperature is above 350 K) to lower the transition temperature to room temperature (say substituting Mn by Fe; such substitution is found to lower the transition temperature in the present study).

It will be interesting to investigate whether other functionalities in $Ni_{50}Mn_{34}In_{16}$ follow a universal curve under various pressures for a constant field excursion as followed by the isothermal entropy change. It is also worth investigating whether any functionality (isothermal magnetic entropy change or any other functional property) follows a universal curve under constant pressures for a constant field excursion in the various alloys formed by chemical substitution. It will also be interesting to investigate such universal curve in other systems exhibiting disorder broadened magnetic field induced first-order phase transition.

It will be interesting to study the various other physical properties like thermal conductivity, thermopower, Hall effect etc. in $Ni_{50}Mn_{34}Sn_{16}$ and $Ni_{50}Mn_{34}In_{16}$, and also the effect of pressure on the functionalities in the alloys formed by further chemical substitutions in $Ni_{50}Mn_{34}Sn_{16}$ and $Ni_{50}Mn_{34}In_{16}$. The prospect of investigations in these directions is already evident in some recent works [8.1, 8.2]

The kinetic arrest of magneto-structural transition has now become a subject of considerable interest [8.3-8.12]. In this respect the $Ni_{50}(Mn,1\%Fe)_{34}In_{16}$ alloy where the signature of the kinetic arrest of austenite to martensite phase transition exists even in zero or low applied magnetic field, provides an interesting platform for further study. It will be interesting to image the austenite to martensite phase transition in $Ni_{50}(Mn,1\%Fe)_{34}In_{16}$ alloy with a scanning Hall probe and also to explore the effect of pressure on the kinetic arrest of the austenite to martensite phase transition.

References

Chapter 1:

[1.1] Buehler W.J. et al. 1963 *J. Appl. Phys*. **34**, 1475

[1.2] Ostuka K. and Wayman C. M. 1998 *Shape Memory Materials* (Cambridge University Press, Cambridge)

[1.3] Ullakko K. et al. 1996 *Appl. Phys. Lett.* **69,** 1966

[1.4] Sozinov A. et al. 2002 *Appl. Phys. Lett.* **80,** 1746

[1.5] Sutou Y. et al. 2004 *Appl. Phys. Lett.* **85**, 4358

[1.6] Blundell S. 2001 *Magnetism in Condensed Matter* (Oxford University Press, New York)

[1.7] Cullity B. D. and Graham C. D. 2009 *Introduction to Magnetic Materials* (IEEE Press, New Jersey)

[1.8] Chikazumi S. 1997 *Physics of Ferromagnetism* (Oxford University Press, New York)

[1.9] Hurd C. M. 1982 *Contemp. Phys*. **23**, 469

[1.10] K. Huang 1963 *Statistical mechanics* (John Willey & Sons, New York)

[1.11] Reichl L. E. 1980 *A modern course in statistical mechanics* (University of Texas press, Austin)

[1.12] Stanley H. E. 1971 *Phase Transitions and Critical Phenomena* (Oxford University Press, New York)

[1.13] Chaikin P. M. and Lubensky T. C. 1998 *Principles of condensed matter physics* (Cambridge University Press, Cambridge)

[1.14] White R. M. and Geballe T. H. 1979 *Long Range Order in Solids* (Academic Press, New York)

[1.15] Imry Y. and Wortis M. 1980 *Phys. Rev.* B **19,** 3580

[1.16] Roy S. B. and Chaddah P. 2004 *Phase Transit.* **77,** 767

[1.17] Chattopadhyay M. K. et al. 2003 *Phys. Rev.* B **68,** 174404

[1.18] Cohen M. et al. 1979 *Proc. ICOMAT* (Cambridge (MA): MIT), p. 1

[1.19] Kernot G. 2000 *Phase transformations in Materials* (Willey-VCH, Weinheim)

[1.20] Ostuka K. and Kakeshita T. 2002 *MRS Bulletin* **27**, 91

[1.21] Bhattacharya K. 2003 Microstructure of Martensite; *Why it forms and How it Gives Rise to Shape Memory Effect* (Oxford University Press, Oxford)

[1.22] Enkovaara J. et al. 2004 *Mater.Sci. Eng.* A **378,** 52

[1.23] Karaca H. E. et al. 2006 *Acta Mater.* **54,** 233

[1.24] Murray S. J. et al. 2000 *Appl. Phys.Lett.* **77**, 886

[1.25] Planes A. et al. 2009 *J. Phys.: Condens. Matter* **21,** 233201

[1.26] Tishin A. M. and Spichkin Y. I. 2003 *The Magnetocaloric Effect and its Applications* (Institute of Physics Publishing, Bristol)

[1.27] Hu F. et al. 2000 *Appl. Phys. Lett.* **76,** 3460

[1.28] Hu F. et al. 2001 *Phys. Rev.* B **64,** 132412

[1.29] Marcos J. et al. 2002 *Phys. Rev.* B **66,** 224413

[1.30] Marcos J. et al. 2003 *Phys. Rev.* B **68,** 094401

[1.31] Srivastava V. K. et al. 2006 *Appl. Phys. Lett.* **89**, 222107

[1.32] Zeng M. et al. 2010 *J. Appl. Phys.* **108**, 053716

[1.33] Krenke T. et al. 2006 *Phys. Rev.* B **73**, 174413

[1.34] Krenke T. et al. 2005 *Phys. Rev.* B **72**, 14412

Chapter2:

[2.1] User's Manual, Tri-arc Furnace Model 5TA (Centorr Vacuum Industries, USA)

[2.2] Dyson N. A. 1973 *X-ray in Atomic and Nuclear Physics* (Cambridge University Press, New York)

[2.3] Leng Y. 2008 *Materials Characterization: Introduction to Microscopic and Spectroscopic Methods* (JohnWiley & Sons (Asia) Pte Ltd, Singapore)

[2.4] Ibach H and Luth H. 1991 *Solid-state Physics: An Introduction to Principles of Material Science* (Springer-Verlag, Berlin)

[2.5] Kittel C. 2001 *Introduction to Solid State Physics* (John Wiley & Sons, Singapore)

[2.6] Cullity B. D. 1978 *Elements of X-ray Diffraction* (Addision-Wesley, Reading, Massachusetts)

[2.7] Aktas B. And Mikailov F. 2009 *Advances in Nanoscale Magnetism* (Springer-Verlag, Berlin)

[2.8] Webster P. J. And Ziebeck 1973 *J. Phys. Chem. Solids* **34,** 1647

[2.9] Ziebeck K. R. A. And Webster P. J. 1974 *J. Phys. Chem. Solids* **35**, 1

[2.10] Ziman Z. M. 1962 *Electrons in Metals* (Taylor and Francis, London)

[2.11] Rossiter P. L. 1991 *The Electrical Resistivity of metals and Alloys* (Cambridge University Press, Cambridge)

[2.12] Coey J. M. D. 2009 *Magnetism and Magnetism and Magnetic Materials* (Cambridge University Press, New York)

[2.13] Janawadkar M. P. et al. 1999 *Current Science* **77,** 759

[2.14] Fossheim K. F. and Sudbo A. 2004 *Superconductivity: Physics and Applications* (John Willey & Sons, Chichester).

[2.15] McElfresh M. 1994 *Fundamentals of magnetism and Magnetic Measurements: Featuring Quantum Design's Magnetic Property Measurement System* (Quantum Design, USA)

[2.16] Jackson J. D. 1999 *Classical Electrodynamics* (John Wiley & Sons, Singapore)

[2.17] Cullity B. D. and Graham C. D. 2009 *Introduction to Magnetic Materials* (John Wiley & Sons, New Jersey)

[2.18] easyLab Mcell-10 User Guide (easyLab Technologies Limited, UK)

[2.19] Heat Capacity Option User's Manual, Physical Property Measurement System (PPMS, Quantum Design, USA)

[2.20] Gabbot P. 2008 *Principles and Applications of Thermal Analysis* (Blackwell Publishing, Oxford)

[2.21] Marcos J. et al. 2003 *Rev. Sci. Inst.* **74**, 4768

[2.22] Scott. M. G. and Ramachnadrarao P. 1977 *Mater. Sci. Eng.* **29**, 137

[2.23] Tishin A. M. and Spichkin Y. I. 2003 *The Magnetocaloric Effect and its Applications* (Institute of Physics Publishing, London).

[2.24] Pecharsky V. K. and Gschneidner K. A. Jr. 1999 *J. Magn. Magn. Mater.* **200**, 44

[2.25] Vendan S. P. et al. 2010 *Acta Technica Corviniensis–Bull. Eng.* Fascicule **3**, 49

[2.26] Pecharsky V. K. and Gschneidner K. A. Jr. 1999 *J. Appl. Phys.* **86,** 565

[2.27] McMichael R. D. et al. 1993 *J. Appl. Phys.***73,** 6946

[2.28] Tocado L. et al. 2009 *J. Appl. Phys.* **105,** 093918

[2.29] Recarte V. et al. 2010 *J. Appl. Phys.* **107,** 053501

[2.30] Murray W. M. and Miller W. R. 1992 *The Bonded Electrical Resistance Strain Gauge* (Oxford University Press, New York)

[2.31] Tokyo Sokki Kenkyujo Co., Ltd., Tokyo-140-8560

[2.32] Okaji M. et al. 1997 *Cryogenics* **37,** 251

[2.33] Martien D. *Introduction to AC Susceptibility, MPMS Application Note* (Quantum Design Inc., USA)]

[2.34] Hein R. A. et al. 1991 *Magnetic Susceptibility of Superconductors and other Spin Systems* (Plenum Press, New York)

[2.35] Ramsden E. 2006 *Hall-Effect Sensors: Theory and Applications* 2ed.(NEWNES, Burlington, USA)

[2.36] G. K. Perkins et al. 2002 *Supercond. Sci. Technol.* **15**, 1156

[2.37] Perkins G. K. et al. 2001 *IEEE Trans. Appl. Supercond.* **11,** 3186

Chapter 3:

[3.1] Sutou Y. et al. 2004 *Appl. Phys. Lett.* **85**, 4358

[3.2] Webster P J and Ziebeck K R A 1973 *J. Phys. Chem. Solids* **34,** 1647

[3.3] Raphael M. P. et al. 2002 *Phys. Rev.* B **66,** 104429

[3.4] FULLPROF [http://www.ill.eu/sites/fullprof/]

[3.5] Krenke T. et al. 2006 *Phys. Rev.* B **73,** 174413

[3.6] Krenke T. et al. 2005 *Phys. Rev.* B **72,** 014412

[3.7] Chernenko V. A. et al. 2003 *Phys. Rev.* B **67,** 064407

[3.8] Brown P. J. 2006 *J. Phys.: Condens. Matter* **18,** 2249

[3.9] Krenke T. et al. 2007 *Phys. Rev.* B **75,** 104414

[3.10] Planes A. et al. 2007 *J. Magn. Magn. Mater.* **310,** 2767

[3.11] Bean C. P. and Rodell D. S. 1962 *Phys. Rev.* **126,** 104

[3.12] Pecharsky V. K. et al. 2003 *Phys. Rev. Lett.* **91,** 197204

[3.13] Roy S. B. et al. 2004 *Phys. Rev. Lett.* **92,** 147203

[3.14] Koyama K. et al. 2006 *Appl. Phys. Lett.* **88,** 132505

[3.15] Chaikin P. M. and Lubensky T. C. 1995 *Principles of Condensed Matter Physics* (Cambridge, Cambridge University Press)

[3.16] Imry Y. and Wortis M. 1980 *Phys. Rev.* B **19,** 3580.

[3.17] Roy S. B. and Chaddah P. 2004 *Phase Transit.* **77,** 767

[3.18] Chattopadhyay M. K. et al. 2003 *Phys. Rev.* B **68,** 174404

[3.19] Tiwari M. K. et al. 2004 *Spectrochim. Acta,* Part B **59**, 1141

[3.20] Pathak A. K. et al. 2007 *Appl. Phys. Lett.* **90**, 262504

[3.21] Bhobe P. A. et al.2008 *J. Phys. D: Appl. Phys.* **41**, 045004

[3.22] Ziman J. M. 1972 *Principles of the Theory of Solids*, 2nd ed. (Press Syndicate of the University of Cambridge, New York), p. 225

[3.23] Bhobe P. A. et al. 2008 *J. Phys. D: Appl. Phys.* **41**, 235006

[3.24] Khan M.et al. 2008 *J. Phys.: Condens. Matter* **20**, 235204

[3.25] Pathak A. K. et al. 2009 *J. Phys. D: Appl. Phys.* **42**, 045004

[3.26] Neumann K.U. et al. 2002 *J. Phys.: Condens. Matter* **14**, 1371

[3.27] Aharoni A. 1996 *Introduction to the Theory of Ferromagnetism* (Oxford University Press, Oxford)

[3.28] Wurmehl S. et al. 2007 *Appl. Phys. Lett.* **91**, 052506

[3.29] Wurmehl S. et al. 2008 *J. Appl. Phys.* **103**, 07D706

Chapter 4:

[4.1] Algarabel P. A. et al.1995 *Appl. Phys. Lett.* **66**, 3062

[4.2 Morellon L. et al.1998 *Appl. Phys. Lett.* **73**, 3462

[4.3] Mira J. et al.2003 *Phys. Rev. Lett.* **90**, 097203

[4.4] Pecharsky V. K. et al. 2003 *Phys. Rev. Lett.* **91,** 197204

[4.5] Pecharsky V. K. and Gschneidner Jr. K. A. 1997 *Phys. Rev. Lett.***78,** 4494

[4.6] Pecharsky V. K. and Gschneidner Jr. K. A. 1997 *Appl. Phys. Lett.***70,** 3299

[4.7] Tegus O. et al. 2002 *Nature* **415,** 150

[4.8] Wada H. and Tanabe Y. 2001 *Appl. Phys. Lett.* **79,** 3302

[4.9] Gama S. et al. 2004 *Phys.Rev. Lett.* **93,** 237202

[4.10] Zhou X. et al. 2004 *J. Phys.:Condens. Matter* **16,** L39

[4.11] Terashita H. et al. 2005 *Phys. Rev.* B **72,** 132415

[4.12] Manekar M. and Roy S. B. 2008 *J. Phys. D: Appl. Phys.***41,** 192004

[4.13] Chattopadhyay M. K. et al. 2006 *J. Phys.D: Appl. Phys.* **39,** 1006

[4.14] Kainuma R et al. 2006 *Appl. Phys. Lett.* **88,** 192513

[4.15] Kainuma R et al. 2006 *Nature* **439,** 957

[4.16] Yu S. Y. et al. 2006 *Appl. Phys. Lett.* **89**,162503

[4.17] Krenke T. et al. 2005 *Nature Mater.* **4,** 450

[4.18] Gomes A. M. et al. 2004 *Appl. Phys. Lett.* **85,** 8794

[4.19] Reis M. S. et al. 2005 *Phys. Rev.* B **71,** 144413

[4.20] Benford S. M. and Brown G. V. 1981 *J. Appl. Phys.* **52,** 2110

[4.21]Oikawa K. et al. 2006 *Appl. Phys. Lett.* **88**,122507

[4.22] Provenzano V. et al. 2004 *Nature* **429,** 853

[4.23] Gschneidner Jr. K. A. et al. 1999 *Mater. Sci. Forum* **315–317,** 69

[4.24] Pecharsky V. K. and Gschneidner Jr. K. A. 2001 *J. Appl. Phys.* **90,** 4614

[4.25] Tishin A. M. and Spichkin Y. I. 2003 *The Magnetocaloric Effect and its Applications* (Institute of Physics Publishing, Bristol)

[4.26] Pecharsky V. K. and Gschneidner K. A. Jr. 1999 *J. Appl. Phys.* **86.** 565

[4.27] Pecharsky V. K. and Gschneidner K. A. Jr. 1999 *J. Appl. Phys.* **86,** 6315

[4.28] Wu G. H. et al. 1999 *Appl.Phys. Lett.* **75,** 2990

[4.29] Vasilev A. N. et al. 2000 *Int. J. Appl. Electromagn. Mech.* **12,** 35

[4.30] Aksoy S. et al. 2007 *Appl. Phys. Lett.***91,** 251915

[4.31] Krenke T. et al. 2007 *Phys. Rev.* B **75,** 104414

Chapter 5:

[5.1] Aharoni A. 1996 *Introduction to the Theory of Ferromagnetism* (Oxford University Press, Oxford)

[5.2] Banerjee S. K. 1964 *Phys. Lett.* **12,** 16

[5.3] Jiang W. et al. 2008 *J. Magn. Magn. Mater.* **320,** 2144

[5.4] Mira J. et al. 2002 *Physica* B **320,** 23

[5.5] Mira J. et al. 1999 *Phys. Rev.* B **60,** 2998

[5.6] Otero-Leal M. et al. 2007 *Phys. Rev.* B **76,** 174413

[5.7] Rivadulla F. et al. 2004 *Phys. Rev.* B **70,** 172410

[5.8] Amaral V. S. et al. 2002 *J. Magn. Magn. Mater.* **242–245,** 655

[5.9] Zhou X. et al. 2006 *Phys. Rev.* B **73,** 012412

[5.10] Roy S. B. et al. 2008 *Acta Mater.* **56,** 5895

[5.11] Ramos R. A. et al. 1999 *Phys. Rev.* B **59,** 9053

[5.12] Bhobe P. A. et al. 2007 *Appl. Phys. Lett.* **91,** 242503

[5.13] Imry Y. and Wortis M. 1979 *Phys. Rev.* B **19,** 3580

[5.14] Manekar M. A. et al. 2001 *Phys. Rev.* B **64,** 104416

[5.15] Roy S. B. and Chaddah P. 2004 *Phase Transit.* **77,** 767

[5.16] Chattopadhyay M. K. et al. 2003 *Phys. Rev.* B **68,** 174404

[5.17] Guenin G. 1989 *Phase Transit.* **14,** 165

[5.18] Chaikin P. M. and Lubensky T. C. 1995 *Principles of Condensed Matter Physics* (Cambridge University Press, Cambridge)

[5.19] Bean C. P. and Rodell D. S. 1962 *Phys. Rev.* **126,** 104

[5.20] Tegus O. et al. 2002 *Physica* B **319,** 174

[5.21] Chattopadhyay M. K. and Roy S. B. 2008 *J. Phys.: Condens. Matter* **20,** 025209

[5.22] White R. M. and Geballe T. H. 1979 *Long Range Order in Solids* (Academic Press, New York)

[5.23] Chattopadhyay M. K. et al. 2006 *J. Phys. D: Appl. Phys.* **39,** 1006

[5.24] Roy S. B. et al. 2004 *Phys. Rev. Lett.* **92,** 147203

[5.25] Moore J. D. 2006 *Phys. Rev.* B **73,** 144426

[5.26] Chattopadhyay M. K. et al. 2005 *Phys. Rev.* B **71,** 024523

[5.27] Avrami M. 1939 *J. Chem. Phys.* **7,** 1103

[5.28] Manekar M. and Roy S. B. 2008 *J. Phys.: Condens. Matter* **20,** 325208

[5.29] Rai A, K, 2009 *J. Nucl. Mater.* **383,** 215

[5.30] Soibel A. 2000 *Nature* **406,** 282

[5.31] Joseph R. I. and Schlomann E. 1965 *J. Appl. Phys.* **36,** 1579

Chapter 6:

[6.1] Planes A. et al. 2009 *J. Phys.: Condens. Matter* **21,** 233201

[6.2] Krenke T. et al. 2007 *J. Magn. Magn. Mater.* **310,** 2788

[6.3] Manosa L. et al. 2008 *Appl. Phys. Lett.* **92,** 012515

[6.4] Krenke T. et al. 2007 *Phys. Rev.* B **75,** 104414

[6.5] Poole C. P. 2004 *Encyclopaedic Dictionary of Condensed Matter Physics* (Academic Press, San Diego, USA)

[6.6] Ye M. et al. 2010 *Phys. Rev. Lett.* **104**, 176401

[6.7]Aksoy S. et al. 2007 *Appl. Phys. Lett.* **91,** 241916

[6.8] Zhang C. L. et al. 2007 *J. Phys. D: Appl. Phys.* **40,** 7287

[6.9] Sutou Y. et al. 2004 *Appl. Phys. Lett.* **85,** 4358

[6.10] Passamani E. C. et al. 2009 *J. Appl. Phys.* **105,** 033919

[6.11] Brown P. J. et al. 2006 *J. Phys.: Condens. Matter* **18,** 2249

[6.12] Khovaylo V. V. et al. 2009 *Phys. Rev.* B **80,** 144409

[6.13] HarrisonW. A. 1999 *Elementary Electronic Structure* (World Scientific, Singapore)

[6.14] Chaikin P. M. and Lubensky T. C. 1995 *Principles of Condensed Matter Physics* (Cambridge University Press, Cambridge)

[6.15] White R. M. and Geballe T. H. 1979 *Long Range Order in Solids* (Academic Press, New York)

[6.16] Pecharsky V. K. and Gschneidner K. A. Jr .1999 *J. Appl Phys.* **86,** 565

[6.17] Benford S. M. and Brown G. V. 1981 *J. Appl. Phys.* **52,** 2110

[6.18] Gschneidner K .A .Jr. et al. 1999 *Mater. Sci. Forum* **315–317,** 69

[6.19] Provenzano V. et al. 2004 *Nature* **429,** 853

[6.20] Tocado L. et al. 2009 *J. Appl. Phys.* **105,** 093918

[6.21] Recarte V. et al. 2010 *J. Appl. Phys.* **107,** 053501

[6.22] Pecharsky V. K. and Gschneidner K. A. Jr. 1997 *Phys. Rev. Lett.* **78,** 4494

[6.23] Kainuma R . *et al.* 2006 *Nature* **439,** 957

[6.24] Caron L. et al. 2009 *J. Magn. Magn. Mater.* **321,** 3559

[6.25]Yasuda T. et al. 2007 *J. Magn. Magn. Mater.* **310**, 2770

[6.26] Sasioglu E. et al. 2004 *Phys. Rev.* B 7**0**, 024427

[6.27] Nayak A. K. et al. 2009 *J. Appl. Phys*. **106**, 053901

[6.28] Albertini F. et al. 2007 *J. Magn. Magn. Mater*. **316**, 364

[6.29] Franco V. et al. 2006 *Appl. Phys. Lett*. **89**, 222512

[6.30] Bonilla C. M. et al. 2010 *J. Appl. Phys*. **107**, 09E131

Chapter 7:

[7.1] Manekar M. A. et al.2003 *Phys. Rev.* B **68**, 174404

[7.2] Roy S. B. et al. 2004 *Phys. Rev. Lett.* **92**, 147203

[7.3]Tang H. et al. 2004 *Phys. Rev.* B **69**, 064410

[7.4] Maat S. et al. 2005 *Phys. Rev.* B **72**, 214432

[7.5] Sengupta K. and Sampathkumaran E. V. 2006 *Phys. Rev.* B **73**, 020406 (R)

[7.6] Mahendiran R. et al.2002 *Phys. Rev. Lett.* **89**,286602

[7.7] Dho J. and Hur N. H. 2003 *Phys. Rev.* B **67**, 214414.

[7.8] Kumar K. et al. 2006 *Phys. Rev*. B **73**, 184435

[7.9] Wu W. et al. 2006 *Nat. Mater.* **5**, 881

[7.10] Roy S. B. and Chaddah P. 2004 *Phase Transitions* **77**, 767

[7.11] Imry Y. and Wortis M. 1979 *Phys. Rev.* B **19**, 3580

[7.12] Dagotto E. 2003 *The Physics of Manganites and Related Compounds* (Springer, Berlin), and references therein.

[7.13] Chattopadhyay M. K. et al. 2005 *Phys. Rev.* B **72**, 180401(R), and references there in.

[7.14] Brawer S. 1985 *Relaxation in Viscous Liquids and Glasses* (The American Ceramic Society, Columbus, Ohio)

[7.15] Debenedetti P. G. and. Stillinger F. H 2001 *Nature* **410**, 259

[7.16] Roy S. B. et al.2006 *Phys. Rev.* B **74**, 012403

[7.17] S. Sarkar et al. 2005 *Phys. Rev. Lett.* **95**, 205702

[7.18] Sharma P. A. et al. 2008 *Phys. Rev.* B**78,** 134205

[7.19] Roy S. B. and Chattopadhyay M. K. 2009 *Phys. Rev. B* **79** 052407, and references therein.

[7.20] Sharma V. K. et al. 2007 *Phys. Rev.* B **76**, 140401(R)

[7.21] Ito W. et al. 2008 *Appl. Phys. Lett.* **92**, 021908

[7.22] Ito W. et al. 2010 *Scripta Mater.* **63**, 73

[7.23] Umestu R. Y. et al. *Scripta Mater.* **60**, 25

[7.24] Xu X. et al. 2009 *Appl. Phys. Lett.* **95**, 181905

[7.25] Kustov S. et al. 2009 *Appl. Phys. Lett.* **94**, 191901

[7.26] Lee Y. et al. 2011 *Scripta Mater.* **64**, 927

[7.27] Chaterjee et al. 2008 *Phys. Rev.* B **77**, 224440

Chapter 8:

[8.1] Sharathchandra L. S. et al. 2010 *Phys. Rev.* B **81**, 195105

[8.2] Chattopadhyay M. K. et al. 2011 *Phys. Rev*. B **84**, 064417

[8.3] Chattopadhyay M. K. et al. 2005 *Phys. Rev*. B **72**, 180401 (R)

[8.4] Sengupta K. and Sampathkumaran E. V. 2006 *Phys. Rev.* B **73**, 020406 (R)

[8.5] Roy S. B. et al. 2006 *Phys. Rev.* B **74**, 012403

[8.6] Roy S. B. et al. 2007 *Phys. Rev. B* **75**,184410

[8.7] Roy S. B. and Chattopadhyay M. K. 2007 *Europhys. Lett.* **79**, 47007

[8.8] Sharma P. A. et al. 2008 *Phys. Rev*. B **78**, 134205

[8.9] Chaddah P. et al. 2008 *Phys. Rev*. B **77**, 100402 (R)

[8.10] Kushwaha P. et al. 2008 *J. Phys.: Condens. Matter* **20**, 022204

[8.11] Banerjee A. 2009 *J. Phys.: Condens. Matter* **21,** 026002

[8.12] Manekar M. et al. 2011 *J. Phys.: Condens. Matter* **23**, 086001